National PhD Program in

Defense against natural risks and ecological transition of built environment

XXXVIII Cycle

Advanced beam finite element models with warping and bond-slip for concrete structures: addressing objectivity issues, prestressing and time-dependent effects

PhD Candidate:

Luca Parente

Advisor:

Prof. Enrico Spacone

Co-Advisor:

Prof. Daniela Addessi

International Co-Advisor:

Prof. Bassam A. Izzuddin

Università di Catania

Università degli Studi "G. d'Annunzio" Chieti – Pescara

SAPIENZA UNIVERSITÀ DI ROMA

Imperial College London

Rome, November 2025

National PhD Program in
Defense against natural risks and ecological transition of built environment

XXXVIII Cycle

PhD Thesis in Structural Engineering

Advanced beam finite element models with warping and bond-slip for concrete structures: addressing objectivity issues, prestressing and time-dependent effects

PhD Candidate: Luca Parente

Advisors:
Prof. *Enrico Spacone*
G. D'Annunzio University of Chieti-Pescara, Department of Engineering and Geology

Prof. *Daniela Addessi*
Sapienza University of Rome, Department of Structural and Geotechnical Engineering

Prof. *Bassam A. Izzuddin*
Imperial College of London, Department of Civil and Environmental Engineering

Administrative seat:
University of Catania, Department of Civil Engineering and Architecture

Affiliations:
G. D'Annunzio University of Chieti-Pescara, Department of Engineering and Geology
Sapienza University of Rome, Department of Structural and Geotechnical Engineering
Imperial College of London, Department of Civil and Environmental Engineering (Visiting Researcher)

PhD scholarship funded by the Italian Ministry of University and Research (MUR) under PNRR – DM 351/2022

Rome, November 2025

Abstract

This thesis investigates advanced beam finite element formulations for the nonlinear analysis of reinforced concrete (RC), prestressed concrete (PC), and composite frames, with the objective of improving numerical and mechanical accuracy while maintaining computational efficiency. This work builds on well-established beam models and examines, under small-strain kinematics, the theoretical equivalence between mixed and force-based formulations. On this basis, a new force-based bond-slip formulation is proposed, where reinforcement-concrete interaction is embedded along the member length and prestressing can be applied directly at the element level. The approach supports arbitrary tendon layouts through appropriate rotations for curved fibers, and accommodates construction stages and time-dependent phenomena (creep, shrinkage, relaxation) via history-dependent internal variables and a consistent numerical solution strategy.

A central contribution is the derivation of enriched elements with warping and bond-slip, including a fully mixed warping-bond-slip formulation. Warping is introduced at the section level through shape functions constructed via dedicated section warping functions, which give an orthogonal basis for the additional displacement field. This yields a compact set of warping degrees of freedom, reduces the size of the section operators, and lowers the overall computational cost, while enhancing section kinematics in the presence of shear and torsion. The constitutive framework integrates three-dimensional plasticity and plastic-damage with one-dimensional cyclic laws for steel reinforcement, prestressing tendons, concrete, bond-slip and other materials used in the fiber sections. Within this framework, a consistent algorithmic tangent for the 3D damage/plasticity model is derived and implemented, ensuring robust quadratic convergence of the global Newton iterations.

From a computational standpoint, this work formalizes the selection of shape functions and quadrature rules for the element and the section interpolation, and extends local regularization strategies suitable for softening materials. Nevertheless, both displacement-based, force-based and mixed beam elements suffer from localization issues when softening occurs, leading to mesh-dependent responses, although the mechanisms differ. In this work, attention is focused on localization due to cracking, as localization from concrete crushing has been extensively investigated in previous studies. To overcome these limitations, enhanced formulations with bond-slip and warping have been proposed in both displacement-based (D-BW) and mixed (M-BW) settings. These enrichments restore numerical objectivity by correctly localizing damage and slip, and preventing spurious crack spreading across the mesh.

The proposed models are assessed through an extensive set of applications. These consist of mesh- and integration-objectivity benchmarks; cantilever and beam tests under perfect-bond, no-bond, and general bond conditions; and prestressed elements with draped tendons, staged

transfer, and long-term effects. The results demonstrate accuracy in nonlinear static and time-dependent analyses, computational efficiency with a limited number of elements, fibers, and integration points, and stable performance even in softening regimes. Comparative studies against experimental evidence and refined numerical references confirm the improved predictive fidelity of the formulations and their capacity to capture realistic crack patterns and force redistribution under evolving bond conditions.

Overall, the thesis delivers a cohesive and extensible framework for advanced beam elements that is implementation-ready for general-purpose analysis codes. The block-wise organization naturally supports extensions to different materials and cross-section types, and the enriched kinematics with bond-slip and warping provides an effective route to objectivity and reliability in the analysis of RC, PC, and composite structures subjected to coupled axial-flexural-shear-torsional and time-dependent effects.

Contents

List of Figures

List of Tables

Chapter 1

Introduction

1.1 Motivations and state of the art

Beam finite elements are essential tools for structural analysis and design. They provide a highly efficient and sufficiently accurate means of representing structural members such as beams, columns, and frames in large-scale simulations. Classical formulations, typically displacement-based, have long served as the standard approach for analyzing structures under service-level loads and moderate inelastic deformations.

However, modern structural engineering practice increasingly demands more advanced simulation capabilities. In particular, performance-based design, seismic assessment, and the evaluation of existing infrastructure require models that can accurately predict structural behavior under severe loading conditions, including large inelastic deformations, damage, and potential collapse. Under such conditions, local phenomena play a critical role in governing global structural response. For reinforced concrete and prestressed concrete members, these include bond-slip interaction between steel and concrete, time-dependent effects such as creep and shrinkage, relaxation of prestressing tendons, and degradation mechanisms like corrosion. For thin-walled or slender sections, shear lag and warping effects must be captured to avoid unrealistic predictions of stress and strain distributions.

Conventional beam element formulations often rely on simplifying assumptions, such as plane sections remaining plane and orthogonal to the axis, which limit their ability to represent these local effects. Furthermore, traditional displacement-based and force-based elements can suffer from non-objective behavior when modeling inelastic material responses characterized by strain softening or damage localization, leading to mesh-sensitive and non-physical results.

These limitations highlight the need for advanced beam finite element formulations that can reliably simulate modern structural systems, including composite and prestressed sections with realistic interaction mechanisms and degradation effects, while remaining efficient and robust for large-scale analyses.

To meet these demands, advanced beam finite element formulations must satisfy three essential criteria:

- The formulation must be capable of capturing both global and local structural behaviors.

This includes representing nonlinear inelastic material responses under large deformations, accurately simulating the spread of plasticity, and incorporating critical local phenomena such as bond-slip interaction, warping, and time-dependent effects. Accurate modeling of these mechanisms is vital for realistic prediction of structural performance, especially under ultimate limit states; [10, 11].

- Structural analysis frequently involves large, complex models with thousands of elements and load cases. An effective beam element must achieve high fidelity without excessive computational cost. Classical concentrated plastic hinge models, while computationally cheap, may misrepresent the spread of inelasticity. Fully distributed inelasticity models can be computationally demanding [12], often expending resources on elastic regions. An optimal formulation balances these demands, delivering accuracy where needed while maintaining practical analysis times.
- Numerical stability is essential for practical application, particularly under severe loading conditions that involve material softening, damage, and localization. Force-based and mixed formulations may encounter numerical difficulties when section stiffness matrices become ill-conditioned or singular, especially in the presence of softening [13, 14]. Robust algorithms must ensure reliable convergence, avoiding failure modes that compromise the integrity of the simulation.

This thesis is motivated by the need to address two fundamental challenges in advanced beam finite element modeling:

- Extending beam elements to accurately model reinforced and prestressed sections, with particular focus on concrete. This requires developing formulations capable of representing local interaction mechanisms and long-term behavior [8, 15]. Accurate simulation of these effects is essential for modern design and assessment of reinforced and prestressed concrete structures, which rely on complex internal and external prestressing layouts and multi-material interfaces.
- Resolving objectivity issues inherent in conventional displacement-based and force-based elements. Classical formulations often exhibit non-physical localization and mesh dependence when modeling softening both in tension and compression [16, 17]. This work aims to introduce consistent regularization strategies and advanced formulations that ensure objective, mesh-independent representation of plasticity spread and damage evolution, maintaining physical realism even under severe loading conditions.

The overall objective of this research is to develop a unified framework of advanced beam finite element formulations that achieve high accuracy, computational efficiency, and numerical robustness. The proposed models are intended to support reliable, large-scale nonlinear analysis of reinforced and prestressed concrete structures to meet the demands of modern structural engineering practice.

1.2 Literature review on beam finite elements

Beam finite elements are fundamental building blocks in a structural analysis software, offering an effective balance between accuracy and computational efficiency. Their development is rooted

in classical beam theory, which provides simplified representations of three-dimensional structural behavior by reducing it to a one-dimensional problem along the member axis.

The earliest and most widely used formulation is the Euler–Bernoulli beam theory, which assumes that cross-sections remain plane and perpendicular to the neutral axis during deformation. This formulation is highly efficient and accurate for slender members dominated by axial and flexural effects, making it suitable for many practical applications in structural engineering. However, its neglect of shear deformations limits its applicability to deep beams, short columns, and cases where shear flexibility significantly affects the response [18, 19, 20, 21].

To address these limitations, the Timoshenko beam theory was introduced [22], relaxing the assumption of normality between cross-sections and the axis. By including shear deformation, Timoshenko's model improves the accuracy of predictions for short, deep, or highly sheared members. Both Euler–Bernoulli and Timoshenko theories remain the basis of most displacement-based finite element (DB FE) formulations used in commercial and research codes [23, 24].

Over the decades, structural analysis practice has evolved to demand increasingly realistic modeling of inelastic behavior. Under severe loading conditions, such as earthquakes, structural members may undergo large deformations, local failures, and highly nonlinear material responses [25]. Simulating these phenomena within beam elements requires moving beyond linear assumptions and simple section behaviors, adopting fiber distributed-plasticity [10], mixed formulations [13], shear-enriched sections [11], and interface/bond-slip models [15, 26, 27, 28, 29].

One important advancement over classical displacement-based formulations has been the introduction of force-based [10, 30] and mixed beam element approaches [13, 24].

Force-based formulations improve the representation of nonlinear behavior by satisfying equilibrium along the element length and interpolating section deformations in a way that can capture the spread of plasticity without lumped hinge regions [16, 6]. This allows for more accurate modeling of distributed inelasticity, which is critical for members subjected to severe loading conditions. Under stress-softening, objectivity is recovered by dedicated regularization strategies tailored to force-based frame elements [5, 31].

Mixed formulations further extend these ideas by introducing independent interpolation of displacements, internal forces, and strains within a consistent variational framework. These formulations provide greater flexibility for modeling complex material behavior and local effects, including section warping and bond-slip interaction [15, 27].

While these advanced formulations offer clear improvements over classical approaches, they also introduce new challenges, such as increased computational complexity [30] and the need for robust algorithms to handle highly nonlinear behavior.

Despite these advancements, challenges remain. Classical formulations overlook local deformations and internal interaction effects. Such effects are critical for accurately modeling reinforced concrete and prestressed members, especially under extreme loading conditions [27, 32].

Moreover, displacement-based and force-based formulations can suffer from non-objective results when simulating softening and damage localization, leading to unrealistic localization effects and sensitivity to mesh refinement [33, 5]. Addressing these limitations has become

increasingly important requiring reliable, physically consistent predictions even under severe nonlinear behavior [16, 17].

The development of enriched beam finite element formulations capable of representing these effects is essential to advance structural analysis tools and ensure safe, economical, and sustainable design and assessment of modern infrastructure.

1.3 Review of force-based and mixed beam element formulations

The evolution of beam finite element formulations beyond classical displacement-based approaches has been driven by the need to accurately simulate inelastic structural response under severe loading conditions. Two major developments have shaped this progression: the introduction of force-based and mixed formulations.

This section traces the development of these advanced approaches, highlighting their theoretical foundations, key algorithmic contributions, and major milestones in their adoption for structural analysis of reinforced and prestressed concrete frames.

1.3.1 Force-based formulations

The force-based (FB) formulation emerged to overcome limitations of displacement-based elements in representing distributed inelasticity [12]. Unlike displacement-based approaches that interpolate nodal displacements and deduce internal forces through differentiation, force-based elements start by satisfying equilibrium of internal forces along the element. Compatibility is then enforced weakly through interpolation of section deformations consistent with these internal forces.

The conceptual development of force-based formulations traces back to work at UC Berkeley in the late 1970s and early 1980s, influenced by the collaboration between Ciampi and Powell [34, 35], and Zeris and Mahin [36, 37]. Early ideas on implementing force-based elements within general-purpose finite element software were refined during Ciampi's sabbatical at Berkeley and continued with students and collaborators in Italy and the United States.

Key advances included the formalization of the implementation algorithm for force-based elements (as in the UCB/EERC-91/17 report by Taucer and Spacone [38]), which clarified how equilibrium-based force shape functions could be integrated with nonlinear material models such as the Bouc-Wen hysteretic law. This work established practical procedures for state determination, using numerical integration along the element and iterative correction of unbalanced forces.

Two primary solution algorithms for state determination were developed to handle nonlinear response:

- The N-L algorithm (iterative at element level, non-iterative at section level), used in early implementations by Ciampi and collaborators (including Filippou, Spacone, Taucer, Petrangeli) [13, 10, 11].
- The L-L algorithm (non-iterative at both levels), later refined by Neuenhofer, Filippou and Addessi [25, 14, 5] to improve computational efficiency for elastic-dominated analyses.

These algorithms became the foundation of widely used implementations in research and practice,

including OpenSees [39], FEAP [40], and other platforms.

A major innovation was combining the force-based formulation with fiber section discretizations, enabling detailed modeling of axial, flexural, and shear behavior, as well as nonlinear material constitutive laws at the fiber level (Ciampi, Spacone, Petrangeli, Neuenhofer, Filippou) [13, 10, 25]. This combination provided a robust tool for simulating RC frame members under seismic loading [41].

Despite these strengths, force-based elements presented challenges:

- Loss of objectivity under strain-softening behavior, leading to mesh-dependent localization without appropriate regularization (addressed in later work on fracture energy-based regularization) [16, 17].
- Numerical instability due to ill-conditioned section stiffness matrices, particularly with complex nonlinear materials [42].

These challenges motivated further research into consistent regularization strategies and algorithmic improvements to ensure robust convergence under severe inelastic deformations.

1.3.2 Mixed formulations

Building on the success of force-based elements, mixed formulations were developed to provide even greater theoretical rigor. Mixed formulations derive from variational principles such as the Hu-Washizu or Hellinger-Reissner functionals [43], treating displacements, internal forces, and strains as independent fields.

This approach allows for a consistent weak form that can incorporate complex material behavior while satisfying equilibrium and compatibility conditions in a more flexible manner. By interpolating multiple fields independently, mixed elements can mitigate numerical issues such as shear locking and provide better control over strain distributions, particularly in inelastic analyses.

Pioneering work on mixed beam formulations was carried out by Petrangeli and Ciampi [44], who explored two- and three-field formulations tailored for inelastic frame analysis. Their research highlighted the advantages of mixed approaches in capturing nonlinear material behavior and interaction effects, such as axial–flexural coupling and the spread of plasticity along members.

Subsequent developments included refinements by Taylor and collaborators [23], who provided variationally consistent formulations suitable for implementation in general-purpose FE software. Hjelmstad also contributed significantly by applying the Hellinger-Reissner principle to derive mixed beam elements with improved stability and accuracy [24].

Mixed formulations are particularly valuable when modeling advanced local phenomena that challenge simpler assumptions. For example, they provide a natural framework for incorporating section warping and bond-slip interaction [15, 45] by introducing additional degrees of freedom and enriching the kinematic description. This capability is essential for realistic analysis of RC and prestressed concrete members where bond-slip effects between steel and concrete critically influence structural response.

However, mixed formulations also introduce new complexities:

- Increased computational cost due to additional fields and higher-order interpolation.
- Numerical stability issues when dealing with material softening or damage localization, requiring robust algorithms for state determination and consistent regularization techniques.

In comparison with force-based formulations, mixed elements offer superior theoretical consistency and flexibility, but demand careful implementation to balance accuracy, efficiency, and robustness.

1.4 Enhanced beam finite elements

1.4.1 New beam finite element formulations

Classical beam finite element formulations rely on simplifying assumptions such as plane sections remaining plane and orthogonal to the axis. While effective for many applications, these assumptions limit their ability to capture important local phenomena that significantly influence structural response, especially under severe loading.

Bond-slip interaction between steel reinforcement and concrete is one of the most critical local effects in reinforced concrete structures [46]. When bond deteriorates, slip occurs, increasing the section's flexibility and reducing the overall stiffness. This phenomenon affects hysteretic behavior under cyclic loading and its deformation capacity.

Modeling bond-slip in beam elements has followed three main strategies [15, 28, 27, 45]. Detailed 2D or 3D models can explicitly represent steel-concrete interfaces but are computationally expensive and impractical for large structures. Concentrated analytical models idealize bond-slip as localized springs at member ends, capturing fixed-end rotations but neglecting distributed slip effects. A more practical approach involves macroscopic beam models with fiber sections, which integrate bond-slip effects into the constitutive behavior along the member length.

Key contributions include early work by Ciampi on bond-slip constitutive laws [35], combined with force-based element algorithms (Spacone, Taucer, Petrangeli), which enabled simulation of RC frames with fiber sections under seismic loading. Monti and Spacone further integrated bond-slip in force-based formulations for beam elements [15]. Later, Ayoub and Filippou proposed mixed formulations that ensured variational consistency while representing bond-slip within fiber sections [26, 47, 48, 49]. More recent developments by Lee focused on improving the efficiency and robustness of these models for nonlinear cyclic analysis [50, 51, 52, 53].

Another class of local effects involves section warping and shear-lag, relevant for thin-walled, slender, or prestressed members [54]. Warping describes out-of-plane deformations of the cross-section under torsion or combined loading, while shear-lag refers to non-uniform axial stress distribution in wide flanges. Ignoring these effects can result in inaccurate predictions of stresses, strains, and failure modes.

To address these challenges, enriched beam formulations have been developed to introduce warping degrees of freedom and capture non-uniform stress states [13, 24]. Saritas and Le Corvec

proposed enhanced models with interpolated warping displacements, enforcing equilibrium between fibers to describe shear and torsional effects [55, 56]. Ferradi and Vieira refined this approach by introducing independent warping modes derived from equilibrium conditions [57, 58, 59, 60].

Di Re developed a 3D beam-column finite element with explicit warping degrees of freedom and a fiber section discretization that captures axial, flexural, shear, and torsional coupling [7, 61, 62]. His formulation, based on the Hu-Washizu variational principle, enables simulation of reinforced concrete members with softening behavior, including damage localization under severe loading.

Mixed formulations are particularly suited for these enriched models. By treating displacements, forces, and strains as independent fields, they allow consistent inclusion of bond-slip and warping effects while maintaining equilibrium and compatibility. Such capabilities are critical for modern analysis of RC and prestressed concrete structures where local effects and material degradation must be accurately represented.

1.4.2 Prestressing in beam finite elements

Prestressed concrete (PC) members are increasingly used in bridges and precast construction because prestressing efficiently redistributes stresses and improves serviceability over long spans. From a numerical standpoint, accurately simulating their nonlinear response requires representing: (i) tendon–concrete interaction (including partial or evolving bond and anchorage behavior), (ii) staged construction and staged prestressing, and (iii) time-dependent losses due to concrete creep–shrinkage and tendon relaxation.

In finite element programs, prestressing has often been modeled either by (a) equivalent loads/strains applied to an RC beam, or (b) explicit discretization of the beam together with tendon truss elements [63, 64]. Several displacement-based (DB) formulations for PC and composite members follow this route [65, 66, 67], but typically require dense meshes and, when based on Euler–Bernoulli kinematics, neglect shear strains. Mixed two-field approaches for externally prestressed systems, pioneered by Ayoub and Filippou, introduce enriched kinematics and bond laws between tendon trusses and RC beams with fiber sections, but still rely on fine discretizations to place internal nodes at deviators/anchors where transfer occurs [26, 47, 48, 49]. Within the broader beam-element literature, force-based (FB) and mixed formulations alleviate the interpolation issues of DB elements under localized curvature/shear, and allow distinct interpolation of forces and displacements, features that are especially attractive for bond–slip problems [37, 5, 27, 23, 68, 69, 70].

A practical and efficient route is to apply the prestressing at the fiber level as equivalent initial strains, in the spirit of Doty [71] and Parente et al [72]. In our earlier 3D FB Timoshenko formulation (perfect bond), tendons are treated as additional fully bonded fibers in each section. This lets us accommodate complex internal tendon layouts with very few elements, while keeping the additional computational burden negligible (new fibers and a handful of bookkeeping features only). The element includes shear components through Timoshenko kinematics, and couples a 3D damage–plasticity law for concrete with a condensation algorithm that expands the beam strain field to a full 3D strain vector while enforcing Navier constraints on transverse stresses

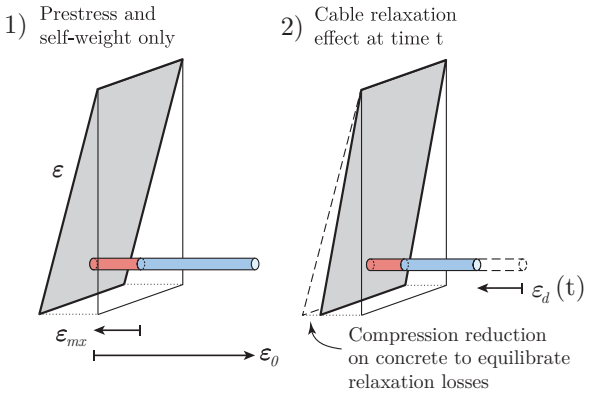

Figure 1.1. Section strain distribution when the positive initial strain $\boldsymbol{\varepsilon}_0(x, t_0)$ and the negative time-dependent strain $\boldsymbol{\varepsilon}_d(x, t)$ are applied to a tendon fiber. Since the tendon tension reduces, compression in the concrete fibers reduces too as a result of equilibrium.

[73, 7, 74, 75]. Figure 1.1 shows how initial strains can easily be applied to tendon fibers to induce prestressing and to evaluate losses such as creep and shrinkage, if applied on concrete fibers, and relaxation, if applied on steel fibers. To prevent pathological localization, a simple local regularization acting on the quadrature scheme is adopted [33, 6, 5]. Implementation-wise, this FB formulation and the prestress/time-dependent logic were realized in OpenSees with the aid of STKO, adding a dedicated load command for prestressing and long-term effects [39, 9]. With this setup, a single element often suffices for typical beams and girders, especially with internal fully bonded tendons.

Building on the above, a new 3D purely force-based beam formulation has been developed to explicitly capture interface bond–slip at the fiber level. The approach assumes only internal force fields and enforces compatibility weakly, introducing interface degrees of freedom governed by nonlinear bond–slip laws. It supports arbitrary 3D tendon paths, staged prestressing, and variable bonding regions (e.g., initially unbonded segments that become bonded, or bond degradation under cyclic/staged loading). Time-dependent losses, concrete creep and shrinkage, and steel relaxation, are incorporated via staged loading techniques that update the fiber-level equivalent strains and tendon stresses over time [76, 49, 77, 78]. The Timoshenko shear description and a 3D damage–plasticity constitutive model for concrete handle coupled shear–flexure failure modes, while localization is controlled with the same efficient local regularization previously adopted. Compared to tendon–beam interaction models tailored to steel–concrete composite systems (mostly planar EB, displacement-based, with interaction concentrated at deviators/anchors) [79, 80, 81, 82, 83, 84, 85, 86, 87, 88], the present formulation targets prestressed concrete members, addresses 3D tendon layouts, progressive bond changes along the strand length, and retains computational efficiency within a beam framework.

Consistent with the enhanced beam-element program outlined above, prestressing is modeled as follows:

1. For fully bonded internal tendons, prestress can be applied at fiber level as equivalent initial strains, with tendons discretized as additional fibers in each section; staged prestress and long-term losses are handled through staged loading updates [71, 76].

2. For cases requiring interface mechanics (partial/evolving bond, anchorage degradation, staged bonding), a bond–slip interaction is introduced in a purely force-based setting, preserving equilibrium in strong form and enforcing compatibility in weak form [26, 47, 48, 49, 27, 23].

3. Shear effects are retained via Timoshenko kinematics, and concrete is modeled by a 3D damage–plasticity law; a condensation step links 3D material behavior to beam strains, and a local regularization of quadrature mitigates mesh sensitivity [73, 7, 75, 33, 6, 5].

This layered strategy provides an efficient default (fully bonded to partially bonded and unbonded tendons), with staged bonding, long term losses and anchorage short term phenomena. It integrates seamlessly with the enriched beam framework used throughout the thesis and will be detailed in the subsequent sections.

1.4.3 Numerical objectivity in beam finite elements

An essential requirement for nonlinear finite element models is the objectivity of the results, i.e. their independence from mesh size and discretization. This aspect is particularly critical in reinforced concrete (RC) structures, where material softening and strain localization occur after cracking and crushing. Without appropriate regularization, displacement-based (DB) and even force-based (FB) beam formulations may exhibit spurious mesh sensitivity, producing unrealistic crack distributions and non-convergent predictions of ductility and energy dissipation [89, 17, 37, 10, 5].

Early remedies such as fracture energy regularization control tensile softening by linking the area under the stress–strain curve to a material parameter with energetic meaning [90, 73, 5]. Although widely adopted, this approach is often insufficient to guarantee full objectivity in beam models with fiber sections, as the localization length is not properly defined at the element level, leading to persistent mesh-dependence [72, 91]. More refined nonlocal and gradient-enhanced formulations address this issue by introducing spatial averaging of strains or damage variables, at the price of additional complexity and higher computational cost.

In the context of beam finite elements, two families of regularization approaches have emerged. Nonlocal integral models average generalized strains or damage variables along the element axis, thereby controlling localization in a mathematically consistent manner [92, 93, 14]. Local techniques, instead, modify the quadrature scheme of the element to enforce a characteristic length scale and stabilize softening responses [33, 6, 5]. The latter are especially appealing in FB and mixed beam formulations, where equilibrium is satisfied in strong form and numerical integration governs the distribution of inelastic demand. By redistributing quadrature weights independently of mesh subdivision, local regularization ensures that localization zones have a consistent physical length, thereby restoring objectivity without altering the element kinematics.

Enhanced kinematic descriptions further contribute to objectivity. By introducing bond–slip and warping degrees of freedom, cracks and strain localizations can be confined within single elements rather than artificially spread over the mesh. These enriched formulations, combined with regularization strategies, enable beam models to represent complex RC behavior in a mesh-independent manner, reproducing realistic crack patterns and post-peak responses [47, 27, 52, 94].

In summary, ensuring numerical objectivity requires a combined strategy: (i) consistent constitutive models capturing softening and damage, (ii) regularization techniques, local or nonlocal, that embed a characteristic length, and (iii) enriched kinematics to localize inelastic phenomena realistically within elements. Only by combining these aspects can beam finite element formulations achieve reliable and mesh-independent predictions of nonlinear RC and PC structures.

1.5 Constitutive laws for structural analysis

The definition of appropriate constitutive laws is a fundamental aspect in developing advanced beam finite element formulations [74, 95]. These constitutive models describe how generalized section forces (such as axial force, bending moments, shear forces, and torsional moments) relate to corresponding deformations (axial strains, curvatures, shear strains, torsional rotations) under both elastic and inelastic conditions.

A classical distinction exists between lumped plasticity and distributed plasticity approaches. Lumped plasticity models concentrate inelastic behavior at specific locations, typically the ends of elements, using nonlinear springs or hinges to capture moment-rotation relationships. Early developments in this area include the seminal work of Clough and [96] and Giberson [97], introducing single-component and multi-component hinge formulations capable of representing moment-rotation or axial-moment interaction. These models remain widely used in practice due to their simplicity and efficiency, but require careful calibration of hinge properties, including the length of the inelastic zone, which can be influenced by boundary conditions and load distribution.

By contrast, distributed plasticity models assume inelastic behavior can develop along the entire member length. These approaches typically discretize the beam into integration sections, each with its own nonlinear constitutive law, allowing for a more realistic representation of the gradual spread of plasticity under loading [10, 44]. Force-based and mixed formulations are particularly well-suited to distributed plasticity, as they naturally enforce equilibrium along the element and accurately capture varying stress and strain distributions without requiring fine meshing.

Within both lumped and distributed approaches, generalized section constitutive models play a central role. These models relate section resultants to generalized deformations, such as moment-curvature laws or axial force–strain relations, and can range from simple elastic-perfectly plastic descriptions to more advanced hardening and cyclic models [3, 98, 46]. Significant contributions in this area include Bazant's work on plastic hinge formulations and nonlinear moment-curvature laws for reinforced concrete sections [99]. Such section-level models can be employed in displacement-based, force-based, or mixed beam elements without restriction, highlighting the modularity and generality of the finite element approach [100, 14, 42].

To enhance the fidelity of nonlinear analyses, fiber section models have become widely adopted [10, 11, 26, 15]. In these models, the cross-section is discretized into fibers, each assigned a uniaxial or multidimensional constitutive law. The section response is obtained by integrating the stress and strain contributions of all fibers, allowing for axial–flexural–shear–torsional interaction, confinement effects, and complex loading histories. This is particularly valuable for representing

the inelastic behavior of RC and prestressed members under seismic loading.

The reliability of fiber models depends critically on the underlying constitutive laws. Experimental evidence by Kupfer, Hilsdorf and Rusch [101] and Karsan and Jirsa [2] highlighted the importance of biaxial effects and the accumulation of plastic strains under cyclic loading. Two key phenomena must be captured: the unilateral effect, whereby stiffness loss in tension is partially recovered in compression but not vice versa, and the growth of plastic strains in both tension and compression.

Early attempts to reproduce these behaviors derived from fracture mechanics [102, 103], cohesive zone models, and embedded discontinuity approaches [104, 105], which are accurate but computationally expensive. Alternative smeared crack and anisotropic damage models were proposed to approximate distributed cracking [106, 107], offering greater efficiency for structural applications.

Continuum damage formulations then became widely adopted. Mazars [108, 109] introduced isotropic damage with separate variables for tension and compression, while Lemaitre [110] coupled plasticity and damage. Subsequent plastic–damage models include the formulation of Lubliner et al. [100], later refined by Lee and Fenves [111] to incorporate two parameters and unilateral effects. Further developments by Comi and Perego, and Faria and Oliver, introduced additional damage variables to differentiate tensile and compressive degradation. Comprehensive overviews can be found in classical references [112, 113, 114, 115].

Within this tradition, Addessi and co-workers [14, 5] developed plastic–damage models suitable for efficient finite element implementations, balancing robustness and computational cost. Building on this work, Di Re [92, 7] and Gatta [93] proposed a three-dimensional plastic–damage model suitable for several brittle and quasi-brittle materials (i.e., concrete and masonry) that accounts for unilateral effects and cyclic degradation for the analysis of RC walls and masonry structures, respectively. These models represent the state-of-the-art in fiber-based simulations, enabling accurate nonlinear analyses of RC and prestressed members under severe loading.

In this work, classical uniaxial laws, such as Menegotto–Pinto [98], elasto-fragile models for FRP, and bond–slip constitutive laws [4], are also used.

1.6 Objectives and scope

The primary objective of this thesis is to develop advanced beam finite element formulations capable of accurately and efficiently simulating the nonlinear behavior of reinforced and prestressed concrete structures under severe loading conditions. The work aims to address limitations of classical approaches by introducing consistent formulations, robust numerical algorithms, and enriched modeling of local effects that significantly influence structural response.

Specifically, the research pursues the following goals:

- Present general and consistent formulations for displacement-based, force-based, and mixed beam finite elements derived within the Hu-Washizu variational framework, enabling unified treatment of equilibrium, compatibility, and constitutive relations.

- Develop robust algorithms for state determination in force-based and mixed elements that avoid numerical instabilities associated with ill-conditioned section stiffness matrices, particularly under material softening or complex nonlinearities.
- Extend displacement-based and force-based formulations to explicitly include bond-slip interaction between reinforcement and concrete, enabling realistic modeling of reinforced concrete members with distributed slip effects.
- Propose displacement-based and mixed formulations that incorporate both warping and bond-slip effects simultaneously, providing a realistic representation of complex section behavior in prestressed and thin-walled members.

The scope of the thesis includes several key thematic areas required to achieve these objectives.

- Computational aspects are addressed by defining suitable interpolation functions for displacement, force, and strain fields, and implementing numerical integration techniques compatible with enriched formulations. Emphasis is placed on ensuring that these choices support accurate and efficient solution procedures while preserving equilibrium and compatibility conditions.
- Local regularization techniques are developed to maintain objectivity in simulations involving strain localization, damage, and softening. These methods aim to eliminate mesh sensitivity and provide physically meaningful, size-independent results critical for reliable structural assessment.
- Advanced constitutive modeling forms another central component. The work includes the development and implementation of 1D plasticity and damage models with appropriate return mapping algorithms for fiber sections, as well as 3D plasticity and coupled damage-plasticity models capable of describing complex material behavior such as cracking, crushing, and unloading effects in concrete.
- Implementation aspects involve integrating these formulations and constitutive laws into efficient finite element algorithms. Particular attention is given to the solution strategies for nonlinear problems, including consistent linearization and iterative schemes required for convergence under severe loading conditions.
- Validation and application are carried out through a series of benchmark tests and practical simulations. Linear tests are used to verify model implementation against analytical solutions, supporting transparency and teaching applications. Numerical tests evaluate the proposed elements under representative conditions, including beams with thin-walled cross-sections, short spans, cyclic loading histories, and prestressed configurations. The models are assessed for their ability to simulate cracking behavior and maintain objectivity in softening regimes.

Overall, the thesis addresses the development, implementation, and validation of enriched beam finite element formulations to support modern performance-based analysis and design of reinforced and prestressed concrete structures. The approach combines theoretical rigor with practical applicability, aiming to improve the reliability of nonlinear structural simulations used in both research and engineering practice.

1.7 Organization of the thesis

The thesis is structured to follow a logical progression from theoretical developments to material modeling, computational aspects, and numerical applications. Each chapter addresses a specific component of the research objectives.

Chapter 2: Beam Finite Element Formulations

This chapter presents the theoretical framework for classical displacement-based, force-based, and mixed beam finite element formulations. The models are then extended to account for bond-slip interaction, prestressing, and time-dependent effects such as creep and shrinkage. Finally, an enhanced formulation with sectional warping and bond-slip is introduced to address objectivity issues and to capture complex sectional behaviors.

Chapter 3: Constitutive Constitutive Laws

This chapter details the material laws adopted in the thesis. One-dimensional constitutive models are first presented, including classical steel models for reinforcement and prestressing tendons. Then, three-dimensional constitutive models for concrete are introduced, covering plasticity and damage approaches suitable for fiber discretizations. Particular attention is given to the performance of these models in reproducing the nonlinear behavior of cementitious materials under multi-axial stress states.

Chapter 4: Computational Aspects

This chapter discusses the implementation of the proposed formulations in a general-purpose finite element solver developed in MATLAB. Algorithms for section and material state determination, numerical integration schemes, and nonlinear solution strategies are described. Particular focus is placed on ensuring robustness and efficiency through Newton-Raphson and arc-length methods, with validation against benchmark solutions.

Chapter 5: Numerical Applications

This chapter presents numerical applications designed to validate the proposed formulations and assess their performance. Three groups of studies are reported. First, conventional beam elements are analyzed to highlight the lack of objectivity and the limitations of fracture-energy regularization. Second, the formulations with bond-slip are applied to prestressed concrete members, extending previous models to account for time stages, differential bond laws, and experimental validations. Third, enhanced beam elements with warping and bond-slip are tested, showing how these enrichments mitigate objectivity issues and improve the representation of cracking and shear-torsion mechanisms.

Conclusions

The final chapter summarizes the main findings of the thesis, emphasizing the contributions to the development of advanced beam finite element formulations for reinforced and prestressed concrete structures. Recommendations are provided for further research, including extensions of the proposed models and potential applications in structural assessment and design.

Chapter 2

Beam finite element formulations

Beam finite elements are fundamental in the nonlinear analysis of reinforced and prestressed concrete structures, offering a good compromise between modeling accuracy and computational efficiency. This work addresses the need for robust formulations capable of capturing complex nonlinear phenomena, such as distributed cracking, reinforcement bond-slip, cross-section warping, and time-dependent effects. These aspects are critical to realistically model RC and PC members under both service and ultimate loading conditions, including static and cyclic excitations.

All the formulations presented in this chapter share a unified conceptual framework based on the discretization the beam axis into two-node one-dimensional elements while resolving the section response through fiber-based integration. Sectional behavior is described through strain-driven constitutive laws applied at the fiber level, which enable the consistent inclusion of nonlinear material response, cyclic degradation, and the coupling between axial, flexural, shear, and torsional effects. The small displacements and small strain assumptions allow a consistent linearization of the kinematics across all approaches.

A key aspect of the presented framework is its modularity. Regardless of the formulation employed, displacement-based (DB), force-based (FB), or mixed, the element-level and section-level operators follow the same logic. Sectional generalized stresses and deformations are related via fiber integration of the constitutive responses, while the element-level equilibrium and compatibility relations are enforced through suitable interpolation schemes and numerical integration of the section generalized fields. This unified approach supports extensions to advanced effects such as bond-slip and warping through consistent modifications of the element kinematics and equilibrium.

Displacement-based formulations interpolate nodal generalized displacements and derive internal strains through differentiation of the shape functions, but they often suffer from convergence issues, locking phenomena and numerical instabilities under highly nonlinear, cyclic conditions [18, 19]. Most of these limitations are explained in Section 5.1.

Force-based formulations overcome most of these limits enforcing equilibrium in strong form along the element axis by exactly expanding generalized stresses along the beam axis rather than displacements, so that specific shape functions for these latter must not be defined beforehand. This approach enables accurate nonlinear response even with coarse meshes. As highlighted in the literature, force-based formulations have been widely adopted for the simulation of RC and PC

frame elements, offering very good accuracy with minimal discretization (see e.g., [10, 25, 116]).

Mixed formulations aim to combine the best features of DB and FB elements by introducing independent interpolations for generalized stress and strain fields. Building on either the Hellinger-Reissner variational principle, for two-field, or the Hu-Washizu variational principle, for three-field mixed formulations, a variationally consistent interpolation is enabled for both force and displacement fields, allowing satisfaction of equilibrium and compatibility equations either in weak or strong-form, depending on the assumptions [23]. These formulations, just like force-based formulations, also facilitate the inclusion of shear strain without locking, ensuring good accuracy under both linear and nonlinear conditions.

An important feature of modern formulations is their ability to account for the nonlinear response along the member length, i.e., distributed plasticity, in contrast with lumped plasticity models, concentrate the nonlinear behavior at the element ends. Other proposals, such as the introduction of variable nonlinear end-zone models (e.g. [116]), address limitations of traditional plastic hinge approaches by explicitly capturing the evolution of plastic zones with minimal integration points.

Recognizing the need to model complex behaviors, this work extends the classical DB, FB, and mixed formulations by incorporating bond-slip at reinforcement interfaces and cross-section warping effects. The reason is for modeling structural elements such as prestressed beams while staying in an efficient two-node environment, to describe more complex section kinematics, as well as to solve objectivity issues with traditional elements. The same modular architecture allows consistent inclusion of bond-slip kinematics, modifying compatibility relations and introducing additional DOFs when needed, and the enrichment of section-level models with warping-induced shear effects. This approach enables the accurate simulation of RC and PC members where slip, warping, and non-uniform stress distributions are significant.

Accordingly, this chapter is structured into three main sections:

- The first introduces the classical formulations, establishing the fundamental operators, interpolation schemes, and variational principles that underpin all variants. These are called D, F and M elements, respectively.
- The second extends these to include bond-slip effects in DB and FB elements, describing the modifications required to enforce equilibrium and compatibility with slip. These are called D-B, F-B and M-B elements, respectively.
- The third section presents the advanced enrichment of DB and mixed formulations with cross-section warping and bond-slip kinematics, capturing the coupling between axial, flexural, shear, and torsional behaviors in a consistent finite element framework. These are called D-BW and M-BW, elements respectively.

This chapter therefore aims to highlight both the shared theoretical foundation of all formulations and the specific enrichments required to address the full range of phenomena considered in this work.

2.1 Element formulation

This section describes the beam formulation at the element level. A standard approach is adopted in which the element is formulated in a local reference system aligned with its axis, and transformed into a basic system in which rigid-body motions are eliminated and only the deformational nodal displacements are retained. This separation of local and basic configurations underpins both displacement-based and force-based formulations, and provides a clear framework for defining kinematic relations, equilibrium equations, and constitutive laws.

The beam element is defined by the two end nodes I and J, located in the global reference system (X, Y, Z). This is shown in Figure 2.1.

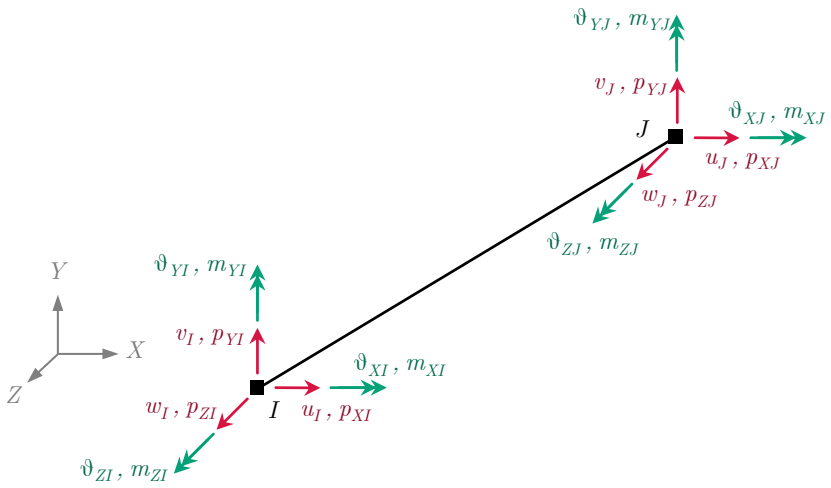

Figure 2.1. Element configuration in the global reference system (X, Y, Z) with nodal displacements and forces.

2.1.1 Local configuration

The local nodes counterparts are i and j, each with 6 degrees of freedom: three translational and three rotational components. The local reference frame is denoted by (x, y, z), with x oriented along the element axis from node i to node j (see Figure 2.2). The local DOFs are obtained by means of the transformation:

$$\mathbf{u}_l = \mathbf{a}_l \mathbf{u}_g \tag{2.1}$$

where $\mathbf{u}_l$ is the local displacements vector with 12 components, $\mathbf{a}_l$ is the global operator that includes booleans and rotational transformations needed to relate the global to the local displacement degrees of freedom, and $\mathbf{u}_g$ is the global displacements vector, containing all the displacement degrees of freedom of the system. The local displacement vector is given by:

$$\mathbf{u}_l = \left\{ \begin{array}{cccc} \mathbf{u}_{li}^T & \boldsymbol{\vartheta}_{li}^T & \mathbf{u}_{lj}^T & \boldsymbol{\vartheta}_{lj}^T \end{array} \right\}^T \tag{2.2}$$

where $\mathbf{u}_{li} = \{u_i \; v_i \; w_i\}^T$, for node i, and $\mathbf{u}_{lj} = \{u_j \; v_j \; w_j\}^T$, for node j, represent displacements about axes x, y, z, respectively, while $\boldsymbol{\vartheta}_{li} = \{\vartheta_{xi} \; \vartheta_{yi} \; \vartheta_{zi}\}^T$, for node i, and $\boldsymbol{\vartheta}_{lj} = \{\vartheta_{xj} \; \vartheta_{yj} \; \vartheta_{zj}\}^T$, for node j, represent rotations around axes x, y, z, respectively.

The nodal force vector in the local system is:

$$\mathbf{p}_l = \left\{ \begin{array}{cccc} \mathbf{p}_{li}^T & \mathbf{m}_{li}^T & \mathbf{p}_{lj}^T & \mathbf{m}_{lj}^T \end{array} \right\}^T \tag{2.3}$$

where $\mathbf{p}_{li} = \{p_{xi}\ p_{yi}\ p_{zi}\}^T$, for node i, and $\mathbf{p}_{lj} = \{p_{xj}\ p_{yj}\ p_{zj}\}^T$, for node j, represent translations along axes x, y, z, respectively, while $\boldsymbol{m}_{li} = \{m_{xi}\ m_{yi}\ m_{zi}\}^T$, for node i, and $\boldsymbol{m}_{lj} = \{m_{xj}\ m_{yj}\ m_{zj}\}^T$, for node j, represent rotations around axes x, y, z, respectively.

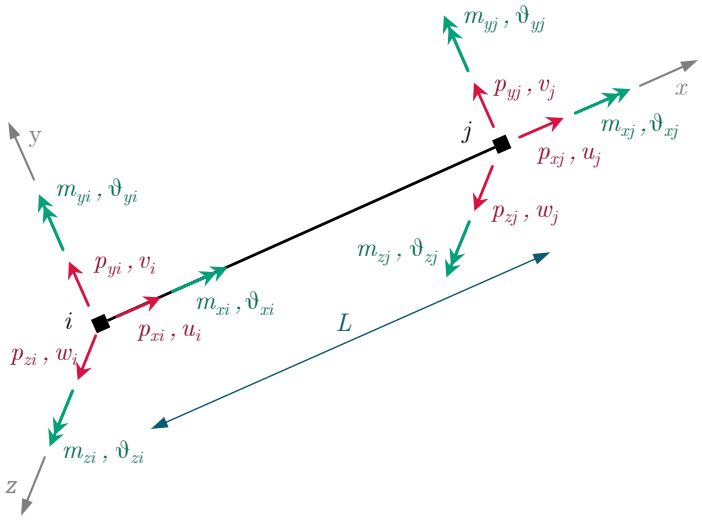

Figure 2.2. Element configuration in the local reference system (x, y, z) with nodal displacements and forces.

2.1.2 Basic configuration

The basic configuration eliminates rigid-body modes, leaving only the deformational degrees of freedom needed to describe the element internal response. This is only strictly needed in a force-based formulation to enforce equilibrium.
The transformation from local nodal displacements to basic displacements is given by:

$$\mathbf{v} = \mathbf{a}_b\ \mathbf{u}_l \tag{2.4}$$

where $\mathbf{a}_b$ is the element kinematic matrix. By adopting the restraint conditions illustrated in Fig. 2.3, the basic displacement vector is:

$$\mathbf{v} = \left\{ \begin{array}{cccccc} \delta_j & \varphi_{zi} & \varphi_{zj} & \varphi_{yi} & \varphi_{yj} & \varphi_{xj} \end{array} \right\}^T \tag{2.5}$$

where δ_j is the axial displacement at node j (axial elongation), φ_{zi}, φ_{zj} are deformational rotations about the local z-axis at nodes i and j, φ_{yi}, φ_{yj} are deformational rotations about the local y-axis, φ_{xj} is the torsional rotation around x at node j.

These basic DOFs fully describe the internal deformation state of the element. Figure 2.3 illustrates this configuration.

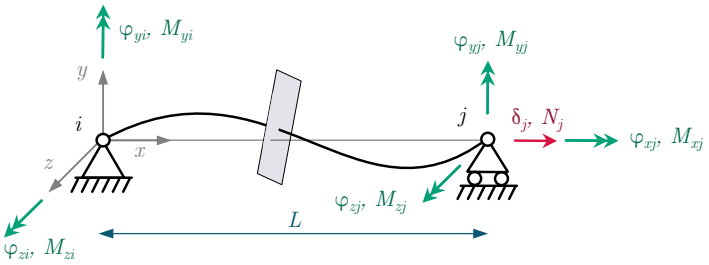

Figure 2.3. Element basic configuration in the local reference system (x, y, z) with nodal displacements and forces.

Expanding the kinematic relation explicitly:

$$\begin{Bmatrix} \delta_j \\ \varphi_{zi} \\ \varphi_{zj} \\ \varphi_{yi} \\ \varphi_{yj} \\ \varphi_{xj} \end{Bmatrix} = \begin{bmatrix} -1 & 0 & 0 & 0 & 0 & 0 & 1 & 0 & 0 & 0 & 0 & 0 \\ 0 & \frac{1}{L} & 0 & 0 & 0 & 1 & 0 & -\frac{1}{L} & 0 & 0 & 0 & 0 \\ 0 & \frac{1}{L} & 0 & 0 & 0 & 0 & 0 & -\frac{1}{L} & 0 & 0 & 0 & 1 \\ 0 & 0 & -\frac{1}{L} & 0 & 1 & 0 & 0 & 0 & \frac{1}{L} & 0 & 0 & 0 \\ 0 & 0 & -\frac{1}{L} & 0 & 0 & 0 & 0 & 0 & \frac{1}{L} & 0 & 1 & 0 \\ 0 & 0 & 0 & -1 & 0 & 0 & 0 & 0 & 0 & 1 & 0 & 0 \end{bmatrix} \begin{Bmatrix} u_i \\ v_i \\ w_i \\ \vartheta_{xi} \\ \vartheta_{yi} \\ \vartheta_{zi} \\ u_j \\ v_j \\ w_j \\ \vartheta_{xj} \\ \vartheta_{yj} \\ \vartheta_{zj} \end{Bmatrix} \tag{2.6}$$

where L is the element length. This matrix encodes rigid-body elimination and maps nodal generalized displacement modes to pure generalized deformation modes.
It is worth noting that other restraint configurations could be adopted to eliminate the rigid-body motions, all leading to the same formulation for the initial free node element.

2.1.3 Element constitutive law in its basic configuration

In the basic system, the element force vector $\mathbf{q}$ is work-conjugate to $\mathbf{v}$ and represents the internal forces:

$$\mathbf{q} = \left\{ \begin{array}{cccccc} N_j & M_{zi} & M_{zj} & M_{yi} & M_{yj} & M_{xj} \end{array} \right\}^T \tag{2.7}$$

where N_j is the axial force at node j, M_{zi}, M_{zj} are bending moments around z at nodes i and j, respectively, M_{yi}, M_{yj} are bending moments around y at nodes i and j, respectively, M_{xj} is the torsional moment around x at node j.

By derivation of the nodal forces $\mathbf{q}$ with respect to the nodal displacements $\mathbf{v}$, the fundamental constitutive relation in the basic system is:

$$\mathbf{k} = \frac{\partial \mathbf{q}}{\partial \mathbf{v}} \tag{2.8}$$

where $\mathbf{k}$ is the element tangent stiffness matrix in the basic system, obtained through integration

of section stiffness contributions. For displacement-based formulations, $\mathbf{k}$ derives from direct interpolation of displacements; for force-based formulations, it results from enforcing equilibrium along the element and integrating flexibility. For mixed formulations, it arises from independent approximations of forces and deformations, further explained in the following sections.

2.1.4 Transformation to local system

By equilibrium between the forces in the basic configuration and the forces in the local configuration, the local force vector is obtained by:

$$\mathbf{p}_l = \mathbf{a}_b{}^T \mathbf{q} \tag{2.9}$$

Similarly, substituting the element constitutive relationship of Eq. (2.8), and the element compatibility of Eq. (2.4), it results:

$$\mathbf{p}_l = \mathbf{a}_b{}^T \mathbf{k}\, \mathbf{a}_b\, \mathbf{u}_l = \mathbf{k}_l \mathbf{u}_l \tag{2.10}$$

where:

$$\mathbf{k}_l = \mathbf{a}_b{}^T \mathbf{k}\, \mathbf{a}_b \tag{2.11}$$

is the element stiffness matrix in the local reference system. This matrix can be then assembled in the global system for structural analysis.

In absence of element forces, initial strains and stresses or anelastic effects, vector $\mathbf{p}_l$ represents all the internal forces in the element. In an incremental notation, this may therefore be rewritten as:

$$-\dot{\mathbf{p}}_l^{int} = \mathbf{k}_l \dot{\mathbf{u}}_l \tag{2.12}$$

The internal forces must equilibrate the external forces, so that the element equilibrium is granted:

$$\mathbf{p}_l^{ext} - \mathbf{p}_l^{int} = 0 \tag{2.13}$$

This equation is rewritten in Chapter 4 to include residuals and extend it to a more general nonlinear framework.

This formulation, rigorously mapping nodal DOFs to basic deformation modes and enforcing equilibrium via transformation matrices, serves as the foundation for all subsequent developments, including displacement-based, force-based, and mixed formulations, as well as extensions for bond-slip and warping effects.

2.2 The Timoshenko formulation

2.2.1 Section kinematics and constitutive law

The Timoshenko beam theory is based on the rigid cross-section assumption. Hence, at each point along the local axis x, the generalized section displacement vector $\mathbf{u}_s(x)$ is defined as:

$$\mathbf{u}_s(x) = \begin{Bmatrix} u(x) & \vartheta_z(x) & \vartheta_y(x) & v(x) & w(x) & \vartheta_x(x) \end{Bmatrix}^T \tag{2.14}$$

where $u(x)$, $v(x)$ and $w(x)$ are the translation components of the cross-section at x, and $\vartheta_x(x)$, $\vartheta_y(x)$ and $\vartheta_z(x)$ are its rotations around axes x, y, z, respectively (see Figure 2.4).

The displacements $\mathbf{u}_m(x, y, z)$ at a generic material point f of the cross-section are described by the three fields $u(x, y, z)$, $v(x, y, z)$ and $w(x, y, z)$, representing the displacement at each material point along x, y and z, respectively. Under the assumption of rigid cross-section, $\mathbf{u}_m(x, y, z)$ corresponds to the rigid section displacement $\mathbf{u}_r(x, y, z)$, which results as:

$$\mathbf{u}_r(x, y, z) = \begin{Bmatrix} u(x, y, z) \\ v(x, y, z) \\ w(x, y, z) \end{Bmatrix} = \mathbf{a}_s(y, z)\, \mathbf{u}_s(x) \tag{2.15}$$

where $u(x, y, z)$, $v(x, y, z)$ and $w(x, y, z)$ are the displacements of the material point along x, y, z,

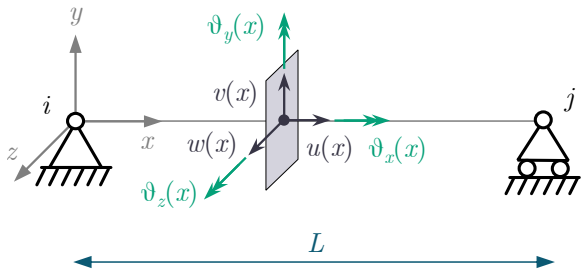

Figure 2.4. Section displacements.

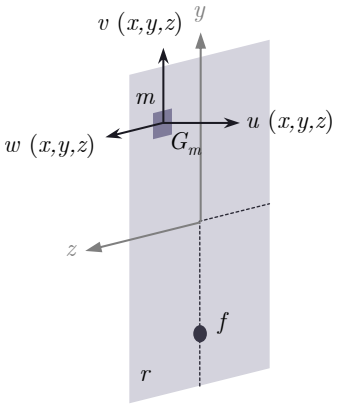

Figure 2.5. Material point displacements.

respectively, associated to the cross-section rigid-body motion and $\mathbf{a}_s(y, z)$ is the compatibility operator. It is defined as:

$$\mathbf{a}_s(y, z) = \begin{bmatrix} 1 & -y & z & 0 & 0 & 0 \\ 0 & 0 & 0 & 1 & 0 & -z \\ 0 & 0 & 0 & 0 & 1 & y \end{bmatrix} \tag{2.16}$$

where y and z here are the general material point coordinates with respect to the section axes. The material point displacements are later taken as fiber displacements, as required in the numerical framework, and share the same notation as shown in Figure 2.5, with G_f being the fiber centroid. The compatible strain vector $\boldsymbol{\varepsilon}_m(x, y, z)$ at point f is described by the three strain

fields $\varepsilon_x(x,y,z)$, $\gamma_{xy}(x,y,z)$ and $\gamma_{xz}(x,y,z)$, corresponding to the material point axial strain along x and the shear strains in the planes xy and xz, respectively.
These are obtained by the derivation of the rigid material point displacements as:

$$\boldsymbol{\varepsilon}_r(x,y,z) = \mathbf{D}(x,y,z)\mathbf{u}_r(x,y,z) \tag{2.17}$$

where

$$\mathbf{D}(x,y,z) = \begin{bmatrix} \dfrac{\partial}{\partial x} & 0 & 0 \\ \dfrac{\partial}{\partial y} & \dfrac{\partial}{\partial x} & 0 \\ \dfrac{\partial}{\partial z} & 0 & \dfrac{\partial}{\partial x} \end{bmatrix} \tag{2.18}$$

As for the displacements, $\boldsymbol{\varepsilon}_m(x,y,z)$ is equivalent to the contribution $\boldsymbol{\varepsilon}_r(x,y,z)$ compatible with the rigid section displacements and resulting as:

$$\boldsymbol{\varepsilon}_r(x,y,z) = \begin{Bmatrix} \varepsilon_x(x,y,z) \\ \gamma_{xy}(x,y,z) \\ \gamma_{xz}(x,y,z) \end{Bmatrix} = \mathbf{a}_s(y,z)\,\mathbf{e}(x) \tag{2.19}$$

The generalized section deformation vector $\mathbf{e}(x)$ is introduced in Eq. (2.19) as:

$$\mathbf{e}(x) = \begin{Bmatrix} \varepsilon_a(x) \\ \chi_z(x) \\ \chi_y(x) \\ \gamma_y(x) \\ \gamma_z(x) \\ \chi_x(x) \end{Bmatrix} = \begin{Bmatrix} u'(x) \\ \vartheta'_z(x) \\ \vartheta'_y(x) \\ v'(x) - \vartheta_z(x) \\ w'(x) + \vartheta_y(x) \\ \vartheta'_x(x) \end{Bmatrix} \tag{2.20}$$

where the symbol $'$ denotes differentiation with respect to x. Here, $\varepsilon_a(x)$ is the axial strain, $\chi_z(x)$ and $\chi_y(x)$ are the flexural curvatures around z and y, respectively, $\chi_x(x)$ is the torsional curvature, and $\gamma_y(x)$ and $\gamma_z(x)$ are the shear strains about y and z, respectively. Eq. (2.20) can also be rewritten as:

$$\mathbf{e}(x) = \mathbf{D}_s(x)\mathbf{u}_s(x) \tag{2.21}$$

where

$$\mathbf{D}_s(x) = \begin{bmatrix} \dfrac{\partial}{\partial x} & 0 & 0 & 0 & 0 & 0 \\ 0 & \dfrac{\partial}{\partial x} & 0 & 0 & 0 & 0 \\ 0 & 0 & \dfrac{\partial}{\partial x} & 0 & 0 & 0 \\ 0 & -1 & 0 & \dfrac{\partial}{\partial x} & 0 & 0 \\ 0 & 0 & 1 & 0 & \dfrac{\partial}{\partial x} & 0 \\ 0 & 0 & 0 & 0 & 0 & \dfrac{\partial}{\partial x} \end{bmatrix} \tag{2.22}$$

The stress components work-conjugated with the strain quantities in $\boldsymbol{\varepsilon}_m(x,y,z)$ are collected in

the stress vector as:

$$\boldsymbol{\sigma}_m(x,y,z) = \begin{Bmatrix} \sigma_x(x,y,z) \\ \tau_{xy}(x,y,z) \\ \tau_{xz}(x,y,z) \end{Bmatrix} \tag{2.23}$$

where σ_x is the normal stress along the beam axis direction, and τ_{xy} and τ_{xz} are the shear stresses in the cross-section planes to xy and xz, respectively.

By enforcing the virtual work equivalence for the cross-section as:

$$\delta\mathbf{e}^T(x)\,\mathbf{s}(x) = \int_A \delta\boldsymbol{\varepsilon}_r^T(x,y,z)\,\boldsymbol{\sigma}_m(x,y,z)\,dA \tag{2.24}$$

the following definition of $\mathbf{s}(x)$ is deduced:

$$\mathbf{s}(x) = \int_A \mathbf{a}_s^T(y,z)\,\boldsymbol{\sigma}_m(x,y,z)\,dA \tag{2.25}$$

with

$$\mathbf{s}(x) = \begin{Bmatrix} N(x) \\ M_z(x) \\ M_y(x) \\ V_y(x) \\ V_z(x) \\ M_x(x) \end{Bmatrix} \tag{2.26}$$

where $N(x)$ is the axial force, $M_z(x)$ and $M_y(x)$ are the bending moments around z and y, respectively, $M_x(x)$ is the torsional moment, and $V_y(x)$ and $V_z(x)$ are the shear forces about y and z, respectively. By differentiating Eq. (2.25) with respect to $\mathbf{e}(x)$, the tangent section stiffness matrix $\mathbf{k}_s(x)$ is obtained:

$$\mathbf{k}_s(x) = \int_A \mathbf{a}_s^T(y,z)\,\mathbf{k}_m(x,y,z)\,\mathbf{a}_s(y,z)\,dA \tag{2.27}$$

governing the incremental generalized section constitutive relation:

$$\dot{\mathbf{s}}(x) = \mathbf{k}_s(x)\,\dot{\mathbf{e}}(x) \tag{2.28}$$

The tangent material stiffness matrix is defined as:

$$\mathbf{k}_m(x,y,z) = \frac{\partial\boldsymbol{\sigma}_m(x,y,z)}{\partial\boldsymbol{\varepsilon}_m(x,y,z)} \tag{2.29}$$

and it governs the material incremental stress-strain law:

$$\dot{\boldsymbol{\sigma}}_m(x,y,z) = \mathbf{k}_m(x,y,z)\,\dot{\boldsymbol{\varepsilon}}_m(x,y,z) \tag{2.30}$$

As a consequence of the rigid section's assumption of Eq. (2.19), the material axial strains $\varepsilon_x(x,y,z)$ assume linear distributions. For linear elastic material, this also implies the same distributions for the material stresses $\sigma_x(x,y,z)$.

In Timoshenko's formulation, shear strains are typically assumed constant, if shear is present, or linearly dependent on torsional curvature, according to:

$$\gamma_{xy}(x,y,z) = \gamma_y(x) - z\,\chi_x(x) \tag{2.31}$$

$$\gamma_{xz}(x,y,z) = \gamma_z(x) + y\,\chi_x(x) \tag{2.32}$$

However, this assumptions leads to the longitudinal equilibrium of the element not being respected [55]. Therefore, classical shear correction factors ζ_y and ζ_z, and the torsional correction factor ζ_x need to be introduced. Eq. (2.19) is thus rewritten introducing a modified matrix $\mathbf{a}_s(y,z)$:

$$\boldsymbol{\varepsilon}_r(x,y,z) = \mathbf{a}_s(y,z)\,\mathbf{e}(x) \tag{2.33}$$

with:

$$\mathbf{a}_s(y,z) = \begin{bmatrix} 1 & -y & z & 0 & 0 & 0 \\ 0 & 0 & 0 & \sqrt{\zeta_y} & 0 & -z\sqrt{\zeta_x} \\ 0 & 0 & 0 & 0 & \sqrt{\zeta_z} & y\sqrt{\zeta_x} \end{bmatrix} \tag{2.34}$$

Accordingly, Eqs. (2.25) and (2.27) become:

$$\mathbf{s}(x) = \int_A \mathbf{a}_s^T(y,z)\,\boldsymbol{\sigma}_m(x,y,z)\,dA \tag{2.35}$$

$$\mathbf{k}_s(x) = \int_A \mathbf{a}_s^T(y,z)\,\mathbf{k}_m(x,y,z)\,\mathbf{a}_s(y,z)\,dA \tag{2.36}$$

For linear elastic material response, $\mathbf{k}_m(x,y,z)$ is a diagonal matrix depending on the Young's and shear moduli, E and G, i.e.:

$$\mathbf{k}_m = \begin{bmatrix} E & 0 & 0 \\ 0 & G & 0 \\ 0 & 0 & G \end{bmatrix} \tag{2.37}$$

For a homogeneous section, the tangent section stiffness matrix $\mathbf{k}_s(x)$ results as:

$$\mathbf{k}_s = \begin{bmatrix} EA & -ES_z & ES_y & 0 & 0 & 0 \\ -ES_z & EI_z & -ES_{yz} & 0 & 0 & 0 \\ ES_y & -ES_{yz} & EI_y & 0 & 0 & 0 \\ 0 & 0 & 0 & \zeta_y GA & 0 & -\sqrt{\zeta_y\zeta_x}\,GS_y \\ 0 & 0 & 0 & 0 & \zeta_z GA & \sqrt{\zeta_z\zeta_x}\,GS_z \\ 0 & 0 & 0 & -\sqrt{\zeta_y\zeta_x}\,GS_y & \sqrt{\zeta_z\zeta_x}\,GS_z & \zeta_x GI_\rho \end{bmatrix} \tag{2.38}$$

where S_y, S_z and S_{yz} are the section first moments of area, I_z and I_y are the second moments of area with respect to z and y respectively, and I_ρ is the polar moment of area. If the local element axes y and z are chosen as the principal cross-section axes, the matrix $\mathbf{k}_s(x)$ assumes

the following standard diagonal form:

$$\mathbf{k}_s = \begin{bmatrix} EA & 0 & 0 & 0 & 0 & 0 \\ 0 & EI_z & 0 & 0 & 0 & 0 \\ 0 & 0 & EI_y & 0 & 0 & 0 \\ 0 & 0 & 0 & GA_y^* & 0 & 0 \\ 0 & 0 & 0 & 0 & GA_z^* & 0 \\ 0 & 0 & 0 & 0 & 0 & GJ \end{bmatrix} \tag{2.39}$$

where EA is the axial stiffness, EI_z and EI_y are the bending stiffnesses, GJ is the torsional stiffness with $J = \zeta_x I_\rho$ the torsional inertia, and $A_y^* = \zeta_y A$ and $A_z^* = \zeta_z A$ are the shear areas. When Eq. (2.39) is considered, no coupling between the generalized section forces exists.

2.2.2 Exact equilibrium equation

The element basic force vector p can be related to the section force vector $\mathbf{s}(x)$ through the equilibrium differential equations, as shown in Figure 2.6:

$$\begin{aligned} N'(x) + p_x(x) &= 0 & \qquad M_z'(x) - V_y(x) + m_z(x) &= 0 \\ -V_y'(x) + p_y(x) &= 0 & \qquad -M_y'(x) + V_z(x) + m_y(x) &= 0 \\ -V_z'(x) + p_z(x) &= 0 & \qquad M_x'(x) + m_x(x) &= 0 \end{aligned} \tag{2.40}$$

where p_x is the axial load, p_y and p_z are the transverse loads along y and z, respectively, and m_x, m_y, m_z are distributed couples around x, y, z, respectively.

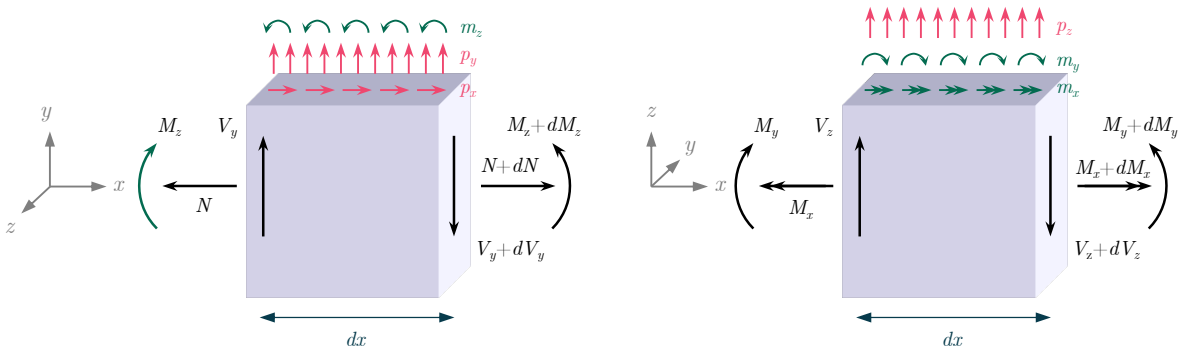

Figure 2.6. Section equilibrium with element loads.

The equilibrium may be written in compact form:

$$\mathbf{D}_s^*(x)\ \mathbf{s}(x) + \mathbf{p}(x) = 0 \tag{2.41}$$

where $\mathbf{D}_s^*(x)$ is:

$$\mathbf{D}_s^*(x) = \begin{bmatrix} \dfrac{\partial}{\partial x} & 0 & 0 & 0 & 0 & 0 \\ 0 & \dfrac{\partial}{\partial x} & 0 & -1 & 0 & 0 \\ 0 & 0 & -\dfrac{\partial}{\partial x} & 0 & 1 & 0 \\ 0 & 0 & 0 & -\dfrac{\partial}{\partial x} & 0 & 0 \\ 0 & 0 & 0 & 0 & -\dfrac{\partial}{\partial x} & 0 \\ 0 & 0 & 0 & 0 & 0 & \dfrac{\partial}{\partial x} \end{bmatrix} \tag{2.42}$$

and $\mathbf{p}(x)$ lists the distributed loads acting along the element:

$$\mathbf{p}(x) = \begin{Bmatrix} p_x(x) \\ m_z(x) \\ m_y(x) \\ p_y(x) \\ p_z(x) \\ m_x(x) \end{Bmatrix} \tag{2.43}$$

2.2.3 Displacement-based approach

The general DB approach is presented first. Only a general approach is reported here as a wide variety of DB formulations can be found in literature.
The section displacement vector $\mathbf{u}_s(x)$ is interpolated from the basic nodal displacements $\mathbf{v}$ by means of the shape function matrix $\mathbf{N}(x)$:

$$\mathbf{u}_s(x) = \mathbf{N}(x)\,\mathbf{v} \tag{2.44}$$

where $\mathbf{N}(x)$ contains the interpolation functions for the element.

The compatibility equation relates generalized section deformations $\mathbf{e}(x)$ to section displacements $\mathbf{u}_s(x)$ through the operator $\mathbf{D}_s(x)$:

$$\mathbf{e}(x) = \mathbf{D}_s(x)\,\mathbf{u}_s(x) \tag{2.45}$$

Substituting Eq. (2.44) into Eq. (2.45):

$$\mathbf{e}(x) = \mathbf{B}(x)\,\mathbf{v} \tag{2.46}$$

where $\mathbf{B}(x) = \mathbf{D}_s(x)\,\mathbf{N}(x)$ is the strain-displacement matrix.

The section constitutive relation is introduced as:

$$\mathbf{s}(x) = \mathbf{k}_s(x)\left(\mathbf{e}(x) - \mathbf{e}_0(x)\right) \tag{2.47}$$

where $\mathbf{e}_0(x)$ collects initial section inelastic contributions (plasticity, creep, thermal strains).

By applying the virtual work equivalence:

$$\delta\mathbf{v}^T\mathbf{q} = \int_0^L \delta\mathbf{e}^T(x)\,\mathbf{s}(x)\,dx - \int_0^L \delta\mathbf{u}_s^T(x)\,\mathbf{p}(x)\,dx \tag{2.48}$$

where $\delta\mathbf{u}_s(x) = \mathbf{N}(x)\,\delta\mathbf{v}$ and $\delta\mathbf{e}(x) = \mathbf{B}(x)\,\delta\mathbf{v}$. From this one, the element weak equilibrium relationship is obtained as:

$$\mathbf{q} = \int_0^L \mathbf{B}^T(x)\ \mathbf{s}(x)\,dx - \int_0^L \mathbf{N}^T(x)\,\mathbf{p}(x)\,dx \tag{2.49}$$

By introducing Eq. (2.47):

$$\mathbf{q} = \mathbf{k}\,\mathbf{v} - \mathbf{q}_0 \tag{2.50}$$

where the stiffness matrix $\mathbf{k}$ and the equivalent nodal forces $\mathbf{q}_0$ are:

$$\mathbf{k} = \int_0^L \mathbf{B}^T(x)\,\mathbf{k}_s(x)\,\mathbf{B}(x)\,dx \tag{2.51}$$

$$\mathbf{q}_0 = \int_0^L \mathbf{B}^T(x)\,\mathbf{k}_s(x)\,\mathbf{e}_0(x)\,dx + \int_0^L \mathbf{N}^T(x)\,\mathbf{p}(x)\,dx \tag{2.52}$$

As is well known, the Timoshenko formulation may suffer from shear locking in the slender limit, unless reduced integration or selective interpolation is employed, or higher interpolation orders are used.

The element equilibrium is finally obtained by applying the basic-to-local transformation:

$$\mathbf{p}_l^{ext} = \mathbf{a}_b^T\mathbf{k}\ \mathbf{v} - \mathbf{a}_b^T\mathbf{q}_0 + \mathbf{p}_{lp} \tag{2.53}$$

where $\mathbf{p}_{lp}$ is the equivalent nodal force vector defined in Section 2.2.2. The governing element equilibrium equation is:

$$\mathbf{p}_l^{ext} + \mathbf{p}_{l0} - \mathbf{p}_l^{int} = 0 \tag{2.54}$$

where $\mathbf{p}_{l0} = \mathbf{a}_b^T\mathbf{q}_0 - \mathbf{p}_{lp}$, and it is assembled to a global external load vector and is added to the global force vector.

Equations (2.54), (2.46) and (2.49) are the governing equations of the DB element:

$$\mathbf{p}_l^{ext} + \mathbf{p}_{l0} - \mathbf{p}_l^{int} = 0 \tag{2.55}$$

$$\mathbf{e}(x) - \mathbf{B}(x)\,\mathbf{v} - \mathbf{e}_0(x) = 0 \tag{2.56}$$

$$\mathbf{q} - \int_0^L \mathbf{B}^T(x)\ \mathbf{s}(x)\,dx + \int_0^L \mathbf{N}^T(x)\,\mathbf{p}(x)\,dx = 0 \tag{2.57}$$

2.2.4 Force-based approach

The section equilibrated stresses can be expressed as:

$$\mathbf{s}(x) = \mathbf{b}(x)\mathbf{q} + \mathbf{s}_p(x) \tag{2.58}$$

where $\mathbf{b}(x)$ is the equilibrium matrix which can be written as follows:

$$\mathbf{b}(x) = \begin{bmatrix} 1 & 0 & 0 & 0 & 0 & 0 \\ 0 & \frac{x}{L} - 1 & \frac{x}{L} & 0 & 0 & 0 \\ 0 & 0 & 0 & \frac{x}{L} - 1 & \frac{x}{L} & 0 \\ 0 & -\frac{1}{L} & -\frac{1}{L} & 0 & 0 & 0 \\ 0 & 0 & 0 & \frac{1}{L} & \frac{1}{L} & 0 \\ 0 & 0 & 0 & 0 & 0 & 1 \end{bmatrix} \tag{2.59}$$

and $\mathbf{s}_p(x)$ represents the contribution of the distributed loads along the element length, which is independent on the basic forces $\mathbf{q}$, and it can be evaluated by solving the equilibrium along the length as follows:

$$\mathbf{s}_p(x) = \mathbf{b}_p(x)\ \mathbf{p}(x) \tag{2.60}$$

where $\mathbf{b}_p$(x) is a matrix that relates the evolution of sectional forces to the applied distributed loads.

For the particular case of constant distributed loads along the element, integration of the equilibrium equations provides explicit expressions for the section forces and moments. For the current basic configuration, $\mathbf{b}_p(x)$ is given by

$$\mathbf{b}_p(x) = \begin{bmatrix} L - x & 0 & 0 & 0 & 0 & 0 \\ 0 & \frac{x(L-x)}{2} & 0 & 0 & 0 & 0 \\ 0 & 0 & \frac{x(L-x)}{2} & 0 & 0 & 0 \\ 0 & 1 & 0 & \frac{L}{2} - x & 0 & 0 \\ 0 & 0 & -1 & 0 & \frac{L}{2} - x & 0 \\ 0 & 0 & 0 & 0 & 0 & L - x \end{bmatrix} \tag{2.61}$$

The element equilibrium must account for the reaction forces, so that Eq. (2.1.4) is modified as follows:

$$\mathbf{p}_l^{ext} + \mathbf{p}_{lp} - \mathbf{p}_l^{int} = 0 \tag{2.62}$$

where $\mathbf{p}_{lq}$ is the vector of the equivalent nodal forces and it contains the reactions that equilibrate the element forces per unit length $\mathbf{p}(x)$. The section constitutive law is enforced as

$$\mathbf{e}(x) = \mathbf{f}_s(x)\,\mathbf{s}(x) + \mathbf{e}_0(x) \tag{2.63}$$

where $\mathbf{f}_s(x) = \mathbf{k}_s^{-1}(x)$ is the section flexibility matrix.

As the force-based approach enforces strong-form equilibrium, the weak-form compatibility can be computed applying the virtual work equivalence, using virtual stresses $\delta(\cdot)$, which gives:

$$\delta\mathbf{q}^T\,\mathbf{v} = \int_0^L \delta\mathbf{s}^T(x)\,\mathbf{e}(x)\,dx \tag{2.64}$$

By introducing the equilibrium in Eq. (2.58), this yields:

$$\delta\mathbf{q}^T\,\mathbf{v} = \delta\mathbf{q}^T \int_0^L \mathbf{b}^T(x)\,\mathbf{e}(x)\,dx \tag{2.65}$$

Leading to the basic nodal displacements:

$$\mathbf{v} = \int_0^L \mathbf{b}^T(x)\,\mathbf{e}(x)\,dx \tag{2.66}$$

Hence by introduction of the section constitutive law in Eq. (2.63), the element flexibility and the equivalent basic displacement vector are:

$$\mathbf{f} = \int_0^L \mathbf{b}^T(x)\,\mathbf{f}_s(x)\,\mathbf{b}(x)\,dx, \tag{2.67}$$

$$\mathbf{v}_0 = \int_0^L \mathbf{b}^T(x)\,\Big(\mathbf{f}_s(x)\,\mathbf{s}_p(x) + \mathbf{e}_0(x)\Big)\,dx. \tag{2.68}$$

The basic incremental constitutive relation follows as

$$\dot{\mathbf{q}} = \mathbf{k}\,\dot{\mathbf{v}} \qquad \mathbf{k} = \mathbf{f}^{-1} \tag{2.69}$$

The element equilibrium is once again obtained by applying the basic-to-local transformation:

$$\mathbf{p}_l^{ext} = \mathbf{a}_b^T\mathbf{f}^{-1}\;\mathbf{v} - \mathbf{a}_b^T\mathbf{f}^{-1}\;\mathbf{v}_0 + \mathbf{p}_{lp} \tag{2.70}$$

where $\mathbf{p}_{lp}$ is the equivalent nodal force vector defined in Section 2.2.2 and $\mathbf{p}_{l0} = \mathbf{a}_b^T\mathbf{f}^{-1}\;\mathbf{v}_0 - \mathbf{p}_{lp}$. The governing element equilibrium equation is once again:

$$\mathbf{p}_l^{ext} - \mathbf{p}_l^{int} + \mathbf{p}_{l0} = 0 \tag{2.71}$$

Equations (2.71), (2.58) and (2.66) are the governing equations of the FB element:

$$\mathbf{p}_l^{ext} + \mathbf{p}_{l0} - \mathbf{p}_l^{int} = 0 \tag{2.72}$$

$$\mathbf{s}(x) - \mathbf{b}(x)\mathbf{q} + \mathbf{s}_p(x) = 0 \tag{2.73}$$

$$\mathbf{v} - \int_L \mathbf{b}^T\mathbf{e}(x)\;dx = 0 \tag{2.74}$$

2.2.5 Mixed approach

The three-field Hu-Washizu functional for the beam can be written as follows:

$$\Pi(\mathbf{u},\boldsymbol{\varepsilon},\boldsymbol{\sigma}) = \Pi^{int} + \Pi^{ext} \tag{2.75}$$

$$\Pi^{int} = \int_\Omega W(\boldsymbol{\varepsilon})\;d\Omega + \int_\Omega \boldsymbol{\sigma}^T\left(\mathbf{D}\mathbf{u} - \boldsymbol{\varepsilon}\right)\;d\Omega \tag{2.76}$$

where $\Omega = A \times [0 \div L]$ is the volume of the beam, A and L are its area and length respectively. The dependencies on x, y, z are dropped here, for brevity. To account for a general nonlinear constitutive response of the material, $W(\boldsymbol{\varepsilon})$ is replaced with $\boldsymbol{\varepsilon}^T\hat{\boldsymbol{\sigma}}$.

The load potential energy can be written as follows:

$$\Pi^{ext} = -\int_0^L \mathbf{u}_s^T \mathbf{p}\, dx - \mathbf{u}_l^T \mathbf{p}_l^{ext} \tag{2.77}$$

Upon substitution of the section resultants and the generalized section strains through the standard operators of Eqs. (2.19), (2.35), (2.17), and (2.15):

$$\mathbf{s} = \int_A \mathbf{a}_s^T \boldsymbol{\sigma}\, dA \qquad\qquad \boldsymbol{\varepsilon} = \mathbf{a}_s \mathbf{e} \qquad\qquad \mathbf{D}\ \mathbf{u} = \mathbf{a}_s \mathbf{D}_s \mathbf{u}_s \tag{2.78}$$

It results:

$$\Pi^{int} = \int_0^L \int_A \mathbf{e}^T\, \mathbf{a}_s^T \hat{\boldsymbol{\sigma}}\, dA\, dx + \int_0^L \int_A \boldsymbol{\sigma}^T \mathbf{a}_s \big(\mathbf{D}_s \mathbf{u}_s - \mathbf{e}\big) dA\, dx \tag{2.79}$$

$$\Pi(\mathbf{u}_s, \mathbf{e}, \mathbf{s}) = \int_0^L \mathbf{e}^T\, \hat{\mathbf{s}}\, dx + \int_0^L \mathbf{s}^T \big(\mathbf{D}_s\, \mathbf{u}_s - \mathbf{e}\big)\, dx \ + \ \Pi^{ext} \tag{2.80}$$

Which may also be rewritten as:

$$\Pi(\mathbf{u}_s, \mathbf{e}, \mathbf{s}) = \int_0^L \mathbf{e}^T\, (\hat{\mathbf{s}} - \mathbf{s})\ dx + \int_0^L \mathbf{s}^T\ \mathbf{D}_s\, \mathbf{u}_s\, dx \ + \ \Pi^{ext} \tag{2.81}$$

By taking its variation and setting it to zero:

$$\delta\Pi = \int_0^L \delta\mathbf{e}^T (\hat{\mathbf{s}} - \mathbf{s})\, dx + \int_0^L \delta\mathbf{s}^T (\mathbf{D}_s \mathbf{u}_s - \mathbf{e})\, dx + \int_0^L (\mathbf{D}_s \delta\mathbf{u}_s)^T \mathbf{s}\, dx + \delta\Pi^{ext} = 0 \tag{2.82}$$

The second integral:

$$\int_0^L \delta\mathbf{s}^T \mathbf{D}_s\, \mathbf{u}_s\, dx = \int_0^L \big(\delta N\, u' + \delta M_z\, \vartheta_z' + \delta M_y\, \vartheta_y' + \delta V_y\, (v' - \vartheta_z) + \delta V_z\, (w' + \vartheta_y) + \delta M_x\, \vartheta_x'\big)\, dx \tag{2.83}$$

Integrating by parts the derivative terms:

$$\int_0^L \delta N\, u'\, dx = \big[\delta N\, u\big]_0^L - \int_0^L \delta N'\, u\, dx \tag{2.84}$$

$$\int_0^L \delta M_z\, \vartheta_z'\, dx = \big[\delta M_z\, \vartheta_z\big]_0^L - \int_0^L \delta M_z'\, \vartheta_z\, dx \tag{2.85}$$

$$\int_0^L \delta M_y\, \vartheta_y'\, dx = \big[\delta M_y\, \vartheta_y\big]_0^L - \int_0^L \delta M_y'\, \vartheta_y\, dx \tag{2.86}$$

$$\int_0^L \delta M_x\, \vartheta_x'\, dx = \big[\delta M_x\, \vartheta_x\big]_0^L - \int_0^L \delta M_x'\, \vartheta_x\, dx \tag{2.87}$$

Substituting, the integral becomes

$$\begin{aligned}\int_0^L \delta\mathbf{s}^T \mathbf{D}_s\, \mathbf{u}_s\, dx &= \big[\delta N\, u + \delta M_z\, \vartheta_z + \delta M_y\, \vartheta_y + \delta M_x\, \vartheta_x\big]_0^L \\ &+ \int_0^L \Big(- \delta N'\, u - \delta M_z'\, \vartheta_z - \delta M_y'\, \vartheta_y - \delta M_x'\, \vartheta_x + \delta V_y\, (v' - \vartheta_z) + \delta V_z\, (w' + \vartheta_y)\Big)\, dx.\end{aligned} \tag{2.88}$$

Using sectional equilibrium relations, which in this case are rewritten from Eq. (2.41) as:

$$\delta N' = 0 \quad \delta M_z' - \delta V_y = 0 \quad \delta M_y' + \delta V_z = 0 \quad \delta M_x' = 0$$

the volume terms cancel, yielding

$$\int_0^L \delta \mathbf{s}^T \mathbf{D}_s \, \mathbf{u}_s \, dx = \delta \mathbf{q}^T \mathbf{v} \tag{2.89}$$

The third integral, similarly:

$$\int_0^L \delta(\mathbf{D}_s \mathbf{u}_s)^T \mathbf{s} \, dx = \int_0^L \left(\delta u' \, N + \delta \vartheta_z' \, M_z + \delta \vartheta_y' \, M_y + \delta(v' - \vartheta_z) \, V_y + \delta(w' + \vartheta_y) \, V_z + \delta \vartheta_x' \, M_x \right) dx \tag{2.90}$$

Integrating by parts the derivative terms:

$$\int_0^L \delta u' \, N \, dx = \left[\delta u \, N \right]_0^L - \int_0^L \delta u \, N' \, dx \tag{2.91}$$

$$\int_0^L \delta \vartheta_z' \, M_z \, dx = \left[\delta \vartheta_z \, M_z \right]_0^L - \int_0^L \delta \vartheta_z \, M_z' \, dx \tag{2.92}$$

$$\int_0^L \delta \vartheta_y' \, M_y \, dx = \left[\delta \vartheta_y \, M_y \right]_0^L - \int_0^L \delta \vartheta_y \, M_y' \, dx \tag{2.93}$$

$$\int_0^L \delta \vartheta_x' \, M_x \, dx = \left[\delta \vartheta_x \, M_x \right]_0^L - \int_0^L \delta \vartheta_x \, M_x' \, dx \tag{2.94}$$

hence:

$$\begin{aligned} \int_0^L \delta(\mathbf{D}_s \mathbf{u}_s)^T \mathbf{s} \, dx = & \left[\delta u \, N + \delta \vartheta_z \, M_z + \delta \vartheta_y \, M_y + \delta \vartheta_x \, M_x \right]_0^L \\ & + \int_0^L \Big(- \delta u \, N' - \delta \vartheta_z \, M_z' - \delta \vartheta_y \, M_y' - \delta \vartheta_x \, M_x' + \delta v' \, V_y - \delta \vartheta_z \, V_y + \delta w' \, V_z + \delta \vartheta_y \, V_z \Big) \, dx \end{aligned} \tag{2.95}$$

Using the section equilibrium in Eq. (2.41), the domain integrals reduce to external load contributions. Collecting terms, it results:

$$\int_0^L \delta(\mathbf{D}_s \mathbf{u}_s)^T \mathbf{s} \, dx = \delta \mathbf{v}^T \mathbf{q} + \int_0^L \delta \mathbf{u}_s^T \mathbf{p} \, dx \tag{2.96}$$

where $\delta \mathbf{v}^T \mathbf{q}$ comes from the boundary terms and $\mathbf{p}$ is the vector of distributed loads.
The variation of the functional becomes:

$$\delta \Pi = \int_0^L \delta \mathbf{e}^T (\hat{\mathbf{s}} - \mathbf{s}) \, dx + \delta \mathbf{q}^T \mathbf{v} - \int_0^L \delta \mathbf{s}^T \mathbf{e} \, dx + \delta \mathbf{v}^T \mathbf{q} + \int_0^L \delta \mathbf{u}_s^T \mathbf{p} \, dx + \delta \Pi^{ext} = 0 \tag{2.97}$$

Since $\delta \Pi^{ext} = - \int_0^L \delta \mathbf{u}_s^T \mathbf{p} \, dx - \delta \Pi_{bc}$, with:

$$\delta \Pi_{bc} = \delta \mathbf{u}_l^T \left(\mathbf{p}_l^{ext} + \mathbf{p}_{l0} \right) \tag{2.98}$$

And $\mathbf{v} = \mathbf{a}_b \mathbf{u}_l$, the final functional is:

$$\delta\Pi = \int_0^L \delta\mathbf{e}^T(\hat{\mathbf{s}} - \mathbf{s})\, dx - \int_0^L \delta\mathbf{s}^T\mathbf{e}\, dx + \delta\mathbf{q}^T\mathbf{v} + \delta\mathbf{u}_l^T\left(\mathbf{a}_b\mathbf{q} - \mathbf{p}_l^{ext} - \mathbf{p}_{l0}\right) = 0 \tag{2.99}$$

When a specific expansion for $\mathbf{s}(x)$ is chosen, the functional can be reduced to three main equations. This involves Eq. (2.58), which however imposes exact equilibrium. The section stresses and the virtual section stresses are written as:

$$\mathbf{s} = \mathbf{b}\mathbf{q} + \mathbf{s}_p \qquad\qquad \delta\mathbf{s} = \mathbf{b}\delta\mathbf{q} \tag{2.100}$$

By replacing the above expressions for $\mathbf{s}$ the functional becomes:

$$\delta\Pi = \int_0^L \delta\mathbf{e}^T(\hat{\mathbf{s}} - \mathbf{b}\mathbf{q} - \mathbf{s}_p)\, dx - \int_0^L \delta\mathbf{q}^T\mathbf{b}^T\mathbf{e}\, dx + \delta\mathbf{q}^T\mathbf{v} + \delta\mathbf{u}_l^T\left(\mathbf{a}_b\mathbf{q} - \mathbf{p}_l^{ext} - \mathbf{p}_{l0}\right) = 0 \tag{2.101}$$

The final functional is:

$$\delta\Pi = \delta\mathbf{e}^T \int_0^L (\hat{\mathbf{s}} - \mathbf{b}\mathbf{q} - \mathbf{s}_p)\, dx + \delta\mathbf{q}^T\left(\mathbf{v} - \int_0^L \mathbf{b}^T\, \mathbf{e}\, dx\right) + \delta\mathbf{u}_l^T\left(\mathbf{a}_b\mathbf{q} - \mathbf{p}_l^{ext} - \mathbf{p}_{l0}\right) = 0 \tag{2.102}$$

Leading down to the very same equations of the force-based formulation $\forall\delta\mathbf{e} \neq 0,\ \forall\delta\mathbf{q} \neq 0, \forall\delta\mathbf{u}_l \neq 0$:

$$\mathbf{p}_l^{ext} + \mathbf{p}_{l0} - \mathbf{p}_l^{int} = 0 \tag{2.103}$$

$$\hat{\mathbf{s}}(x) - \mathbf{b}(x)\mathbf{q} - \mathbf{s}_p(x) = 0 \tag{2.104}$$

$$\mathbf{v} - \int_0^L \mathbf{b}^T(x)\ \mathbf{e}(x)\ dx = 0 \tag{2.105}$$

2.3 Beam FE formulations with bond-slip

2.3.1 Local formulation including bond-slip and prestressing

The element kinematics is expanded to include additional degrees of freedom at the element level. Besides the section displacements and rotations at the reference axis, that under the assumption of plane sections remain plane, defining the section strains, a section bond-slip displacement $u_b(x)$ is assigned to each fiber reinforcement or tendon fiber with bond-slip, as shown in Figure 2.7. The additional displacements are stacked in the local displacement vector $\tilde{\mathbf{u}}_l$, modified from

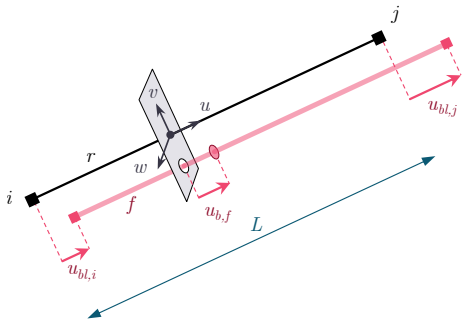

Figure 2.7. Bond-slip degrees of freedom for a single tendon.

Eq. (2.2), which in this case becomes:

$$\tilde{\mathbf{u}}_l = \left\{ \begin{array}{cc} \mathbf{u}_l^T & \mathbf{u}_{bl}^T \end{array} \right\}^T \tag{2.106}$$

where $\mathbf{u}_{bl}$ are the bond-slip displacements parallel to the tendons at node i, j and optional intermediate nodes. More details on the section kinematics are presented in Section 2.3.2. The dual force vector $\tilde{\mathbf{p}}_l$, modified from Eq. (2.3), contains the corresponding work conjugate forces:

$$\tilde{\mathbf{p}}_l = \left\{ \begin{array}{cc} \mathbf{p}_l^T & \mathbf{p}_{bl}^T \end{array} \right\}^T \tag{2.107}$$

where $\mathbf{p}_{bl}$ are the forces work-conjugates to the bond-slip displacements parallel to the tendons at node i, j and optional intermediate nodes.
In the basic system, without rigid body modes, the displacement vector is $\tilde{\mathbf{v}}$ and the force vector is $\tilde{\mathbf{q}}$. They are defined expanding $\mathbf{v}$ and $\mathbf{q}$ of Eqs. 2.5, and 2.7, respectively, by adding the degrees of freedom corresponding to bond-slip displacements $\mathbf{v}_b$ and $\mathbf{q}_b$, such that:

$$\tilde{\mathbf{v}} = \left\{ \begin{array}{cc} \mathbf{v}^T & \mathbf{v}_b^T \end{array} \right\}^T \qquad \tilde{\mathbf{q}} = \left\{ \begin{array}{cc} \mathbf{q}^T & \mathbf{q}_b^T \end{array} \right\}^T \tag{2.108}$$

Here, $\mathbf{v}_b$ and $\mathbf{q}_b$ contain all the bond-slip displacements and tendon force values in the interpolation points, as shown in Figure 2.8, where m_f is the number of interpolation points along the fibers with bond-slip. If n_f is the number of fibers with bond-slip, the size of $\mathbf{v}_b$ and $\mathbf{q}_b$ is $m_f \cdot n_f$. In the FB formulation, the exact internal force distribution along the element can be derived from the end forces $\mathbf{q}$ and no internal nodes are needed. On the other hand, the bond force distribution along the element is unknown beforehand, so the vector $\mathbf{q}_b$ of nodal bond forces is enriched with internal nodes. For example, for $m_f = 4$ in Figure 2.8, third order interpolation functions can be used. More details on the interpolations are provided in Chapter 4.

Finally, a compatibility matrix $\tilde{\mathbf{a}}_g$, which definition depends on the element formulation and is detailed in Sections 2.3.4 and 2.3.5, is used to eliminate the rigid body modes from the local displacements $\tilde{\mathbf{u}}_l$ such that:

$$\tilde{\mathbf{v}} = \tilde{\mathbf{a}}_g \ \tilde{\mathbf{u}}_l \tag{2.109}$$

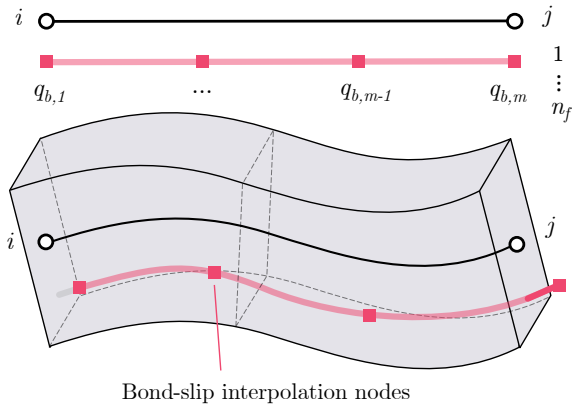

Figure 2.8. 3D local configuration detailing interpolation nodes and quadrature points for classical degrees of freedom and additional ones in the case of multiple tendons.

2.3.2 Enriched section with bond-slip and prestressing

The cross section arrays include the terms corresponding to cross section remaining plane (denoted by subscript r, for rigid), the terms corresponding to the fibers allowed to slip (denoted by subscript f), plus the terms that define bond-slip (denoted by subscript b). The axial displacement u_x of each fiber f is rewritten from Eq. (2.15) as follows:

$$\begin{aligned} u_x\left(x,y,z\right) &= u_r(x,y,z) + u_{b,f}(x,y,z) \\ u_x\left(x,y,z\right) &= \begin{bmatrix} 1 & -y & z \end{bmatrix} \begin{bmatrix} u(x) \\ \vartheta_z(x) \\ \vartheta_y(x) \end{bmatrix} + u_b(x, y_f, z_f) \end{aligned} \tag{2.110}$$

where $u_{b,f}(x,y,z)$ is the bond-slip displacement defined for each f^{th} fiber with bond-slip (from 1 to n_f), and $y_f(x), z_f(x)$ are its cross section coordinates along the axis of the beam. The section bond-slip displacements vector is:

$$\mathbf{u}_b(x) = \begin{Bmatrix} u_{b,1} & \cdots & u_{b,n_f} \end{Bmatrix}^T \tag{2.111}$$

where $u_{b,f} = u_b(x, y_f, z_f)$. The rigid section strain vector $\mathbf{e}(x)$ remains the same, but an additional section bond-slip strain vector is defined as:

$$\mathbf{e}_b(x) = \begin{Bmatrix} \varepsilon_{b,1} & \cdots & \varepsilon_{b,n_f} \end{Bmatrix}^T \tag{2.112}$$

where $\varepsilon_{b,1} \quad \cdots \quad \varepsilon_{b,n_f}$ are the bond-slip displacement derivatives, one for each of the n_f fibers with bond-slip. The section bond force vector dual to $\mathbf{u}_b(x)$ is:

$$\mathbf{p}_b(x) = \left\{ \begin{array}{ccc} p_{b,1} & \cdots & p_{b,n_f} \end{array} \right\}^T \tag{2.113}$$

where $p_{b,f} = \int_{l_b} \tau_{b,f}\, dl$ is the bond force per unit length of the f^{th} fiber with bond-slip, and l_b is the fiber perimeter. The stresses $\tau_{b,1} \quad \cdots \quad \tau_{b,n_f}$ are the bond shear stresses of the f^{th} fiber with bond-slip. The section stresses $\mathbf{s}(x)$ dual to the section strains $\mathbf{e}(x)$ are unchanged. It is though necessary to define a vector with the stresses of all the fibers with bond-slip as follows:

$$\mathbf{s}_b(x) = \left\{ \begin{array}{ccc} N_{b,1} & \cdots & N_{b,n_f} \end{array} \right\}^T \tag{2.114}$$

The forces $N_{b,1} \quad \cdots \quad N_{b,n_f}$ are the axial forces in each one of the n_f tendons. From equilibrium, the bond-slip forces $\mathbf{p}_b(x)$ are the derivatives of $\mathbf{s}_b(x)$ with respect to x.

Having defined the section strain arrays, the material strains $\boldsymbol{\varepsilon}_m$ at any section point can be written as:

$$\boldsymbol{\varepsilon}_m(x,y,z) = \mathbf{a}_s(y,z)\ \mathbf{e}(x) + \ \boldsymbol{\varepsilon}_{b,f}(x,y,z) \tag{2.115}$$

where $\boldsymbol{\varepsilon}_m(x,y,z)$ and $\mathbf{a}_s(y,z)$ are unchanged from the perfect bond case, while $\mathbf{e}_b(x,y,z)$ is only axial and present in the n_f fibers with bond-slip.

$$\boldsymbol{\varepsilon}_{b,f}(x,y,z) = \left\{ \begin{array}{c} \varepsilon_{b,f} \\ 0 \\ 0 \end{array} \right\} \tag{2.116}$$

Figure 2.9 shows the displacement, strain, force and stress distributions considering bond between the different fibers.

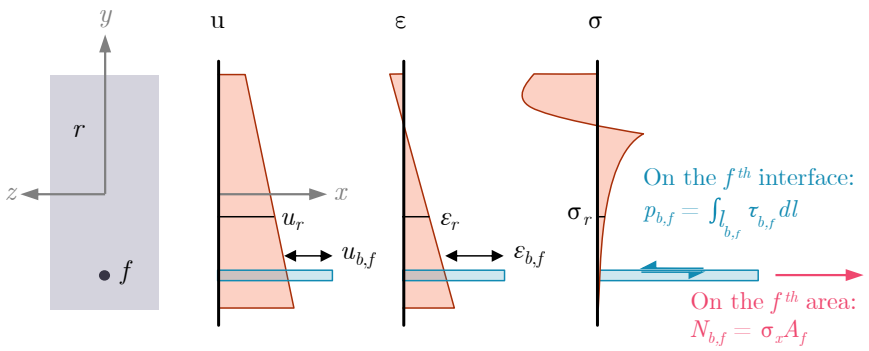

Figure 2.9. Section displacement, strain, force and stress distributions.

Prestress can be modeled as an imposed initial strain $\boldsymbol{\varepsilon}_{0,f}(x,y,z)$ that is the axial strain along the tendon axis [71, 72]. By rewriting Eq. 2.115, it results:

$$\boldsymbol{\varepsilon}_m(x,y,z) \ = \mathbf{R}_s(x,y,z)\ \mathbf{a}_s(y,z)\ \mathbf{e}(x) + \boldsymbol{\varepsilon}_{b,f}(x,y,z) + \boldsymbol{\varepsilon}_{0,f}(x,y,z) \tag{2.117}$$

where $\boldsymbol{\varepsilon}_{0,f}(x,y,z)$ is introduced to apply prestress:

$$\boldsymbol{\varepsilon}_{0,f}(x,y,z) = \{ \ \varepsilon_{0,f}(x,y,z) \quad 0 \quad 0 \ \}^T \tag{2.118}$$

while $\mathbf{R}_s(x,y,z)$ is a fiber-wise 3×3 rotation matrix that projects the tendon strains onto the tendon axis, defined in Section 4.2.1.

2.3.3 Section constitutive relations

By applying the virtual works over the section, the section force $\mathbf{s}$ can be computed as:

$$\mathbf{s} = \int_A \tilde{\mathbf{a}}_s^T \boldsymbol{\sigma} \ dA \qquad\qquad \boldsymbol{\sigma} = \mathbf{k}_m \boldsymbol{\varepsilon} \tag{2.119}$$

where $\tilde{\mathbf{a}}_s = \mathbf{R}\ \mathbf{a}_s$ and $\mathbf{k}_m$ is the material point stiffness. By introducing Eq. (2.117):

$$\mathbf{k}_s = \int_A \tilde{\mathbf{a}}_s^T \mathbf{k}_m \tilde{\mathbf{a}}_s \ dA \tag{2.120}$$

where $\mathbf{k}_s$ is the section stiffness.
The sole response of every fiber with bond-slip is N_b so that:

$$N_{b,f} = \int_{A_f} \sigma \ dA \quad \text{for each fiber } f \tag{2.121}$$

where A_f is the area of the f^{th} fiber with bond-slip.
In the bond interface, each bond-slip displacement u_b is treated as an independent variable. For each interface, the bond stress τ_b, force per unit length p_b and section bond stiffness k_{sb} are given by:

$$p_b = \int_{l_b} \tau_b \ dl, \quad \tau_b = k_b \ u_b \tag{2.122}$$

$$k_{sb} = \int_{l_b} k_b \ dl, \quad p_b = k_{sb}\, u_b, \quad \text{for each fiber } f \tag{2.123}$$

2.3.4 Displacement-based approach

The section bond-slip displacements $\mathbf{u}_b(x)$ are independently interpolated from the basic bond-slip displacements $\mathbf{v}_b$ by means of dedicated shape functions $\mathbf{N}_b(x)$:

$$\mathbf{u}_b(x) = \mathbf{N}_b(x)\ \mathbf{v}_b \tag{2.124}$$

$$\begin{Bmatrix} u_{b,1}(x) \\ \vdots \\ u_{b,n_f}(x) \end{Bmatrix} = \begin{bmatrix} \mathbf{N}_{b,1}(x) & 0 & \cdots & 0 \\ 0 & \mathbf{N}_{b,2}(x) & \cdots & 0 \\ \vdots & \vdots & \ddots & \vdots \\ 0 & 0 & \cdots & \mathbf{N}_{b,n_f}(x) \end{bmatrix} \begin{Bmatrix} \mathbf{v}_{b,1} \\ \mathbf{v}_{b,2} \\ \vdots \\ \mathbf{v}_{b,n_f} \end{Bmatrix} \tag{2.125}$$

where $\mathbf{N}_b(x)$ is size $n_f \times (m_f \cdot n_f)$, and the eligible shape functions $\mathbf{N}_{b,f}(x)$, which are one-row vectors of size m_f, are detailed in Section 4.1.1.

Then, Eq. (2.44) can be modified as follows:

$$\tilde{\mathbf{u}}_s(x) = \tilde{\mathbf{N}}(x)\,\tilde{\mathbf{v}} \tag{2.126}$$

where:

$$\tilde{\mathbf{u}}_s(x) = \begin{bmatrix} \mathbf{u}_s \\ \mathbf{u}_b \end{bmatrix} \qquad \tilde{\mathbf{N}}(x) = \begin{bmatrix} \mathbf{N} & \mathbf{0} \\ \mathbf{0} & \mathbf{N}_b \end{bmatrix} \tag{2.127}$$

Each of these operators has additional n_f rows, while the matrices also have additional $n_f \cdot m_f$ columns. The compatibility equation requires to compute the bond-slip displacements' first derivatives $\mathbf{e}_b(x)$ as:

$$\mathbf{e}_b(x) = \frac{\partial}{\partial x}\ \mathbf{u}_b(x) = \mathbf{B}_b(x)\ \mathbf{v}_b \tag{2.128}$$

where:

$$\mathbf{B}_b(x) = \frac{\partial}{\partial x}\mathbf{N}_b(x) \tag{2.129}$$

Eq. (2.46) can also be written in a compact form:

$$\tilde{\mathbf{e}}(x) = \tilde{\mathbf{B}}(x)\,\tilde{\mathbf{v}} \tag{2.130}$$

where:

$$\tilde{\mathbf{e}}_s(x) = \begin{Bmatrix} \mathbf{e}_s \\ \mathbf{e}_b \end{Bmatrix} \qquad \tilde{\mathbf{B}}(x) = \begin{bmatrix} \mathbf{B} & \mathbf{0} \\ \mathbf{0} & \mathbf{B}_b \end{bmatrix} \tag{2.131}$$

The section stress $\tilde{\mathbf{s}}(x)$ and the section tangent stiffness $\tilde{\mathbf{k}}_s(x)$ are still obtained from the fiber section response of Eq (2.36), where the operators are modified to accommodate for bond-slip derivatives. The section constitutive relation is introduced as:

$$\tilde{\mathbf{s}}(x) = \tilde{\mathbf{k}}_s(x)\left(\tilde{\mathbf{e}}(x) - \tilde{\mathbf{e}}_0(x)\right) \tag{2.132}$$

where:

$$\tilde{\mathbf{e}}_0(x) = \begin{Bmatrix} \mathbf{e}_0 \\ \mathbf{0} \end{Bmatrix} \tag{2.133}$$

While the bond-slip constitutive relationship, which acts on the interface $A_b = l_b \times [0\ \ L]$ between the rigid component r and the ones with bond-slip f, is according to Eq. (2.123), which in vector notation becomes:

$$\boldsymbol{\tau}_b(x) = \mathbf{k}_b(x)\ \mathbf{u}_b(x) \tag{2.134}$$

$$\mathbf{p}_b(x) = \int_{l_b} \boldsymbol{\tau}_b(x)\ dl \tag{2.135}$$

Writing the virtual works and applying the weak form of equilibrium with virtual displacements $\delta\tilde{\mathbf{u}}_l$ now gives:

$$\delta\tilde{\mathbf{v}}^T\tilde{\mathbf{q}} = \int_0^L \delta\tilde{\mathbf{e}}^T(x)\,\tilde{\mathbf{s}}(x)\,dx + \int_0^L \delta\mathbf{u}_b^T(x)\ \mathbf{p}_b(x)\ dx - \int_0^L \delta\tilde{\mathbf{u}}_s^T(x)\,\tilde{\mathbf{p}}(x)\,dx \tag{2.136}$$

where $\delta\tilde{\mathbf{u}}_s(x) = \tilde{\mathbf{a}}(x)\,\delta\tilde{\mathbf{v}}$, $\delta\tilde{\mathbf{e}}(x) = \tilde{\mathbf{B}}(x)\,\delta\tilde{\mathbf{v}}$ and $\delta\mathbf{u}_b = \mathbf{N}_b(x)\delta\mathbf{v}_b$.
To solve this, two different element sections requiring similar operators can be identified, one for the fiber sections, and one for the bond sections.

Fiber section operators can be expressed as:

$$\tilde{\mathbf{B}}(x) = \begin{bmatrix} \mathbf{B} & \mathbf{0} \\ \mathbf{0} & \mathbf{B}_b \end{bmatrix} \qquad (6+n_f) \times (6+m_f \cdot n_f) \tag{2.137}$$

$$\tilde{\mathbf{e}}(x) = \begin{bmatrix} \mathbf{e} \\ \mathbf{e}_b \end{bmatrix} \qquad \tilde{\mathbf{s}}(x) = \begin{bmatrix} \hat{\mathbf{s}} \\ \hat{\mathbf{s}}_b \end{bmatrix} \qquad (6+n_f) \times 1 \tag{2.138}$$

Bond section operators can be expressed as:

$$\tilde{\mathbf{B}}(x) = \begin{bmatrix} \mathbf{0} & \mathbf{B}_b \end{bmatrix} \qquad n_f \times (6+m_f \cdot n_f) \tag{2.139}$$

$$\tilde{\mathbf{e}}(x) = \mathbf{u}_b \qquad \tilde{\mathbf{s}}(x) = \hat{\mathbf{p}}_b \qquad n_f \times 1 \tag{2.140}$$

where the hat $\hat{\cdot}$ indicates that these forces are obtained from the material constitutive laws. This allows to unify the notation so that the equilibrium is finally obtained, $\forall\delta\tilde{\mathbf{v}} \neq \mathbf{0}$:

$$\tilde{\mathbf{q}} = \int_0^L \tilde{\mathbf{B}}^T(x)\,\tilde{\mathbf{s}}(x)\,dx - \int_0^L \tilde{\mathbf{a}}^T(x)\,\tilde{\mathbf{p}}(x)\,dx \tag{2.141}$$

By applying Eq. (2.47):

$$\tilde{\mathbf{q}} = \tilde{\mathbf{k}}\,\tilde{\mathbf{v}} - \tilde{\mathbf{q}}_0, \tag{2.142}$$

where the stiffness matrix $\tilde{\mathbf{k}}$ and the equivalent nodal forces $\tilde{\mathbf{q}}_0$ are:

$$\tilde{\mathbf{k}} = \int_0^L \tilde{\mathbf{B}}^T(x)\,\tilde{\mathbf{k}}_s(x)\,\tilde{\mathbf{B}}(x)\,dx, \tag{2.143}$$

$$\tilde{\mathbf{q}}_0 = \int_0^L \tilde{\mathbf{B}}^T(x)\,\tilde{\mathbf{k}}_s(x)\,\tilde{\mathbf{e}}_0(x)\,dx + \int_0^L \tilde{\mathbf{N}}^T(x)\,\tilde{\mathbf{p}}(x)\,dx. \tag{2.144}$$

The element equilibrium is finally obtained by applying the basic-to-local transformation:

$$\tilde{\mathbf{p}}_l^{ext} = \tilde{\mathbf{a}}_g^T\tilde{\mathbf{k}}\,\tilde{\mathbf{v}} - \tilde{\mathbf{a}}_g^T\tilde{\mathbf{q}}_0 + \tilde{\mathbf{p}}_{lp} \tag{2.145}$$

where $\tilde{\mathbf{p}}_{lp}$ has only zero values in the components allocated for bond-slip DOFs. However, something must be said for matrix $\tilde{\mathbf{a}}_g$: the bond-slip DOFs at the end nodes must be compatible at the global scale with adjacent elements. As for the other nodes, these may either be condensed or have no transformation applied, and saved as individual global DOFs. In the latter case, $\tilde{\mathbf{a}}_g$ will result as:

$$\tilde{\mathbf{a}}_g(x) = \begin{bmatrix} \mathbf{a}_g & \mathbf{0} \\ \mathbf{0} & \mathbf{I}_{m_f \cdot n_f} \end{bmatrix} \tag{2.146}$$

where $\mathbf{I}_{m_f \cdot n_f}$ is an identity matrix of size $m_f \cdot n_f$.

The governing element equilibrium equation is once again:

$$\tilde{\mathbf{p}}_l^{ext} + \tilde{\mathbf{p}}_{l0} - \tilde{\mathbf{p}}_l^{int} = 0 \tag{2.147}$$

And the final governing equations are the same with different operators:

$$\tilde{\mathbf{p}}_l^{ext} + \tilde{\mathbf{p}}_{l0} - \tilde{\mathbf{p}}_l^{int} = 0 \tag{2.148}$$

$$\tilde{\mathbf{e}}(x) - \tilde{\mathbf{B}}(x)\,\tilde{\mathbf{v}} - \tilde{\mathbf{e}}_0(x) = 0 \tag{2.149}$$

$$\tilde{\mathbf{q}} - \int_0^L \tilde{\mathbf{B}}^T(x)\,\tilde{\mathbf{s}}(x)\,dx + \int_0^L \tilde{\mathbf{N}}^T(x)\,\tilde{\mathbf{p}}(x)\,dx = 0 \tag{2.150}$$

2.3.5 Force-based approach

In the force-based approach, the section forces $\mathbf{s}(x)$ and $\mathbf{s}_b(x)$, and the bond-slip distributed forces $\mathbf{p}_b(x)$ are interpolated by introducing the following relations:

$$\mathbf{s}(x) = \mathbf{b}(x)\mathbf{q} + \mathbf{s}_p(x) \tag{2.151}$$

$$\mathbf{s}_b(x) = \mathbf{b}_b(x)\mathbf{q}_b \tag{2.152}$$

$$\mathbf{p}_b(x) = \mathbf{b}_{b,x}(x)\mathbf{q}_b \tag{2.153}$$

where $\mathbf{b}(x)$ is the conventional equilibrium matrix that imposes constant axial forces, shear forces and torsional moments, and linear bending moments in $\mathbf{s}(x)$ along the beam. $\mathbf{s}_p(x)$ are the exact section forces due to the element loads, if present. $\mathbf{b}_b(x)$ are the interpolation functions of the axial loads in the fibers with bond-slip, and $\mathbf{b}_{b,x}$, the derivatives of $\mathbf{b}_b(x)$ with respect to x, are the interpolation functions of the bond force per unit length in the fibers with bond-slip. Details on the shape of the interpolation functions are given in Section 4.1.1. It is worth pointing out here that the first relation yields the exact distributions of the section forces along the element, while the other two are approximated distributions that depend on the number of the interpolation points used for the fibers with bond-slip (see Figure 2.8).

The governing equations are derived using the principle of virtual works in a full force-based framework. The total domain Ω is partitioned into three subdomains: the domains are Ω_r, where plane sections remain plane, Ω_f, domain of the fibers with bond-slip, and the bond interface A_b, such that:

$$\Omega_r = A_r \times [0, L] \qquad \Omega_f = A_f \times [0, L] \qquad A_b = l_b \times [0, L] \tag{2.154}$$

The internal virtual work is defined as:

$$\delta W^{int} = \int_\Omega \delta\boldsymbol{\sigma}^T\boldsymbol{\varepsilon}\; dV + \int_{A_b} \delta\boldsymbol{\tau}_b^T\mathbf{u}_b\; dx = \int_L\int_A \delta\boldsymbol{\sigma}^T\boldsymbol{\varepsilon}\; dA\; dx + \int_L \delta\mathbf{p}_b^T\mathbf{u}_b dx \tag{2.155}$$

where $\Omega = \Omega_r + \Omega_f$ and $A = A_r + A_f$.
For linearity, the first integral can be rewritten by introducing the section's definitions of Eqs. (2.119) and Eq. (2.121):

$$\int_{A_r} \delta\boldsymbol{\sigma}^T\boldsymbol{\varepsilon}\; dA \; + \int_{A_f} \delta\boldsymbol{\sigma}^T\boldsymbol{\varepsilon}\; dA \; = \delta\mathbf{s}^T\mathbf{e} + \delta\mathbf{s}_b^T\mathbf{e}_b \tag{2.156}$$

Leading to:

$$\delta W^{int} = \int_L (\delta\mathbf{s}^T\mathbf{e} + \delta\mathbf{s}_b^T\;\mathbf{e}_b)dx + \int_L \delta\mathbf{p}_b^T\mathbf{u}_b dx = \int_L \delta\tilde{\mathbf{s}}^T\tilde{\mathbf{e}} dx \tag{2.157}$$

Two different element sections requiring similar operators can be identified, one for the fiber

section, and one for the bond section.

Fiber section operators can be expressed as:

$$\tilde{\mathbf{b}}(x) = \begin{bmatrix} \mathbf{b} & \mathbf{0} \\ \mathbf{0} & \mathbf{b_b} \end{bmatrix} \qquad \big(6+n_f\big) \times \big(6+m_f \cdot n_f\big)$$
$$\tilde{\mathbf{e}}(x) = \begin{bmatrix} \mathbf{e} \\ \mathbf{e}_b \end{bmatrix} \qquad \tilde{\mathbf{s}}(x) = \begin{bmatrix} \hat{\mathbf{s}} \\ \hat{\mathbf{s}}_b \end{bmatrix} \qquad \tilde{\mathbf{s}}_p(x) = \begin{bmatrix} \mathbf{s}_p \\ \mathbf{0} \end{bmatrix} \qquad (6+n_f) \times 1 \tag{2.158}$$

where the hat $\hat{\cdot}$ indicates that these forces are obtained from the material constitutive laws.
Bond section operators can be expressed as:

$$\tilde{\mathbf{b}}(x) = \begin{bmatrix} \mathbf{0} & \mathbf{b}_{b,x} \end{bmatrix} \qquad n_f \times \big(6+m_f \cdot n_f\big)$$
$$\tilde{\mathbf{e}}(x) = \mathbf{u}_b \qquad \tilde{\mathbf{s}}(x) = \hat{\mathbf{p}}_b \qquad n_f \times 1 \tag{2.159}$$

If the local and basic configurations' operators are organized as follows:

$$\tilde{\mathbf{u}}_l = \begin{bmatrix} \mathbf{u}_l \\ \mathbf{u}_{bl} \end{bmatrix} \qquad \tilde{\mathbf{p}}_l^{ext} = \begin{bmatrix} \mathbf{p}_l \\ \mathbf{p}_{bl} \end{bmatrix} \qquad \tilde{\mathbf{p}}_{lp} = \begin{bmatrix} \mathbf{p}_{lp} \\ \mathbf{0} \end{bmatrix} \qquad \tilde{\mathbf{p}}_l^{int} = \tilde{\mathbf{a}}_g^T \tilde{\mathbf{q}} \qquad (12+2\,n_f) \times 1$$
$$\tilde{\mathbf{a}}_g = \begin{bmatrix} \mathbf{a}_g & \mathbf{0} \\ \mathbf{0} & \mathbf{a}_{bg} \end{bmatrix} \qquad \big(6+m_f \cdot n_f\big) \times \big(12+2\,n_f\big)$$
$$\tilde{\mathbf{v}} = \begin{bmatrix} \mathbf{v} \\ \mathbf{v}_b \end{bmatrix} \qquad \tilde{\mathbf{q}} = \begin{bmatrix} \mathbf{q} \\ \mathbf{q}_b \end{bmatrix} \qquad (6+m_f \cdot n_f) \times 1 \tag{2.160}$$

where the compatibility sub-matrix $\mathbf{a}_{bg}$ is defined as a result of the integration by parts:

$$\mathbf{a}_{bg} = \begin{bmatrix} -\mathbf{b}_{b,1}^T(0) & \mathbf{b}_{b,1}^T(L) & \mathbf{0} & \cdots & \mathbf{0} \\ \mathbf{0} & -\mathbf{b}_{b,2}^T(0) & \mathbf{b}_{b,2}^T(L) & \cdots & \mathbf{0} \\ \vdots & \vdots & \ddots & & \mathbf{0} \\ \mathbf{0} & \mathbf{0} & \mathbf{0} & -\mathbf{b}_{b,n_f}^T(0) & \mathbf{b}_{b,n_f}^T(L) \end{bmatrix} \tag{2.161}$$

and $\mathbf{p}_p$ are the equilibrated local reaction forces of the element loads $\mathbf{s}_p(x)$.
Then, the following expression stands:

$$\delta W^{int} = \int_L \delta\tilde{\mathbf{s}}^T \tilde{\mathbf{e}}\; dx = \delta\tilde{\mathbf{q}}^T \int_L \tilde{\mathbf{b}}^T \tilde{\mathbf{e}}\; dx \tag{2.162}$$

The external virtual work can be written as:

$$\delta W^{ext} = \delta\tilde{\mathbf{q}}^T \tilde{\mathbf{v}} \tag{2.163}$$

Because $\delta W^{int} - \delta W^{ext} = 0$, this leads to, $\forall \delta\tilde{\mathbf{q}} \neq \mathbf{0}$:

$$\tilde{\mathbf{v}} - \int_L \tilde{\mathbf{b}}^T \tilde{\mathbf{e}}\; dx = 0 \tag{2.164}$$

By introducing both fiber and bond sections' constitutive laws, respectively, since $\tilde{\mathbf{f}}_s = \tilde{\mathbf{k}}_s^{-1}$:

$$\delta W^{int} = \delta\tilde{\mathbf{q}}^T \int_L \tilde{\mathbf{b}}^T \, \tilde{\mathbf{f}}_s \, \tilde{\mathbf{b}} \, dx \, \tilde{\mathbf{q}} \tag{2.165}$$

Which leads to the modified element flexibility $\tilde{\mathbf{f}}$:

$$\tilde{\mathbf{f}} = \int_L \tilde{\mathbf{b}}^T \, \tilde{\mathbf{f}}_s \, \tilde{\mathbf{b}} \, dx \tag{2.166}$$

So that a modified element constitutive relationship is defined:

$$\tilde{\mathbf{v}} = \tilde{\mathbf{f}} \, \tilde{\mathbf{q}} \tag{2.167}$$

The equilibrium equation of the element in the global configuration, the same as Eq. (2.103), can also be obtained by applying the basic-to-local transformation:

$$\tilde{\mathbf{p}}_l^{ext} = \tilde{\mathbf{a}}_g^T \, \tilde{\mathbf{f}}^{-1} \, \tilde{\mathbf{v}} - \tilde{\mathbf{a}}_g^T \, \tilde{\mathbf{f}}^{-1} \, \tilde{\mathbf{v}}_0 + \tilde{\mathbf{p}}_{lp} \tag{2.168}$$

where $\tilde{\mathbf{p}}_{lp}$ and $\tilde{\mathbf{v}}_0$ have $\tilde{\mathbf{0}}$ in the additional components related to bond, and where $\tilde{\mathbf{p}}_{l0} = \tilde{\mathbf{a}}_g^T \, \tilde{\mathbf{f}}^{-1} \, \tilde{\mathbf{v}}_0 - \tilde{\mathbf{p}}_{lp}$. The governing element equilibrium equation is:

$$\tilde{\mathbf{p}}_l^{ext} - \tilde{\mathbf{p}}_l^{int} + \tilde{\mathbf{p}}_{l0} = 0 \tag{2.169}$$

By adding the contribution of the external work, the governing equations are, as in [23, 52]:

$$\tilde{\mathbf{p}}_l^{ext} + \tilde{\mathbf{p}}_{l0} - \tilde{\mathbf{p}}_l^{int} = 0 \tag{2.170}$$

$$\tilde{\mathbf{s}} - \tilde{\mathbf{b}}\tilde{\mathbf{q}} - \tilde{\mathbf{s}}_p = 0 \tag{2.171}$$

$$\tilde{\mathbf{v}} - \int_L \tilde{\mathbf{b}}^T \tilde{\mathbf{e}} \, dx = 0 \tag{2.172}$$

After introducing the interpolation functions for the tendon forces, and performing the standard integration by parts, the results are consistent with the force-based formulation and global governing equations expressed in the same form as those given in Eqs. (2.72)-(2.74).

In this case however, with respect to the displacement-based approach of Section 2.3.4, the section bond-slip $\mathbf{u}_b(x)$ and the nodal bond-slip $\mathbf{v}_b$ are independent from each other as only weak form compatibility is imposed on these. Also, continuity on adjacent elements is imposed on $\mathbf{v}_b$ but not on $\mathbf{u}_b(x)$, which allows for different slip displacements in the same node of two contiguous elements, which is a better hypothesis to model fractures within beam elements.

2.3.6 Mixed approach

The governing equations can also be derived from a four-field Hu-Washizu variational principle, here extended to include bond-slip effects at discrete interface regions, according to [52]. Among several possible procedures listed in the paper, where either $\mathbf{u}_b(x)$, $\mathbf{s}_b(x)$, or both are taken as field variables, only $\mathbf{s}_b(x)$ is here interpolated, as it produces the same favorable physical outcomes as the pure force-based approach.

The axial force in the bond-slip fibers is interpolated as:

$$\hat{\mathbf{s}}_b(x) = \mathbf{b}_b(x)\,\mathbf{q}_b \tag{2.173}$$

The generalized Hu-Washizu functional for the beam with bond-slip can be expressed as:

$$\Pi(\mathbf{u}_m, \boldsymbol{\varepsilon}_m, \boldsymbol{\sigma}_m, \mathbf{u}_b) = \Pi^{int} + \Pi^{ext} \tag{2.174}$$

$$\Pi^{int} = \int_\Omega W(\boldsymbol{\varepsilon}, \mathbf{e}_b)\, d\Omega + \int_{A_b} W_b(\mathbf{u}_b)\, dA + \int_\Omega \boldsymbol{\sigma}^T \big(\mathbf{D}\mathbf{u} - \boldsymbol{\varepsilon}\big)\, d\Omega + \int_{\Omega_f} \boldsymbol{\sigma}^T \big(\mathbf{u}_b' - \mathbf{e}_b\big)\, d\Omega \tag{2.175}$$

where $\Omega = \Omega_r \cup \Omega_f \cup A_b$ and $\Omega = \Omega_r \cup \Omega_f$, and $\mathbf{u}_b' = \partial/\partial x\ \mathbf{u}_b$.
The external load potential energy is:

$$\Pi^{ext} = -\mathbf{u}_l^T \big(\mathbf{p}_l^{ext} - \mathbf{p}_{l0}\big) - \mathbf{u}_{bl}^T \mathbf{p}_{bl} \tag{2.176}$$

Figure 2.10 shows the different beam domains.

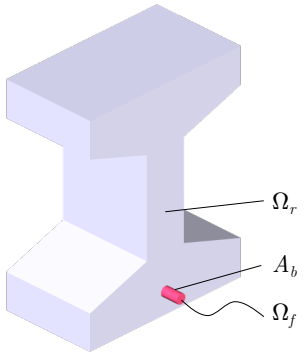

Figure 2.10. Beam sub-domains.

To account for a general nonlinear constitutive response of the materials, the energy densities are replaced as follows:

$$W(\boldsymbol{\varepsilon}, \mathbf{e}_b) = \boldsymbol{\varepsilon}^T \hat{\boldsymbol{\sigma}}, \qquad\qquad W_b(\mathbf{u}_b) = \mathbf{u}_b^T \hat{\boldsymbol{\tau}}_b \tag{2.177}$$

where the $\hat{\cdot}$ refers to the constitutive response. Upon substitution of the section resultants, using the definitions $\Omega_r = A_r \times [0, L]$, $\Omega_f = A_f \times [0, L]$, $A_b = l_b \times [0, L]$, the following expression is obtained:

$$\begin{aligned}\Pi^{int} = &\int_0^L \int_A \boldsymbol{\varepsilon}^T\, \mathbf{a}_s^T \hat{\boldsymbol{\sigma}}\, dA\, dx + \int_0^L \int_{l_b} \mathbf{u}_b^T \hat{\boldsymbol{\tau}}_b\, dl\, dx + \\ &+ \int_0^L \int_A \boldsymbol{\sigma}^T \mathbf{a}_s \big(\mathbf{D}_s \mathbf{u}_s - \boldsymbol{\varepsilon}\big) dA\, dx + \int_0^L \int_{A_f} \boldsymbol{\sigma}^T dA\, \big(u_b' - \mathbf{e}_b\big) dx\end{aligned} \tag{2.178}$$

$$\Pi^{int} = \int_0^L \mathbf{e}^T\, \hat{\mathbf{s}}\, dx + \int_0^L \mathbf{u}_b^T \hat{\mathbf{p}}_b\, dx + \int_0^L \mathbf{s}^T \big(\mathbf{D}_s \mathbf{u}_s - \mathbf{e}\big) dx + \int_0^L \mathbf{s}_b^T \big(\mathbf{u}_b' - \mathbf{e}_b\big) dx \tag{2.179}$$

By substituting the interpolated force $\hat{\mathbf{s}}_b(x) = \mathbf{b}_b(x)\,\mathbf{q}_b$:

$$\int_0^L \mathbf{s}_b^T \big(\mathbf{u}_b' - \mathbf{e}_b\big) dx = \mathbf{q}_b^T \int_0^L \mathbf{b}_b^T \big(\mathbf{u}_b' - \mathbf{e}_b\big)\, dx \tag{2.180}$$

Integrating by parts the first term,

$$\int_0^L \mathbf{b}_b^T \mathbf{u}_b' \, dx = \mathbf{a}_{bg} \, \mathbf{u}_{bl} - \int_0^L \mathbf{b}_{b,x}^T \mathbf{u}_b \, dx \tag{2.181}$$

where $\mathbf{a}_{bg}$ is the same as Eq. (2.161). This leads to:

$$\int_0^L \mathbf{s}_b^T \left(\mathbf{u}_b' - \mathbf{e}_b\right) dx = \mathbf{q}_b^T \left(\mathbf{a}_{bg} \, \mathbf{u}_{bl} - \int_0^L (\mathbf{b}_{b,x}^T \mathbf{u}_b + \mathbf{b}_b^T \mathbf{e}_b) dx\right) \tag{2.182}$$

The variation of the functional is:

$$\delta\Pi^{int} = \delta\Pi_{pb} + \delta\Pi_b = 0 \tag{2.183}$$

$$\delta\Pi_{pb}^{int} = \int_0^L \delta\mathbf{e}^T (\hat{\mathbf{s}} - \mathbf{s}) \, dx + \int_0^L \delta\mathbf{s}^T (\mathbf{D}_s \mathbf{u}_s - \mathbf{e}) \, dx + \int_0^L (\mathbf{D}_s \delta\mathbf{u}_s)^T \mathbf{s} \, dx \tag{2.184}$$

$$\delta\Pi_b^{int} = \int_0^L \delta\mathbf{e}_b^T \hat{\mathbf{s}}_b \, dx + \int_0^L \delta\mathbf{u}_b^T \hat{\mathbf{p}}_b \, dx + \delta\mathbf{q}_b^T \left(\mathbf{a}_{bg}\mathbf{u}_{bl} - \int_0^L (\mathbf{b}_{b,x}^T \mathbf{u}_b + \mathbf{b}_b^T \mathbf{e}_b) dx\right) + \tag{2.185}$$

$$- \mathbf{q}_b^T \int_0^L (\mathbf{b}_{b,x}^T \delta\mathbf{u}_b + \mathbf{b}_b^T \delta\mathbf{e}_b) \, dx \tag{2.186}$$

where $\delta\Pi_{pb}^{int}$ is the classical three-field functional with perfect bond that leads to Eq. (2.82) when the section equations are considered. $\delta\Pi_b^{int}$ is the new term accounting for the presence of bond slip.
The variation of the external load potential energy is:

$$\delta\Pi^{ext} = \delta\Pi_{pb}^{ext} + \delta\Pi_b^{ext} \tag{2.187}$$

$$\delta\Pi_{pb}^{ext} = -\delta\mathbf{u}_l^T \left(\mathbf{p}_l^{ext} + \mathbf{p}_{l0}\right) \tag{2.188}$$

$$\delta\Pi_b^{ext} = -\delta\mathbf{u}_{bl}^T \mathbf{p}_{bl} \tag{2.189}$$

Thus, the variation of the second functional is rewritten as:

$$\delta\Pi_b = \int_0^L \delta\mathbf{e}_b^T \left(\hat{\mathbf{s}}_b - \mathbf{b}_b \mathbf{q}_b\right) dx + \int_0^L \delta\mathbf{u}_b^T \left(\hat{\mathbf{p}}_b - \mathbf{b}_{b,x} \mathbf{q}_b\right) dx + \delta\mathbf{q}_b^T \left(\mathbf{a}_{bg}\mathbf{u}_{bl} - \int_0^L (\mathbf{b}_{b,x}^T \mathbf{u}_b + \mathbf{b}_b^T \mathbf{e}_b) \, dx\right) - \delta\mathbf{u}_{bl}^T \mathbf{p}_{bl} \tag{2.190}$$

In this formulation, $\mathbf{u}_b(x)$ and $\mathbf{u}_{bl}$ are independent variables, just like in the FB approach. Continuity is imposed on $\mathbf{u}_{bl}$ but not on $\mathbf{u}_b(x)$, which allows discontinuities at shared nodes of contiguous elements.

Finally, the weak form yields three new equations:

$$\int_0^L (\hat{\mathbf{s}}_b - \mathbf{b}_b \mathbf{q}_b)\, dx = 0 \tag{2.191}$$

$$\int_0^L \left(\hat{\mathbf{p}}_b - \mathbf{b}_{b,x} \mathbf{q}_b\right) dx = 0 \tag{2.192}$$

$$\mathbf{a}_{bg} \mathbf{u}_{bl} - \int_0^L \left(\mathbf{b}_{b,x}^T \mathbf{u}_b + \mathbf{b}_b^T \mathbf{e}_b\right) dx = 0 \tag{2.193}$$

Respectively, $\forall \delta \mathbf{u}_b^T$, $\forall \delta \mathbf{q}_b^T$, $\forall \delta \mathbf{e}_b^T$, $\forall \delta u_b^T \neq 0$.

These equations actually match the condensed governing relations presented in Section 2.3.5 when the operators are stacked as in Eqs. 2.158 to 2.160, for both fiber section and bond sections, Eqs. 2.191 and 2.192 are condensed into Eq. 2.171, and Eq. 2.193 in Eq. 2.172.

In this specific case, where small strains are considered, where the axial force in the fibers with bond-slip $\mathbf{s}_b(x)$ is interpolated and after the computational procedure is deduced, the mixed approach is once again the same as the force-based one.

2.3.7 Prestressing techniques

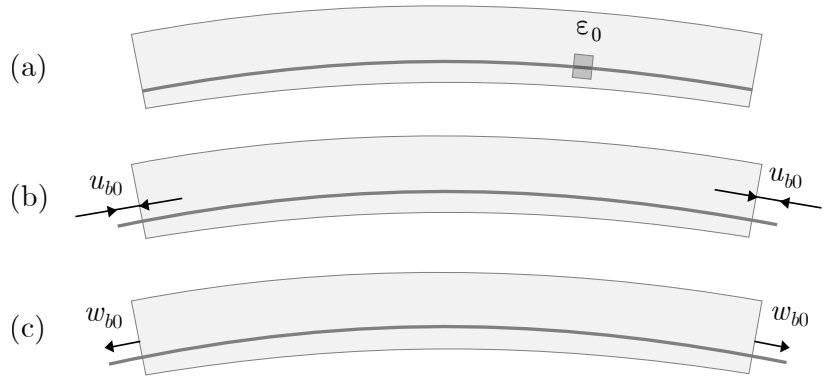

Figure 2.11. Alternative strategies for applying prestressing in the finite element model (a) initial strain ε_0, (b) applied anchorage displacements, (c) applied anchorage force.

Prestressing in the proposed finite element framework can be introduced in three alternative ways, as illustrated in Fig. 2.11:

- initial strain application: an initial strain ε_0 is directly assigned to the tendon fibers. This approach is ideal to model uniformly or non-uniformly distributed prestressing stresses and is particularly suited for pretensioned tendons or bonded tendons;
- slip displacement control: prestress is applied by imposing displacements at the displacements of the anchorage points. This is equivalent to prescribing the tendon extraction length at the anchorages, as in jack-controlled post-tensioning. It is best suited for unbonded or post-tensioned tendons during the tensioning phase, when bond is intentionally neglected;
- bond force application: instead of prescribing a displacement, the conjugate force is applied directly to the anchorage points, corresponding to the force in the hydraulic jack. This method is equivalent to load control during post-tensioning and can be used under the same conditions as the displacement-controlled approach.

2.4 Beam FE formulations with warping and bond-slip

2.4.1 Local formulation including warping and bond-slip

In this section the previous formulations are extended by introducing the out-of-plane warping of the cross-sections. In this way, the classical assumption of rigid cross-sections is partially relaxed, allowing the element kinematics to reproduce non-uniform shear and torsional effects, consistently with the approaches proposed in [92, 61]. At the same time, the interaction between concrete and reinforcement is enriched through a bond-slip relationship, leading to a more general description of reinforced and prestressed members.

Two new elements are formulated here:

- the first one is a DB formulation according to [94], where the number of displacement DOFS has been increased to better interpolate both axial and trasverse displacement fields, as well as to eliminate shear locking;
- the second one is a mixed formulation, based on [7] and [61], where warping is accounted through a Hu-Washizu variational formulation. Bond-slip is also considered making this a new element proposal for this work.

The element kinematics is here extended to simultaneously account for warping deformations of the cross-section and bond-slip effects at the reinforcement level. In addition to the standard section displacements $\mathbf{u}_s(x)$ at the reference axis, and to the bond-slip displacements $u_b(x, y, z)$ assigned to each fiber with bond-slip, the out-of-plane warping displacement $u_w(x, y, z)$ is introduced to describe the out-of-plane deformation of the cross-section. This enrichment allows the element to reproduce the interaction of torsion with axial and shear stresses, which cannot be captured if plane sections assumption holds.

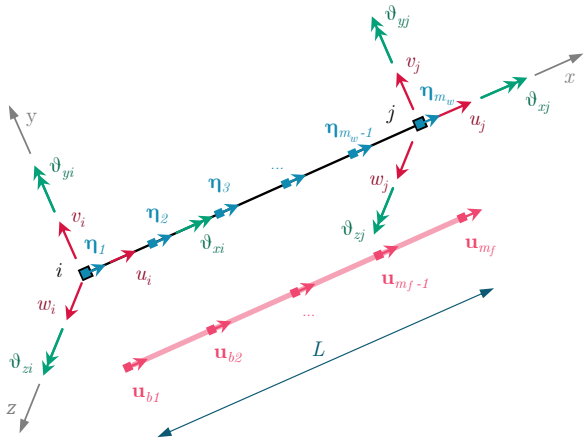

Figure 2.12. Element configuration in the local reference system (x, y, z) with nodal displacements, bond-slip nodal displacements and warping nodal DOFs.

The local displacement vector is thus modified from Eq. (2.2) to include both bond-slip and warping degrees of freedom:

$$\tilde{\mathbf{u}}_l = \left\{ \begin{array}{ccc} \mathbf{u}_l^T & \mathbf{u}_{bl}^T & \mathbf{u}_{wl}^T \end{array} \right\}^T \tag{2.194}$$

where the local displacement vector $\mathbf{u}_l$ collects both the standard nodal displacements at the

element ends i and j, and the additional displacements introduced at the intermediate nodes for enhanced interpolation; $\mathbf{u}_{bl}$ denote the nodal bond-slip displacements parallel to the tendons at nodes i, j and intermediate ones; and $\mathbf{u}_{wl}$ are the nodal warping DOFs at nodes i, j and intermediate ones. The latter correspond to the additional warping degrees of freedom $\boldsymbol{\eta}_w(x, y, z)$ along the axis and over the cross-section, as illustrated in Figure 2.12.

The dual local force vector becomes:

$$\tilde{\mathbf{p}}_l = \left\{ \begin{array}{ccc} \mathbf{p}_{l,i}^T & \mathbf{p}_{bl}^T & \mathbf{p}_{wl}^T \end{array} \right\}^T \tag{2.195}$$

where $\mathbf{p}_{wl}$ are the generalized warping forces, work-conjugated to the nodal warping displacements.

In the basic system, the displacement and force vectors defined in the previous sections are enriched accordingly:

$$\tilde{\mathbf{v}} = \left\{ \mathbf{v}_r^T \quad \mathbf{v}_b^T \quad \mathbf{v}_w^T \right\}^T \qquad \tilde{\mathbf{q}} = \left\{ \mathbf{q}_r^T \quad \mathbf{q}_b^T \quad \mathbf{q}_w^T \right\}^T \tag{2.196}$$

where $\mathbf{v}_r$ and $\mathbf{q}_r$ contain $\mathbf{v}$ and $\mathbf{q}$ and may be expanded as explained in Section 2.4.5, $\mathbf{v}_b$ and $\mathbf{q}_b$ collect the bond-slip displacements and tendon forces at the interpolation points, while $\mathbf{v}_w$ and $\mathbf{q}_w$ collect the interpolated warping displacements and generalized warping forces. The size of $\mathbf{v}_b$ and $\mathbf{q}_b$ is $m_f \cdot n_f$ if m_f interpolation points are used per f fiber and n_f is the number of fibers with bond-slip, while the size of $\mathbf{v}_w$ and $\mathbf{q}_w$ is $m_w \cdot n_w$ if m_w is the number of interpolation points used for every warping DOF, which are n_w on total.

The transformation from local nodal displacements to basic displacements is still given by:

$$\tilde{\mathbf{v}} = \tilde{\mathbf{a}}_g \, \tilde{\mathbf{u}}_l \tag{2.197}$$

where $\tilde{\mathbf{a}}_g$ is the element's kinematic transformation matrix that eliminates the rigid body modes, which is different for displacement-based or mixed approaches and is detailed in the respective Sections 2.4.5 and 2.4.6.

2.4.2 Element kinematics with warping

At each point of the local axis x, the generalized section displacement vector $\mathbf{u}_s(x)$ is defined according to the classical assumption of rigid plane cross-sections of Eq. (2.15), as shown in Fig. 2.13, and can be rewritten as:

$$\mathbf{u}_s(x) = \left\{ u(x) \quad \theta_z(x) \quad v(x) \quad \theta_x(x) \quad \theta_y(x) \quad w(x) \right\}^T \tag{2.198}$$

To account for the warping of beam cross-sections, this hypothesis is partially relaxed, assuming that the cross-sections can undergo out-of-plane distortions while remaining rigid in their own plane. The displacement field at a generic material point f of the cross-section is then expressed as the additive composition of the rigid part $\mathbf{u}_r(x, y, z)$ and the warping contribution $\mathbf{u}_m(x, y, z)$:

$$\mathbf{u}_m(x, y, z) = \mathbf{u}_r(x, y, z) + \mathbf{u}_w(x, y, z) \tag{2.199}$$

where $\mathbf{u}_w(x, y, z)$ represents the additional displacement field associated with the warping. As

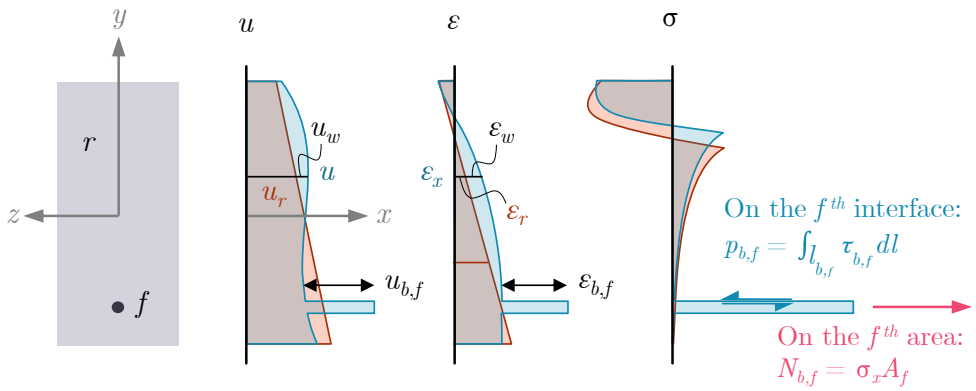

Figure 2.13. Section displacement, strain, force and stress distributions with warping.

a consequence of the in-plane section undeformability assumption, i.e. $\varepsilon_y = \varepsilon_z = \gamma_{yz} = 0$, the warping displacement field exhibits non-zero values only in the x-direction:

$$\mathbf{u}_w(x,y,z) = \{\, u_w(x,y,z) \quad 0 \quad 0 \,\}^T \tag{2.200}$$

Hence, the displacement vector at any point m of the section can be expressed as:

$$\mathbf{u}_m(x,y,z) = \mathbf{a}_s(y,z)\,\mathbf{u}_s(x) + \mathbf{u}_w(x,y,z) \tag{2.201}$$

where $\mathbf{a}_s(y,z)$ is the section interpolation matrix previously defined in Eq. (2.16). Applying the compatibility operator, the material strain components result as:

$$\varepsilon_x(x,y,z) = \frac{\partial u(x)}{\partial x} - y\frac{\partial \theta_z(x)}{\partial x} + z\frac{\partial \theta_y(x)}{\partial x} + \frac{\partial u_w(x,y,z)}{\partial x} \tag{2.202}$$

$$\gamma_{xy}(x,y,z) = -\theta_z(x) + \frac{\partial v(x)}{\partial x} - z\frac{\partial \theta_x(x)}{\partial x} + \frac{\partial u_w(x,y,z)}{\partial y} \tag{2.203}$$

$$\gamma_{xz}(x,y,z) = \theta_y(x) + \frac{\partial w(x)}{\partial x} + y\frac{\partial \theta_x(x)}{\partial x} + \frac{\partial u_w(x,y,z)}{\partial z} \tag{2.204}$$

2.4.3 Warping displacement interpolation over the section

Warping displacements are interpolated over the section through specific polynomial shape functions, which can be formulated according to Di Re [7], Addessi et al [61], or Sio et al [94]. In Addessi et al, the model adopted regards specifically the Simplified Warping Mixed Element (SWME). In this case, a similar approach is adopted and the warping displacements may therefore be computed as:

$$\mathbf{u}_w(x,y,z) = \mathbf{M}_\eta(y,z)\boldsymbol{\eta}(x) \tag{2.205}$$

where $\mathbf{M}_\eta(y,z)$ is a warping section interpolation matrix and $\boldsymbol{\eta}(x)$ lists all the n_w section warping DOFs, $\eta_1(x) \cdots \eta_{n_w}(x)$. By linking the material point warping displacements $\mathbf{u}_w(x,y,z)$ to a general set of warping degrees of freedom $\boldsymbol{\eta}(x)$, the interpolation over the section may be performed through predefined functions. Although there are several interpolation possibilities, in this case polynomial functions are used.

In the 2D case first, for simplicity, the warping displacement field along the y-axis is inter-

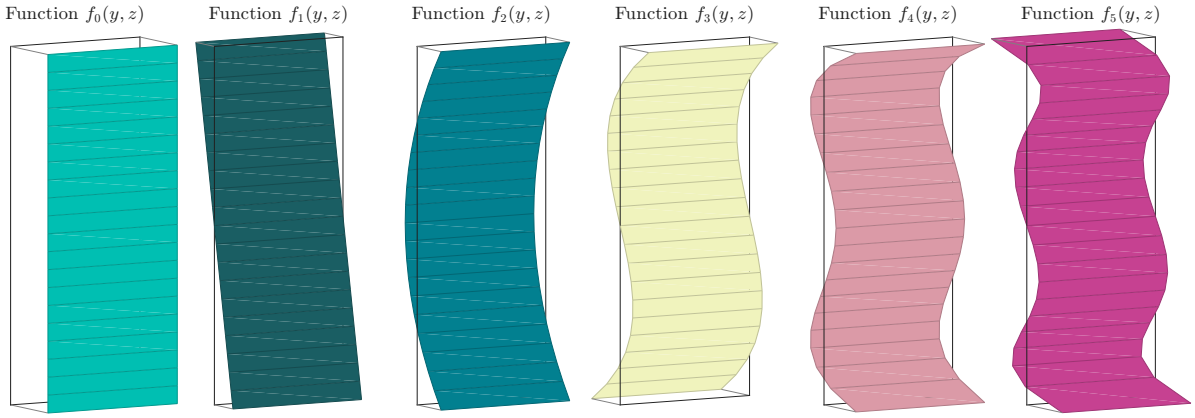

Figure 2.14. Warping interpolations for a 2D beam problem.

polated by means of polynomial functions $f_j(y)$ obtained through an orthogonalization process. Starting from the monomials $\{1, y, y^2, y^3, \dots\}$, each new function $f_j(y)$ is determined by enforcing two conditions:

1. Orthogonality:
$$\langle f_j, f_k \rangle = \int_{-h/2}^{h/2} f_j(y)\, f_k(y)\, dy = 0 \qquad \forall\, k < j \tag{2.206}$$
which ensures that each $f_j(y)$ is orthogonal to all the previous ones.

2. Normalization:
$$\langle f_j, f_j \rangle = \int_{-h/2}^{h/2} f_j(y)^2\, dy \;=\; \int_{-h/2}^{h/2} y^2\, dy \tag{2.207}$$
i.e., the self-product of each function is scaled to coincide with the second-order geometric moment $\int y^2$ of the section.

The resulting set of functions $\{f_0(y), f_1(y), \dots, f_n(y)\}$ thus constitutes a Gram–Schmidt orthogonalization of the polynomial basis, with each function uniquely defined and consistently scaled. Here are few examples when taken up to the fourth order:

$$\begin{aligned}
f_0(y,h) &= 1, \\
f_1(y,h) &= -\,y, \\
f_2(y,h) &= -\tfrac{\sqrt{15}}{12}\,h \;+\; \tfrac{\sqrt{15}}{h}\,y^2, \\
f_3(y,h) &= -\tfrac{\sqrt{21}}{2}\,y \;+\; \tfrac{10\sqrt{21}}{3h^2}\,y^3, \\
f_4(y,h) &= \tfrac{3\sqrt{3}}{16}\,h \;-\; \tfrac{15\sqrt{3}}{2h}\,y^2 \;+\; \tfrac{35\sqrt{3}}{h^3}\,y^4.
\end{aligned} \tag{2.208}$$

An example of the first warping functions in this 2D case is shown in Fig. 2.14.

In the case of the 3D interpolation, the same procedure is extended to the monomial basis $\{1, y, z, y^2, yz, z^2, y^3, y^2z, yz^2, z^3, \dots\}$, so that the functions span the two-dimensional polynomial space. The resulting warping modes can be organized analogously to a Tartaglia triangle, with one function for each independent monomial combination of degree n_w. Orthogonalization ensures that each $f_i(y,z)$ is independent and hierarchically ordered. Figure 2.15 shows the first functions up to the third order.

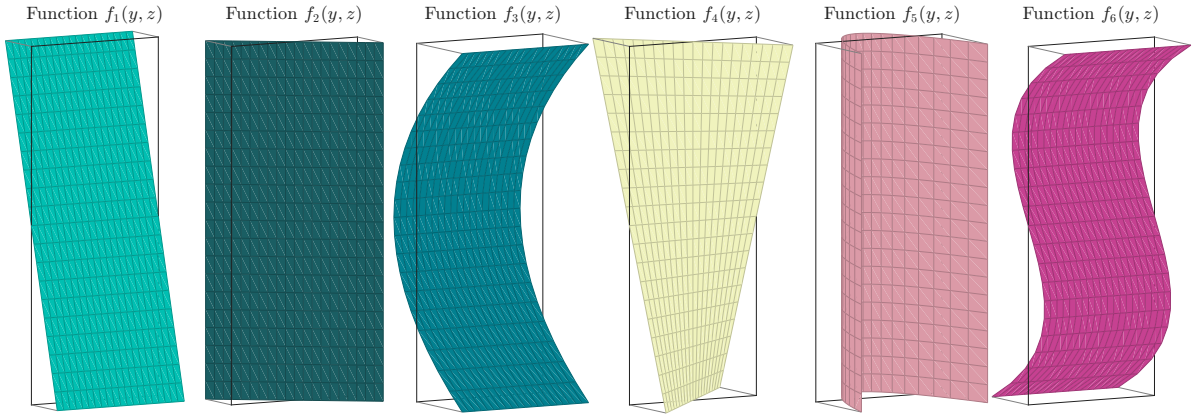

Figure 2.15. Warping interpolations for a 3D beam problem.

Alternatively, besides the general polynomial hierarchy, particular warping functions can be associated to shear and torsional actions. In Addessi et al [61], these functions were not directly postulated as stated here, but they are derived by running a more sophisticated warping model, called Enriched Warping Mixed Element, where unitary actions V_y, V_z, and M_x were imposed one at a time to compute the section's warping shape functions for every contribution. This procedure leads to three distinct warping modes, each corresponding to the deformation pattern activated by the individual generalized force.

A reduced set of warping functions can be selected up to the cubic order through a Gram–Schmidt orthogonalization of the polynomial basis. This choice aims at lowering the overall number of warping degrees of freedom, while still capturing the essential symmetry and physical content of shear and torsional warping. Accordingly, three special functions can be identified:

- a function $f_{Vy}(y,z)$, representing the warping induced by a shear force V_y;
- a function $f_{Vz}(y,z)$, representing the warping induced by a shear force V_z;
- a function $f_{Mx}(y,z)$, representing the torsional warping under a torsion M_x.

These special functions play a key role in reproducing shear and torsion effects, since they ensure the correct physical interpretation of the warping field, as illustrated in Fig. 2.16, where function combinations of the third order are chosen. It is therefore convenient to store all the warping

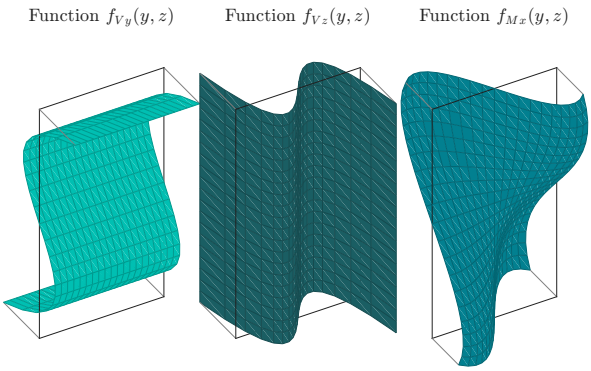

Figure 2.16. Specific warping interpolations on a 3D section related to shear contribution $V_y(x), V_z(x)$ about axes y, z, respectively, and torsion $M_x(x)$ defined around axis x.

functions in a row matrix that allows to compute the warping displacement in every material point. Eq. (2.205) can be written as follows:

$$u_w(x,y,z) = \begin{bmatrix} f_1(y,z) & f_2(y,z) & \dots & f_{n_w}(y,z) \end{bmatrix} \begin{Bmatrix} \eta_1(x) \\ \eta_2(x) \\ \vdots \\ \eta_{n_w}(x) \end{Bmatrix} \tag{2.209}$$

this allows to compute the warping displacements freely with as many section DOFs as required.

2.4.4 Enriched section with warping and bond-slip

By substituting Eq. (2.205) in Eq. (2.201), it results:

$$\mathbf{u}_m(x,y,z) = \mathbf{a}_s(y,z)\,\mathbf{u}_s(x) + \begin{Bmatrix} \mathbf{M}_\eta(y,z)\boldsymbol{\eta}(x) \\ 0 \\ 0 \end{Bmatrix} \tag{2.210}$$

By defining the warping generalized strain vector $\boldsymbol{\varepsilon}_w(x,y,z)$ at the material point as the direct derivative of $\mathbf{u}_w(x,y,z)$ with respect to x:

$$\boldsymbol{\varepsilon}_w(x,y,z) = \mathbf{D}(x,y,z)\mathbf{u}_w(x,y,z) = \begin{bmatrix} \mathbf{0} & \mathbf{M}_\eta(y,z) \\ \dfrac{\partial \mathbf{M}_\eta(y,z)}{\partial y} & \mathbf{0} \\ \dfrac{\partial \mathbf{M}_\eta(y,z)}{\partial z} & \mathbf{0} \end{bmatrix} \begin{Bmatrix} \boldsymbol{\eta}(x) \\ \dfrac{\partial \boldsymbol{\eta}(x)}{\partial x} \end{Bmatrix} \tag{2.211}$$

the material point strains components are:

$$\begin{Bmatrix} \varepsilon_x(x,y,z) \\ \gamma_{xy}(x,y,z) \\ \gamma_{xz}(x,y,z) \end{Bmatrix} = \mathbf{a}_s(y,z)\mathbf{e}(x) + \begin{bmatrix} \mathbf{0} & \mathbf{M}_\eta(y,z) \\ \dfrac{\partial \mathbf{M}_\eta(y,z)}{\partial y} & \mathbf{0} \\ \dfrac{\partial \mathbf{M}_\eta(y,z)}{\partial z} & \mathbf{0} \end{bmatrix} \begin{Bmatrix} \boldsymbol{\eta}(x) \\ \dfrac{\partial \boldsymbol{\eta}(x)}{\partial x} \end{Bmatrix} \tag{2.212}$$

If the material points belongs to a f fiber with bond-slip, then a bond-slip component $\varepsilon_b(x, y_f, z_f)$ has to be summed to the axial strain:

$$\varepsilon_x(x,y,z) = \varepsilon_a - y\chi_z + z\chi_y + \varepsilon_b(x,y_f,z_f) + \mathbf{M}_\eta(y,z)\frac{\partial \boldsymbol{\eta}_x(x)}{\partial x} \tag{2.213}$$

Then a modified compatibility equation may be rewritten:

$$\boldsymbol{\varepsilon}_m(x,y,z) = \tilde{\mathbf{a}}_s(y,z)\tilde{\mathbf{e}}(x) \tag{2.214}$$

where:

$$\tilde{\mathbf{a}}_s(y,z) = \begin{bmatrix} 1 & -y & z & 0 & 0 & 0 & \boldsymbol{\delta}_b(y,z) & \mathbf{0} & \mathbf{M}_\eta(y,z) \\ 0 & 0 & 0 & s_y(y) & 0 & -z & \mathbf{0} & \mathbf{M}_{\eta,y}(y,z) & \mathbf{0} \\ 0 & 0 & 0 & 0 & s_z(z) & y & \mathbf{0} & \mathbf{M}_{\eta,z}(y,z) & \mathbf{0} \end{bmatrix} \tag{2.215}$$

and $\tilde{\mathbf{e}}(x)$ is reorganized as follows:

$$\tilde{\mathbf{e}}(x) = \begin{Bmatrix} \mathbf{e} \\ \mathbf{e}_b \\ \boldsymbol{\eta} \\ \boldsymbol{\eta}_x \end{Bmatrix} = \begin{Bmatrix} \mathbf{e} \\ \mathbf{e}_b \\ \mathbf{e}_w \end{Bmatrix} \tag{2.216}$$

where $\boldsymbol{\delta}_b(y,z) = \begin{Bmatrix} \delta_1 & \cdots & \delta_f & \cdots & \delta_{n_f} \end{Bmatrix}$ is a one-row matrix of Kronecker deltas of size n_f, so that:

$$\delta_f(y,z) = \begin{cases} 1 & \text{for fiber } f, \\ 0 & \text{otherwise.} \end{cases} \tag{2.217}$$

and the matrices $\mathbf{M}_{\eta,y}(y,z) = \dfrac{\partial \mathbf{M}_\eta(y,z)}{\partial y}$, $\mathbf{M}_{\eta,z}(y,z) = \dfrac{\partial \mathbf{M}_\eta(y,z)}{\partial z}$ are the derivatives of the section warping shape function matrices with respect to y and z, respectively. They are all one-row matrices of size n_w. This means that $\tilde{\mathbf{e}}$ contains the following additional section strain DOFs:

1. the derivatives with respect to x of the bond-slip displacements $\mathbf{e}_b$, one for each fiber with bond-slip, total size n_f;
2. the section warping DOFs $\boldsymbol{\eta}$, size n_w;
3. their derivatives with respect to x, $\boldsymbol{\eta}_x = \dfrac{\partial \boldsymbol{\eta}}{\partial x}$, also of size n_w.

The vectors are reorganized so that $\mathbf{e}_w = \{\boldsymbol{\eta} \quad \boldsymbol{\eta}_x\}^T$ stores all the components related to warping. It is worth noting that both the generalized section warping displacement vector and its derivative with respect to x are stored in $\mathbf{e}_w$. This reorganization does not introduce new assumptions, but allows the compatibility equation (2.214) to be written in a compact matrix form, instead of as a sum of separate operator contributions as in earlier formulations (e.g. [61]). The new section DOFs are illustrated in Figure 2.17. A vector $\tilde{\mathbf{s}}(x)$, work conjugate to $\tilde{\mathbf{e}}(x)$, can be defined as

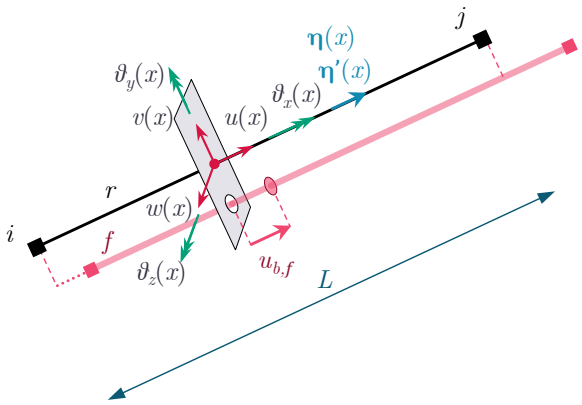

Figure 2.17. Basic element configuration with the additional section warping and bond-slip DOFs.

follows:

$$\tilde{\mathbf{s}}(x) = \begin{Bmatrix} \mathbf{s} \\ \mathbf{s}_b \\ \mathbf{V}_w \\ \mathbf{V}_{w,x} \end{Bmatrix} = \begin{Bmatrix} \mathbf{s} \\ \mathbf{s}_b \\ \mathbf{s}_w \end{Bmatrix} \tag{2.218}$$

where $\mathbf{s}_b$ contains the axial forces of the n_f fibers with bond-slip, as in Section 2.3.2, $\mathbf{V}_w$ contains the forces work conjugates of $\boldsymbol{\eta}$ and $\mathbf{V}_{w,x}$, those work conjugates of $\boldsymbol{\eta}_x$.
The vectors are reorganized so that $\mathbf{s}_w = \{\mathbf{V}_w \quad \mathbf{V}_{w,x}\}$ stores all the forces related to warping.

By enforcing the virtual work equivalence at the cross-section level, just like in Eq. (2.24), the following definition of $\tilde{\mathbf{s}}(x)$ and $\tilde{\mathbf{k}}_s(x)$ are deduced:

$$\tilde{\mathbf{s}}(x) = \int_A \tilde{\mathbf{a}}_s^T(y,z)\, \boldsymbol{\sigma}_m(x,y,z)\, dA \tag{2.219}$$

$$\tilde{\mathbf{k}}_s(x) = \int_A \tilde{\mathbf{a}}_s^T(y,z)\, \mathbf{k}_m(x,y,z)\, \tilde{\mathbf{a}}_s(y,z)\, dA \tag{2.220}$$

The material stress $\boldsymbol{\sigma}_m$ and stiffness matrix $\mathbf{k}_m$ are the same as in Eq. (2.29).

2.4.5 Displacement-based approach

In this approach, additional nodal DOFs are introduced to better interpolate the section displacements $\mathbf{u}_s(x)$, as a general 3D extension of [94]. To do that, three nodes are added in the beam at $[L/2,\ L/4,\ 3L/4]$ and the new DOFs are organized as follows in $\mathbf{v}_r$:

$$\mathbf{v}_r = \begin{Bmatrix} \mathbf{v}^T & u_2 & v_4 & v_5 & w_4 & w_5 & \varphi_{y,2} & \varphi_{z,2} \end{Bmatrix}^T \tag{2.221}$$

where $\mathbf{v}$ is the conventional basic displacement vector defined in (2.5), while the others are needed to interpolate each section field as follows:

- $u(x) = \mathbf{N}_u(x)\ \{u_2\ u_3\}^T$
- $v(x) = \mathbf{N}_v(x)\ \{v_4\ v_5\}^T$
- $w(x) = \mathbf{N}_v(x)\ \{w_4\ w_5\}^T$
- $\vartheta_z(x) = \mathbf{N}_\vartheta(x)\ \{\varphi_{z,1}\ \varphi_{z,2}\ \varphi_{z,3}\}^T$
- $\vartheta_y(x) = \mathbf{N}_\vartheta(x)\ \{\varphi_{y,1}\ \varphi_{y,2}\ \varphi_{y,3}\}^T$
- $\vartheta_z(x) = N_{\vartheta x}(x)\ \varphi_{x,j}$

where the components related to the basic nodes 1 and 3 correspond to those of the local nodes i and j, respectively, and no transformation is needed. Node 2 is located at $x = L/2$, node 4 is located at $x = L/4$, node 5 is located at $x = 3L/4$. $\mathbf{N}_u(x)$, $\mathbf{N}_v(x)$, $\mathbf{N}_\vartheta(x)$, and $N_{\vartheta,x}(x)$ are shape functions. More details about their choice are given in Section 4.1.1.
Figure 2.18 shows the additional nodes position and their associated DOFs. These may all be written in a compact form as follows:

$$\mathbf{u}_s(x) = \mathbf{N}_r(x)\mathbf{v}_r \tag{2.222}$$

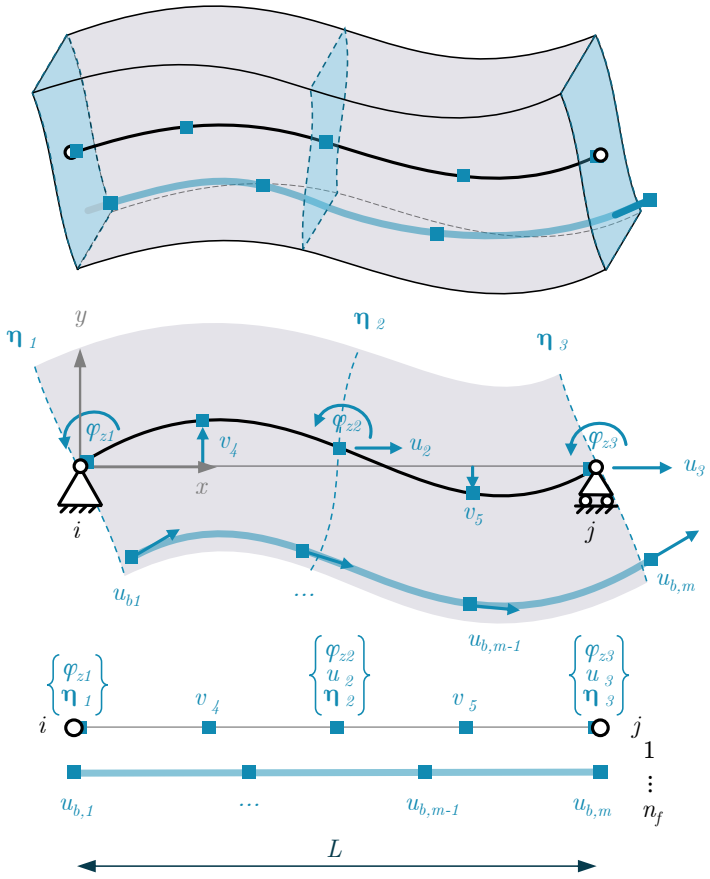

Figure 2.18. Element DOFs in the DB formulation, shown in the xy plane.

where $\mathbf{N}(x)$ is the shape function matrix:

$$\mathbf{N}(x) = \begin{bmatrix} \mathbf{N}_u(x) & \mathbf{0} & \mathbf{0} & \mathbf{0} & \mathbf{0} & 0 \\ \mathbf{0} & \mathbf{N}_v(x) & \mathbf{0} & \mathbf{0} & \mathbf{0} & 0 \\ \mathbf{0} & \mathbf{0} & \mathbf{N}_v(x) & \mathbf{0} & \mathbf{0} & 0 \\ \mathbf{0} & \mathbf{0} & \mathbf{0} & \mathbf{N}_\vartheta(x) & \mathbf{0} & 0 \\ \mathbf{0} & \mathbf{0} & \mathbf{0} & \mathbf{0} & \mathbf{N}_\vartheta(x) & 0 \\ 0 & 0 & 0 & 0 & 0 & N_{\vartheta x}(x) \end{bmatrix} \tag{2.223}$$

The compatible strains can still be written as:

$$\mathbf{e}(x) = \mathbf{D}_s(x)\mathbf{u}_s(x) = \mathbf{D}_s(x)\mathbf{N}_r(x)\mathbf{v}_r \tag{2.224}$$

where $\mathbf{D}_s(x)$ is the same operator defined in Section 2.2.1. The new compatibility equation will result in:

$$\mathbf{e}(x) = \mathbf{B}_r(x)\mathbf{v}_r \tag{2.225}$$

where:

$$\mathbf{B}_r(x) = \begin{bmatrix} \mathbf{N}_{u,x} & \mathbf{0} & \mathbf{0} & \mathbf{0} & \mathbf{0} & 0 \\ \mathbf{0} & \mathbf{N}_{v,x} & \mathbf{0} & \mathbf{0} & \mathbf{0} & 0 \\ \mathbf{0} & \mathbf{0} & \mathbf{N}_{v,x} & \mathbf{0} & \mathbf{0} & 0 \\ \mathbf{0} & -\mathbf{N}_v & \mathbf{0} & \mathbf{N}_{\vartheta,x} & \mathbf{0} & 0 \\ \mathbf{0} & \mathbf{0} & \mathbf{N}_v & \mathbf{0} & \mathbf{N}_{\vartheta,x} & 0 \\ 0 & 0 & 0 & 0 & 0 & N_{\vartheta x,x} \end{bmatrix} \tag{2.226}$$

The bond-slip DOFs are again written as:

$$\mathbf{u}_b\left(x\right) = \mathbf{N}_b\left(x\right)\mathbf{v}_b \tag{2.227}$$

$$\mathbf{e}_b\left(x\right) = \mathbf{B}_b\left(x\right)\mathbf{v}_b \tag{2.228}$$

The warping DOFs are interpolated as follows:

$$\begin{Bmatrix} \eta_1(x) \\ \eta_2(x) \\ \vdots \\ \eta_{n_w}(x) \end{Bmatrix} = \begin{bmatrix} \mathbf{N}_{w,1}(x) & 0 & \cdots & 0 \\ 0 & \mathbf{N}_{w,2}(x) & \cdots & 0 \\ \vdots & \vdots & \ddots & \vdots \\ 0 & 0 & \cdots & \mathbf{N}_{w,n_w}(x) \end{bmatrix} \begin{Bmatrix} \mathbf{v}_{w,1} \\ \mathbf{v}_{w,2} \\ \vdots \\ \mathbf{v}_{w,n_w} \end{Bmatrix} \tag{2.229}$$

where $\mathbf{N}_{w,1} \ \cdots \ \mathbf{N}_{w,n_w}$ are n_w shape functions for warping, detailed in Section 4.1.1, each one of size $1 \times m_w$.
This allows to write the section warping DOFs as:

$$\boldsymbol{\eta}\left(x\right) = \mathbf{N}_w\left(x\right)\mathbf{v}_w \tag{2.230}$$

$$\boldsymbol{\eta}_x\left(x\right) = \mathbf{N}_{w,x}\left(x\right)\mathbf{v}_w \tag{2.231}$$

where $\mathbf{N}_w(x)$ and $\mathbf{N}_{w,x}(x) = \dfrac{\partial}{\partial x}\mathbf{N}_w(x)$ are size $n_w \times (m_w \cdot n_w)$.
In a compact form:

$$\mathbf{e}_w(x) = \mathbf{B}_w(x)\ \mathbf{v}_w \tag{2.232}$$

where:

$$\mathbf{B}_w(x) = \begin{bmatrix} \mathbf{N}_w \\ \mathbf{N}_{w,x} \end{bmatrix} \tag{2.233}$$

The compatibility equation that allows to go from the basic displacements $\tilde{\mathbf{v}}$ to the section strains can be recovered in the same form as before as:

$$\tilde{\mathbf{e}}(x) = \tilde{\mathbf{a}}(x)\,\tilde{\mathbf{v}} \tag{2.234}$$

where:

$$\tilde{\mathbf{e}}(x) = \begin{Bmatrix} \mathbf{e} \\ \mathbf{e}_b \\ \mathbf{e}_w \end{Bmatrix} \qquad \tilde{\mathbf{B}}(x) = \begin{bmatrix} \mathbf{B}_r & \mathbf{0} & \mathbf{0} \\ \mathbf{0} & \mathbf{B}_b & \mathbf{0} \\ \mathbf{0} & \mathbf{0} & \mathbf{B}_w \end{bmatrix} \tag{2.235}$$

The section stress $\tilde{\mathbf{s}}(x)$ and the section tangent stiffness $\tilde{\mathbf{k}}_s(x)$ are obtained from the modified fiber section response of Eq (2.220), where the operators accommodate for bond-slip derivatives:

$$\tilde{\mathbf{s}}(x) = \tilde{\mathbf{k}}_s(x) \left(\tilde{\mathbf{e}}(x) - \tilde{\mathbf{e}}_0(x) \right) \tag{2.236}$$

where:

$$\tilde{\mathbf{e}}_0(x) = \begin{Bmatrix} \mathbf{e}_0 \\ \mathbf{0} \\ \mathbf{0} \end{Bmatrix} \tag{2.237}$$

The bond-slip constitutive response on the bond-interface A_b (Eq. (2.135)) is unchanged here.

Since the operators are the same and only their structure has changed, there is also no need to rewrite the virtual works equation as it is exactly the same as the one written in Section 2.3.4.

The fiber section operators are unchanged from Eq. (2.138), while the bond section operators require extra zero components for consistency:

$$\tilde{\mathbf{B}}(x) = \begin{bmatrix} \mathbf{0} & \mathbf{N}_b & \mathbf{0} \end{bmatrix} \qquad n_f \times (6 + m_f \cdot n_f + m_w \cdot n_w) \tag{2.238}$$

$$\tilde{\mathbf{e}}(x) = \mathbf{u}_b \qquad \tilde{\mathbf{s}}(x) = \hat{\mathbf{p}}_b \qquad n_f \times 1 \tag{2.239}$$

This allows to unify the notation so that the equilibrium is obtained, $\forall \delta\tilde{\mathbf{v}} \neq \mathbf{0}$:

$$\tilde{\mathbf{q}} = \int_0^L \tilde{\mathbf{B}}^T(x)\, \tilde{\mathbf{s}}(x)\, dx - \int_0^L \tilde{\mathbf{N}}^T(x)\, \tilde{\mathbf{p}}(x)\, dx \tag{2.240}$$

where the tilde version $\tilde{\cdot}$ of every new modified operator, such as $\tilde{\mathbf{N}}$, has zeros in the places allocated for bond-slip and warping. By applying Eq. (2.47):

$$\tilde{\mathbf{q}} = \tilde{\mathbf{k}}\, \tilde{\mathbf{v}} - \tilde{\mathbf{q}}_0, \tag{2.241}$$

where the stiffness matrix $\tilde{\mathbf{k}}$ and the equivalent nodal forces $\tilde{\mathbf{q}}_0$ are:

$$\tilde{\mathbf{k}} = \int_0^L \tilde{\mathbf{B}}^T(x)\, \tilde{\mathbf{k}}_s(x)\, \tilde{\mathbf{B}}(x)\, dx \tag{2.242}$$

$$\tilde{\mathbf{q}}_0 = \int_0^L \tilde{\mathbf{B}}^T(x)\, \tilde{\mathbf{k}}_s(x)\, \tilde{\mathbf{e}}_0(x)\, dx + \int_0^L \tilde{\mathbf{N}}^T(x)\, \tilde{\mathbf{p}}(x)\, dx \tag{2.243}$$

The element equilibrium is finally obtained by applying the basic-to-local transformation:

$$\tilde{\mathbf{p}}_l^{ext} = \tilde{\mathbf{a}}_g^T \tilde{\mathbf{k}}\, \tilde{\mathbf{v}} - \tilde{\mathbf{a}}_g^T \tilde{\mathbf{q}}_0 + \tilde{\mathbf{p}}_{lq} = \tilde{\mathbf{p}}_l^{int} - \tilde{\mathbf{p}}_{l0} \tag{2.244}$$

The local-to-basic transformation matrix $\tilde{\mathbf{a}}_g$:

$$\tilde{\mathbf{a}}_g(x) = \begin{bmatrix} \mathbf{a}_g & \mathbf{0} & \mathbf{0} \\ \mathbf{0} & \mathbf{I}_{m_f \cdot n_f} & \mathbf{0} \\ \mathbf{0} & \mathbf{0} & \mathbf{I}_{m_w \cdot n_w} \end{bmatrix} \tag{2.245}$$

The governing equations have still the same structure as in Section 2.3.4 but use different operators:

$$\tilde{\mathbf{p}}_l^{ext} + \tilde{\mathbf{p}}_{l0} - \tilde{\mathbf{p}}_l^{int} = 0 \tag{2.246}$$

$$\tilde{\mathbf{e}}(x) - \tilde{\mathbf{B}}(x)\,\tilde{\mathbf{v}} - \tilde{\mathbf{e}}_0(x) = 0 \tag{2.247}$$

$$\tilde{\mathbf{q}} - \int_0^L \tilde{\mathbf{B}}^T(x)\,\tilde{\mathbf{s}}(x)\,dx + \int_0^L \tilde{\mathbf{N}}^T(x)\,\tilde{\mathbf{p}}(x)\,dx = 0 \tag{2.248}$$

2.4.6 Mixed approach

The force-based approach is not proposed as a viable solution, since interpolating the generalized forces work-conjugate to the warping displacements does not enforce compatibility on local displacements at nodes, unlike the displacement-based formulation for warping.
The mixed approach proposed here addresses a problem that includes additional bond-slip and warping fields:

- Bond-slip fields are defined by enforcing element equilibrium and interpolating forces;
- Warping fields are defined by enforcing element compatibility and interpolating displacements.

To do so, a convenient rearrangement of the basic operators is proposed:

$$\tilde{\mathbf{v}} = \{\mathbf{v}_s \;\; \mathbf{v}_w\} \qquad\qquad \tilde{\mathbf{q}} = \{\mathbf{q}_s \;\; \mathbf{q}_w\} \tag{2.249}$$

where:

$$\mathbf{v}_s = \{\mathbf{v} \;\; \mathbf{v}_b\} \qquad\qquad \mathbf{q}_s = \{\mathbf{q} \;\; \mathbf{q}_b\} \tag{2.250}$$

The subscript s here refers to the variables interpolated through force-based functions, while the subscript w refers to the variables interpolated through displacement-based functions.

The interpolations of the section fields may be written as:

$$\mathbf{s}_s(x) = \mathbf{b}_s(x)\mathbf{q}_s \tag{2.251}$$

$$\mathbf{e}_w(x) = \mathbf{B}_w(x)\mathbf{v}_w \tag{2.252}$$

where the new s operators are:

$$\mathbf{b}_s(x) = \begin{bmatrix} \mathbf{b} & 0 \\ 0 & \mathbf{b}_b \end{bmatrix}, \quad \mathbf{s}_s = \begin{Bmatrix} \mathbf{s} \\ \mathbf{s}_b \end{Bmatrix} \tag{2.253}$$

Figure 2.19 shows the additional nodes position and their associated DOFs.

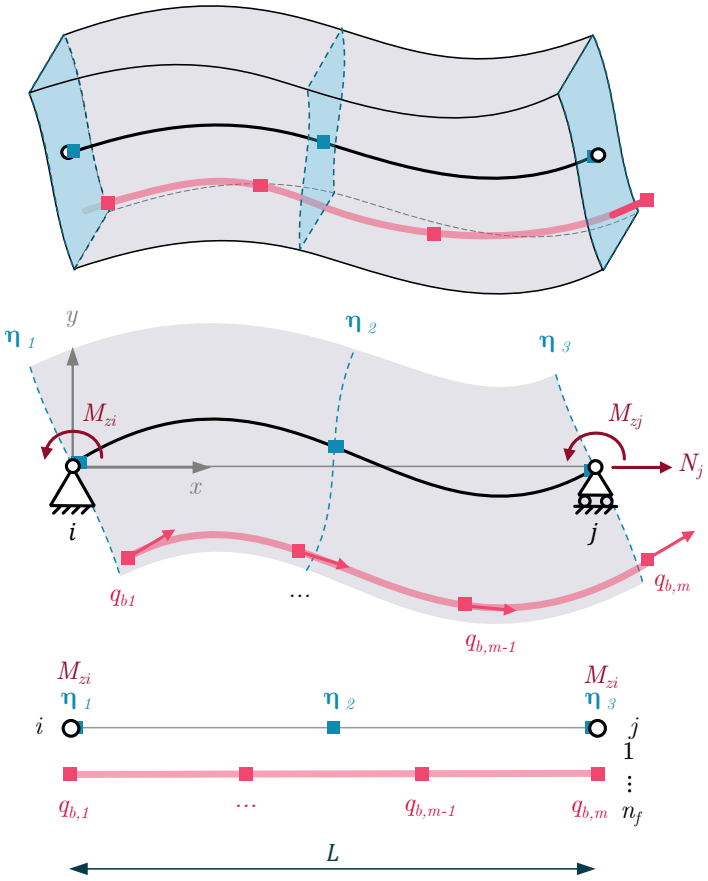

Figure 2.19. Element DOFs in the mixed formulation, shown in the xy plane. Red depicts force DOFs being interpolated, while blue depicts displacement DOFs being interpolated.

The section incremental constitutive response may be written as follows:

$$\dot{\mathbf{s}} = \mathbf{k}_s \dot{\mathbf{e}} \tag{2.254}$$

To prevent the notation from being too cumbersome, the $\tilde{\cdot}$ is avoided here, but the vectors are still the modified ones, i.e. $\dot{s} = \dot{\tilde{s}}$. The section stiffness matrix can be conveniently partitioned. Therefore:

$$\begin{Bmatrix} \dot{\mathbf{s}}_s \\ \dot{\mathbf{s}}_w \end{Bmatrix} = \begin{bmatrix} \mathbf{k}_{ss} & \mathbf{k}_{sw} \\ \mathbf{k}_{ws} & \mathbf{k}_{ww} \end{bmatrix} \begin{Bmatrix} \dot{\mathbf{e}}_s \\ \dot{\mathbf{e}}_w \end{Bmatrix} \tag{2.255}$$

where $\mathbf{e}_s$ is defined consistently to $\mathbf{s}_s$:

$$\mathbf{e}_s = \begin{Bmatrix} \mathbf{e} \\ \mathbf{e}_b \end{Bmatrix} \tag{2.256}$$

Writing down the first line of Eq. (2.255) one obtains:

$$\dot{\mathbf{s}}_s = \mathbf{k}_{ss} \dot{\mathbf{e}}_s + \mathbf{k}_{sw} \dot{\mathbf{e}}_w \tag{2.257}$$

By introducing Eqs. (2.252) and (2.251):

$$\dot{\mathbf{e}}_s = \mathbf{k}_{ss}^{-1} \left(\mathbf{b}_s \dot{\mathbf{q}}_s - \mathbf{k}_{sw} \mathbf{B}_w \dot{\mathbf{v}}_w \right) \tag{2.258}$$

By writing down the second line of Eq. (2.255):

$$\dot{\mathbf{s}}_w = \mathbf{k}_{ws}\dot{\mathbf{e}}_s + \mathbf{k}_{ww}\mathbf{B}_w\dot{\mathbf{v}}_w \tag{2.259}$$

Introducing Eq. (2.258):

$$\dot{\mathbf{s}}_w = \mathbf{k}_{ws}\mathbf{k}_{ss}^{-1}\mathbf{b}_s\dot{\mathbf{q}}_s + \left(\mathbf{k}_{ww} - \mathbf{k}_{ws}\mathbf{k}_{ss}^{-1}\mathbf{k}_{sw}\right)\mathbf{B}_w\dot{\mathbf{v}}_w \tag{2.260}$$

By enforcing weak-form equilibrium on the warping w components:

$$\begin{aligned}\dot{\mathbf{q}}_w &= \int_0^L \mathbf{B}_w^T\dot{\mathbf{s}}_w\,dx \\ &= \int_0^L \mathbf{B}_w^T\mathbf{k}_{ws}\mathbf{k}_{ss}^{-1}\mathbf{b}_s\,dx\,\dot{\mathbf{q}}_s + \int_0^L \mathbf{B}_w^T\left(\mathbf{k}_{ww} - \mathbf{k}_{ws}\mathbf{k}_{ss}^{-1}\mathbf{k}_{sw}\right)\mathbf{B}_w\,dx\,\dot{\mathbf{v}}_w\end{aligned} \tag{2.261}$$

which can be written compactly as:

$$\dot{\mathbf{q}}_w = \mathbf{b}_{ws}\dot{\mathbf{q}}_s + \mathbf{k}_w\dot{\mathbf{v}}_w \tag{2.262}$$

By inverting this relation, one obtains:

$$\dot{\mathbf{v}}_w = \mathbf{k}_w^{-1}\left(\dot{\mathbf{q}}_w - \mathbf{b}_{ws}\dot{\mathbf{q}}_s\right) \tag{2.263}$$

By enforcing weak-form compatibility on the s components:

$$\dot{\mathbf{s}}_s = \int_0^L \mathbf{b}_s^T\dot{\mathbf{e}}_s\,dx \tag{2.264}$$

Substituting (2.258):

$$\int_0^L \mathbf{b}_s^T\mathbf{k}_{ss}^{-1}\left(\mathbf{b}_s\dot{\mathbf{q}}_s - \mathbf{k}_{sw}\mathbf{B}_w\dot{\mathbf{v}}_w\right)dx \tag{2.265}$$

Rearranging terms:

$$\left(\int_0^L \mathbf{b}_s^T\mathbf{k}_{ss}^{-1}\mathbf{b}_s\,dx\right)\dot{\mathbf{q}}_s \;-\; \left(\int_0^L \mathbf{b}_s^T\mathbf{k}_{ss}^{-1}\mathbf{k}_{sw}\mathbf{B}_w\,dx\right)\dot{\mathbf{v}}_w \tag{2.266}$$

Defining compact operators

$$\mathbf{f}_s = \int_0^L \mathbf{b}_s^T\mathbf{k}_{ss}^{-1}\mathbf{b}_s\,dx, \qquad \mathbf{b}_{sw} = \int_0^L \mathbf{b}_s^T\mathbf{k}_{ss}^{-1}\mathbf{k}_{sw}\mathbf{B}_w\,dx$$

one obtains:

$$\dot{\mathbf{v}}_s = \mathbf{f}_s\dot{\mathbf{q}}_s - \mathbf{b}_{sw}\dot{\mathbf{v}}_w \tag{2.267}$$

Finally, substituting (2.263), and introducing:

$$\mathbf{f}_w = \mathbf{b}_{sw}\mathbf{k}_w^{-1}\mathbf{b}_{ws} \tag{2.268}$$

the compatibility equation becomes:

$$\dot{\mathbf{v}}_s = \big(\mathbf{f}_s + \mathbf{f}_w\big)\dot{\mathbf{q}}_s - \mathbf{b}_{sw}\mathbf{k}_w^{-1}\dot{\mathbf{q}}_w \tag{2.269}$$

The mixed equilibrium operators $\mathbf{b}_{sw}$ and $\mathbf{b}_{ws}$, the section stiffness related to warping $\mathbf{k}_w$, and the flexibility matrices $\mathbf{f}_s$ and $\mathbf{f}_w$ are therefore computed as:

$$\mathbf{b}_{sw} = \int_0^L \mathbf{b}_s^T \mathbf{k}_{ss}^{-1}\mathbf{k}_{sw}\mathbf{B}_w \, dx \tag{2.270}$$

$$\mathbf{b}_{ws} = \int_0^L \mathbf{B}_w^T \mathbf{k}_{ws}\mathbf{k}_{ss}^{-1}\mathbf{b}_s \, dx \tag{2.271}$$

$$\mathbf{f}_s = \int_0^L \mathbf{b}_s^T \mathbf{k}_{ss}^{-1}\mathbf{b}_s \, dx \tag{2.272}$$

$$\mathbf{f}_w = \int_0^L \mathbf{b}_{sw}\mathbf{k}_w^{-1}\mathbf{b}_{ws} \, dx \tag{2.273}$$

$$\mathbf{k}_w = \int_0^L \mathbf{B}_w^T\big(\mathbf{k}_{ww} - \mathbf{k}_{ws}\mathbf{k}_{ss}^{-1}\mathbf{k}_{sw}\big)\mathbf{B}_w \, dx \tag{2.274}$$

The element basic stiffness matrix can then be assembled by writing these components in a compact notation:

$$\dot{\mathbf{v}} = \mathbf{f}\,\dot{\mathbf{q}} \tag{2.275}$$

$$\begin{Bmatrix} \dot{\mathbf{v}}_s \\ \dot{\mathbf{v}}_w \end{Bmatrix} = \begin{bmatrix} \mathbf{f}_{ss} & \mathbf{f}_{sw} \\ \mathbf{f}_{ws} & \mathbf{f}_{ww} \end{bmatrix} \begin{Bmatrix} \dot{\mathbf{q}}_s \\ \dot{\mathbf{q}}_w \end{Bmatrix} \tag{2.276}$$

where:

$$\mathbf{f}_{ss} = \mathbf{f}_s + \mathbf{f}_w, \qquad \mathbf{f}_{sw} = -\,\mathbf{b}_{sw}\mathbf{k}_w^{-1}, \qquad \mathbf{f}_{ws} = -\,\mathbf{b}_{ws}\mathbf{k}_w^{-1}, \qquad \mathbf{f}_{ww} = \mathbf{k}_w^{-1} \tag{2.277}$$

Then everything is assembled back to the local configuration by imposing the element equilibrium and compatibility according to Eq. (2.252):

$$\mathbf{k}_l = \mathbf{a}_g^T \mathbf{f}^{-1}\mathbf{a}_g \tag{2.278}$$

Variational formulation

In this case, a modified five-fields Hu-Washizu functional must be written to incorporate warping and bond-slip:

$$\Pi(\mathbf{u}_m, \boldsymbol{\varepsilon}_m, \boldsymbol{\sigma}_m, \mathbf{u}_w, \mathbf{u}_b) = \Pi^{int} + \Pi^{ext} \tag{2.279}$$

$$\begin{aligned}\Pi^{int} = &\int_\Omega \boldsymbol{\varepsilon}_m^T\,\hat{\boldsymbol{\sigma}}_m \, d\Omega + \int_{A_b} \mathbf{u}_b^T\,\hat{\boldsymbol{\tau}}_b \, dA + \int_\Omega \boldsymbol{\sigma}_m^T \mathbf{D}(\mathbf{u}_r - \boldsymbol{\varepsilon}_r) \, d\Omega \\ &+ \int_{\Omega_f} \boldsymbol{\tau}_f^T\,[\mathbf{u}_b' - \mathbf{e}_b] \, d\Omega + \int_\Omega \boldsymbol{\sigma}_m^T\,\mathbf{D}(\mathbf{u}_w - \boldsymbol{\varepsilon}_w) \, d\Omega\end{aligned} \tag{2.280}$$

$$\Pi^{ext} = -\mathbf{u}_l^T\,\mathbf{p}_l^{ext} - \int_0^L \mathbf{u}_s^T\,\mathbf{p}_p \, dx \tag{2.281}$$

Here, $\mathbf{u}_m(x,y,z) = \mathbf{u}_r(x,y,z) + \mathbf{u}_w(x,y,z)$ are the material-point displacements and $\mathbf{u}_s(x)$ are the section displacements; $\hat{\boldsymbol{\tau}}_b(x)$ is the bond stress and $\boldsymbol{\sigma}_s(x,y)$ is the stress in the slipping components. The volumes Ω and Ω_f refer to the whole beam and to the fibers with bond-slip, respectively.

The introduction of Eq. (2.214), Eq. (2.220) and the other definitions in Section 2.3.5, considering how the section operators are composed, the functional can be expressed in terms of the section operators $\mathbf{u}_s(x)$ and $\mathbf{e}(x)$:

$$\begin{aligned}\Pi(\mathbf{u}_s,\mathbf{e},\mathbf{s},\boldsymbol{\eta},\mathbf{u}_b) = &\int_0^L \mathbf{e}^T\,\hat{\mathbf{s}}\,dx \;+\; \int_0^L \mathbf{u}_b^T\,\hat{\mathbf{p}}_b\,dx \;+\; \int_0^L \mathbf{s}^T\,[\mathbf{e}(\mathbf{u}_s,\boldsymbol{\eta}) - \mathbf{e}]\,dx \\ &+ \int_0^L \mathbf{s}_b^T\,[\mathbf{u}_b' - \mathbf{e}_b]\,dx \;-\; \mathbf{u}_l^T\,\mathbf{p}_l^{ext} \;-\; \int_0^L \mathbf{u}_s^T\,\mathbf{p}_p\,dx\end{aligned} \tag{2.282}$$

Let us momentarily abuse the notation and stack some of the section fields on top of each other (the ones related to the force-based interpolation), so that:

$$\mathbf{e} \leftarrow \begin{Bmatrix}\mathbf{e}\\ \mathbf{e}_b\\ \mathbf{u}_b\end{Bmatrix} \qquad \mathbf{s} \leftarrow \begin{Bmatrix}\mathbf{s}\\ \mathbf{s}_b\\ \mathbf{p}_b\end{Bmatrix} \tag{2.283}$$

This leads to a simplified four-field functional:

$$\Pi(\mathbf{u}_s,\mathbf{e},\mathbf{s},\boldsymbol{\eta}) = \int_0^L \mathbf{e}^T\,\hat{\mathbf{s}}\,dx + \int_0^L \mathbf{s}^T\,[\mathbf{e}(\mathbf{u}_s,\boldsymbol{\eta}) - \mathbf{e}]\,dx - \mathbf{u}_l^T\,\mathbf{p}_l^{ext} - \int_0^L \mathbf{u}_s^T\,\mathbf{p}_p\,dx \tag{2.284}$$

The variation of the functional is:

$$\delta\Pi = \delta\Pi^{int} + \delta\Pi^{ext} = 0 \tag{2.285}$$

where the internal variation is:

$$\begin{aligned}\delta\Pi^{int} = &\int_0^L \delta\mathbf{e}^T\,\hat{\mathbf{s}}\,dx + \int_0^L \delta\mathbf{s}^T\,[\mathbf{e}(\mathbf{u}_s,\boldsymbol{\eta}) - \mathbf{e}]\,dx \\ &+ \int_0^L \mathbf{s}^T\,\delta\mathbf{e}(\mathbf{u}_s,\boldsymbol{\eta})\,dx - \int_0^L \mathbf{s}^T\,\delta\mathbf{e}\,dx\end{aligned} \tag{2.286}$$

and the external variation is:

$$\delta\Pi^{ext} = -\delta\mathbf{u}_l^T\,\mathbf{p}_l^{ext} - \int_0^L \delta\mathbf{u}_s^T\,\mathbf{p}_p\,dx \tag{2.287}$$

Since $\mathbf{e}(\mathbf{u}_s,\boldsymbol{\eta}) = \mathbf{D}\mathbf{u}_s$, then $\delta\mathbf{e}(\mathbf{u}_s,\boldsymbol{\eta}) = \mathbf{D}\delta\mathbf{u}_s$.
The variation becomes:

$$\begin{aligned}\delta\Pi^{int} = &\int_0^L \delta\mathbf{e}^T(\hat{\mathbf{s}} - \mathbf{s})\,dx + \int_0^L \delta\mathbf{s}^T[\mathbf{D}\mathbf{u}_s - \mathbf{e}]\,dx \\ &+ \int_0^L (\mathbf{D}\delta\mathbf{u}_s)^T\mathbf{s}\,dx\end{aligned} \tag{2.288}$$

Integrating by parts the third term, since $\mathbf{D}^*\mathbf{s} + \mathbf{p}_p = \mathbf{0}$:

$$\int_0^L (\mathbf{D}\delta\mathbf{u}_s)^T \mathbf{s}\, dx = \int_0^L \delta\mathbf{u}_s^T \mathbf{D}^*\mathbf{s}\, dx + \delta\mathbf{u}_s^T \mathbf{s}\big|_0^L \tag{2.289}$$

$$= -\int_0^L \delta\mathbf{u}_s^T \mathbf{p}_p\, dx + \delta\mathbf{u}^T[\mathbf{a}_g^T\mathbf{q} - \mathbf{p}_{l0}] \tag{2.290}$$

The complete variation is:

$$\begin{aligned}\delta\Pi = &\int_0^L \delta\mathbf{e}^T(\hat{\mathbf{s}} - \mathbf{s})\, dx + \int_0^L \delta\mathbf{s}^T(\mathbf{D}\mathbf{u}_s - \mathbf{e})\, dx \\ &+ \delta\mathbf{u}^T[\mathbf{a}_g^T\mathbf{q} - \mathbf{p}_{l0} - \mathbf{p}_l^{ext}] = 0\end{aligned} \tag{2.291}$$

Setting $\delta\Pi = 0$ for all admissible virtual fields yields the following equations:

1. Section constitutive law $\forall\delta\mathbf{e} \neq 0$:

$$\int_0^L \delta\mathbf{e}^T(\hat{\mathbf{s}} - \mathbf{s})\, dx = 0 \tag{2.292}$$

Which requires:

$$\hat{\mathbf{s}}(x) - \mathbf{s}(x) = 0 \tag{2.293}$$

or equivalently:

$$\hat{\mathbf{s}}(x) - \mathbf{b}(x)\mathbf{q} + \mathbf{s}_p(x) = 0 \tag{2.294}$$

2. Element compatibility expressed in weak form $\forall\delta\mathbf{s} \neq 0$:

$$\int_0^L \delta\mathbf{s}^T(\mathbf{D}\mathbf{u}_s - \mathbf{e})\, dx = 0 \tag{2.295}$$

Substituting $\delta\mathbf{s} = \mathbf{b}(x)\delta\mathbf{q}$:

$$\delta\mathbf{q}^T \int_0^L \mathbf{b}^T(\mathbf{D}\mathbf{u}_s - \mathbf{e})\, dx = 0 \tag{2.296}$$

Which yields:

$$\mathbf{v} - \int_0^L \mathbf{b}^T\mathbf{e}\, dx = 0 \tag{2.297}$$

where $\mathbf{v} = \int_0^L \mathbf{b}^T\mathbf{D}\mathbf{u}_s\, dx$ (according to Eq. (2.89)).

3. Element equilibrium conditions expressed in weak form $\forall\delta\mathbf{u}_s \neq 0$:

$$\delta\mathbf{u}^T[\mathbf{a}_g^T\mathbf{q} - \mathbf{p}_{l0} - \mathbf{p}_l^{ext}] = 0 \tag{2.298}$$

Yielding:

$$\mathbf{p}_l^{ext} + \mathbf{p}_{l0} - \mathbf{a}_g^T\mathbf{q} = 0 \tag{2.299}$$

4. Cross-section equilibrium conditions related to warping. For the warping field $\boldsymbol{\eta}$, considering

the partitioned form:

$$\delta\Pi_w = \delta\mathbf{v}_w^T \left(\mathbf{q}_w - \int_0^L \mathbf{B}_w^T \hat{\mathbf{s}}_w \, dx \right) = 0 \tag{2.300}$$

For all $\delta\mathbf{v}_w \neq 0$:

$$\mathbf{q}_w - \int_0^L \mathbf{B}_w^T \hat{\mathbf{s}}_w \, dx = 0 \tag{2.301}$$

where the basic warping displacements $\mathbf{v}_w$ equal the local ones $\mathbf{u}_w$, same for their work conjugates.

This concludes the mixed approach using virtual fields, providing sufficient governing equations, and leading back to the same three equations as before plus an additional equation that links the generalized warping forces components $\mathbf{q}_w$ to the generalized section warping forces $\mathbf{s}_w(x)$ by means of a weak-form equilibrium equation:

$$\mathbf{p}_l^{ext} + \mathbf{p}_{l0} - \mathbf{p}_l^{int} = 0 \tag{2.302}$$

$$\hat{\mathbf{s}}(x) - \mathbf{b}(x)\mathbf{q} - \mathbf{s}_p(x) = 0 \tag{2.303}$$

$$\mathbf{v} - \int_0^L \mathbf{b}^T(x) \; \mathbf{e}(x) \; dx = 0 \tag{2.304}$$

$$\mathbf{q}_w - \int_0^L \mathbf{B}_w^T \hat{\mathbf{s}}_w \, dx = 0 \tag{2.305}$$

Chapter 3

Material Constitutive Laws

In civil and structural engineering, materials exhibit diverse inelastic responses that must be accurately represented in computational models. In particular, ductile materials such as steel reinforcement and prestressing tendons can be effectively described using classical elasto-plasticity, while brittle or quasi-brittle materials such as concrete and FRP require more advanced formulations involving damage or coupled plastic-damage mechanisms.
This chapter presents the constitutive laws adopted in this work, highlighting both consolidated formulations and specific extensions introduced herein. The discussion is organized into two main parts.

For three-dimensional continua, constitutive laws relate the stress tensor $\boldsymbol{\sigma}$ to the strain tensor $\boldsymbol{\varepsilon}$ under general loading conditions. We adopt Voigt notation, expressing these tensors as six-dimensional vectors:

$$\boldsymbol{\sigma} = \begin{Bmatrix} \sigma_x & \sigma_y & \sigma_z & \sigma_{xy} & \sigma_{yz} & \sigma_{zx} \end{Bmatrix}^T, \quad \boldsymbol{\varepsilon} = \begin{Bmatrix} \varepsilon_x & \varepsilon_y & \varepsilon_z & \gamma_{xy} & \gamma_{yz} & \gamma_{zx} \end{Bmatrix}^T \tag{3.1}$$

where the shear strains satisfy

$$\gamma_{ij} = 2\varepsilon_{ij}, \quad i \neq j \tag{3.2}$$

Within this framework:

- the 3D elastic constitutive relationship is briefly described in Section 3.1;
- the Von Mises and Drucker-Prager plasticity models [74] are presented in Sections 3.1 and 3.2.2, which provide the reference background for ductile metals and pressure-sensitive materials;
- the 3D plastic-damage constitutive law proposed by Di Re et al. [7] is introduced in Section 3.3, specifically developed to reproduce the response of cementitious and brittle concrete-like materials under complex tri-axial stress states;
- this formulation is extended in Section 3.3.3 by deriving the consistent tangent constitutive matrix, which represents a distinctive contribution of this work.

Classical plasticity models, such as Von Mises and Drucker-Prager, represent the foundation of the adopted framework and are well suited for ductile materials. However, for brittle or quasi-brittle materials more advanced approaches are required, including damage mechanics,

smeared-crack or phase-field formulations.
Among these, the plastic-damage model by Di Re et al [7] adopted in this work is further extended here by deriving its consistent tangent operator to ensure robust numerical implementation.

In addition, several one-dimensional constitutive laws are presented and adopted in this work, as they are directly employed in the fiber discretization of beam cross-sections:

- the classical Menegotto-Pinto model [3] for steel reinforcement and prestressing tendons;
- a simplified elasto-fragile law for carbon fiber reinforced polymers (CFRP) strips;
- the phenomenological bond law by Lowes et al. [4], typically used for bond-slip interfaces and pinching effects.

This organization ensures that the chapter first addresses general three-dimensional constitutive formulations for both ductile and brittle materials, and then narrows down to one-dimensional laws tailored for reinforcement, tendons and bond interfaces, consistently covering all the material behaviors required in the proposed beam finite element framework.

3.1 3D Elastic Constitutive Law

Under isotropic linear elasticity, stress and strain are related by:

$$\boldsymbol{\sigma} = \mathbf{C}\,\boldsymbol{\varepsilon} \tag{3.3}$$

where $\mathbf{C}$ depends on the bulk modulus K and the shear modulus G:

$$\mathbf{C} = K\,\mathbf{I}_{vol} + 2G\,\mathbf{I}_{dev} \tag{3.4}$$

The volumetric projection matrix in Voigt notation is given by:

$$\mathbf{I}_{vol} = \mathbf{I}_2\,\mathbf{I}_2^T \tag{3.5}$$

with

$$\mathbf{I}_2 = [1\ 1\ 1\ 0\ 0\ 0]^T \tag{3.6}$$

The deviatoric projection matrix is defined as:

$$\mathbf{I}_{dev} = \mathbf{I}_6 - \frac{1}{3}\,\mathbf{I}_{vol} \tag{3.7}$$

where $\mathbf{I}_6$ is the 6×6 identity matrix. The bulk and shear moduli are expressed in terms of Young's modulus E and Poisson ratio ν as:

$$K = \frac{E}{3(1-2\nu)}, \quad G = \frac{E}{2(1+\nu)} \tag{3.8}$$

3.2 3D Plastic Constitutive Laws

3.2.1 Von Mises Plasticity Model

The Von Mises plasticity model, also known as the J2 model, depends solely on the second invariant of the deviatoric stress vector. This invariant can be expressed in Voigt notation as:

$$J_2 = \frac{1}{2}\left[(\mathrm{tr}\,\boldsymbol{\sigma})^2 - \mathrm{tr}\left(\boldsymbol{\sigma}^2\right)\right] = \sigma_x\sigma_y + \sigma_y\sigma_z + \sigma_z\sigma_x - \sigma_{xy}^2 - \sigma_{yz}^2 - \sigma_{zx}^2 \tag{3.9}$$

where $\mathrm{tr}(\boldsymbol{\sigma})$ denotes the trace of the stress vector, i.e. the sum of its normal components $\mathrm{tr}(\boldsymbol{\sigma}) = \sigma_x + \sigma_y + \sigma_z$. The total strain is additively decomposed into elastic and plastic parts:

$$\boldsymbol{\sigma} = \mathbf{C}\,(\boldsymbol{\varepsilon} - \boldsymbol{\varepsilon}^p) = \mathbf{C}\,\boldsymbol{\varepsilon}^e \tag{3.10}$$

where $\mathbf{C}$ is the isotropic elastic constitutive matrix defined in Eq. (3.4).
The yield surface defines the boundary of the elastic domain and is written as:

$$f(\eta, \alpha) = \eta - \sqrt{\frac{2}{3}}\left(\sigma_y + H_i\alpha\right) \tag{3.11}$$

where η is defined as:

$$\eta = |\mathbf{q} - \boldsymbol{\zeta}| \tag{3.12}$$

Here, $\boldsymbol{\zeta}$ is the back-stress vector representing kinematic hardening, σ_y is the initial uniaxial yield stress, H_i is the isotropic hardening modulus, α is the isotropic hardening variable, and $\mathbf{q}$ is the deviatoric stress vector defined as:

$$\mathbf{q} = \mathbf{P}\,\boldsymbol{\sigma} = \boldsymbol{\sigma} - \mathbf{p} \tag{3.13}$$

where the spherical stress component is given by:

$$\mathbf{p} = \frac{\sigma_x + \sigma_y + \sigma_z}{3}\,\mathbf{I}_2 \tag{3.14}$$

The evolution of these internal variables with respect to a pseudo-time parameter describes the associated flow rule, governed by the evolution of the plastic strains:

$$\dot{\boldsymbol{\varepsilon}}^p = \dot{\lambda}\frac{\partial f}{\partial \boldsymbol{\sigma}} = \dot{\lambda}\,\hat{\mathbf{n}} \tag{3.15}$$

$$\dot{\alpha} = \sqrt{\frac{2}{3}}\,\dot{\lambda} \tag{3.16}$$

$$\dot{\boldsymbol{\zeta}} = \frac{2}{3}H_k\,\dot{\boldsymbol{\varepsilon}}^p \tag{3.17}$$

where λ is the plastic multiplier, subject to the Kuhn-Tucker conditions:

$$\dot{\lambda} \geq 0, \quad f \leq 0, \quad \dot{\lambda}\,f = 0 \tag{3.18}$$

where the flow direction (unit normal to the yield surface) is given by:

$$\hat{\mathbf{n}} = \frac{\mathbf{q} - \boldsymbol{\zeta}}{\eta} \tag{3.19}$$

and H_k is the kinematic hardening modulus.
The consistent elastoplastic tangent operator for the Von Mises model with combined isotropic and kinematic hardening can be written in compact form as:

$$\mathbf{C}^{ep} = \mathbf{C} - \frac{\mathbf{C}\,\hat{\mathbf{n}}\,\hat{\mathbf{n}}^T\,\mathbf{C}}{\hat{\mathbf{n}}^T\,\mathbf{C}\,\hat{\mathbf{n}} + H} \tag{3.20}$$

where H is the combined hardening modulus, typically given by

$$H = \frac{2}{3}\,(H_i + H_k) \tag{3.21}$$

This expression ensures consistency with the return mapping algorithm by satisfying the consistency condition and providing quadratic convergence in Newton-Raphson schemes.
Figure 3.1 shows the 3D J2 elastic limit domain for a specific yield tension σ_y.

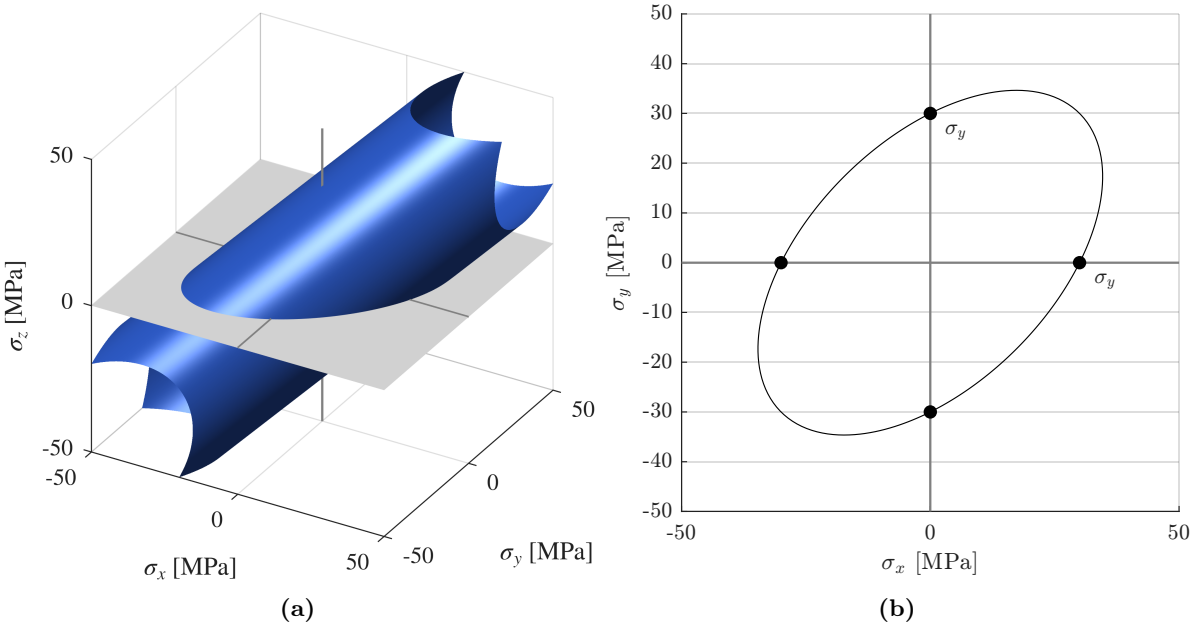

Figure 3.1. J2 elastic limit domains for yield stress $\sigma_y = 30$ MPa: (a) 3D J2 cylindrical surface; (b) intersection with plane $\sigma_z = 0$.

3.2.2 Drucker-Prager Plasticity Model

The Drucker-Prager model extends the Von Mises (J2) plasticity to account for pressure sensitivity and asymmetric strength in tension and compression, which are essential features for brittle materials like concrete. Unlike Von Mises, which assumes a pressure-insensitive, cylindrical yield surface in the principal stress space, the Drucker-Prager model introduces a conical yield surface whose opening angle depends on the material friction parameter μ.

This extension enables the model to capture higher compressive strength relative to tensile strength, reproducing the non-symmetric behavior observed experimentally in cementitious materials.

The yield function is written in Voigt notation as:

$$f(\eta, p, \alpha) = \eta + \mu\, p - \sqrt{\frac{2}{3}}\left(\sigma_y + H_i \alpha\right) \leq 0 \tag{3.22}$$

where:

- p is the mean (volumetric) stress component, already defined as:

$$p = \frac{\sigma_x + \sigma_y + \sigma_z}{3}$$

- $\eta = |\mathbf{q} - \boldsymbol{\zeta}|$ is the norm of the shifted deviatoric stress vector, including kinematic hardening effects;
- μ is the Drucker-Prager friction parameter, controlling the pressure dependence of yielding;
- σ_y is the initial yield stress in an equivalent isotropic hardening formulation;
- H_i and H_k are the isotropic and kinematic hardening moduli, respectively;
- α is the accumulated isotropic hardening variable governed by the same evolution law as in Eq. (3.16).

The initial uniaxial yield stress σ_y and the friction parameter μ, which governs the coupling between pressure and shear, can be calibrated from the uniaxial tensile (σ_t) and compressive (σ_c) strengths as:

$$\sigma_y = \frac{2\,\sigma_c\,\sigma_t}{\sigma_c + \sigma_t}, \quad \mu = \sqrt{\frac{2}{3}}\,\frac{\sigma_c - \sigma_t}{\sigma_c + \sigma_t} \tag{3.23}$$

This formulation ensures that the yield surface intersects the principal stress axes at the uniaxial tensile and compressive strengths.

The flow direction for associative plasticity is given by:

$$\hat{\mathbf{n}} = \frac{\mathbf{q} - \boldsymbol{\zeta}}{\eta} + \mu\, \mathbf{I}_2 \tag{3.24}$$

The evolution equations for the internal variables remain similar to the Von Mises case:

$$\dot{\boldsymbol{\varepsilon}}^p = \dot{\lambda}\, \hat{\mathbf{n}}, \quad \dot{\alpha} = \sqrt{\frac{2}{3}}\,\dot{\lambda}, \quad \dot{\boldsymbol{\zeta}} = \frac{2}{3} H_k\, \dot{\boldsymbol{\varepsilon}}^p \tag{3.25}$$

with the plastic multiplier λ once again satisfying the standard Kuhn-Tucker conditions:

$$\dot{\lambda} \geq 0, \quad f \leq 0, \quad \dot{\lambda}\, f = 0 \tag{3.26}$$

Finally, the consistent elastoplastic tangent operator retains the same compact form used for Von Mises, ensuring numerical consistency:

$$\mathbf{C}^{ep} = \mathbf{C} - \frac{\mathbf{C}\,\hat{\mathbf{n}}\,\hat{\mathbf{n}}^T\,\mathbf{C}}{\hat{\mathbf{n}}^T\,\mathbf{C}\,\hat{\mathbf{n}} + H} \tag{3.27}$$

Compared to the J2 model, the essential difference lies in the pressure-dependent yield function and the flow direction, which includes a volumetric component scaled by μ. This allows Drucker-Prager plasticity to realistically simulate materials with frictional behavior and different strengths in tension and compression.
Figure 3.2 shows the 3D Drucker-Prager elastic limit domain for specific yield stresses σ_t ad σ_c.

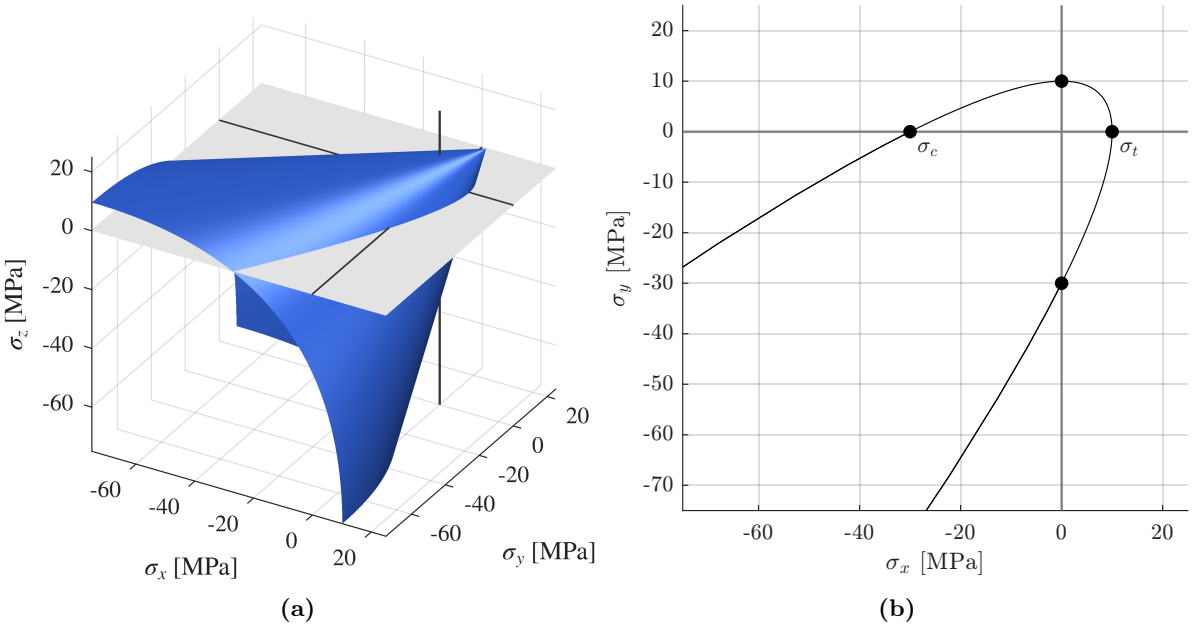

Figure 3.2. Drucker-Prager elastic limit domains for yield stresses $\sigma_t = 10$ MPa and $\sigma_c = 30$ MPa: (a) 3D conic surface; (b) intersection with plane $\sigma_z = 0$.

3.3 3D Damage-Plastic Constitutive Law

3.3.1 Damage model

This damage model was proposed by Di Re et al. [7] alongside the formulation presented in [93], the latter adopting a Von Mises plasticity criterion instead. Both approaches can be seen as developments of the earlier proposal by Addessi et al. [14]. The main features are briefly recalled here.

In this model, to account for the unilateral effects due to the re-closure in compression of the tensile cracks, two different damage variables are used, D_t and D_c, that measure damage for prevailing tensile and compressive states, respectively. These evolve independently with the constraint $D_t \geq D_c$. Both range between 0 and 1 and satisfy the thermodynamic irreversibility condition $\dot{D}_t \geq 0$ and $\dot{D}_c \geq 0$. The damage-associated variables, Y_t, Y_c, Y_t^e and Y_c^e are defined as:

$$Y_t = \sqrt{\sum_{i=1}^{3} \langle e_i \rangle_+^2}, \quad Y_t^e = \sqrt{\sum_{i=1}^{3} \langle e_i^e \rangle_+^2}, \tag{3.28}$$

$$Y_c = \sqrt{\sum_{i=1}^{3} \langle e_i \rangle_-^2 - \beta \sum_{j \neq i=1}^{3} \langle e_i \rangle_- \langle e_j \rangle_-}$$

$$Y_c^e = \sqrt{\sum_{i=1}^{3} \langle e_i^e \rangle_-^2 - \beta \sum_{j \neq i=1}^{3} \langle e_i^e \rangle_- \langle e_j^e \rangle_-} \tag{3.29}$$

where brackets $\langle \cdot \rangle_\pm$ compute the positive/negative part of the quantity, and β is a material parameter influencing the shape of the damage limit function in compression. The terms e_i and e_i^e are evaluated from the principal total strains, $\hat{\varepsilon}_i$, as well as the elastic strains, $\hat{\varepsilon}_i^e$, respectively, as:

$$e_i = (1 - 2\nu)\hat{\varepsilon}_i + \nu \sum_{j=1}^{3} \hat{\varepsilon}_j, \qquad e_i^e = (1 - 2\nu)\hat{\varepsilon}_i^e + \nu \sum_{j=1}^{3} \hat{\varepsilon}_j^e \tag{3.30}$$

The overall damage variable D is the linear combination of D_t and D_c:

$$D = \alpha_t D_t + \alpha_c D_c \tag{3.31}$$

where the two weight factors α_t and α_c are evaluated as:

$$\alpha_t = \frac{\eta_t^2}{\eta_t^2 + \eta_c^2}, \quad \alpha_c = \frac{\eta_c^2}{\eta_t^2 + \eta_c^2} = 1 - \alpha_t \tag{3.32}$$

and

$$\eta_h = \frac{Y_h^e}{Y_{0h} + D(a_h Y_h^e + b_h)} \tag{3.33}$$

where the subscript h is replaced by t for tension and c for compression, respectively.

The damage limit functions in tension and compression are defined as:

$$f_h(Y_h, D_h) = Y_h - Y_{0h} - D_h(a_h Y_h + b_h) \tag{3.34}$$

where the evolution of D_h, follows the Karush-Kuhn-Tucker conditions:

$$\dot{D}_h \geq 0, \quad f_h \leq 0, \quad \dot{D} f_h = 0, \quad \dot{D}_h \dot{f}_h = 0 \tag{3.35}$$

3.3.2 Damage-plastic model

Given the six-component strain vector $\boldsymbol{\varepsilon}$, the work-conjugate stress vector $\boldsymbol{\sigma}$ is obtained through the following equation:

$$\boldsymbol{\sigma} = (1-D)^2 \mathbf{C}(\boldsymbol{\varepsilon} - \boldsymbol{\varepsilon}^p) = (1-D)^2 \mathbf{C}\boldsymbol{\varepsilon}^e = (1-D)^2 \bar{\boldsymbol{\sigma}} \tag{3.36}$$

where $\boldsymbol{\sigma}$ is the stress vector, $\boldsymbol{\varepsilon}$, $\boldsymbol{\varepsilon}^e$ and $\boldsymbol{\varepsilon}^p$ are the total, elastic and plastic strains, respectively; D is a scalar damage variable that ranges from 0 (that represents the undamaged elastic material state) to 1 (corresponding to a completely damaged material); $\bar{\boldsymbol{\sigma}}$ is the effective stress vector.

This constitutive law is extremely versatile and allows to model from ductile to fragile materials by accurately tuning the material parameters. In particular, this constitutive law requires 13 parameters:

- 2 for the elastic behavior: the Young's modulus E and the Poisson ratio ν;
- 4 for plasticity: the uniaxial compression and tension yielding thresholds σ_c and σ_t, the kinematic hardening parameter H_k and the isotropic hardening parameter H_i that control the yielding and back-stress rates, respectively;
- 7 for damage: Y_{0c} and Y_{0t}, that control the strain value where damage starts, b_t and b_c, that control the maximum material strengths, a_t and a_c, that mainly control the softening branches, and β, that is a parameter that influences the shape of the damage limit function in compression.

A typical uniaxial cyclic concrete test is shown in Figure 3.3a for axial behavior and in Figure 3.3b for shear behavior. The parameters used in this example are reported in Table 3.1. It is worth noting that, due to the isotropic nature of the adopted damage model, the overall damage variable D equally affects all components of the 3D constitutive matrix. Consequently, the shear behavior is also governed by D, with the contributions of D_t and D_c properly weighted.

Elastic and plastic parameters					
E [GPa]	ν	H_k	H_i	σ_t [MPa]	σ_c [MPa]
30	0.2	$0.5E$	$0.1E$	3.3	15

Damage parameters						
Y_{t0}	a_t	b_t	Y_{c0}	a_c	b_c	β
$7.92{\cdot}10^{-5}$	0.8	$8{\cdot}10^{-5}$	$3.6{\cdot}10^{-4}$	0.1	$5{\cdot}10^{-3}$	1

Table 3.1. Material parameters for concrete used in Figure 3.3

A few examples are presented here to illustrate how the model can be tuned to closely reproduce the experimental behavior of concrete specimens. Figure 3.4a shows an experimental comparison for a tensile setup with unloading, performed by Gopalaratnam and Shah [1]. The relevant model parameters are the Young's modulus $E = 30$ GPa, the Poisson ratio $\nu = 0.2$, and

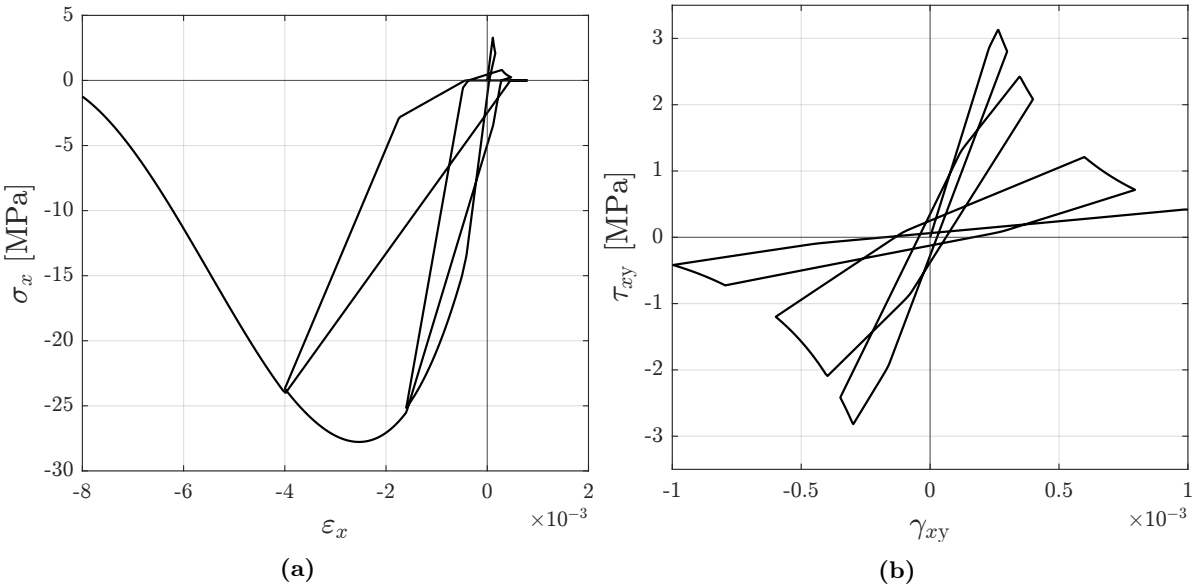

(a) **(b)**

Figure 3.3. Uni-axial damage-plastic cyclic test for concrete with the parameters of Tables 3.1: (a) Axial test on ε_x; (b) Shear test on γ_{xy}.

the peak tensile strength $f_t = 3.5$ MPa. The parameters are the same as in Table 3.1, except for:

1. $\sigma_t = 3.5$ MPa, which controls the onset of tensile plastic strains (yielding), occurring at $\varepsilon_x = \sigma_t / E$;
2. $Y_{t0} = 8.4 \cdot 10^{-5}$, which controls the onset of damage, occurring at $\varepsilon_x = Y_{t0}/(1 - \nu - 2\nu^2)$ according to [92].

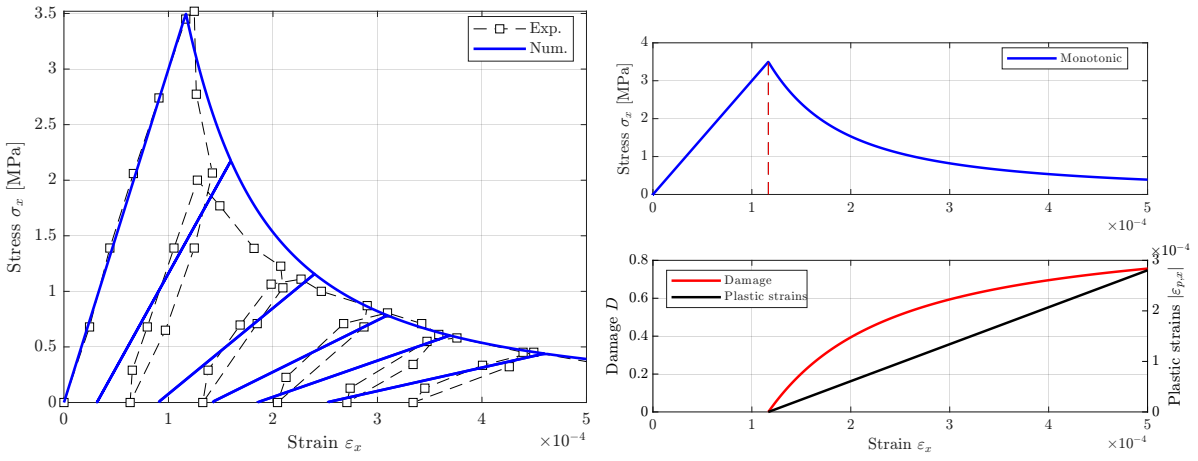

(a) **(b)**

Figure 3.4. Numerical and experimental tensile response of concrete [1]: (a) cyclic behavior and (b) monotonic behavior with damage and plastic strain variables evolution.

Figure 3.5a shows an experimental comparison for a compression setup with unloading, performed by Karsan and Jirsa [2]. The relevant model parameters are the Young's modulus $E = 30$ GPa, the Poisson ratio $\nu = 0.2$, and the peak compressive strength $f_c = 27$ MPa. The parameters are the same as in Table 3.1, except for:

1. $\sigma_c = 30$ MPa, which controls the onset of compressive plastic strains (yielding), occurring

at $\varepsilon_x = \sigma_c/E$;

2. $b_c = 4.5 \cdot 10^{-3}$, which governs the evolution of damage, with higher values leading to slower damage development as strain increases.

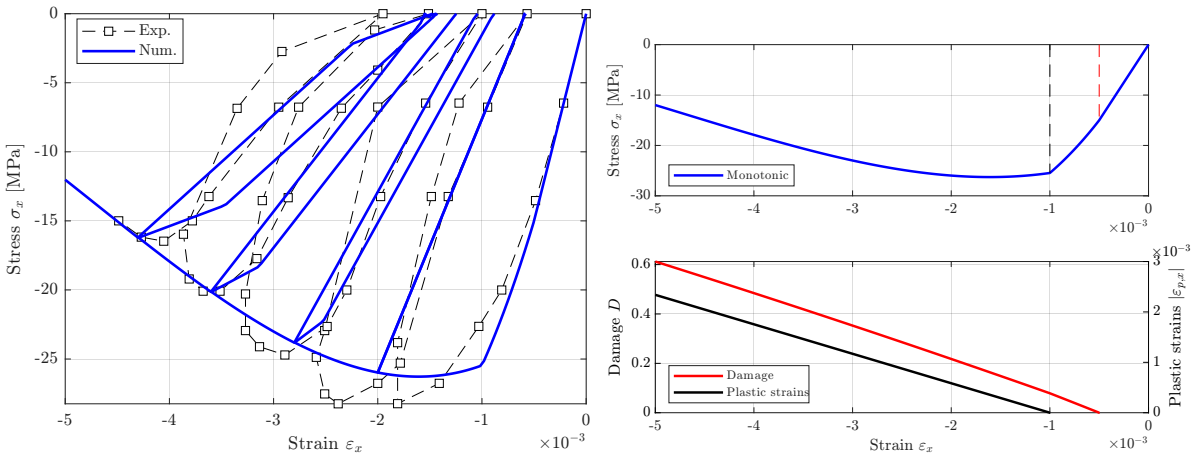

(a) **(b)**

Figure 3.5. Numerical and experimental compression response of concrete [2]: (a) cyclic behavior and (b) monotonic behavior with damage and plastic strain variables evolution..

These numerical cases demonstrate that, for different concrete specimens, only small adjustments in the damage parameters are sufficient to reproduce the expected response.

3.3.3 Consistent Tangent Constitutive Matrix

While previous formulations of this damage-plasticity model mainly focused on the strain-stress relation and its evolution, the consistent tangent operator was not explicitly derived [92].
Here, the full derivation of the algorithmic tangent is provided, ensuring a rigorous linearization of the constitutive law and enabling quadratic convergence of the global Newton-Raphson iterations. This represents a distinctive contribution of the present work.

The stress vector in the adopted scalar damage-plasticity model is defined, according to Eq. (3.36) as:

$$\boldsymbol{\sigma} = (1 - D)^2 \, \mathbf{C}_{ep} \; \boldsymbol{\varepsilon}^e \tag{3.37}$$

where $D \in [0, 1]$ is the scalar damage variable, $\mathbf{C}_{ep}$ is the elastoplastic consistent tangent matrix of the undamaged material.
Differentiating $\boldsymbol{\sigma}$ with respect to the total strain yields:

$$\dot{\boldsymbol{\sigma}} = \mathbf{C}_t \; \dot{\boldsymbol{\varepsilon}} = (1 - D)^2 \, \mathbf{C}_{ep} \; \dot{\boldsymbol{\varepsilon}}^e - 2(1 - D) \, \bar{\boldsymbol{\sigma}} \left(\frac{\partial D}{\partial \boldsymbol{\varepsilon}^e} \; \dot{\boldsymbol{\varepsilon}}^e \right) \tag{3.38}$$

with $\bar{\boldsymbol{\sigma}} = \mathbf{C}_{ep} \boldsymbol{\varepsilon}^e$ being the effective stress.
Thus, the consistent algorithmic tangent is:

$$\mathbf{C}_t = (1 - D)^2 \, \mathbf{C}_{ep} - 2(1 - D) \, \bar{\boldsymbol{\sigma}} \frac{\partial D}{\partial \boldsymbol{\varepsilon}} \tag{3.39}$$

The damage variable is defined as in Eq. (3.31), here reported for convenience:

$$D = \alpha_t D_t + \alpha_c D_c \tag{3.40}$$

The weighting factors α_t and α_c are driven by the elastic strain energy and thus depend on $\boldsymbol{\varepsilon}^e$ only, according to Eqs. (3.32) and (3.33). This complies with the classical formulation of damage models based on energy release, where damage evolution is assumed to result solely from the elastic part of the strain.
The gradient:

$$\frac{\partial D}{\partial \boldsymbol{\varepsilon}} = \frac{\partial D}{\partial \boldsymbol{\varepsilon}^e} \cdot \frac{\partial \boldsymbol{\varepsilon}^e}{\partial \boldsymbol{\varepsilon}} = \frac{\partial D}{\partial \boldsymbol{\varepsilon}^e} \tag{3.41}$$

since plasticity is assumed to be frozen during the damage update, this assumption means that $\partial \boldsymbol{\varepsilon}^e / \partial \boldsymbol{\varepsilon} = \mathbf{I}$, the identity matrix, hence the simplification.
The damage-driving quantities depend on the spectral decomposition of the elastic strain tensor:

$$\boldsymbol{\varepsilon}^e = \sum_{i=1}^{3} \hat{\varepsilon}_i^e \, \mathbf{v}_i \otimes \mathbf{v}_i \tag{3.42}$$

where $\hat{\varepsilon}_i^e$ are the principal elastic strains and $\mathbf{v}_i$ are their associated orthonormal eigenvectors. From these, the following quantities are computed:

$$e_i^e = (1 - 2\nu)\hat{\varepsilon}_i^e + \nu \sum_{j=1}^{3} \hat{\varepsilon}_j^e \tag{3.43}$$

The directional derivative of D with respect to $\boldsymbol{\varepsilon}^e$ is:

$$\frac{\partial D}{\partial \boldsymbol{\varepsilon}^e} = \sum_{i=1}^{3} \frac{\partial D}{\partial \hat{\varepsilon}_i^e} \cdot \frac{\partial \hat{\varepsilon}_i^e}{\partial \boldsymbol{\varepsilon}^e} \tag{3.44}$$

The sensitivity of the eigenvalue $\hat{\varepsilon}_i^e$ to the tensor components is given by:

$$\frac{\partial \hat{\varepsilon}_i^e}{\partial \varepsilon_j^e} = \mathbf{v}_i^T \cdot \mathbf{M}_j \cdot \mathbf{v}_i \tag{3.45}$$

where $\mathbf{M}_j$ is the symmetric mask tensor corresponding to Voigt index $j = 1, \ldots, 6$, i.e.,

$$\mathbf{M}_1 = \begin{bmatrix} 1 & 0 & 0 \\ 0 & 0 & 0 \\ 0 & 0 & 0 \end{bmatrix}, \qquad \mathbf{M}_4 = \begin{bmatrix} 0 & 0.5 & 0 \\ 0.5 & 0 & 0 \\ 0 & 0 & 0 \end{bmatrix}, \qquad \ldots$$

These matrices project each Voigt component into the 3x3 strain tensor form.
The total derivative $\partial D / \partial \hat{\varepsilon}_i^e$ involves all chain-rule contributions stemming from α, D_t, and D_c as functions of Y_t^e and Y_c^e, which in turn depend on e_i^e and thus on $\hat{\varepsilon}_i^e$, as defined in Eqs. (3.28) and (3.29):

$$\frac{\partial D}{\partial \hat{\varepsilon}_i^e} = \frac{\partial \alpha}{\partial \hat{\varepsilon}_i^e}(D_t - D_c) + \alpha \frac{\partial D_t}{\partial \hat{\varepsilon}_i^e} + (1-\alpha)\frac{\partial D_c}{\partial \hat{\varepsilon}_i^e} \tag{3.46}$$

For $\partial \alpha / \partial \hat{\varepsilon}_i^e$, one obtains:

$$\frac{\partial \alpha}{\partial \hat{\varepsilon}_i^e} = \frac{\partial \alpha}{\partial \eta_t}\frac{\partial \eta_t}{\partial Y_t^e}\frac{\partial Y_t^e}{\partial \hat{\varepsilon}_i^e} + \frac{\partial \alpha}{\partial \eta_c}\frac{\partial \eta_c}{\partial Y_c^e}\frac{\partial Y_c^e}{\partial \hat{\varepsilon}_i^e} \tag{3.47}$$

The derivatives of Y_t^e and Y_c^e with respect to $\hat{\varepsilon}_i^e$ are computed by first differentiating with respect to e_j^e:

$$\frac{\partial Y_t^e}{\partial e_j^e} = \begin{cases} \frac{e_j^e}{Y_t^e}, & e_j^e > 0 \\ 0, & \text{otherwise} \end{cases}, \qquad \frac{\partial Y_c^e}{\partial e_j^e} = \begin{cases} \frac{e_j^e - \beta \sum_{k \neq j} e_k^e}{Y_c^e}, & e_j^e < 0 \\ 0, & \text{otherwise} \end{cases} \tag{3.48}$$

Define:

$$\frac{\partial Y_t^e}{\partial \hat{\varepsilon}_k^e} = \sum_{i=1}^{3} \frac{\partial Y_t^e}{\partial e_i^e} \cdot \left[(1-2\nu)\delta_{ik} + \nu\right] \tag{3.49}$$

$$\frac{\partial Y_c^e}{\partial \hat{\varepsilon}_k^e} = \sum_{i=1}^{3} \frac{\partial Y_c^e}{\partial e_i^e} \cdot \left[(1-2\nu)\delta_{ik} + \nu\right] \tag{3.50}$$

The derivatives of the equivalent strain indicators are:

$$\frac{\partial \eta_t}{\partial Y_t^e} = \frac{Y_{t0} + D^k(a_t Y_t^e + b_t) - D^k a_t Y_t^e}{\left[Y_{t0} + D^k(a_t Y_t^e + b_t)\right]^2} \tag{3.51}$$

$$\frac{\partial \eta_c}{\partial Y_c^e} = \frac{Y_{c0} + D^k(a_c Y_c^e + b_c) - D^k a_c Y_c^e}{\left[Y_{c0} + D^k(a_c Y_c^e + b_c)\right]^2} \tag{3.52}$$

The derivatives of D_t and D_c are:

$$\frac{\partial D_t}{\partial Y_t^e} = \frac{a_t Y_t^e + b_t - a_t(Y_t^e - Y_{t0})}{(a_t Y_t^e + b_t)^2} \tag{3.53}$$

$$\frac{\partial D_c}{\partial Y_c^e} = \frac{a_c Y_c^e + b_c - a_c(Y_c^e - Y_{c0})}{(a_c Y_c^e + b_c)^2} \tag{3.54}$$

Then:

$$\frac{\partial D_t}{\partial \hat{\varepsilon}_k^e} = \frac{\partial D_t}{\partial Y_t^e} \cdot \frac{\partial Y_t^e}{\partial \hat{\varepsilon}_k^e} \tag{3.55}$$

$$\frac{\partial D_c}{\partial \hat{\varepsilon}_k^e} = \frac{\partial D_c}{\partial Y_c^e} \cdot \frac{\partial Y_c^e}{\partial \hat{\varepsilon}_k^e} \tag{3.56}$$

Assemble:

$$\frac{\partial D}{\partial \hat{\varepsilon}_k^e} = \frac{\partial \alpha}{\partial \hat{\varepsilon}_k^e}(D_t - D_c) + \alpha \frac{\partial D_t}{\partial \hat{\varepsilon}_k^e} + (1-\alpha)\frac{\partial D_c}{\partial \hat{\varepsilon}_k^e} \tag{3.57}$$

Project to Voigt notation using the eigenvalue sensitivities:

$$\frac{\partial \hat{\varepsilon}_i^e}{\partial \varepsilon_l^e} = \mathbf{v}_i^T \cdot \mathbf{M}_l \cdot \mathbf{v}_i \tag{3.58}$$

where $\mathbf{M}_l$ are the symmetric Voigt projection matrices. Final damage derivative in Voigt notation:

$$\frac{\partial D}{\partial \boldsymbol{\varepsilon}^e} = \sum_{i=1}^{3} \frac{\partial D}{\partial \hat{\varepsilon}_i^e} \cdot \left[\mathbf{v}_i^T \cdot \mathbf{M}_l \cdot \mathbf{v}_i\right]_{l=1}^{6} \tag{3.59}$$

This provides a fully consistent and differentiable expression for the damage gradient needed in the tangent operator.

To conclude this section, a set of uniaxial numerical examples is presented to illustrate the tangent stiffness' values obtained in the adopted plastic-damage model.
The following figures report strain-stress, stiffness, and damage evolutions under compression (Fig. 3.6), tension (Fig. 3.7), and cyclic loading (Fig. 3.8), comparing the responses obtained with plasticity only, damage only, and the coupled plastic-damage formulation.
The material parameters are reported in Table 3.2.

Elastic and plastic parameters					
E [GPa]	ν	H_k [GPa]	H_i [GPa]	σ_t [MPa]	σ_c [MPa]
46	0.2	30	0.3	90	90

Damage parameters						
Y_{t0}	a_t	b_t	Y_{c0}	a_c	b_c	β
$2 \cdot 10^{-5}$	0.95	$5 \cdot 10^{-5}$	$4 \cdot 10^{-4}$	0.85	$1.7 \cdot 10^{-3}$	1

Table 3.2. Material parameters for concrete used in Figures 3.6, 3.7 and 3.8.

These examples highlight how the proposed tangent operator ensures a stable and accurate description of the constitutive response across different loading conditions.

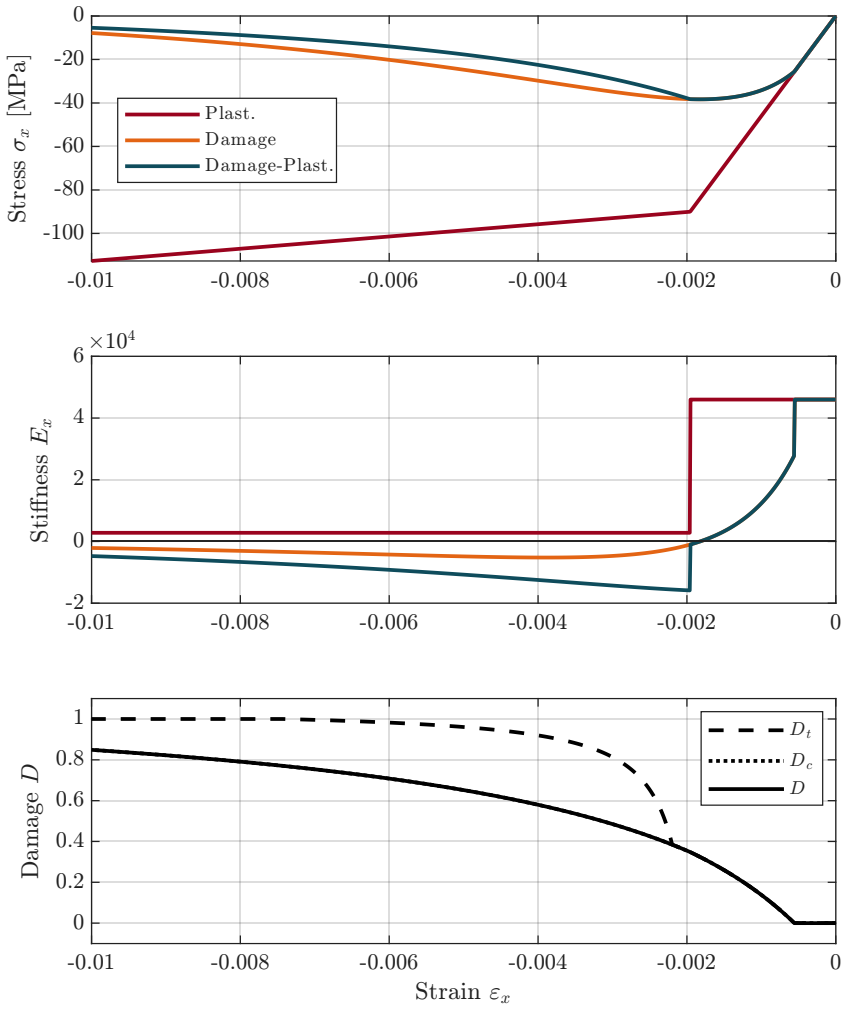

Figure 3.6. strain-stress, stiffness, and damage evolutions under compression loading.

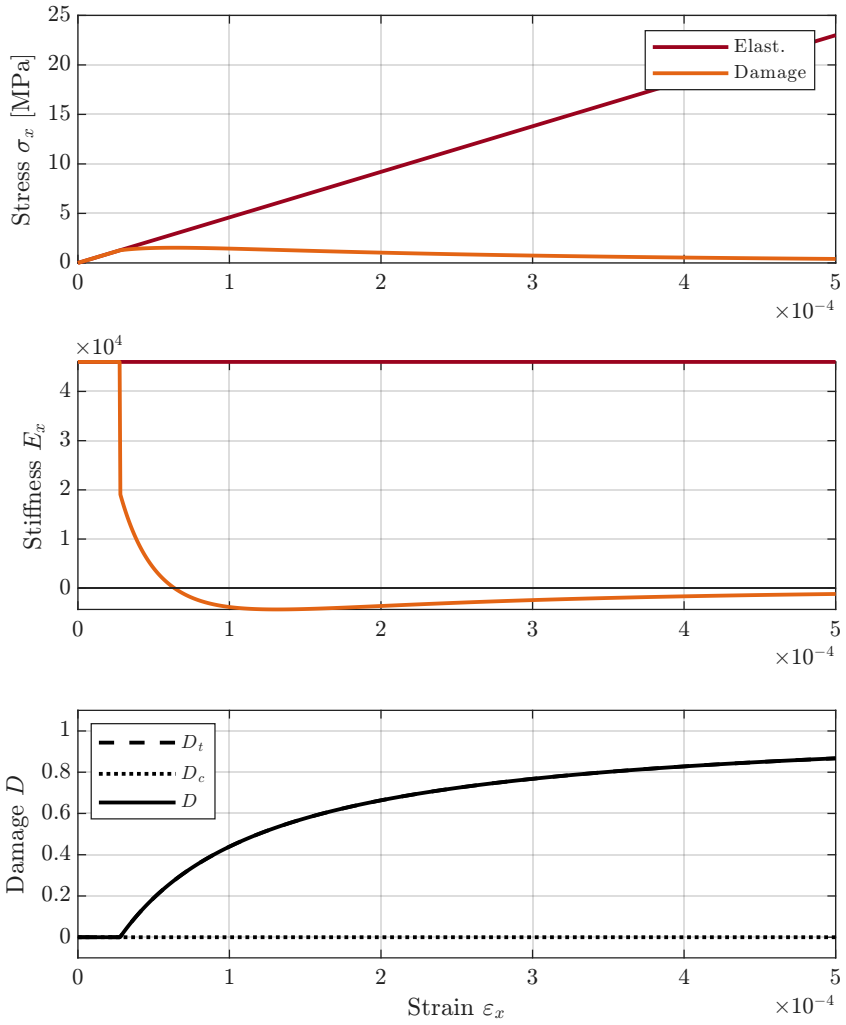

Figure 3.7. strain-stress, stiffness, and damage evolutions under tension loading.

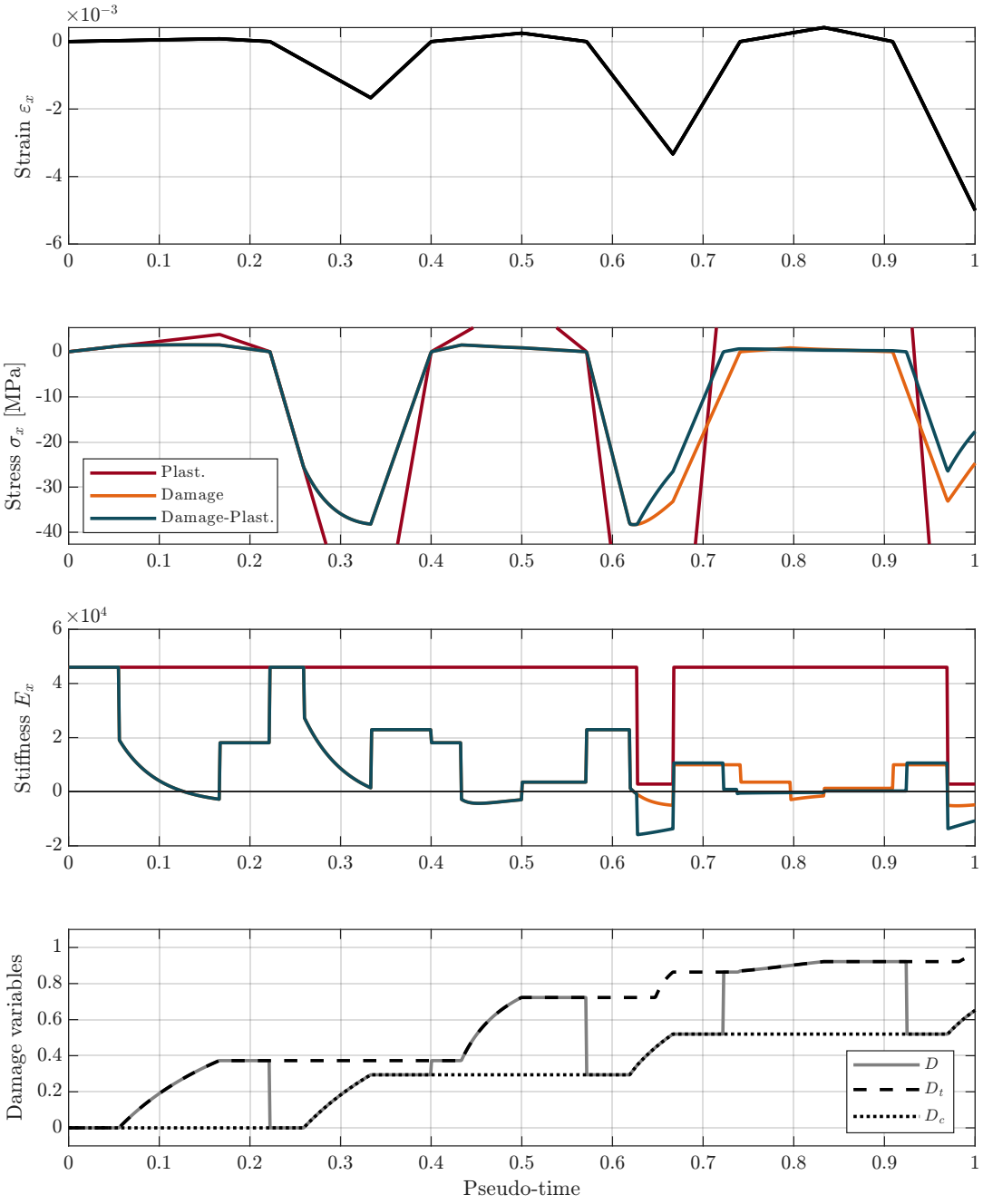

Figure 3.8. strain-stress, stiffness, and damage evolutions under cyclic loading.

3.4 1D Damage and Plasticity Models

3.4.1 Menegotto-Pinto Model for steel

The uniaxial constitutive law proposed by Menegotto and Pinto [3] is widely adopted to reproduce the cyclic response of reinforcing steel in fiber-based finite element formulations. The model is based on a smooth transition between two linear asymptotes: the initial elastic one, with stiffness E, and the post-yielding one, with reduced stiffness bE, where b is the strain-hardening ratio. The transition is governed by a curvature parameter R, which controls the sharpness of the curve and evolves during load reversals, thus reproducing the Bauschinger effect. This makes the model particularly effective in capturing the cyclic degradation and the kinematic hardening typically observed in reinforcing steel.

In normalized form, the strain-stress relation is expressed as:

$$\sigma^* = b\,\varepsilon^* + (1-b)\,\frac{\varepsilon^*}{\left(1+|\varepsilon^*|^R\right)^{1/R}} \tag{3.60}$$

where σ^* and ε^* denote the normalized stress and strain, defined with respect to the last reversal point and the updated yield surface. The model thus provides a continuous transition between the elastic and the plastic branches, ensuring numerical stability and robustness in nonlinear structural analyses. An example is shown in Figure 3.9. The strain and stress pairs $(\varepsilon_r, \sigma_r)$ and $(\varepsilon_0, \sigma_0)$ are updated after each strain reversal.

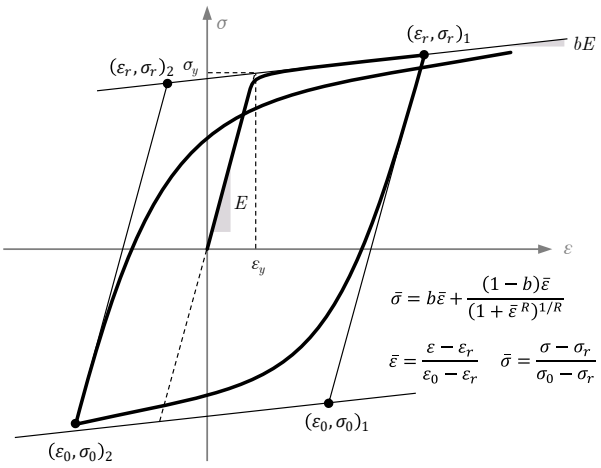

Figure 3.9. Menegotto and Pinto uniaxial plastic constitutive law [3].

A subsequent extension by Filippou et al. (1983) introduced isotropic hardening in addition to the original kinematic formulation, improving the description of reloading paths after partial unloading [117]. For these reasons, the Menegotto-Pinto model (and its variants) remains a reference constitutive law for reinforcing steel in the context of nonlinear beam-column finite element simulations.

3.4.2 Elastic-fragile Model

The model incorporates J2 plasticity with a linear isotropic hardening, along with an exponential damage evolution law for softening, making it suitable for simulating materials subjected to

severe loading. The constitutive framework is based on the additive decomposition of the total strain into elastic and plastic components:

$$\varepsilon = \varepsilon^e + \varepsilon^p \tag{3.61}$$

where ε^e and ε^p denote the elastic and plastic strain components, respectively. The plastic response is governed by the J2 yield criterion:

$$f(\sigma, \alpha) = |\sigma| - \sigma_y(\alpha) \leq 0 \tag{3.62}$$

where σ is the stress and $\sigma_y(\alpha)$ is the yield stress that evolves with the accumulated plastic strain α through linear isotropic hardening:

$$\sigma_y(\alpha) = \sigma_y + H_i\alpha \tag{3.63}$$

where σ_y is the initial yield stress and H_i is the isotropic hardening modulus.
The accumulated plastic strain evolves as:

$$\dot{\alpha} = |\dot{\varepsilon}^p| \tag{3.64}$$

The damage evolution activates when the strain magnitude exceeds a threshold value ε_u:

$$D = 1 - e^{-a(|\varepsilon| - \varepsilon_u)^b}, \quad \text{if } |\varepsilon| > \varepsilon_u \tag{3.65}$$

where D is the damage variable (ranging from 0 to 1), a controls the damage evolution rate, and b is the damage evolution exponent.
The effective stress accounting for damage is:

$$\sigma_{eff} = \frac{\sigma}{1 - D} \tag{3.66}$$

The constitutive model is characterized by the following parameters:

- E: Initial elastic modulus
- σ_y: Initial yield stress
- H_i: Isotropic hardening modulus
- ε_u: Damage threshold strain
- a: Damage evolution parameter
- b: Damage evolution exponent

This formulation provides a simple yet effective framework for modeling the coupled effects of plasticity and damage, enabling simulation of material behavior including plastic hardening, progressive failure, and post-peak softening.

3.4.3 Bond-slip Model

The bond-slip constitutive law used in the numerical applications is based on Lowes et al [4]. The model captures pinching effects that simulate the opening and closing of cracks in cyclic loading, along with three damage parameters that simulate cyclic strength and stiffness degradation.

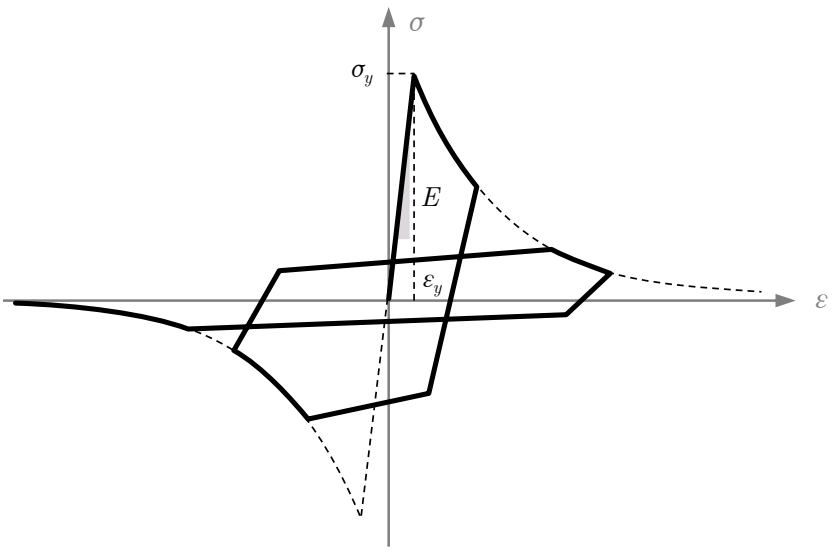

Figure 3.10. strain-stress response of the damage-plasticity model showing elastic behavior and damage-induced softening.

A backbone curve is defined by four control points in both positive and negative directions.
Positive envelope:

$$(\varepsilon_{1p}, \sigma_{1p}), (\varepsilon_{2p}, \sigma_{2p}), (\varepsilon_{3p}, \sigma_{3p}), (\varepsilon_{4p}, \sigma_{4p}) \tag{3.67}$$

Negative envelope:

$$(\varepsilon_{1n}, \sigma_{1n}), (\varepsilon_{2n}, \sigma_{2n}), (\varepsilon_{3n}, \sigma_{3n}), (\varepsilon_{4n}, \sigma_{4n}) \tag{3.68}$$

The stress along the envelope is computed through linear interpolation between adjacent points:

$$\sigma = \sigma_i + \frac{\sigma_{i+1} - \sigma_i}{\varepsilon_{i+1} - \varepsilon_i}(\varepsilon - \varepsilon_i) \tag{3.69}$$

The pinching behavior is controlled by three parameters:

- r_{disp}: displacement ratio for pinching
- r_{force}: force ratio for pinching
- u_{force}: ultimate force ratio

These parameters define the unloading and reloading paths that create the characteristic "pinched" hysteretic loops.
The model incorporates three types of degradation:
Stiffness Degradation:

$$\gamma_K = \gamma_{K1} \left(\frac{u_{max}}{u_{ult}} \right)^{\gamma_{K3}} + \gamma_{K2} \left(\frac{E_{dis}}{E_{cap}} \right)^{\gamma_{K4}} \tag{3.70}$$

Strength Degradation:

$$\gamma_F = \gamma_{F1} \left(\frac{u_{max}}{u_{ult}} \right)^{\gamma_{F3}} + \gamma_{F2} \left(\frac{E_{dis}}{E_{cap}} \right)^{\gamma_{F4}} \tag{3.71}$$

Displacement Degradation:

$$\gamma_D = \gamma_{D1} \left(\frac{u_{max}}{u_{ult}} \right)^{\gamma_{D3}} + \gamma_{D2} \left(\frac{E_{dis}}{E_{cap}} \right)^{\gamma_{D4}} \tag{3.72}$$

where:

- u_{max} is the maximum displacement demand
- u_{ult} is the ultimate displacement capacity
- E_{dis} is the cumulative dissipated energy
- E_{cap} is the energy capacity

The model operates in five distinct states:

- State 0: Initial elastic behavior
- State 1: Loading along positive envelope
- State 2: Loading along negative envelope
- State 3: Unloading from positive to negative
- State 4: Unloading from negative to positive

The degraded material properties are updated as:

$$K_{deg} = K_{init}(1 - \gamma_K) \tag{3.73}$$

$$\sigma_{deg} = \sigma_{env}(1 - \gamma_F) \tag{3.74}$$

$$\varepsilon_{deg} = \varepsilon_{env}(1 + \gamma_D) \tag{3.75}$$

The energy dissipation is computed incrementally:

$$\Delta E = \frac{1}{2}(\sigma_n + \sigma_{n+1})\Delta\varepsilon \tag{3.76}$$

The elastic strain energy is:

$$E_{elastic} = \frac{\sigma^2}{2K_{deg}} \tag{3.77}$$

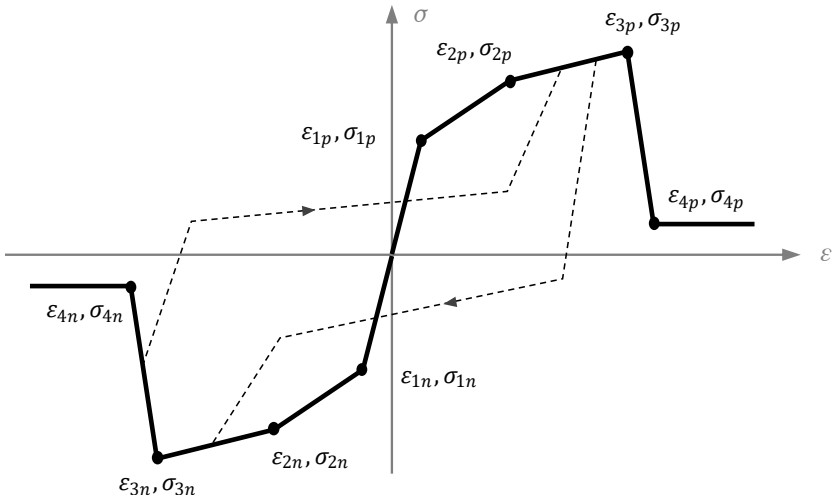

Figure 3.11. Typical strain-stress response of the constitutive model by [4].

This model provides a comprehensive framework for simulating progressive degradation and pinching effects. In practical applications, it is also frequently adopted to represent bond-slip mechanisms. An example is shown in Figure 3.11.

Chapter 4

Computational aspects

4.1 Interpolation functions

4.1.1 Discussion on interpolation function choice

The generalized section stresses in $\mathbf{s}(x)$ are computed by means of $\mathbf{b}(x)$ which imposes exact equilibrium. The bond-related fields $\mathbf{s}_b(x)$ and $\mathbf{p}_b(x)$ are interpolated using $\mathbf{b}_b(x)$ and $\mathbf{b}_{b,x}(x)$, respectively. In the linear elastic case, exact equilibrium may be achieved depending on the number of interpolation nodes and functions. In this paper, either piecewise linear interpolations or not-a-knot cubic splines are used: the not-a-knot condition imposes continuity of the third derivative at the first and last internal nodes, effectively treating the first two and last two intervals as single cubic segments, and avoiding arbitrary boundary constraints. An example of a linear piecewise interpolation is shown in Figure 4.1.

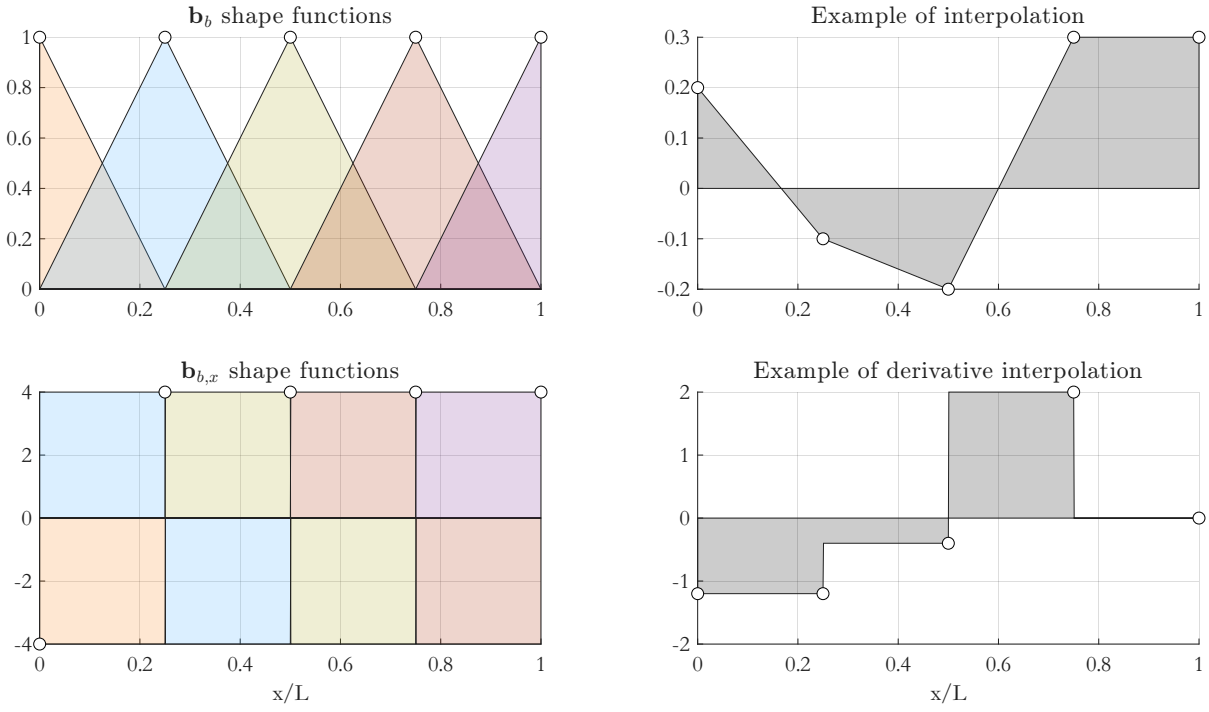

Figure 4.1. Linear piece-wise interpolations.

The order of the Lagrange interpolation depends on the number of points used, i.e., if four

points are used, four interpolation coefficients are defined so that the interpolating expression is cubic, that is $a + bx + cx^2 + dx^3$. In Figure 4.2, five evenly distributed points are used for identification, leading to a smooth interpolation. In Figure 4.3, ten evenly distributed points are used for identification, leading to a rather unstable interpolation, especially at the ends. A similar behavior is observed for the derivative interpolation.

This is widely known as Runge's phenomenon, which is a problem of oscillation at the edges of an interval that occurs when using interpolation with polynomials of high degree over a set of equispaced interpolation points. This leads to ill-conditioned matrices and may cause numerical issues when many quadrature cross-sections are placed along the element length, as shown in Di Re and Sanchez [118]. In Figure 4.4, ten points are used, but instead of being evenly distributed, a Gauss-Lobatto distribution is adopted. This reduces the oscillations, but the function order remains high, making it impractical as it constrains the choice of quadrature points, which must be sufficiently high for integrability.

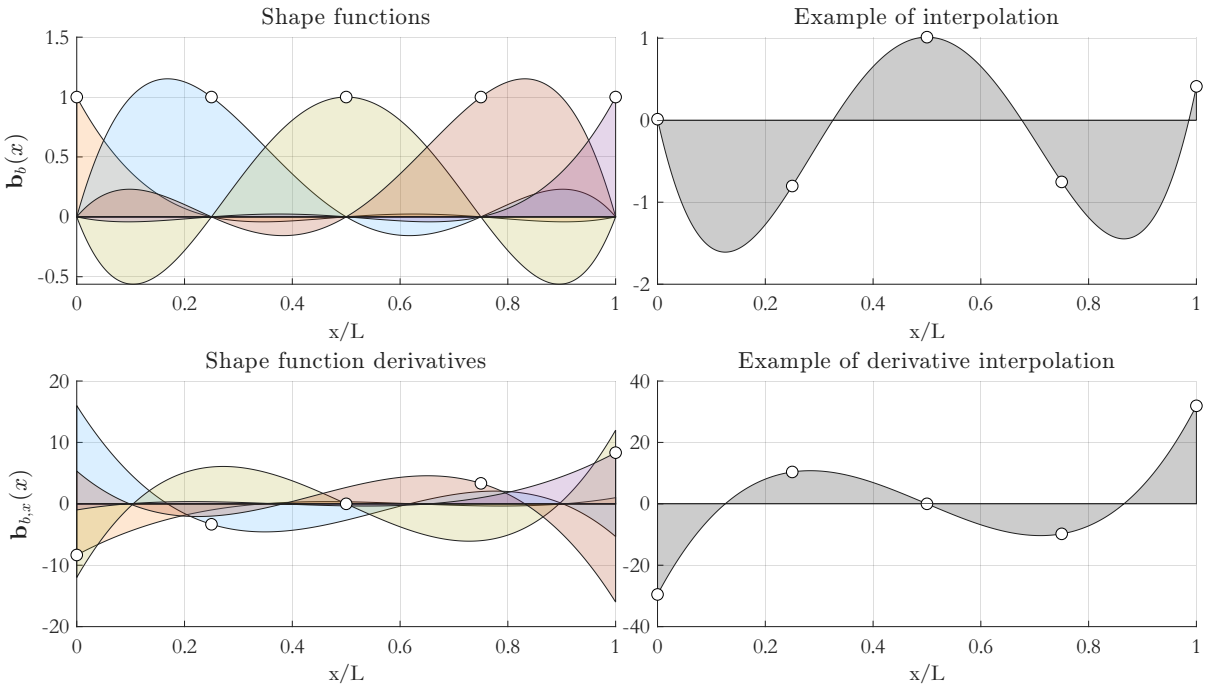

Figure 4.2. Lagrange interpolations on five evenly distributed points.

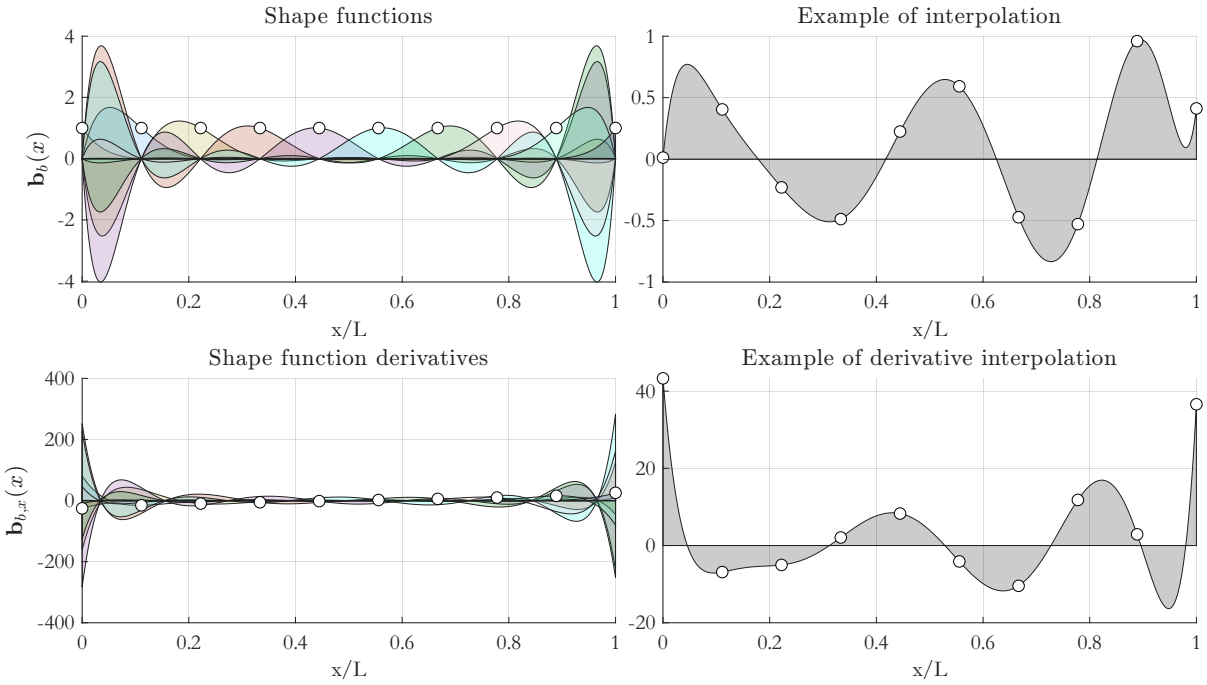

Figure 4.3. Lagrange interpolations on ten evenly distributed points.

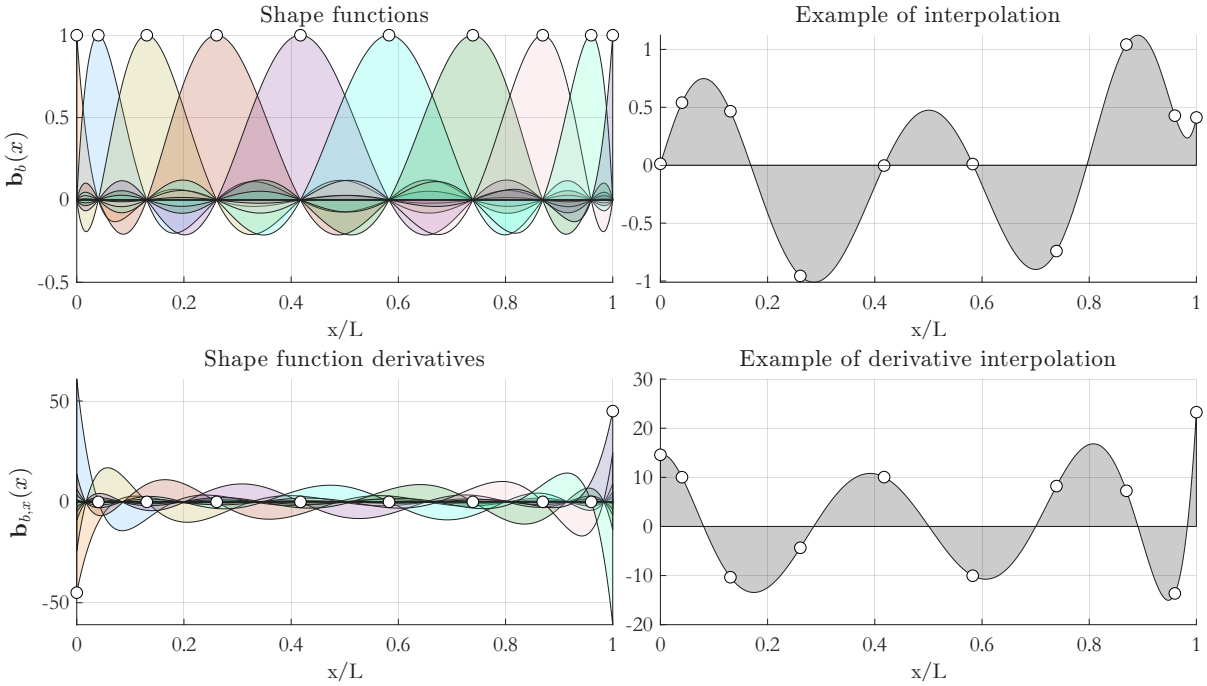

Figure 4.4. Lagrange interpolations on ten points using a Gauss-Lobatto distribution.

Figures 4.5-4.7 show the same interpolations obtained using cubic not-a-knot splines. This interpolation is advantageous for two main reasons: the interpolation order never exceeds three, so that even a small number of quadrature points allows exact integration, and no remarkable oscillations are observed [119]
These functions ensure a good compromise between interpolation accuracy and maximum integration order. The choice of the number of quadrature points, n for the fiber sections, and n_b for the bond sections, depends on the number of interpolation nodes, which is always m for both sections, as fiber sections depend on $\mathbf{s}_b$ and bond sections depend on $\mathbf{p}_b(x) = \mathbf{s}_b'(x)$, which is its derivative with respect to x.

Once the order of the interpolation function and the number of interpolation points m has been

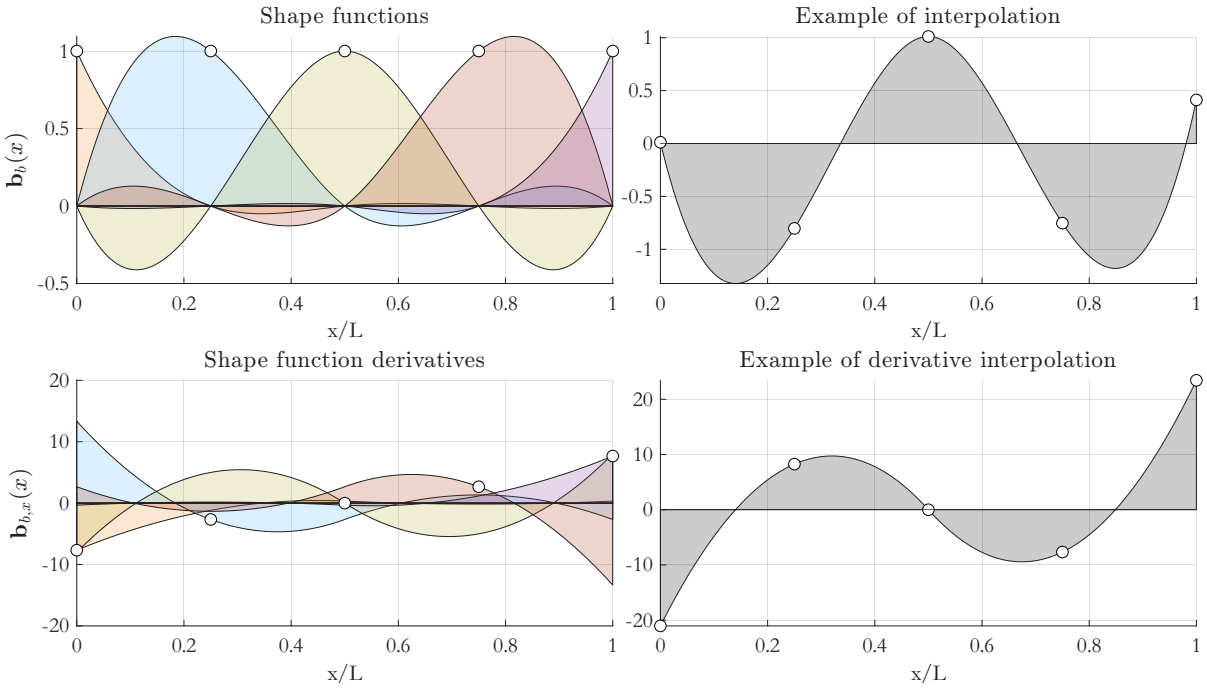

Figure 4.5. Cubic spline interpolations on 5 evenly distributed points.

selected, the number of the integration points is set so to obtain up to the maximum integration order h according to the specific quadrature rule, i.e. $h = 2n - 1$ for Legendre distributions, $h = 2n - 2$ for Radau distributions, $h = 2n - 3$ for Lobatto distributions.
The minimum integration order requirement is given by the integration of the flexibility matrix, Eqs. (2.166) in the model with bond-slip, and (2.272) in the model with warping and bond-slip, that for the fiber section reads:

$$\tilde{\mathbf{f}} = \int_L \tilde{\mathbf{b}}^T \, \tilde{\mathbf{f}}_s \, \tilde{\mathbf{b}} \, dx, \quad \tilde{\mathbf{b}} = \begin{bmatrix} \mathbf{b} & \mathbf{0} \\ \mathbf{0} & \mathbf{b}_b \end{bmatrix}$$

where $\tilde{\mathbf{f}}_s(x)$ is made of constants, $\mathbf{b}(x)$ is up to order 1, $\mathbf{b}_b$ is up to order 3 for cubic splines, and up to order $(m-1)$ for polynomials. Since the integrand is $\tilde{\mathbf{b}}$ multiplied twice, the minimum integration order is $h_{min} = 6$ for cubic splines and $h_{min} = 2(m-1)$ for polynomials. By enforcing $h > h_{min}$, the minimum number of integration points m required can be computed.

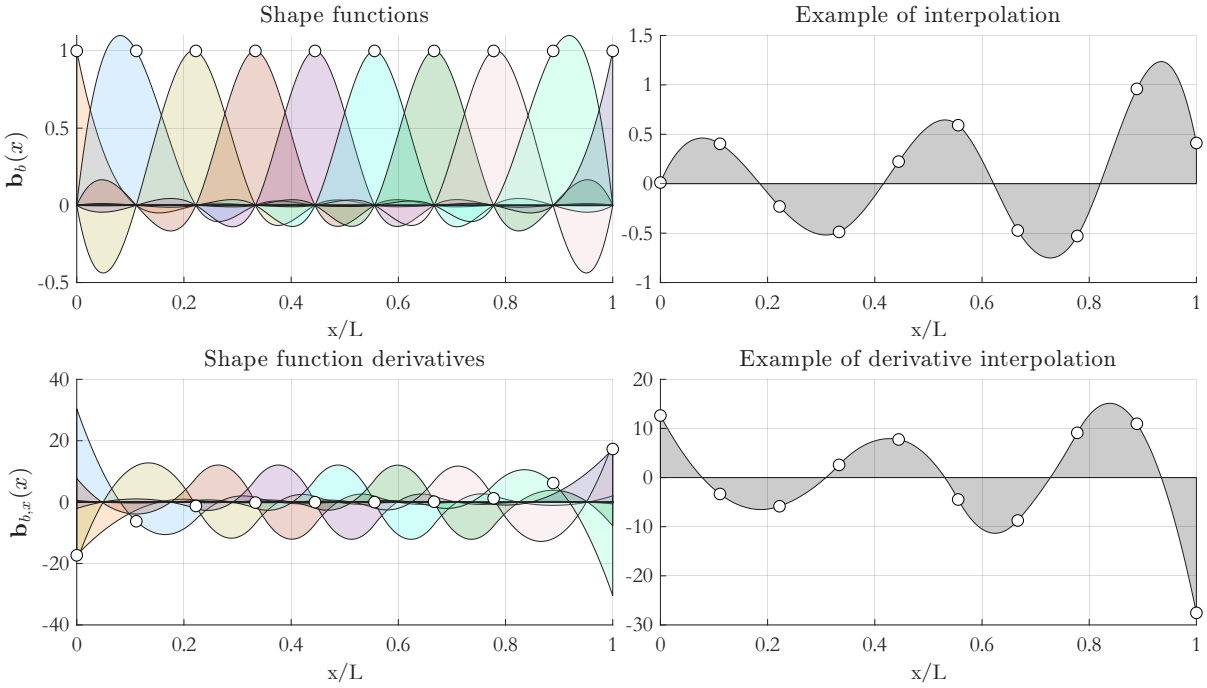

Figure 4.6. Cubic spline interpolations on 10 evenly distributed points.

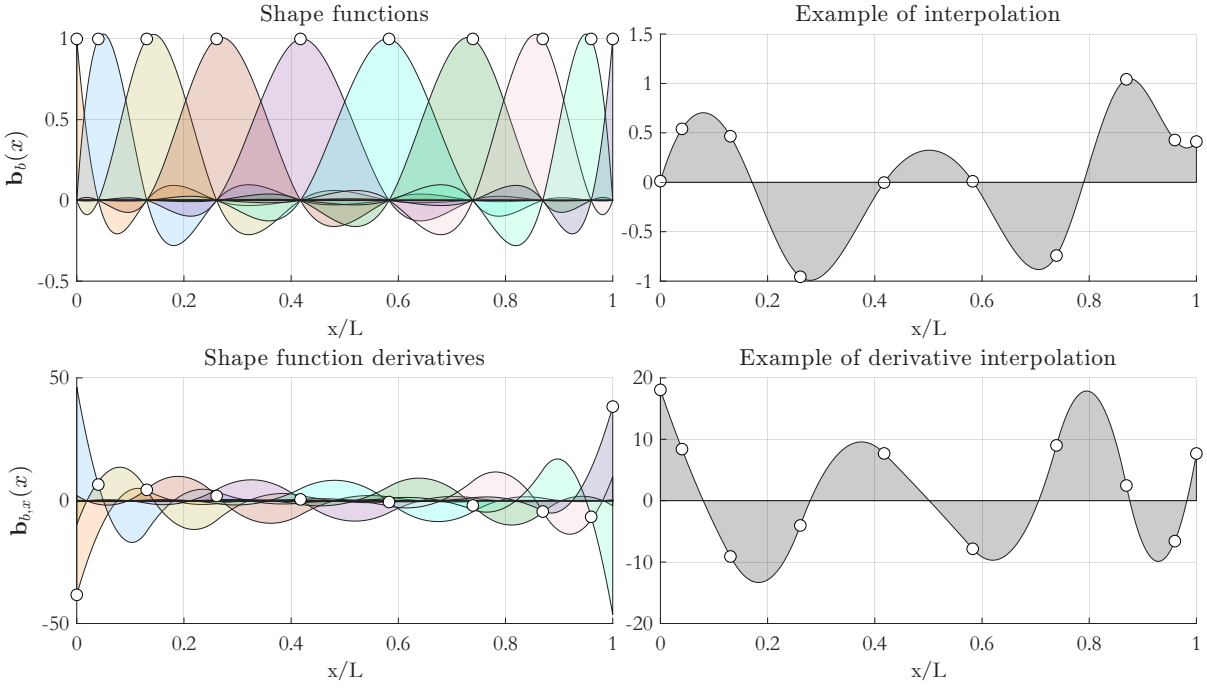

Figure 4.7. Cubic spline interpolations on 10 points using a Gauss-Lobatto distribution.

4.1.2 Interpolation function matrices assembly

Although the model allows the choice of different interpolation functions, cubic splines are always preferred in this thesis according to Figures 4.5-4.7. They are used both for bond-slip DOFs and warping DOFs interpolation, as long as they satisfy Eq. (2.153) and Eq. (2.252), respectively:

$$\begin{aligned}
\mathbf{s}_b(x) &= \mathbf{b}_b(x)\mathbf{q} \\
\frac{\partial \mathbf{s}_b(x)}{\partial x} &= \mathbf{p}_b(x) = \mathbf{b}_{b,x}(x)\mathbf{q} \\
\boldsymbol{\eta}(x) &= \mathbf{B}_w(x)\mathbf{v}_w \\
\frac{\partial \boldsymbol{\eta}_x(x)}{\partial x} &= \boldsymbol{\eta}_x(x) = \mathbf{B}_{w,x}(x)\mathbf{v}_w
\end{aligned}$$

The shape function matrices are assembled in the element initialization process and are unchanged throughout the analysis. The following procedure is followed:

1. choice of interpolation points number (m_b and m_w for bond-slip and warping, respectively) and distribution along the axis (evenly distributed, Lobatto, others);
2. computation of their positions ($x_{b,1}\ \ x_{b,2}\ \ \cdots x_{b,m_b}$ and $x_{w,1}\ \ x_{w,2}\ \ \cdots x_{w,m_w}$ for bond-slip and warping, respectively)
3. evaluation of every contribution:

$$\begin{aligned}
\mathbf{b}_{b,f}(x) &= \begin{Bmatrix} b_{b,1}(x) & b_{b,2}(x) & \cdots & b_{b,m_b}(x) \end{Bmatrix} \\
\mathbf{b}_{b,x,f}(x) &= \begin{Bmatrix} b_{b,x,1}(x) & b_{b,x,2}(x) & \cdots & b_{b,x,m_b}(x) \end{Bmatrix} \\
\mathbf{B}_{w,i}(x) &= \begin{Bmatrix} B_{w,1}(x) & B_{w,2}(x) & \cdots & B_{w,m_w}(x) \end{Bmatrix} \\
\mathbf{B}_{w,x,i}(x) &= \begin{Bmatrix} B_{w,x,1}(x) & B_{w,x,2}(x) & \cdots & B_{w,x,m_w}(x) \end{Bmatrix}
\end{aligned}$$

   for $b = 1, 2, \ldots, n_f$ and $i = 1, 2, \ldots, n_w$

4. assemble:

$$\mathbf{b}_b(x) = \begin{bmatrix} \mathbf{b}_{b,1} & \mathbf{0} & \cdots & \mathbf{0} \\ \mathbf{0} & \mathbf{b}_{b,2} & \cdots & \mathbf{0} \\ \vdots & \vdots & \ddots & \mathbf{0} \\ \mathbf{0} & \mathbf{0} & \mathbf{0} & \mathbf{b}_{b,n_f} \end{bmatrix} \qquad \mathbf{B}_w(x) = \begin{bmatrix} \mathbf{B}_{w,1} & \mathbf{0} & \cdots & \mathbf{0} \\ \mathbf{0} & \mathbf{B}_{w,2} & \cdots & \mathbf{0} \\ \vdots & \vdots & \ddots & \mathbf{0} \\ \mathbf{0} & \mathbf{0} & \mathbf{0} & \mathbf{B}_{w,n_w} \end{bmatrix}$$

$$\mathbf{b}_{b,x}(x) = \begin{bmatrix} \mathbf{b}_{b,x,1} & \mathbf{0} & \cdots & \mathbf{0} \\ \mathbf{0} & \mathbf{b}_{b,x,2} & \cdots & \mathbf{0} \\ \vdots & \vdots & \ddots & \mathbf{0} \\ \mathbf{0} & \mathbf{0} & \mathbf{0} & \mathbf{b}_{b,x,n_f} \end{bmatrix} \qquad \mathbf{B}_{w,x}(x) = \begin{bmatrix} \mathbf{B}_{w,x,1} & \mathbf{0} & \cdots & \mathbf{0} \\ \mathbf{0} & \mathbf{B}_{w,x,2} & \cdots & \mathbf{0} \\ \vdots & \vdots & \ddots & \mathbf{0} \\ \mathbf{0} & \mathbf{0} & \mathbf{0} & \mathbf{B}_{w,x,n_w} \end{bmatrix}$$

The bond-slip interpolation functions $\mathbf{b}_b(x)$ and $\mathbf{b}_{b,x}(x)$ result in n_f rows and $m_f \cdot n_f$ columns. This way, every axial force $N_f(x)$ is interpolated on the f^{th} fiber at all m_f interpolation points. The same applies to every warping variable.

The warping interpolation functions $\mathbf{B}_w(x)$ and $\mathbf{B}_{w,x}(x)$ result in n_w rows and $m_w \cdot n_w$ columns. This way, every section warping DOF $\eta_i(x)$ is interpolated on the i^{th} slot at all m_w interpolation points.

4.2 Non-orthogonal and prestressed components

Prestressed members are characterized by the presence of tendons or cables, which can be either straight or follow a draped trajectory along the element. In structural design, these tendons may be internal and bonded to the surrounding structure, or external and post-tensioned, and their geometry strongly influences the stress distribution within the beam.
From a computational perspective, the introduction of prestressing requires the fiber section model to accommodate components that are not necessarily aligned with the principal axes of the section. This means that tendons cannot be treated as conventional straight fibers, but must be described by their actual position and orientation along the member axis.
The following subsections illustrate how this aspect is handled in the present formulation, starting from the representation of non-orthogonal fibers within the section and proceeding to the numerical treatment of draped tendon profiles.

4.2.1 Section response with non-orthogonal components

The tendons work as a fiber in the section model, therefore, to define its profile, it is sufficient to know the tendon's positions $y_f(x), z_f(x)$ at the quadrature points. An example is shown in Figure 4.8.

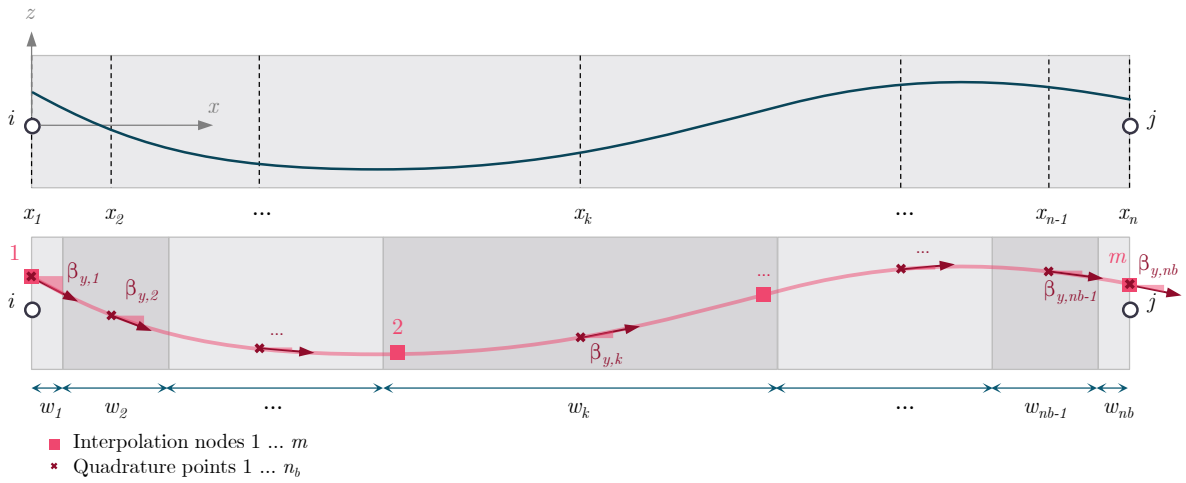

Figure 4.8. Numerical model of a prestressed beam with a draped tendon with $n = 7$ quadrature points.

The effect of tendons or cables along the element can be considered by introducing a rotation matrix to correctly reproduce the interaction between the section and the rotated steel components. The tendons' position along the beam axis is usually given in some reference sections depending on the construction drawings, so preprocessing is needed to construct the numerical input model.

This can be done for bonded cables as shown in [72] but computing the tendons' slopes β and ψ can be cumbersome for users. An alternate method is proposed here following an isoparametric

approach, where the same shape functions used to expand the tendon's bond-slip fields are used to compute the tendons' position and rotation along x. This is done by considering the physical projections of the tendon's directional vectors v_y over yz plane and v_z over xz plane. β_y is the angle between v_y and x axis, β_z is the angle between v_z and x axis, as shown in Figure 4.9.

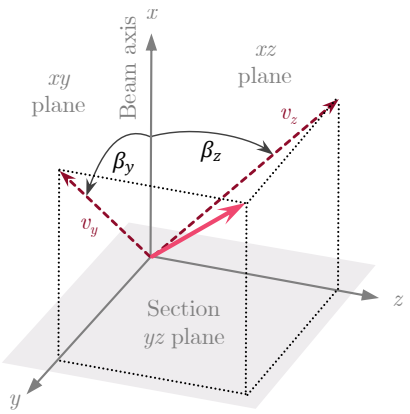

Figure 4.9. Tendon's angles and initial strain direction with respect to the section's axes.

Tipically, the tendons' profiles are known in a finite number of points. Their coordinates are expressed in a matrix such as:

$$\mathbf{P}_f = \begin{bmatrix} x_1 & x_2 & \cdots & x_r & \cdots & x_{n_r} \\ y_1 & y_2 & \cdots & y_r & \cdots & y_{n_r} \\ z_1 & z_2 & \cdots & z_r & \cdots & z_{n_r} \end{bmatrix}_f = \begin{bmatrix} \mathbf{P}_x \\ \mathbf{P}_y \\ \mathbf{P}_z \end{bmatrix}_f \tag{4.1}$$

where the subscript f indicates the tendon number (with $f = 1, 2 \cdots n_f$), x_r, y_r, z_r are the coordinates of a generic known point $r = 1, 2 \cdots n_r$ along the tendon, n_r is the number of input points.

To compute the compatibility matrix of the section, the positions y, z and the angles β_y, β_z must be calculated at the quadrature points $\mathbf{x}_g$ and the bond-slip field interpolation points $\mathbf{x}_b$, which generally differ from $\mathbf{P}_x$.

The matrices $\mathbf{b}_b$ and $\mathbf{b}_{b,x}$ shown in Section 4.1.1 can be used for such purpose. The coordinates are:

$$\begin{bmatrix} y(x) \\ z(x) \end{bmatrix}_f = \begin{bmatrix} \mathbf{b}_b(x) & 0 \\ 0 & \mathbf{b}_b(x) \end{bmatrix}_f \begin{bmatrix} \mathbf{P}_y \\ \mathbf{P}_z \end{bmatrix}_f \tag{4.2}$$

While the tendons' slopes are taken as their derivatives:

$$\begin{bmatrix} \beta_y(x) \\ \beta_z(x) \end{bmatrix}_f = \begin{bmatrix} \mathbf{b}_{b,x}(x) & 0 \\ 0 & \mathbf{b}_{b,x}(x) \end{bmatrix}_f \begin{bmatrix} \mathbf{P}_y \\ \mathbf{P}_z \end{bmatrix}_f \tag{4.3}$$

The angles are computed only at the beginning of the analysis and are kept unchanged. Given these angles, a projection allows to go from the rigid section's set of forces to the tendon's axial reference and viceversa. Figure 4.10 shows how the tendon force $N_b(x)$ of the f^{th} fiber with bond-slip interacts with the rest of the section.

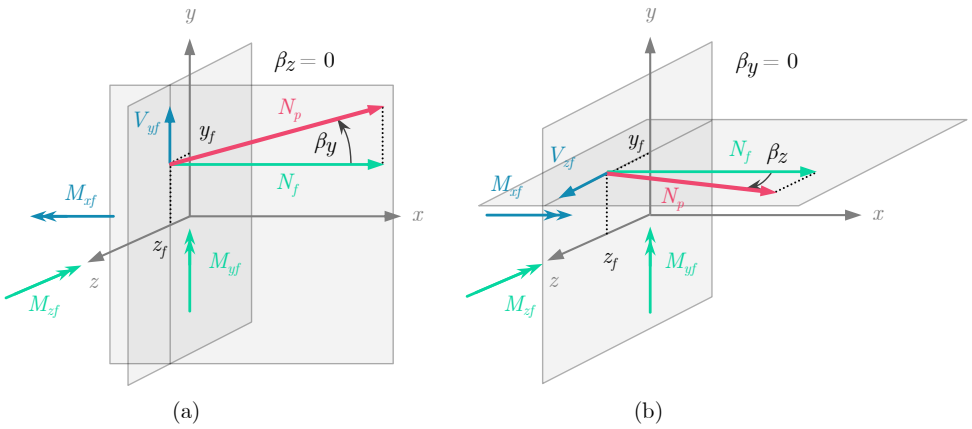

Figure 4.10. Section generalized stresses (denoted with f subscript) induced by the tendon fiber's axial force N_b when: (a) $\beta_y \neq 0$ only, and (b) $\beta_z \neq 0$ only.

4.2.2 Tendon fiber rotation matrix

An optimal choice in this framework is to actually project the rigid section's strains onto the tendon when computing its axial fiber deformation. To do so, a rotation matrix $\mathbf{R}$ can be defined using Rodrigues' rotation formula [120]:

$$\mathbf{R} = \mathbf{I}\cos\beta + \widehat{\boldsymbol{\beta}}\sin\beta + \boldsymbol{\beta}\otimes\boldsymbol{\beta}(1-\cos\beta) \tag{4.4}$$

where $\mathbf{I}$ is the identity matrix, $\boldsymbol{\beta}$ is the unit vector defining the axis of rotation, $\widehat{\boldsymbol{\beta}}$ is its skew-symmetric matrix, and β is the angle between the tendon tangent and the global x-axis. The angle can be computed as:

$$\beta = \tan^{-1}\left\|\bar{\boldsymbol{\beta}}\right\| \tag{4.5}$$

where $\bar{\boldsymbol{\beta}}$ is the rotation axis vector, defined by:

$$\bar{\boldsymbol{\beta}} = \begin{bmatrix}\beta_x & \beta_y & \beta_z\end{bmatrix}^T \tag{4.6}$$

where $\beta_x = 0$. The normalized axis is:

$$\boldsymbol{\beta} = \frac{\bar{\boldsymbol{\beta}}}{\left\|\bar{\boldsymbol{\beta}}\right\|} \tag{4.7}$$

Its associated skew-symmetric matrix is:

$$\widehat{\boldsymbol{\beta}} = \begin{bmatrix}0 & -\beta_z & \beta_y \\ \beta_z & 0 & -\beta_x \\ -\beta_y & \beta_x & 0\end{bmatrix} \tag{4.8}$$

and the dyadic product is:

$$\boldsymbol{\beta}\otimes\boldsymbol{\beta} = \boldsymbol{\beta}\boldsymbol{\beta}^T = \begin{bmatrix}\beta_x^2 & \beta_x\beta_y & \beta_x\beta_z \\ \beta_y\beta_x & \beta_y^2 & \beta_y\beta_z \\ \beta_z\beta_x & \beta_z\beta_y & \beta_z^2\end{bmatrix} \tag{4.9}$$

This rotation matrix enables the transformation from the global beam coordinate system to the local tendon axis system, as illustrated in Figure 4.11. Similar steps can be followed to write

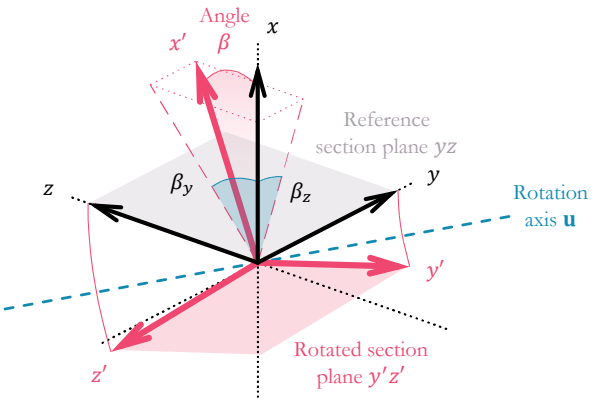

Figure 4.11. Change of reference system from the beam's local system xyz (grey) to the tendon's one $x'y'z'$ (red) by means of the two rotations around axes y and z.

the section kinematics in order to obtain the same expression as Eq. 2.117, where bond-slip and initial strains can be added as these are tangent to the tendon in x.

The tendon profile's accuracy is exact when a sufficient amount and distribution of quadrature points are used, such as using Lobatto as demonstrated in [72] for a draped tendon.

4.3 Local regularization techniques

In nonlinear finite element analyses of reinforced and prestressed concrete members, strain-softening phenomena arising from cracking and crushing lead to localization of strains. Since the materials under investigation are brittle and exhibit post-peak degradation, regularization is required to restore objectivity with respect to the discretization [17, 16, 5]. In this work, two local regularization strategies are adopted and applied in parallel to the beam finite element formulations: the first is based on modified integration rules, while the second relies on fracture energy concept. Both approaches are briefly reviewed in the following sections, as they are necessary to ensure mesh-independent responses in the applications presented throughout the thesis.

4.3.1 Integration-rule based regularization

The Gauss integration rule is commonly used in FE formulations. However, in frame elements undergoing special loading conditions where usually the section stresses attain their maximum values at the element ends, the Gauss-Lobatto rule is preferred in order to directly control the element end sections. In addition, since cementitious composite structures generally exhibit a softening behavior, localization of strains and damage may arise, a well-known issue in nonlinear finite element analyses. In the context of force-based frame elements, this problem was first highlighted by Coleman and Spacone [16], and it was demonstrated that the localization region is dependent on the Gauss point's weight [5]. This can lead to non objective numerical results and strongly dependent on the selected integration rule. To overcome this numerical pathology and obtain objective results, the modified integration rule proposed in [5] and [6], is here introduced.

According to [5], the element is divided into three regions, where the two end regions can have 2 or 3 Gauss-Lobatto integration points and lengths L_c/w_1 where L_c is the characteristic length and w_1 is the first Gauss point's weight. The order of accuracy is $2n-3$, for each region, being n the number of points per region.

Following [6], a Gauss-Lobatto distribution is used for the whole element but two more points are added within the expected localization region. Their weights are $w_1(L-L_c)$, so that L_c can be unlimited, and the Lobatto distribution is restored in the rest of the beam. The order of accuracy however reduces to $n-3$.

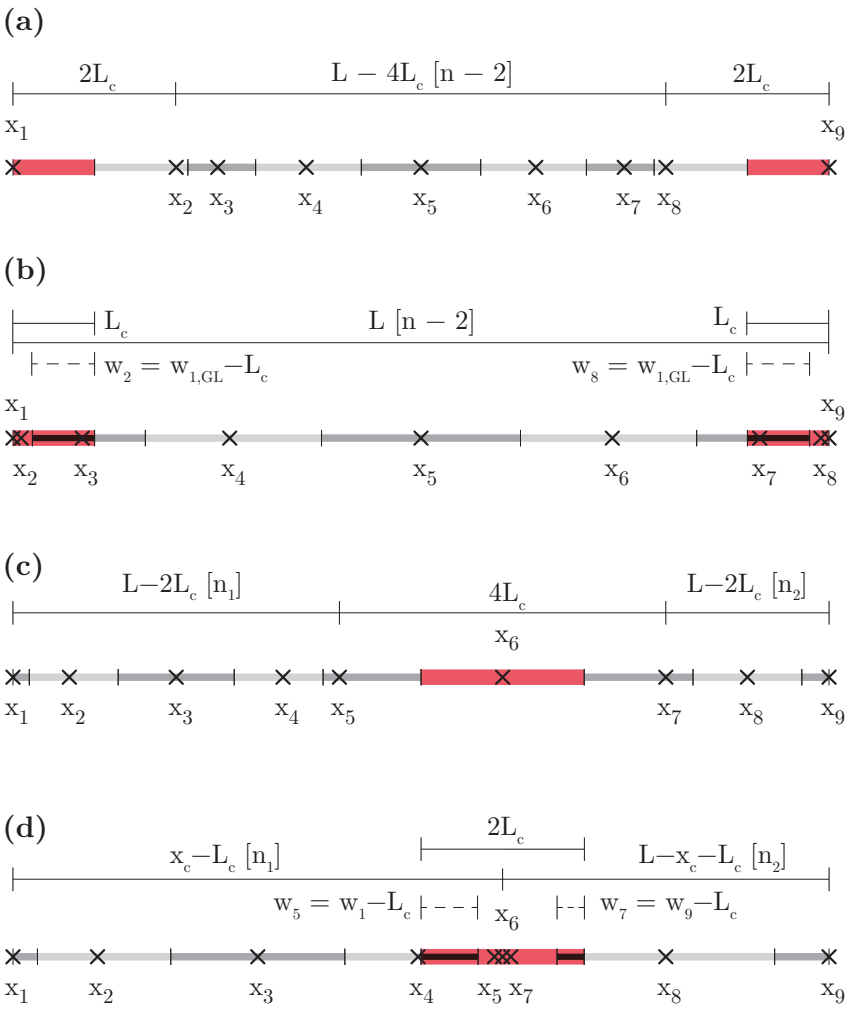

Figure 4.12. 9-point Gauss-Lobatto regularized integration schemes proposed by: (a) Addessi and Ciampi [5]; (b) Scott and Hamutçuoğlu [6]. Proposed extended distributions for: (c) scheme [5]; (d) scheme [6].

The key parameter is the characteristic length L_c, that governs the size of the localization region. This is usually taken as the plastic hinge length, and can be evaluated by adopting existing formulae, as described in Bazant et al [107], but also in Almeida et al [31] and Feng et al [121].

The two regularization techniques described above are schematically shown in Figure 4.12 (a) and (b). The methods become particularly efficient when using single and slender elements in seismic frames since the localization is typically expected to occur at the end sections. In this thesis, an extension is proposed to allow localization to occur at any integration point along

the beam. It still requires the analyst to choose beforehand the position where the damage can localize. If the localization point x_c is internal, it divides the beam in two regions and the other integration points are properly redistributed.
Some examples of the integration scheme arrangements are shown in Figure 4.12 (c) and (d), respectively.

Proposed local regularization technique

The procedure is here briefly described. Let L be the element length, L_c the characteristic length defining the regularized zone, and $x_c \in [0, L]$ the prescribed localization position. The element is discretized into n quadrature points, obtained by a modified Gauss-Lobatto rule.

The element is divided into three subdomains:

$$\Omega_1 = [0,\, x_c - L_c], \qquad \Omega_c = [x_c - L_c,\, x_c + L_c], \qquad \Omega_2 = [x_c + L_c,\, L]. \tag{4.10}$$

The central subdomain Ω_c has fixed length $2L_c$ and represents the localization region.
The choice of L_c is therefore critical, as it reflects the characteristic dimension of the fracture or process zone and depends on both material and geometric parameters. In conventional applications, L_c is often calibrated with respect to localized failures expected at member ends, however, if damage is anticipated to localize at different positions along the element, an alternative calibration of L_c may be introduced, provided that sufficient mechanical or experimental information is available to justify such choice.

In Ω_1 and Ω_2 a standard Gauss-Lobatto rule with n_1 and n_2 points is applied:

$$\{(\xi_i^{(1)}, w_i^{(1)})\}_{i=1}^{n_1} = \mathrm{GL}(0,\, x_c - L_c,\, n_1)\,, \qquad \{(\xi_j^{(2)}, w_j^{(2)})\}_{j=1}^{n_2} = \mathrm{GL}(x_c + L_c,\, L,\, n_2) \tag{4.11}$$

The central subdomain Ω_c is condensed into a single integration point located at x_c, with weight equal to the whole region length:

$$\xi_c = x_c, \qquad w_c = 2L_c \tag{4.12}$$

The modified integration scheme is finally given by

$$\{(\xi_i, w_i)\}_{i=1}^{n} = \{(\xi_i^{(1)}, w_i^{(1)})\}_{i=1}^{n_1} \cup \{(\xi_c, w_c)\} \cup \{(\xi_j^{(2)}, w_j^{(2)})\}_{j=1}^{n_2} \tag{4.13}$$

with $n = n_1 + n_2 + 1$. The values n_1 and n_2 are chosen such that the quadrature points are proportionally distributed with respect to the lengths $L_1 = x_c - L_c$ and $L_2 = L - x_c - L_c$, i.e.

$$\frac{n_1}{n_2} \approx \frac{L_1}{L_2} \tag{4.14}$$

- Two additional integration points adjacent to x_c can be added, so the Scott-Hamutçuoğlu rule is used instead. The weight of these points is set as $w_{n,GL} - L_c$, where $w_{n,GL}$ is the weight of the end point, and may even be negative;

- For $x_c = 0$, $x_c = L$ or both ends, the scheme reduces to the Addessi-Ciampi rule or Scott-Hamutçuoğlu (localization at the element ends);
- For arbitrary x_c the rule allows localization at any point of the element, generalizing either of the rules;
- The order of accuracy in the side regions remains that of the Gauss–Lobatto rule, while the localization zone at x_c is integrated exactly by condensing its length into a single point weighted $2L_c$.

Regularization technique validation

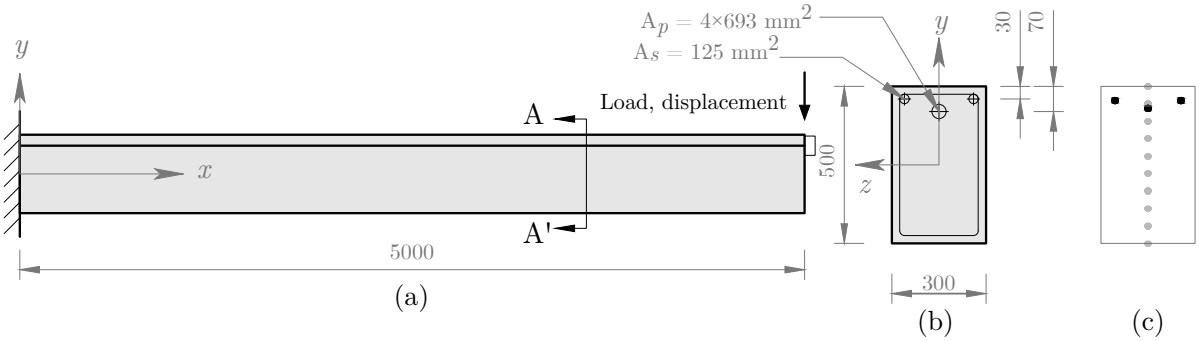

Figure 4.13. Geometry of the PC cantilever beam: (a) longitudinal view; (b) cross-section A-A'; (c) fibers' location.

A pushover test on a simple PC cantilever beam is carried out. This is a theoretical case for the validation of the proposed regularization technique. The prestressing cable area is large enough to apply a high compression force to the beam. Severe softening is expected due not only to section cracking, but also to compression in the concrete. The beam geometry is shown in Figure 4.13. The tendon is straight and its position in the cross-section is constant along the beam. Two different tests are carried out, the first one using the concrete 3D damage plastic model of Chapter 3 (3DDP) and the second one using the 1D model by Yassin [8] (1DD). The first test uses a Timoshenko beam formulation, the second one uses an Euler-Bernoulli formulation. Since the cantilever beam of Figure 4.13 is slender, the shear strains are negligible. The concrete compression and tension strengths are 38 MPa and 3 MPa, respectively.
The concrete and steel properties are reported in Table 4.1. The corresponding uni-axial tension and compression laws are shown in Figure 4.16b. There is no steel strain hardening. The prestressing is imposed by applying the initial strain $\varepsilon_0 = 0.005$, that corresponds to the stress $\sigma_0 = E_p\varepsilon_0 = 975$ MPa applied before the beam shortens.

Fiber	E [GPa]	ν	H_k [GPa]	H_i [GPa]	σ_t [MPa]	σ_c [MPa]	Y_{t0}	a_t	b_t	Y_{c0}	a_c	b_c	β
Concrete	30	0.2	21	0	3	60	$2.16 \cdot 10^{-4}$	0.9	10^{-4}	$7.20 \cdot 10^{-4}$	0.9	$3.25 \cdot 10^{-3}$	1
Steel	210	0.3	0	0	450	450	-	-	-	-	-	-	-
Tendon	195	0.3	0	0	1325	1325	-	-	-	-	-	-	-

Table 4.1. Elastic, plastic, and damage parameters for concrete, steel, and tendons. Damage parameters apply only to concrete.

The regularization is carried out by modifying the layout of the mesh as described in section

4.3.1, with the localization zone at $x_c = 0$ mm (the fixed end), and a characteristic length $L_c = 0.1L$. Figure 4.14 shows the structural response of the cantilever beam where the vertical reaction F is measured with respect to an imposed displacement v up to a value $v_f = 400$ mm. The number of integration points varies as indicated in the legend of Figure 4.14. Since there are only negligible differences, the element can be considered regularized.

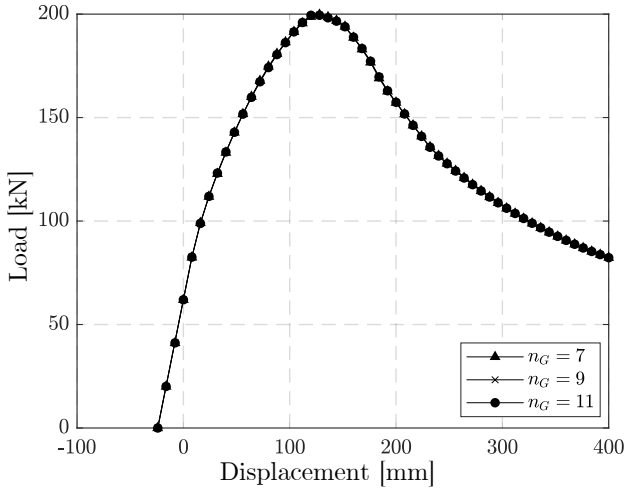

Figure 4.14. Displacement-controlled test on the cantilever beam in Figure 4.13 with different numbers of integration points.

The moment and curvature distributions along the beam in Figure 4.15 show how the strains are correctly localized within the characteristic region, where the curvature shows the actual weight applied to the end points.

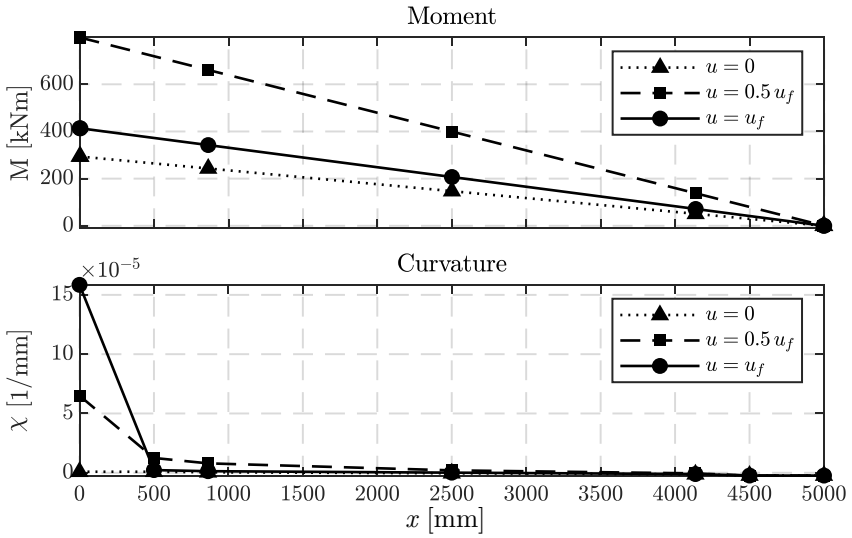

Figure 4.15. Moment and curvature distributions at specific steps of the global response curves in Figure 4.14 with 7 integration points.

Changes in the localization length L_c only modify the softening branch without affecting the pre-peak response. Figure 4.16a shows the curves for different values of L_c for both the damage-plasticity material 3DDP and the 1DD models.

The two cases show a similar trend in the first part, since the two concrete laws have the same compression strength. Some differences are to be expected since the softening behavior is

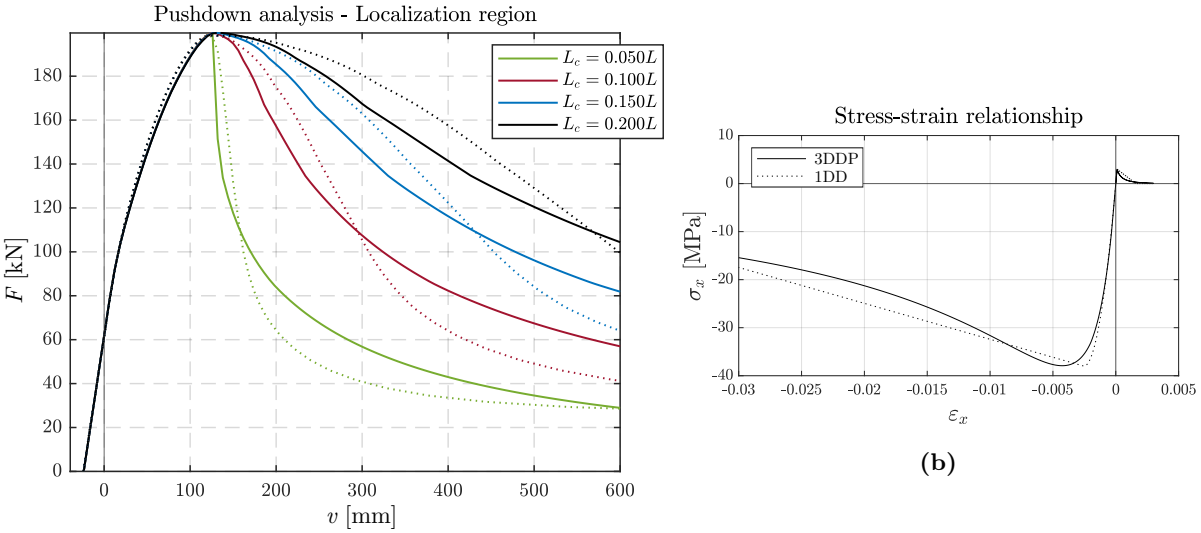

(a) **(b)**

Figure 4.16. (a) Pushover response curve of the PC cantilever beam in Figure 4.13 with different L_c in the localization zone; (b) Concrete constitutive laws: plastic-damage model [7] and uni-axial concrete model with linear softening [8].

linear in 1DD and nonlinear in 3DDP.

4.3.2 Fracture energy regularization

A widely employed local regularization strategy for quasi-brittle materials is the fracture energy approach. The fundamental idea is to replace softening stress-strain laws, which lead to mesh-sensitive dissipation, with formulations expressed in terms of fracture energy G_f, i.e., the energy required to create a unit area of crack. Within a finite element discretization, the localization band is assumed to have a characteristic length l_{ch}, often related to the element size or to a phenomenological plastic hinge length. The softening branch of the stress-strain law is then rescaled such that the area under the stress-crack opening curve $\sigma(w)$ is equal to G_f, independently of the chosen discretization. For a uniaxial tension law, the crack opening displacement is related to the strain by $w = \varepsilon \cdot l_{ch}$, and the regularized ultimate strain is defined as $\varepsilon_u = w_u / l_{ch}$, where w_u is the critical crack opening at complete stress release. This guarantees that the energy dissipated per unit volume,

$$\int_0^{\varepsilon_u} \sigma(\varepsilon)\, d\varepsilon = \frac{G_f}{l_{ch}} \tag{4.15}$$

remains constant with respect to the mesh.

This concept was first formalized in the crack band theory of Bažant and Oh [107], and subsequently generalized to smeared crack and continuum damage formulations [122, 89]. The method has since become a standard in nonlinear finite element analysis of concrete and masonry, being simple to implement and consistent with experimental observations on fracture energy dissipation. Recent works (e.g., Petracca et al. [9]) have extended the approach to both tensile and compressive regimes by introducing distinct fracture energies G_f and G_c, ensuring mesh-independent softening in damage-plasticity constitutive laws. In this context, the discrete softening modulus is defined in terms of l_{ch} and the material tensile strength f_t, leading to equivalent exponential or bilinear laws calibrated to preserve the correct dissipation. Figure 4.17

shows how the characteristic length choice influences the dissipation area of the softening curve.

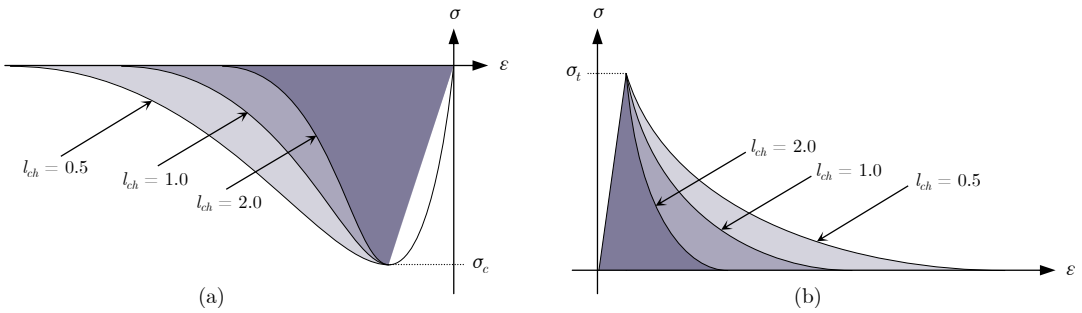

Figure 4.17. Influence of the characteristic length choice l_{ch} expressed in arbitrary length units, shown here only to illustrate its effect on the softening curves in (a) the compression part and (b) the tensile part.

In practice, the characteristic length can be associated with either the finite element size, in purely numerical regularization, or with structural measures such as effective crack spacing or reinforcement detailing, when a phenomenological interpretation is desired. This flexibility explains why fracture energy regularization is now ubiquitous in computational mechanics of cementitious composites, and why it is also adopted in the present work for the applications involving reinforced and prestressed concrete members.

This model has proven to be largely ineffective on beam finite elements, especially when using very low fracture energy values, as those typically required for the tensile response of concrete. Despite its popularity, fracture energy regularization produces unrealistic crack spacing and prevents convergence of the global response, even though energy dissipation is preserved at the material point level [91]. As a result, the approach exhibits pathological mesh dependency and a lack of objectivity, which ultimately makes it unsuitable for conventional beam formulations. Numerical applications illustrating this issue are reported in Section 5.1.

4.4 Element state determination

The nonlinear solution of frame structures by means of beam finite elements is generally carried out through an incremental-iterative Newton-Raphson (N-R) procedure. At each iteration of a given load step, the global algorithm requires the evaluation of the resisting forces and of the tangent operator of each finite element, corresponding to the trial values of the nodal displacements. This task, commonly referred to as *element state determination*, is at the core of the computational strategy, since its efficiency and robustness directly influence the overall convergence of the analysis.

From a general standpoint, the element state determination involves the simultaneous enforcement of element compatibility and equilibrium. In displacement-based formulations, compatibility is satisfied by construction but equilibrium is only fulfilled in an approximate sense, often requiring fine meshes to capture localized nonlinearities. On the contrary, force-based and mixed formulations provide higher accuracy and mesh objectivity by interpolating the internal force fields. However, this advantage comes at the cost of a more elaborate solution procedure, since the resisting basic forces and the tangent flexibility matrix must be consistently evaluated at each N-R iteration.

Early solution algorithms were proposed for the classical force-based Timoshenko element, and later extended to more advanced formulations such as enhanced Timoshenko models and mixed elements [13]. The original approach relied on a nested iterative scheme at the element level, simultaneously enforcing equilibrium and compatibility during each global iteration. An improved non-iterative variant was subsequently introduced by Neuenhofer and Filippou [25], where element residual deformations are determined and stored within the current N-R iteration and updated in the following one. In this way, only a linear approximation of the element response is computed at each iteration, while the compatibility and equilibrium conditions are strictly recovered at convergence, leading to a substantial reduction in computational cost without loss of accuracy. A unified description of both versions was later provided in [51].

The same algorithmic framework can be generalized to enhanced beam formulations including additional kinematic fields, such as bond-slip or section warping, where the element state determination must account for the enlarged set of generalized deformations and internal forces. In all cases, the computational process can be regarded as hierarchical:

1. *Element level* - evaluation of the resisting forces and tangent operator under the trial basic deformations, enforcing equilibrium and compatibility.

2. *Section level* - determination of the cross-section response through fiber discretization, enabling a consistent multi-axial coupling of axial, flexural, shear and torsional components.

3. *Material level* - integration of the nonlinear constitutive relations at each fiber, including plasticity, damage, or plastic-damage models.

By structuring the algorithm into these nested layers, one achieves both generality and computational efficiency. Linearized non-iterative schemes are adopted in this work, as they preserve the quadratic convergence of the global N-R procedure while significantly reducing the number of operations required at the element level.

Five element state determination procedures are reported next for the following beam element formulations:

1. **D** element: perfect bond displacement-based formulation;
2. **D-B** and **D-BW** elements: bond-slip, bond-slip and warping displacement-based formulations;
3. **F** and **M** elements: perfect bond force-based and mixed formulations;
4. **F-B** and **M-B** elements: bond-slip force-based and mixed formulations;
5. **M-BW** elements: bond-slip and warping mixed formulation.

Prestressed and curved components preprocessing

The special components such as fibers with bond-slip, prestressed tendons, and components with curved profiles, must be properly processed to compute the section and fiber operators required for analysis. Also, it has to be considered that the same interpolation points and functions are used for fiber sections and bond sections (m_f in number), but the quadrature points locations and weights are different (n_g and n_b in number, respectively).

The following algorithm is proposed to compute all required geometrical information starting from the general coordinates in the global reference system of every f^{th} component.

Let the profile of the f^{th} tendon be defined by a set of input coordinates

$$\mathbf{P}_f = \begin{bmatrix} x_1 & \cdots & x_{n_r} \\ y_1 & \cdots & y_{n_r} \\ z_1 & \cdots & z_{n_r} \end{bmatrix}$$

where n_r is the number of input points.
The goal is to evaluate the tendon positions and tangents at the quadrature points $\mathbf{x}_g = \{x_j\}_{j=1}^{n_g}$ and at the bond-slip interpolation points $\mathbf{x}_b = \{x_k\}_{k=1}^{m}$.

Step 1. Interpolation of positions
For each quadrature abscissa x_j:

$$\begin{bmatrix} y_f(x_j) \\ z_f(x_j) \end{bmatrix} = \begin{bmatrix} \mathbf{b}_b(x_j) & 0 \\ 0 & \mathbf{b}_b(x_j) \end{bmatrix} \begin{bmatrix} \mathbf{P}_y \\ \mathbf{P}_z \end{bmatrix}$$

where $\mathbf{b}_b(x_j)$ is the interpolation matrix (e.g. piecewise linear, Lagrange, Hermite).

Step 2. Evaluation of slopes
The derivatives of the interpolants provide the tendon slopes:

$$\begin{bmatrix} \beta_y(x_j) \\ \beta_z(x_j) \end{bmatrix} = \arctan \begin{bmatrix} \mathbf{b}_{b,x}(x_j) & 0 \\ 0 & \mathbf{b}_{b,x}(x_j) \end{bmatrix} \begin{bmatrix} \mathbf{P}_y \\ \mathbf{P}_z \end{bmatrix}$$

So that the tendon tangent vector is

$$\mathbf{t}_f(x) = \frac{1}{\sqrt{1+\beta_y^2+\beta_z^2}} \begin{bmatrix} 1 \\ \beta_y(x) \\ \beta_z(x) \end{bmatrix}$$

Step 3. Rotation operators Given $\mathbf{t}_f(x)$, construct the tendon rotation matrix $\mathbf{R}(x)$ as in Section 4.2.1, using Rodrigues' formula with axis

$$\bar{\boldsymbol{\beta}} = \begin{bmatrix} 0 & -\beta_z(x) & \beta_y(x) \end{bmatrix}^T$$

normalized to obtain $\boldsymbol{\beta}$.

Step 4. Bond-slip quadrature (optional for fibers with bond-slip)
If bond-slip is considered, meaning perfect bond is not enforced on curved tendons, define a second set of points $\mathbf{x}_b$:

$$\mathbf{x}_b \leftarrow \begin{cases} \text{Gauss-Lobatto rule,} & \text{Quadrature scheme 1} \\ \text{Multi-region rules,} & \text{Quadrature scheme 2} \end{cases}$$

The two quadrature schemes are depicted in Figure 4.18.

Step 5. Assembly
Collect the results in the element storage:

$$\mathbf{Y}_f = \{y_f(x_j)\}, \quad \mathbf{Z}_f = \{z_f(x_j)\}, \quad \boldsymbol{\beta}_f = \{\beta_y(x_j), \beta_z(x_j)\}, \quad \mathbf{R}_f = \{\mathbf{R}(x_j)\}.$$

These data is used to build the section compatibility matrix in every section upon each element's initialization, as shown in Section 4.5.

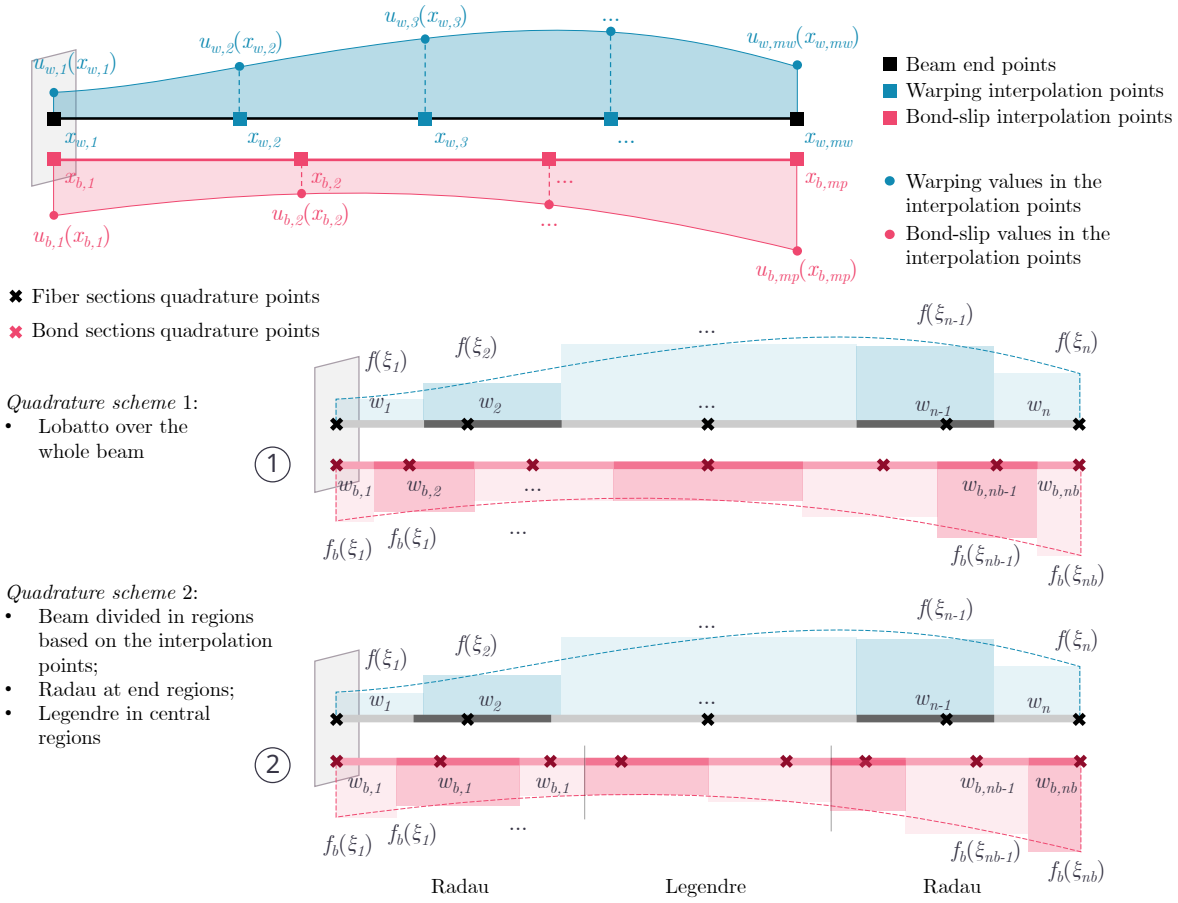

Figure 4.18. Integration points and quadrature schemes for the beam formulations including bond-slip and warping degrees of freedom.

4.4.1 D element state determination

The governing equations are the numerical approximations of Eqs. (2.55)-(2.57):

$$\mathbf{p}_l^{ext} + \mathbf{p}_{l0} - \mathbf{p}_l^{int} = \mathbf{0} \tag{4.16}$$

$$\mathbf{e}_j = \mathbf{B}_j \mathbf{v} + \mathbf{e}_{pj} \quad \text{for every section } j \tag{4.17}$$

$$\mathbf{q} = \sum_{j=1}^{n_g} \mathbf{B}_j^T \mathbf{s}_j \, w_j - \sum_{j=1}^{n_g} \mathbf{N}_j^T \mathbf{p}_j \, w_j \tag{4.18}$$

This model is so simple that it can be applied as-is, with no need to write residual or incremental version of these formulas. The whole procedure is reported in Figure 4.19.

Initialization

Compute functions $\mathbf{N}(x)$ and $\mathbf{B}(x)$. The whole procedure is not reported here as it can be found in several literature references.

Vector $\mathbf{p}_{lp}$, which depends on the element loads, is initialized to zero and then is updated at every global step.

History variables

Only the history variables at the material level are saved here at every global step i. No history variables at the element level are required instead.

D element state determination

	for every element $1{:}\,n_e$	*Description*
e_1	$\mathbf{v} = \mathbf{a}_g \mathbf{u}_l$	Compute basic displacements from local displacements
e_2	Initialize $\mathbf{q}$ and $\mathbf{k}$ to zero	Section initialization
	for every section $1{:}\,n_g$	**Sections**
s_1	$\mathbf{e} = \mathbf{B}\mathbf{v} + \mathbf{e}_p$	Compute section strain from basic displacements
s_2	Section CL $\rightarrow$ $\hat{\mathbf{s}}, \mathbf{k}_s$	Compute fiber section response
s_3	$\mathbf{q} = \mathbf{q} + w\,(\mathbf{B}^T\hat{\mathbf{s}} + \mathbf{N}^T\mathbf{p})$	Sum basic forces
s_4	$\mathbf{k} = \mathbf{k} + w\mathbf{a}^T\mathbf{k}_s\mathbf{B}$	Sum basic stiffness
e_3	$\mathbf{p}_l = \mathbf{a}_g^T\mathbf{q} + \mathbf{p}_{lp}$	Compute local forces
e_4	$\mathbf{k}_l = \mathbf{a}_g^T\mathbf{k}\,\mathbf{a}_g$	Compute local stiffness

Figure 4.19. D element state determination algorithm.

4.4.2 D-B and D-BW element state determination

The governing equations are the following, in their numerical counterpart of Eqs. (2.148)-(2.150):

$$\tilde{\mathbf{p}}_l^{ext} + \tilde{\mathbf{p}}_{l0} - \tilde{\mathbf{p}}_l^{int} = \mathbf{0} \tag{4.19}$$

$$\tilde{\mathbf{e}}_j = \tilde{\mathbf{B}}_j\, \tilde{\mathbf{v}} + \tilde{\mathbf{e}}_{0j} \qquad \text{for every section } j = 1, \dots, n_g \tag{4.20}$$

$$\tilde{\mathbf{q}} = \sum_{j=1}^{n_g} \tilde{\mathbf{B}}_j^T\, \tilde{\mathbf{s}}_j\, w_j - \sum_{j=1}^{n_g} \tilde{\mathbf{N}}_j^T\, \tilde{\mathbf{p}}_j\, w_j \tag{4.21}$$

The whole procedure is reported in Figure 4.21.

Element initialization

In the initialization procedure, the element data are read. The number of local degrees of freedom d_l is:

$$\begin{aligned} d_l &= 12 + n_f m_f, && \text{for D-B} \\ d_l &= 12 + n_f m_f + n_w m_w, && \text{for D-BW} \end{aligned}$$

where 12 correspond to the standard beam kinematics, m_f is the number of interpolation points for bond-slip, n_f is the number of fibers with bond-slip, m_w is the number of interpolation points for warping, and n_w is the number of warping variables.
The basic number of degrees of freedom d_b is:

$$\begin{aligned} d_b &= 6 + n_f m_f, && \text{for D-B} \\ d_b &= 6 + n_f m_f + n_w m_w, && \text{for D-BW} \end{aligned}$$

The section components are:

$$\begin{aligned} d_s &= 6 + n_f, && \text{for D-B} \\ d_s &= 6 + n_f + 2n_w, && \text{for D-BW} \end{aligned}$$

The interpolation points and the quadrature scheme for both fiber and bond sections is initialized. In this case,

$$\begin{aligned} \{x_j, w_j\}_{j=1}^{n_g} &= \texttt{Domain}(L, n_g), \\ \{x_j, w_j\}_{j=1}^{n_b} &= \texttt{Domain}(L, n_b). \end{aligned}$$

where the `Domain` function computes all the x_j and w_j, which are the quadrature points' coordinates on the axis and the weights over the element length L, respectively, both on the fiber and bond sections:

- the fiber sections' quadrature points are indicated as n_g;
- the bond sections' quadrature points are indicated as n_b.

It is worth noting that the warping part belongs to the fiber sections.
Vector $\tilde{\mathbf{p}}_{lp}$, which depends on the element loads, is initialized to zero and then is updated at

every global step.

Fiber sections initialization

For each fiber section $j = 1, \ldots, n_g$, the section-level variables are initialized.
The section shape functions are calculated. For each coordinate $x = X_j$, the beam shape function matrices $\mathbf{N}_r$ and $\mathbf{B}_r$ for the standard components are computed, depending on the formulation (first, second orders and so on).
The bond-slip shape function matrices $\mathbf{N}_b$ and $\mathbf{B}_b$ are also computed.
The beam shape function matrices are assembled for the **D-B** element as:

$$\tilde{\mathbf{B}} = \begin{bmatrix} \mathbf{B}_r & \mathbf{0}_{6\times m_f \cdot n_f} \\ \mathbf{0}_{n_f\times 6} & \mathbf{B}_b \end{bmatrix}$$

$$\tilde{\mathbf{N}} = \begin{bmatrix} \mathbf{N}_r & \mathbf{0}_{6\times m_f \cdot n_f} \\ \mathbf{0}_{n_f\times 6} & \mathbf{0}_{n_f\times m_f \cdot n_f} \end{bmatrix}$$

If warping is included, the warping bond-slip shape function matrix $\mathbf{B}_w$ is computed. The **D-BW** element matrices are:

$$\tilde{\mathbf{B}} = \begin{bmatrix} \mathbf{B}_r & \mathbf{0}_{6\times m_f \cdot n_f} & \mathbf{0}_{6\times m_w n_w} \\ \mathbf{0}_{n_f\times 6} & \mathbf{B}_b & \mathbf{0}_{n_f\times m_w n_w} \\ \mathbf{0}_{2n_w\times 6} & \mathbf{0}_{2n_w\times m_f n_f} & \mathbf{B}_w \end{bmatrix}$$

$$\tilde{\mathbf{N}} = \begin{bmatrix} \mathbf{N}_r & \mathbf{0}_{6\times (m_f n_f + m_w n_w)} \\ \mathbf{0}_{(n_f+2n_w)\times 6} & \mathbf{0}_{(n_f+2n_w)\times (m_f n_f + m_w n_w)} \end{bmatrix}$$

It is worth noting that $\mathbf{B}_w$ is the assembly of two submatrices, as per Eq. (2.233):

$$\mathbf{B}_w = \begin{bmatrix} \mathbf{N}_w \\ \mathbf{N}_{w,x} \end{bmatrix}$$

Bond sections initialization

A second loop is performed for each bond section $j = 1, \ldots, n_b$.
The beam shape functions matrix is, for the **D-B** element:

$$\tilde{\mathbf{B}} = \begin{bmatrix} \mathbf{0}_{n_f\times 6} & \mathbf{N}_b \end{bmatrix}$$

The beam shape functions matrix is, for the **D-BW** element:

$$\tilde{\mathbf{B}} = \begin{bmatrix} \mathbf{0}_{n_f\times 6} & \mathbf{N}_b & \mathbf{0}_{n_f+m_w n_w} \end{bmatrix}$$

Thus completing the initialization process.

The rest is initialized within the *section state determination* framework, and is explained in Sec. 4.5. Prestressed and curved components are handled at fiber level and are discussed later on.

History variables

Only the history variables at the material level are saved here at every global step i. No history variables at the element level are required instead.

D-B and **D-W** element state determination

	for every element $1:n_e$	*Description*
e_1	$\tilde{\mathbf{v}} = \tilde{\mathbf{a}}_g \tilde{\mathbf{u}}_l$	Compute basic displacements from local displacements
e_2	Initialize $\tilde{\mathbf{q}}$ and $\tilde{\mathbf{k}}$ to zero	Section initialization
	for every **fiber** section $1:n_g$	**Fiber sections**
s_1	$\tilde{\mathbf{e}} = \tilde{\mathbf{B}}\tilde{\mathbf{v}} + \tilde{\mathbf{e}}_p$	Compute section strain from basic displacements
s_2	Fiber section CL $\rightarrow$ $\hat{\mathbf{s}}, \mathbf{k}_s$	Compute fiber section response
s_3	$\tilde{\mathbf{q}} = \tilde{\mathbf{q}} + w\left(\tilde{\mathbf{B}}^T\hat{\mathbf{s}} + \tilde{\mathbf{N}}^T\tilde{\mathbf{p}}\right)$	Sum basic forces
s_4	$\tilde{\mathbf{k}} = \tilde{\mathbf{k}} + w\tilde{\mathbf{B}}^T\mathbf{k}_s\tilde{\mathbf{B}}$	Sum basic stiffness
	for every **bond** section $1:n_b$	**Bond sections**
s_9	$\mathbf{u}_b = \tilde{\mathbf{B}}\tilde{\mathbf{v}}$	Compute section bond-slip from basic displacements
	Bond section CL $\rightarrow$ $\hat{\mathbf{p}}_b, \mathbf{k}_{bs}$	Compute fiber section response
	$\tilde{\mathbf{q}} = \tilde{\mathbf{q}} + w\tilde{\mathbf{B}}^T\hat{\mathbf{p}}_b$	Sum basic forces
	$\tilde{\mathbf{k}} = \tilde{\mathbf{k}} + w\tilde{\mathbf{B}}^T\tilde{\mathbf{k}}_{bs}\tilde{\mathbf{B}}$	Sum basic stiffness
	$\tilde{\mathbf{p}}_l = \tilde{\mathbf{a}}_g^T\tilde{\mathbf{q}} + \tilde{\mathbf{p}}_{lp}$	Compute local forces
e_4	$\tilde{\mathbf{k}}_l = \tilde{\mathbf{a}}_g^T\tilde{\mathbf{k}}\,\tilde{\mathbf{a}}_g$	Compute local stiffness

Figure 4.20. D-B and D-W element state determination.

4.4.3 F and M element state determination

The governing equations derived from the mixed variational formulation are written in numerical form as:

$$\mathbf{a}_g^T \mathbf{q} = \mathbf{p}_l^{ext} + \mathbf{p}_{l0} \tag{4.22}$$

$$\mathbf{a}_g \mathbf{v} = \sum_{j=1}^{n_g} \mathbf{b}_j^T \mathbf{e}_j \, w_j \tag{4.23}$$

$$\mathbf{b}_j \mathbf{q} = \hat{\mathbf{s}}_j - \mathbf{s}_{pj} \quad \text{for every section } j \tag{4.24}$$

where $\mathbf{a}_g$ is the boundary operator relating nodal forces to element forces, $\mathbf{q}$ is the vector of element forces (basic forces), $\mathbf{v}$ is the vector of element displacements (basic displacements), $\mathbf{b}_j$ is the equilibrium matrix at section j, $\mathbf{e}_j$ is the vector of generalized section strains at section j, $\hat{\mathbf{s}}_j$ are the section stresses from the constitutive law, $\mathbf{s}_{pj}$ are the particular stresses due to distributed loads, and w_j are the integration weights for the n_g Gauss quadrature points.

Incremental formulation The section stresses from the constitutive law can be written incrementally as:

$$\Delta\hat{\mathbf{s}}_j = \frac{\partial \hat{\mathbf{s}}_j}{\partial \mathbf{e}_j} \Delta\mathbf{e}_j = \mathbf{k}_{sj} \Delta\mathbf{e}_j \tag{4.25}$$

Taking the variation of the governing equations leads to the incremental form:

$$\mathbf{R}_v = \mathbf{a}_g^T \Delta\mathbf{q} \tag{4.26}$$

$$\mathbf{R}_q = \mathbf{a}_g \Delta\mathbf{v} - \sum_{j=1}^{n_g} \mathbf{b}_j^T \Delta\mathbf{e}_j \, w_j \tag{4.27}$$

$$\mathbf{R}_e = \mathbf{k}_{sj} \Delta\mathbf{e}_j - \mathbf{b}_j \Delta\mathbf{q} \tag{4.28}$$

where $\mathbf{R}_v$, $\mathbf{R}_q$, and $\mathbf{R}_e$ are the residual vectors.
Since continuity is guaranteed only on displacements, only the first residual must vanish, while the others can be condensed. From the third equation, isolating $\Delta\mathbf{e}_j$:

$$\Delta\mathbf{e}_j = \mathbf{k}_{sj}^{-1} \left(\mathbf{b}_j \Delta\mathbf{q} + \mathbf{s}_u^j \right) \tag{4.29}$$

where $\mathbf{s}_u^j = \mathbf{R}_e^j$ are the unbalanced section stresses, calculated as the difference between equilibrated stresses and those from the constitutive law:

$$\mathbf{s}_u^j = \mathbf{b}_j \mathbf{q} + \mathbf{s}_{pj} - \hat{\mathbf{s}}_j \tag{4.30}$$

Substituting into the second equation:

$$\mathbf{R}_q = \mathbf{a}_g \Delta\mathbf{v} - \sum_{j=1}^{n_g} \mathbf{b}_j^T \mathbf{k}_{sj}^{-1} \left(\mathbf{b}_j \Delta\mathbf{q} + \mathbf{s}_u^j \right) w_j \tag{4.31}$$

$$\mathbf{R}_q = \mathbf{a}_g \Delta\mathbf{v} - \mathbf{f} \Delta\mathbf{q} - \mathbf{v}_u \tag{4.32}$$

where the element flexibility matrix in the basic system is:

$$\mathbf{f} = \sum_{j=1}^{n_g} \mathbf{b}_j^T \mathbf{k}_{sj}^{-1} \mathbf{b}_j \, w_j \tag{4.33}$$

and the element displacement residual due to unbalanced stresses is:

$$\mathbf{v}_u = \sum_{j=1}^{n_g} \mathbf{b}_j^T \mathbf{k}_{sj}^{-1} \mathbf{s}_u^j \, w_j \tag{4.34}$$

Isolating $\Delta\mathbf{q}$:

$$\Delta\mathbf{q} = \mathbf{f}^{-1} \left(\mathbf{a}_g \Delta\mathbf{v} - \mathbf{v}_u - \mathbf{R}_q \right) \tag{4.35}$$

where $\mathbf{R}_q$ is practically zero or very close to it due to roundoff errors [23].
Substituting $\Delta\mathbf{q}$ into the first equation:

$$\mathbf{R}_v = \mathbf{a}_g^T \mathbf{f}^{-1} \left(\mathbf{a}_g \Delta\mathbf{v} - \mathbf{v}_u - \mathbf{R}_q \right) \tag{4.36}$$

The tangent element stiffness matrix is obtained as:

$$\mathbf{k}_l = \mathbf{a}_g^T \mathbf{f}^{-1} \mathbf{a}_g \tag{4.37}$$

The computational steps for the element implementation are organized as follows. The variables stored from the previous step i are: $\mathbf{q}$, $\mathbf{f}$, $\mathbf{v}_u$ for every element, $\mathbf{s}_u$, $\mathbf{k}_s$, $\mathbf{e}$ for every section.

Elements initialization
In the initialization procedure, the element data are read for every element.

- The number of local degrees of freedom $d_l = 12$
- The basic number of degrees of freedom $d_b = 6$
- The section components are $d_s = 6$

The interpolation points and the quadrature scheme for the fiber sections is initialized. In this case,

$$\{x_j, w_j\}_{j=1}^{n_g} = \texttt{Domain}(L, n_g)$$

where the `Domain` function computes all the x_j and w_j, which are the quadrature points' coordinates on the axis and the weights over the element length L, respectively, on the fiber sections, and n_g is the total number.

Let the index i indicate the global iteration. At the element level, the element history variables at $i = 0$ are initialized to zero,

$$\mathbf{v}^{i=0} = \mathbf{0}_{6\times1}, \quad \mathbf{q}^{i=0} = \mathbf{0}_{6\times1}, \quad \mathbf{v}_u^{i=0} = \mathbf{0}_{6\times1}$$

The flexibility matrix $\mathbf{f}^{i=0}$ is initialized by considering everything linear elastic.

Sections initialization The section quantities are initialized for each quadrature section

$j = 1, \ldots, n_g$. The section compatibility matrix $\mathbf{b}$ is evaluated at every position x_j from Eq. (2.59).
The section history variables are set to zero,

$$\mathbf{e}^{i=0} = \mathbf{0}_{d_s \times 1}, \quad \mathbf{s}^{i=0} = \mathbf{0}_{d_s \times 1}, \quad \mathbf{s}_u^{i=0} = \mathbf{0}_{d_s \times 1}$$

where d_s is the number of section degrees of freedom.
The sections stiffness matrix $\mathbf{k}_s^{i=0}$ is initialized by considering everything linear elastic, and is computed from Eq. (2.39).

The rest is initialized within the *section state determination* framework, and is explained in Sec. 4.5. Prestressed and curved components are handled at fiber level and are discussed later on.

History variables
At every successful global step, the following vectors at the previous step i are updated for the next step $i + 1$:

- $\mathbf{q}^{i+1} = \mathbf{q}^i$, $\mathbf{f}^{i+1} = \mathbf{f}^i$ and $\mathbf{v}_u^{i+1} = \mathbf{v}_u^i$ at the element level;
- $\mathbf{e}^{i+1} = \mathbf{e}^i$, $\mathbf{k}_s^{i+1} = \mathbf{k}_s^i$ and $\mathbf{s}_u^{i+1} = \mathbf{s}_u^i$ at the section level, i.e., for every quadrature point.

This ensures a non-iterative, linearized procedure consistent with the global Newton-Raphson scheme, in line with the frameworks in [25, 26, 27, 5].

	F and **M** element state determination	
	for every element $1{:}\,n_e$	*Description*
e_1	$\Delta\mathbf{v} = \mathbf{a}_g \Delta\mathbf{u}_l$	Compute basic displacement from local displacement (increments)
e_2	$\Delta\mathbf{q} = \mathbf{f}^{-1}\Delta\mathbf{v}$	Compute trial basic force from basic displacement (increments)
e_3	$\mathbf{q} = \mathbf{q} + \Delta\mathbf{q}$	Update basic force (total)
e_4	Initialize $\mathbf{v}_u$ and $\mathbf{f}$ to zero	Section initialization
	for every section $1{:}\,n_g$	**Sections**
s_1	$\Delta\mathbf{s} = \mathbf{b}\Delta\mathbf{q} + \mathbf{s}_p + \mathbf{s}_u$	Compute section stress from basic force (increments)
s_2	$\Delta\mathbf{e} = \mathbf{k}_s^{-1}\Delta\mathbf{s}$	Compute section strain from section stress (increments)
s_3	$\mathbf{e} = \mathbf{e} + \Delta\mathbf{e}$	Update section strain (total)
s_4	Section CL $\rightarrow$ $\hat{\mathbf{s}}, \mathbf{k}_s$	Compute fiber section response
s_5	$\mathbf{s}_u = \mathbf{b}\mathbf{q} - \hat{\mathbf{s}}$	Compute unbalanced section stress
s_6	$\mathbf{e}_u = \mathbf{k}_s^{-1}\mathbf{s}_u$	Compute unbalanced section strain
s_7	$\mathbf{v}_u = \mathbf{v}_u + w\,\mathbf{b}^T(\mathbf{e} + \mathbf{e}_u)$	Sum unbalanced basic displacement
s_8	$\mathbf{f} = \mathbf{f} + w\,\mathbf{b}^T\mathbf{k}_s^{-1}\mathbf{b}$	Sum basic flexibility
e_5	$\mathbf{q} = \mathbf{q} - \mathbf{f}^{-1}\mathbf{v}_u$	Update basic force (total)
	for every section $1{:}\,n_g$	**Sections**
s_9	$\mathbf{s}_u = \mathbf{b}\mathbf{q} - \hat{\mathbf{s}}$	Update unbalanced section stress for next iteration
e_6	$\mathbf{p}_l = \mathbf{a}_g^T\mathbf{q} + \mathbf{p}_{lp}$	Compute local internal forces
e_7	$\mathbf{k}_l = \mathbf{a}_g^T\mathbf{k}\,\mathbf{a}_g$	Compute local stiffness

Figure 4.21. F and M non-iterative element state determination algorithm.

4.4.4 F-B and M-B element state determination

The governing equations of the bond-slip force-based and mixed formulations are an extension of those in the perfect bond case, enriched by the additional bond-slip degrees of freedom and internal forces. In numerical form they read:

$$\tilde{\mathbf{a}}_g^T \, \tilde{\mathbf{q}} = \tilde{\mathbf{p}}_l^{ext} + \tilde{\mathbf{p}}_{l0} \tag{4.38}$$

$$\tilde{\mathbf{a}}_g \, \tilde{\mathbf{v}} = \sum_{j=1}^{n_g} \tilde{\mathbf{b}}_j^T \, \tilde{\mathbf{e}}_j \, w_j \tag{4.39}$$

$$\tilde{\mathbf{b}}_j \, \tilde{\mathbf{q}} = \hat{\tilde{\mathbf{s}}}_j - \tilde{\mathbf{s}}_{pj} \qquad j = 1, \ldots, n_g \tag{4.40}$$

where $\tilde{\mathbf{q}}$ and $\tilde{\mathbf{v}}$ are the element basic forces and deformations (now including the bond-slip variables), $\tilde{\mathbf{b}}_j$ is the compatibility matrix at section j, $\hat{\tilde{\mathbf{s}}}_j$ are the section stresses from the constitutive law, and $\tilde{\mathbf{s}}_{pj}$ the section stresses due to the element loads.
This allows to take the same steps as Section 4.4.3 using the modified operators.

Elements initialization
In the initialization procedure, the element data are read for every element.

- The number of local degrees of freedom $d_l = 12 + 2n_f$
- The basic number of degrees of freedom $d_b = 6 + m_f n_f$
- The section components are $d_s = 6 + n_f$

The interpolation points and the quadrature scheme for both fiber and bond sections is initialized. In this case,

$$\{x_j, w_j\}_{j=1}^{n_g} = \texttt{Domain}(L, n_g)$$
$$\{x_j, w_j\}_{j=1}^{n_b} = \texttt{Domain}(L, n_b)$$

where the `Domain` function computes all the x_j and w_j, which are the quadrature points' coordinates on the axis and the weights over the element length L, respectively, both on the fiber and bond sections:

- the fiber sections' quadrature points are indicated as n_g;
- the bond sections' quadrature points are indicated as n_b.

Let the index i indicate the global iteration. At the element level, the element history variables at $i = 0$ are initialized to zero,

$$\mathbf{v}^{i=0} = \mathbf{0}_{d_b}, \quad \mathbf{q}^{i=0} = \mathbf{0}_{d_b}, \quad \mathbf{v}_u^{i=0} = \mathbf{0}_{d_b}$$

The flexibility matrix $\mathbf{f}^{i=0}$ is initialized by considering everything linear elastic.

Fiber sections initialization
For each fiber section $j = 1, \ldots, n_g$, the section-level variables are initialized.
For each coordinate $x = X_j$, the beam equilibrium matrix $\mathbf{b}$ for the standard components is

computed.
The bond-slip shape function matrix $\mathbf{b}_{b,x}$ is also computed.
The beam shape function matrices are assembled for the **F-B** and **M-B** elements as:

$$\tilde{\mathbf{b}} = \begin{bmatrix} \mathbf{b} & \mathbf{0}_{6\times m_f \cdot n_f} \\ \mathbf{0}_{n_f\times 6} & \mathbf{b}_{b,x} \end{bmatrix}$$

The section history variables are set to zero,

$$\tilde{\mathbf{e}}^{i=0} = \mathbf{0}_{d_s\times 1}, \quad \tilde{\mathbf{s}}^{i=0} = \mathbf{0}_{d_s\times 1}, \quad \tilde{\mathbf{s}}_u^{i=0} = \mathbf{0}_{d_s\times 1}$$

The sections stiffness matrix $\mathbf{k}_s^{i=0}$ is initialized by considering everything linear elastic.

Bond sections initialization
A second loop is performed for each bond section $j = 1, \ldots, n_b$.
The equilibrium matrix is, for the **F-B** and **M-B** elements:

$$\tilde{\mathbf{b}} = \begin{bmatrix} \mathbf{0}_{n_f\times 6} & \mathbf{b}_b \end{bmatrix}$$

Thus completing the initialization process.

History variables
At every successful global step, the following vectors at the previous iteration i are updated for the next iteration $i+1$:

- $\tilde{\mathbf{q}}^{i+1} = \tilde{\mathbf{q}}^i$, $\tilde{\mathbf{f}}^{i+1} = \tilde{\mathbf{f}}^i$ and $\tilde{\mathbf{v}}_u^{i+1} = \tilde{\mathbf{v}}_u^i$ at the element level;
- $\tilde{\mathbf{e}}^{i+1} = \tilde{\mathbf{e}}^i$, $\tilde{\mathbf{k}}_s^{i+1} = \tilde{\mathbf{k}}_s^i$ and $\tilde{\mathbf{s}}_u^{i+1} = \tilde{\mathbf{s}}_u^i$ at the section level, i.e., for every quadrature point.

F-B and **M-B** element state determination

	for every element $1:n_e$	*Description*
e_1	$\Delta\tilde{\mathbf{v}} = \tilde{\mathbf{a}}_g \Delta\tilde{\mathbf{u}}_l$	Compute basic displacements from local displacements (increments)
e_2	$\Delta\tilde{\mathbf{q}} = \tilde{\mathbf{f}}^{-1}\Delta\tilde{\mathbf{v}}$	Compute trial basic force from basic displacements (increments)
e_3	$\tilde{\mathbf{q}} = \tilde{\mathbf{q}} + \Delta\tilde{\mathbf{q}}$	Update basic force (total)
e_4	Initialize $\tilde{\mathbf{v}}_u$ and $\tilde{\mathbf{f}}$ to zero	Section initialization
	for every fiber section $1:n_g$	**Fiber sections**
s_1	$\Delta\tilde{\mathbf{s}} = \tilde{\mathbf{b}}\Delta\tilde{\mathbf{q}} + \tilde{\mathbf{s}}_p + \tilde{\mathbf{s}}_u$	Compute section stress from basic force (increments)
s_2	$\Delta\tilde{\mathbf{e}} = \tilde{\boldsymbol{k}}_s^{-1}\Delta\tilde{\mathbf{s}}$	Compute section strain from section stress (increments)
s_3	$\tilde{\mathbf{e}} = \tilde{\mathbf{e}} + \Delta\tilde{\mathbf{e}}$	Update section strain (total)
s_4	Fiber section CL $\rightarrow \hat{\tilde{\mathbf{s}}}, \tilde{\mathbf{k}}_s$	Compute **fiber** section response
s_5	$\tilde{\mathbf{s}}_u = \tilde{\mathbf{b}}\tilde{\mathbf{q}} - \hat{\tilde{\mathbf{s}}}$	Compute unbalanced section stress
s_6	$\tilde{\mathbf{e}}_u = \tilde{\mathbf{k}}_s^{-1}\tilde{\mathbf{s}}_u$	Compute unbalanced section strain
s_7	$\tilde{\mathbf{v}}_u = \tilde{\mathbf{v}}_u + w\,\tilde{\mathbf{b}}^T(\tilde{\mathbf{e}} + \tilde{\mathbf{e}}_u)$	Sum unbalanced basic displacement
s_8	$\tilde{\mathbf{f}} = \tilde{\mathbf{f}} + w\,\tilde{\mathbf{b}}^T\tilde{\mathbf{k}}_s^{-1}\tilde{\mathbf{b}}$	Sum basic flexibility
	for every bond section $1:n_b$	**Bond sections**
s_9	$\Delta\mathbf{p}_b = \tilde{\mathbf{b}}\Delta\tilde{\mathbf{q}} + \mathbf{p}_{bu}$	Compute bond-slip stress from basic force (increments)
s_{10}	$\Delta\mathbf{u}_b = \mathbf{k}_{sb}^{-1}\Delta\mathbf{p}_b$	Compute bond-slip displacement from bond-slip stress (increments)
s_{11}	$\mathbf{u}_b = \mathbf{u}_b + \Delta\mathbf{u}_b$	Update section bond-slip displacement (total)
s_{12}	Bond section CL $\rightarrow \hat{\mathbf{p}}_b, \tilde{\mathbf{k}}_{sb}$	Compute **bond** section response
s_{13}	$\mathbf{p}_{bu} = \tilde{\mathbf{b}}\tilde{\mathbf{q}} - \hat{\mathbf{p}}_b$	Compute unbalanced section bond-slip stress
s_{14}	$\mathbf{u}_{bu} = \mathbf{k}_{sb}^{-1}\mathbf{p}_{bu}$	Compute unbalanced section bond-slip displacement
s_{15}	$\tilde{\mathbf{v}}_u = \tilde{\mathbf{v}}_u + w\,\tilde{\mathbf{b}}^T(\mathbf{u}_b + \mathbf{u}_{bu})$	Sum unbalanced basic displacement
s_{16}	$\tilde{\mathbf{f}} = \tilde{\mathbf{f}} + w\,\tilde{\mathbf{b}}^T\mathbf{k}_{sb}^{-1}\tilde{\mathbf{b}}$	Sum basic flexibility
e_5	$\tilde{\mathbf{q}} = \tilde{\mathbf{q}} - \tilde{\mathbf{f}}^{-1}\tilde{\mathbf{v}}_u$	Update basic force (total)
	for every fiber section $1:n_g$	**Sections**
s_{17}	$\tilde{\mathbf{s}}_u = \tilde{\mathbf{b}}\tilde{\mathbf{q}} - \hat{\tilde{\mathbf{s}}}$	Update unbalanced section stress for next iteration
	for every bond section $1:n_b$	**Bond sections**
s_{18}	$\mathbf{p}_{bu} = \tilde{\mathbf{b}}\tilde{\mathbf{q}} - \hat{\tilde{\mathbf{s}}}$	Update unbalanced section stress for next iteration
e_6	$\tilde{\mathbf{p}}_l = \tilde{\mathbf{a}}_g^T\tilde{\mathbf{q}} + \tilde{\mathbf{p}}_{lp}$	Compute local internal forces
e_7	$\tilde{\mathbf{k}}_l = \tilde{\mathbf{a}}_g^T\tilde{\mathbf{k}}\,\tilde{\mathbf{a}}_g$	Compute local stiffness

Figure 4.22. F-B and M-B non-iterative element state determination algorithm.

4.4.5 M-BW element state determination

The incremental element equations can be derived directly from the mixed formulation introduced in Section 2.4.6. The governing relations (2.302)-(2.304), together with the additional equilibrium of the warping forces, already provide the basic structure of the formulation. In order to obtain a numerical solution scheme, these equations are expressed in incremental form and the sectional fields are condensed.
The extended vectors are denoted with tilde notation as:

$$\tilde{\mathbf{q}} = \begin{Bmatrix} \mathbf{q}_s \\ \mathbf{q}_w \end{Bmatrix} \qquad \tilde{\mathbf{v}} = \begin{Bmatrix} \mathbf{v}_s \\ \mathbf{v}_w \end{Bmatrix} \tag{4.41}$$

The numerical form of the governing equations becomes

$$\mathbf{a}_g^T \tilde{\mathbf{q}} = \mathbf{p}_l^{ext} + \mathbf{p}_{l0} \tag{4.42}$$

$$\mathbf{b}_{s,j}\mathbf{q}_s = \hat{\mathbf{s}}_{s,j} - \mathbf{s}_{ps,j} \quad j = 1, \dots, n_g \tag{4.43}$$

$$\mathbf{v}_s = \sum_{j=1}^{n_g} \mathbf{b}_{s,j}^T \mathbf{e}_{s,j}\, w_j \tag{4.44}$$

$$\mathbf{q}_w = \sum_{j=1}^{n_g} \mathbf{B}_{w,j}^T \hat{\mathbf{s}}_{w,j}\, w_j \tag{4.45}$$

Incremental formulation
Starting from the incremental constitutive relation in partitioned form, cf. Eq. (2.255), the sectional stress increments read

$$\begin{Bmatrix} \Delta\mathbf{s}_s \\ \Delta\mathbf{s}_w \end{Bmatrix} = \begin{bmatrix} \mathbf{k}_{ss} & \mathbf{k}_{sw} \\ \mathbf{k}_{ws} & \mathbf{k}_{ww} \end{bmatrix} \begin{Bmatrix} \Delta\mathbf{e}_s \\ \Delta\mathbf{e}_w \end{Bmatrix} \tag{4.46}$$

The incremental form leads to the following residual equations:

$$\mathbf{R}_v = \mathbf{a}_g^T \Delta\tilde{\mathbf{q}} \tag{4.47}$$

$$\mathbf{R}_s = \mathbf{b}_s \Delta\mathbf{q}_s - \Delta\mathbf{s}_s \tag{4.48}$$

$$\mathbf{R}_q = \Delta\mathbf{v}_s - \sum_{j=1}^{n_g} \mathbf{b}_s^T \Delta\mathbf{e}_s\, w \tag{4.49}$$

$$\mathbf{R}_w = \Delta\mathbf{q}_w - \sum_{j=1}^{n_g} \mathbf{B}_w^T \Delta\mathbf{s}_w\, w \tag{4.50}$$

To ease the notation, subscript j indicating the section has been removed.
Since only the residual of Eq. (4.47) must vanish globally while the others can be condensed. Starting from Eq. (4.48), and by substitution of the first expression of Eq. (4.46):

$$\Delta\mathbf{e}_s = \mathbf{k}_{ss}^{-1} \left(\mathbf{b}_s \Delta\mathbf{q}_s - \mathbf{k}_{sw} \Delta\mathbf{e}_w + \mathbf{s}_{su} \right) \tag{4.51}$$

where $\mathbf{s}_{su} = \mathbf{b}_s\mathbf{q}_s + \mathbf{s}_{ps} - \hat{\mathbf{s}}_s$ are the unbalanced section stresses for the force-based components.

From Eq. (4.49) and substituting the second expression of Eq. (4.46), by setting $\mathbf{R}_w = 0$ [23]:

$$\Delta\mathbf{v}_s - \sum_{j=1}^{n_g} \mathbf{b}_s^T \Delta\mathbf{k}_{ss}^{-1} \left(\mathbf{b}_s \Delta\mathbf{q}_s - \mathbf{k}_{sw}\Delta\mathbf{e}_w + \mathbf{s}_{su}\right) w = \mathbf{0} \tag{4.52}$$

$$\Delta\mathbf{v}_s = \mathbf{f}_s \Delta\mathbf{q}_s - \mathbf{b}_{sw}\Delta\mathbf{v}_w - \mathbf{v}_{su} \tag{4.53}$$

Defining the additional operators:

$$\mathbf{f}_s = \sum_{j=1}^{n_g} \mathbf{b}_s^T \mathbf{k}_{ss}^{-1} \mathbf{b}_s \, w \qquad \mathbf{b}_{sw} = \sum_{j=1}^{n_g} \mathbf{b}_s^T \mathbf{k}_{ss}^{-1} \mathbf{k}_{sw} \mathbf{B}_w \, w \qquad \mathbf{v}_{su} = \sum_{j=1}^{n_g} \mathbf{b}_s^T \mathbf{k}_{ss}^{-1} \mathbf{s}_{su} \, w \tag{4.54}$$

From Eq. (4.50) and substituting the first expression of Eq. (4.46), by setting $\mathbf{R}_w = 0$:

$$\Delta\mathbf{q}_w - \sum_{j=1}^{n_g} \mathbf{B}_w^T (\mathbf{k}_{ws}\Delta\mathbf{e}_s + \mathbf{k}_{ww}\Delta\mathbf{e}_w) w = 0 \tag{4.55}$$

$$\Delta\mathbf{v}_w = \mathbf{k}_w^{-1} \left(\Delta\mathbf{q}_w - \mathbf{b}_{ws}\Delta\mathbf{q}_s - \mathbf{q}_{wu}\right) \tag{4.56}$$

Defining the mixed equilibrium operators:

$$\mathbf{b}_{ws} = \sum_{j=1}^{n_g} \mathbf{B}_w^T \mathbf{k}_{ws} \mathbf{k}_{ss}^{-1} \mathbf{b}_s \, w \qquad \mathbf{k}_w = \sum_{j=1}^{n_g} \mathbf{B}_w^T \bar{\mathbf{k}}_{ww} \mathbf{B}_w \, w \qquad \mathbf{q}_{wu} = \sum_{j=1}^{n_g} \mathbf{B}_w^T \mathbf{k}_{ws} \mathbf{k}_{ss}^{-1} \mathbf{s}_{su} \, w \tag{4.57}$$

By substituting Eq. (4.56) into Eq. (4.53):

$$\Delta\mathbf{v}_s - (\mathbf{f}_s + \mathbf{f}_w)\Delta\mathbf{q}_s + \mathbf{b}_{sw}\mathbf{k}_w^{-1}\Delta\mathbf{q}_w - (\mathbf{v}_{su} + \mathbf{b}_{sw}\mathbf{k}_w^{-1}\mathbf{q}_{wu}) = \mathbf{0} \tag{4.58}$$

where $\mathbf{f}_w = \mathbf{b}_{sw}\mathbf{k}_w^{-1}\mathbf{b}_{ws}$.
The complete incremental relationship in the basic system can be written in matrix form form Eq. (4.58) and Eq. (4.56) as:

$$\begin{Bmatrix} \Delta\mathbf{v}_s \\ \Delta\mathbf{v}_w \end{Bmatrix} = \begin{bmatrix} \mathbf{f}_{ss} & \mathbf{f}_{sw} \\ \mathbf{f}_{ws} & \mathbf{f}_{ww} \end{bmatrix} \begin{Bmatrix} \Delta\mathbf{q}_s \\ \Delta\mathbf{q}_w \end{Bmatrix} - \begin{Bmatrix} \mathbf{v}_{su} \\ \mathbf{v}_{wu} \end{Bmatrix} \tag{4.59}$$

where the flexibility matrix blocks are:

$$\mathbf{f}_{ss} = \mathbf{f}_s + \mathbf{f}_w = \mathbf{f}_s + \mathbf{b}_{sw}\mathbf{k}_w^{-1}\mathbf{b}_{ws} \tag{4.60}$$

$$\mathbf{f}_{sw} = -\mathbf{b}_{sw}\mathbf{k}_w^{-1} \tag{4.61}$$

$$\mathbf{f}_{ws} = -\mathbf{k}_w^{-1}\mathbf{b}_{ws} \tag{4.62}$$

$$\mathbf{f}_{ww} = \mathbf{k}_w^{-1} \tag{4.63}$$

$$\tilde{\mathbf{v}}_{su} = \mathbf{v}_{su} - \mathbf{b}_{sw}\mathbf{k}_w^{-1}\mathbf{q}_{wu} \tag{4.64}$$

$$\tilde{\mathbf{v}}_{wu} = \mathbf{k}_w^{-1}\mathbf{q}_{wu} \tag{4.65}$$

So the compact form of Eq. (4.59) reads once again:

$$\Delta\tilde{\mathbf{v}} = \tilde{\mathbf{f}}\Delta\tilde{\mathbf{q}} + \tilde{\mathbf{v}}_u \tag{4.66}$$

The local tangent element stiffness matrix and the local forces are obtained as:

$$\tilde{\mathbf{k}}_l = \tilde{\mathbf{a}}_g^T \tilde{\mathbf{f}}^{-1} \tilde{\mathbf{a}}_g \tag{4.67}$$

$$\tilde{\mathbf{p}}_l = \tilde{\mathbf{a}}_g^T \tilde{\mathbf{q}} \tag{4.68}$$

Elements initialization
In the initialization procedure, the element data are read for every element.

- The number of local degrees of freedom $d_l = 12 + 2n_f + m_w n_w$
- The basic number of degrees of freedom $d_b = 6 + m_f n_f + m_w n_w$
- The section components are $d_s = 6 + n_f + 2n_w$

The interpolation points and the quadrature scheme for both fiber and bond sections is initialized. In this case,

$$\{x_j, w_j\}_{j=1}^{n_g} = \texttt{Domain}(L, n_g)$$
$$\{x_j, w_j\}_{j=1}^{n_b} = \texttt{Domain}(L, n_b)$$

where the `Domain` function computes all the x_j and w_j, which are the quadrature points' coordinates on the axis and the weights over the element length L, respectively, both on the fiber and bond sections:

- the fiber sections' quadrature points are indicated as n_g;
- the bond sections' quadrature points are indicated as n_b.

It is worth noting that the warping part belongs to the fiber sections.

Let the index i indicate the global iteration. At the element level, the element history variables at $i = 0$ are initialized to zero,

$$\mathbf{v}^{i=0} = \mathbf{0}_{d_b}, \quad \mathbf{q}^{i=0} = \mathbf{0}_{d_b}, \quad \mathbf{v}_u^{i=0} = \mathbf{0}_{d_b}$$

The flexibility matrix $\mathbf{f}^{i=0}$ is initialized by considering everything linear elastic.

Fiber sections initialization
For each fiber section $j = 1, \ldots, n_g$, the section-level variables are initialized.
The equilibrium matrices are computed:

- the standard equilibrium matrix $\mathbf{b}_s$ is computed, depending on the formulation. In the Timoshenko formulation, $\mathbf{b}_s$ is size 6×6;
- the bond-slip equilibrium matrix $\mathbf{b}_b$ is obtained by evaluating the shape functions at the bond interpolation points. The complete equilibrium matrix for the section is:

$$\tilde{\mathbf{b}} = \begin{bmatrix} \mathbf{b}_s & \mathbf{0}_{6 \times m_f n_f} \\ \mathbf{0}_{n_f \times 6} & \mathbf{b}_b \end{bmatrix}$$

The warping compatibility matrix $\mathbf{B}_w$ is assembled by interpolating the warping shape functions and their derivatives:

$$\mathbf{B}_w = \begin{bmatrix} \mathbf{N}_w \\ \mathbf{N}_{w,x} \end{bmatrix}$$

The section history variables are initialized as

$$\tilde{\mathbf{e}}^{i=0} = \mathbf{0}_{d_s \times 1}, \quad \tilde{\mathbf{s}}^{i=0} = \mathbf{0}_{d_s \times 1}, \quad \tilde{\mathbf{s}}_u^{i=0} = \mathbf{0}_{d_s \times 1}$$

and the section stiffness matrix $\mathbf{k}_s^{i=0}$ is initially linear.

Bond sections initialization

A second loop is performed for each bond section $j = 1, \ldots, n_b$.
The equilibrium matrix is:

$$\tilde{\mathbf{b}} = \begin{bmatrix} \mathbf{0}_{n_f \times 6} & \mathbf{b}_{b,x} \end{bmatrix}$$

Thus completing the initialization process.

History variables

At every successful global step, the following vectors at the previous iteration i are updated for the next iteration $i + 1$:

- $\tilde{\mathbf{q}}^{i+1} = \tilde{\mathbf{q}}^i$, $\tilde{\mathbf{f}}^{i+1} = \tilde{\mathbf{f}}^i$ and $\tilde{\mathbf{v}}_u^{i+1} = \tilde{\mathbf{v}}_u^i$ at the element level;
- $\tilde{\mathbf{e}}^{i+1} = \tilde{\mathbf{e}}^i$, $\tilde{\mathbf{k}}_s^{i+1} = \tilde{\mathbf{k}}_s^i$ and $\tilde{\mathbf{s}}_u^{i+1} = \tilde{\mathbf{s}}_u^i$ at the section level, i.e., for every quadrature point.

M-BW element state determination

		Description
	for every element $1{:}\,n_e$	
e_1	$\Delta\tilde{\mathbf{v}} = \tilde{\mathbf{a}}_g \Delta\tilde{\mathbf{u}}_l$	Compute basic displacement from local displacement (increments, full vector)
e_2	$\Delta\tilde{\mathbf{q}} = \tilde{\mathbf{f}}^{-1}\Delta\tilde{\mathbf{v}}$	Compute trial basic force from basic displacement (increments, full vector)
e_3	$\mathbf{q}_s = \mathbf{q}_s + \Delta\mathbf{q}_s$	Update basic force (total, «s» partition of q)
e_4	Initialize $\mathbf{v}_{su}$ $\mathbf{f}_s$ $\mathbf{b}_{sw}$ $\mathbf{b}_{ws}$ $\mathbf{k}_w$ $\mathbf{q}_w$ to zero	Section initialization
	for every **fiber** section $1{:}\,n_g$	**Fiber sections**
s_1	$\Delta\mathbf{s}_s = \mathbf{b}_s\Delta\mathbf{q}_s + \mathbf{s}_p - \mathbf{s}_{su}$	Compute section stress from basic force (increments, «s» partition of $\mathbf{s}(x)$)
s_2	$\Delta\mathbf{e}_w = \mathbf{B}_w\Delta\mathbf{v}_w$	Compute section strain from section stress (increments, «w» partition of $\mathbf{e}(x)$)
s_3	$\Delta\mathbf{e}_s = \mathbf{k}_{ss}^{-1}(\Delta\mathbf{s}_s - \mathbf{k}_{sw}\Delta\mathbf{e}_w)$	Update section strain (total, «s» partition of $\mathbf{e}(x)$)
s_4	$\tilde{\mathbf{e}} = \begin{Bmatrix}\mathbf{e}_s\\ \mathbf{e}_w\end{Bmatrix} + \begin{Bmatrix}\Delta\mathbf{e}_s\\ \Delta\mathbf{e}_w\end{Bmatrix}$	Update section strain (total, full partition of $\mathbf{e}(x)$)
s_5	Fiber section CL $\rightarrow$ $\hat{\tilde{\mathbf{s}}}, \tilde{\mathbf{k}}_s$	Compute **fiber** section response
s_6	$\mathbf{q}_w = \mathbf{q}_w + w\,\mathbf{B}_w^T\hat{\mathbf{s}}_w$	Update basic forces (total, «w» partition of $\mathbf{q}$)
s_7	$\mathbf{s}_{su} = \mathbf{b}_s\mathbf{q}_s - \hat{\mathbf{s}}_s$	Compute unbalanced section stress (only for «s» components)
s_8	$\mathbf{v}_{su} = \mathbf{v}_{su} + w\,\mathbf{b}_s^T(\mathbf{e}_s + \mathbf{k}_{ss}^{-1}\mathbf{s}_{su})$	Sum vector $\mathbf{v}_{su}$
s_9	$\mathbf{q}_{wu} = \mathbf{q}_{wu} + w\,\mathbf{B}_w^T\mathbf{k}_{ws}\mathbf{k}_{ss}^{-1}\mathbf{s}_{su}$	Sum vector $\mathbf{q}_{wu}$
s_{10}	$\mathbf{f}_s = \mathbf{f}_s + w\,\mathbf{b}_s^T\mathbf{k}_{ss}^{-1}\mathbf{b}_s$	Sum matrix $\mathbf{f}_s$
s_{11}	$\mathbf{b}_{sw} = \mathbf{b}_{sw} + w\,\mathbf{b}_s^T\mathbf{k}_{ss}^{-1}\mathbf{k}_{sw}\mathbf{B}_w$	Sum matrix $\mathbf{b}_{sw}$
s_{12}	$\mathbf{b}_{ws} = \mathbf{b}_{ws} + w\,\mathbf{B}_w^T\mathbf{k}_{ws}\mathbf{k}_{ss}^{-1}\mathbf{B}_s$	Sum matrix $\mathbf{b}_{ws}$
s_{13}	$\mathbf{k}_w = \mathbf{k}_w + \mathbf{B}_w^T(\mathbf{k}_{ww} - \mathbf{k}_{ws}\mathbf{k}_{ss}^{-1}\mathbf{k}_{sw})\mathbf{B}_w$	Sum matrix $\mathbf{k}_w$
	for every **bond** section $1{:}\,n_b$	**Bond sections**
s_{14}	$\Delta\mathbf{p}_b = \tilde{\mathbf{b}}\Delta\tilde{\mathbf{q}} + \mathbf{p}_{bu}$	Compute bond-slip stress from basic force (increments)
s_{15}	$\Delta\mathbf{u}_b = \mathbf{k}_{sb}^{-1}\Delta\mathbf{p}_b$	Compute bond-slip displacement from bond-slip stress (increments)
s_{16}	$\mathbf{u}_b = \mathbf{u}_b + \Delta\mathbf{u}_b$	Update section bond-slip displacement (total)
s_{17}	Bond section CL $\rightarrow$ $\hat{\mathbf{p}}_b, \tilde{\mathbf{k}}_{sb}$	Compute **bond** section response
s_{18}	$\mathbf{p}_{bu} = \tilde{\mathbf{b}}\tilde{\mathbf{q}} - \hat{\mathbf{p}}_b$	Compute unbalanced section bond-slip stress
s_{19}	$\mathbf{u}_{bu} = \mathbf{k}_{sb}^{-1}\mathbf{p}_{bu}$	Compute unbalanced section bond-slip displacement
s_{20}	$\mathbf{v}_{su} = \mathbf{v}_{su} + w\,\tilde{\mathbf{b}}^T(\mathbf{u}_b + \mathbf{u}_{bu})$	Sum unbalanced basic displacement
s_{21}	$\mathbf{f}_s = \mathbf{f}_s + w\,\tilde{\mathbf{b}}^T\tilde{\mathbf{k}}_{sb}^{-1}\tilde{\mathbf{b}}$	Sum matrix $\mathbf{f}_s$
e_5	$\mathbf{f} = \begin{bmatrix}\mathbf{f}_s + \mathbf{b}_{sw}\mathbf{k}_w^{-1}\mathbf{b}_{ws} & -\mathbf{b}_{sw}\mathbf{k}_w^{-1}\\ -\mathbf{k}_w^{-1}\mathbf{b}_{ws} & \mathbf{k}_w^{-1}\end{bmatrix}$	Assemble basic flexibility
e_6	$\mathbf{v}_u = \begin{Bmatrix}\mathbf{v}_{su} - \mathbf{b}_{sw}\mathbf{k}_w^{-1}\mathbf{q}_{wu}\\ \mathbf{k}_w^{-1}\mathbf{q}_{wu}\end{Bmatrix}$	Assemble basic displacements residuals
e_7	$\mathbf{q} = \mathbf{q} - \mathbf{f}^{-1}\mathbf{v}_u$	Update basic force (total, «s» partition of $\mathbf{q}$)
	for every **fiber** section $1{:}\,n_g$	**Sections**
s_{22}	$\tilde{\mathbf{s}}_u = \tilde{\mathbf{b}}\tilde{\mathbf{q}} - \hat{\tilde{\mathbf{s}}}$	Update unbalanced section stress for next iteration
	for every **bond** section $1{:}\,n_b$	**Bond sections**
s_{23}	$\mathbf{p}_{bu} = \tilde{\mathbf{b}}\tilde{\mathbf{q}} - \hat{\tilde{\mathbf{s}}}$	Update unbalanced section stress for next iteration
e_8	$\tilde{\mathbf{p}}_l = \tilde{\mathbf{a}}_g^T\tilde{\mathbf{q}} + \tilde{\mathbf{p}}_{lp}$	Compute local internal forces
e_9	$\tilde{\mathbf{k}}_l = \tilde{\mathbf{a}}_g^T\tilde{\mathbf{k}}\,\tilde{\mathbf{a}}_g$	Compute local stiffness

Figure 4.23. M-BW non-iterative element state determination algorithm.

4.5 Section state determination

The determination of the section state represents a fundamental step in the nonlinear solution procedure. Following the classical fiber approach, the generalized section forces and deformations are obtained by enforcing compatibility over the discretized cross-section, while the nonlinear constitutive laws are evaluated at the material level. This strategy allows to naturally capture the multi-axial coupling of axial, flexural, shear and torsional effects, and to directly include additional contributions such as bond-slip fields or external prestressing.

The procedure is always the same for every element as it leverages on the same approach. Since the conventional strain driven constitutive laws shown in Chapter 3 are adopted, both D, F and M element formulations are so that, from the total section generalized strains $\mathbf{e}$, the total section generalized stresses $\mathbf{s}(x)$ are computed:

$$\mathbf{s}(x) = \hat{\mathbf{s}}[\mathbf{e}(x)], \qquad \mathbf{k}_s(x) = \hat{\mathbf{k}}_s[\mathbf{e}(x)]$$

where the tangent section stiffness is:

$$\hat{\mathbf{k}}_s = \frac{\partial \hat{\mathbf{s}}}{\partial \mathbf{e}}$$

So for all elements, fiber sections are computed as shown in Figure 4.24, where, for the enriched element formulations D-B, D-BW, F-B, M-B, M-BW, the modified operators denoted with tilde $\tilde{\cdot}$ are taken instead.

Fiber section state determination		
	Initialize $\hat{\mathbf{s}}$ and $\mathbf{k}_s$ to zero	*Description*
	for every fiber	
s_1	$\boldsymbol{\varepsilon} = \mathbf{a}_s \mathbf{e} + \boldsymbol{\varepsilon}_0$	Compute fiber strain
s_2	Material CL $\rightarrow \hat{\boldsymbol{\sigma}}, \mathbf{k}_m$	Apply const. law to compute fiber stress and stiffness
s_3	$\hat{\mathbf{s}} = \hat{\mathbf{s}} + A\, \mathbf{a}_s^T \hat{\boldsymbol{\sigma}}$	Sum section stress
s_4	$\mathbf{k}_s = \mathbf{k}_s + A\, \mathbf{a}_s^T \mathbf{k}_m \mathbf{a}_s$	Sum section stiffness

Figure 4.24. Fiber section state determination algorithm where A is the fiber's area.

For bond sections, a different section state determination algorithm is applied, as shown in Figure 4.25, where, from the bond-slip displacements, the forces in the bond interfaces $\mathbf{s}_b$.

Bond section state determination		
	for every fiber with bond-slip	*Description*
s_1	$u_{b,f} = \mathbf{e}(f)$	Select bond-slip displacement at fiber f
s_2	Bond CL $\rightarrow \hat{\tau}_{b,f} \quad k_{b,f}$	Apply bond-slip law to compute shear stress and stiffness
s_3	$\hat{\mathbf{s}}_b(f) = l_{b,f}\, \hat{\tau}_{b,f}$	Sum section stress
s_4	$\mathbf{k}_{sb}(f,f) = l_{b,f}\, k_{b,f}$	Sum section stiffness

Figure 4.25. Bond section state determination algorithm.

4.5.1 D, F and M section state determination

The section compatibility matrix must be computed in the section initialization process. It can be defined recalling Eq. (2.34):

$$\boldsymbol{\varepsilon}_m = \mathbf{R}\ \mathbf{a}_s\, \mathbf{e} + \boldsymbol{\varepsilon}_0 \tag{4.69}$$

where, in the case of the Timoshenko formulation the section compatibility matrix is defined as in Eq. (2.16):

$$\mathbf{a}_s = \begin{bmatrix} 1 & -y & z & 0 & 0 & 0 \\ 0 & 0 & 0 & s_y & 0 & -z\sqrt{\zeta_x} \\ 0 & 0 & 0 & 0 & s_z & y\sqrt{\zeta_x} \end{bmatrix} \tag{4.70}$$

and the rotation matrix $\mathbf{R}$ is an identity matrix in case of straight fibers, while it is computed according to (4.4) for curved fibers.

The following information has to be stored for every fiber:

- positions y, z;
- area A;
- angles β_y and β_z for curved fibers;
- constitutive law;
- initial strain $\boldsymbol{\varepsilon}_0$ which is dependent on the global time step i;
- s_y and s_z values for shear interpolation;
- ζ_x values for the torsion adjustment.

No section history variables are needed.

4.5.2 D-B, F-B and M-B section state determination

The section compatibility matrix must be computed in the section initialization process. It can be defined recalling Eq. (2.117):

$$\boldsymbol{\varepsilon} = \mathbf{R}\ \tilde{\mathbf{a}}_s\, \tilde{\mathbf{e}} + \boldsymbol{\varepsilon}_0 \tag{4.71}$$

where $\tilde{\mathbf{a}}_s$ is, in the case of the Timoshenko formulation:

$$\tilde{\mathbf{a}}_s = \begin{bmatrix} 1 & -y & z & 0 & 0 & 0 & \boldsymbol{\delta}_b \\ 0 & 0 & 0 & s_y & 0 & -z\sqrt{\zeta_x} & \mathbf{0} \\ 0 & 0 & 0 & 0 & s_z & y\sqrt{\zeta_x} & \mathbf{0} \end{bmatrix}$$

and

$$\tilde{\mathbf{e}} = \begin{Bmatrix} \mathbf{e} \\ \mathbf{e}_b \end{Bmatrix}$$

and the rotation matrix $\mathbf{R}$ is an identity matrix in case of straight fibers, while it is computed according to (4.4) for curved fibers.

The following information has to be stored for every fiber:

- positions y, z;

- area A;
- angles β_y and β_z for curved fibers;
- constitutive law;
- initial strain $\boldsymbol{\varepsilon}_0$ which is dependent on the global time step i;
- the row vector $\boldsymbol{\delta}_b$ has length n_f and it has 1 in the f^{th} position for the corresponding fiber with bond-slip and 0 everywhere else. It is used to select $\varepsilon_{b,f}$ out of vector $\mathbf{e}_b$.

No section history variables are needed.

4.5.3 D-BW and M-BW section state determination

The section compatibility matrix must be computed in the section initialization process. It can be defined recalling Eq. (2.214):

$$\boldsymbol{\varepsilon}_m = \mathbf{R}\ \tilde{\mathbf{a}}_s\ \tilde{\mathbf{e}} + \boldsymbol{\varepsilon}_0 \tag{4.72}$$

where:

$$\tilde{\mathbf{a}}_s = \begin{bmatrix} 1 & -y & z & 0 & 0 & 0 & \boldsymbol{\delta}_b & \mathbf{0} & \mathbf{M}_\eta \\ 0 & 0 & 0 & s_y & 0 & -z & \mathbf{0} & \mathbf{M}_{\eta,y} & \mathbf{0} \\ 0 & 0 & 0 & 0 & s_z & y & \mathbf{0} & \mathbf{M}_{\eta,z} & \mathbf{0} \end{bmatrix} \tag{4.73}$$

and the modified section strains $\tilde{\mathbf{e}}$ are:

$$\tilde{\mathbf{e}} = \begin{Bmatrix} \mathbf{e} \\ \mathbf{e}_b \\ \boldsymbol{\eta} \\ \boldsymbol{\eta}_x \end{Bmatrix} = \begin{Bmatrix} \mathbf{e} \\ \mathbf{e}_b \\ \mathbf{e}_w \end{Bmatrix} \tag{4.74}$$

The following information has to be stored for every fiber:

- positions y, z;
- area A;
- angles β_y and β_z for curved fibers;
- constitutive law;
- initial strain $\boldsymbol{\varepsilon}_0$ which is dependent on the global time step i;
- the row vector $\boldsymbol{\delta}_b$;
- every section warping interpolation function $\mathbf{M}_\eta$, $\mathbf{M}_{\eta,y}$ and $\mathbf{M}_{\eta,z}$.

No section history variables are needed.

4.6 Material state determination

The goal of the Material State Determination is to compute the stresses $\boldsymbol{\sigma}_m(x,y,z)$ and the tangent stiffness matrix $\mathbf{k}_m(x,y,z)$ for the given material strains $\boldsymbol{\varepsilon}_m(x,y,z)$ at each fiber integration point M. This procedure is required at every Gauss point of the section integration scheme, in order to transfer the material nonlinearities to the section and, subsequently, to the element level. Formally, the process may be expressed as

$$\boldsymbol{\sigma}_m(x,y,z) = \hat{\boldsymbol{\sigma}}_m\big[\boldsymbol{\varepsilon}_m(x,y,z)\big], \qquad \mathbf{k}_m(x,y,z) = \hat{\mathbf{k}}_m\big[\boldsymbol{\varepsilon}_m(x,y,z)\big]$$

where the tangent section stiffness is:

$$\hat{\mathbf{k}}_m(x,y,z) = \frac{\partial \hat{\boldsymbol{\sigma}}_m(x,y,z)}{\partial \boldsymbol{\varepsilon}_m(x,y,z)}$$

To carry out this operation two tasks must be addressed.
First, in the beam element context, only a subset of the six stress/strain components is relevant, depending on the adopted formulation. For instance, in Timoshenko-type formulations the independent strains are

$$\boldsymbol{\varepsilon}_m = \{\varepsilon_x \ \gamma_{xy} \ \gamma_{xz}\}^T$$

with the corresponding work-conjugate stresses

$$\boldsymbol{\sigma}_m = \{\sigma_x \ \tau_{xy} \ \tau_{xz}\}^T$$

The remaining components,

$$\boldsymbol{\varepsilon}_c = \{\varepsilon_y, \ \varepsilon_z, \ \gamma_{yz}\}^T \qquad \boldsymbol{\sigma}_c = \{\sigma_y, \ \sigma_z, \ \tau_{yz}\}^T$$

must be eliminated through a static condensation procedure, since they do not correspond to independent section variables.

First, referring to a general 3D constitutive model, an algorithm must be defined to evaluate the six-component stress vector $\boldsymbol{\sigma}(x,y,z)$ and the full tangent stiffness matrix $\mathbf{C}_t$, given a six-component strain vector $\boldsymbol{\varepsilon}(x,y,z)$. This part depends on the specific constitutive law adopted (plasticity, damage, plastic-damage, etc.), and is here referred to as the 3D Material State Determination.

4.6.1 Nonlinear static condensation

To include the general 3D material model into the fiber formulation, a nonlinear static condensation is performed. The incremental constitutive relation can be written as

$$\Delta\boldsymbol{\sigma} = \mathbf{C}_t \, \Delta\boldsymbol{\varepsilon} \quad \rightarrow \quad \begin{Bmatrix} \Delta\boldsymbol{\sigma}_m \\ \Delta\boldsymbol{\sigma}_c \end{Bmatrix} = \begin{bmatrix} \mathbf{C}_{t,mm} & \mathbf{C}_{t,mc} \\ \mathbf{C}_{t,cm} & \mathbf{C}_{t,cc} \end{bmatrix} \begin{Bmatrix} \Delta\boldsymbol{\varepsilon}_m \\ \Delta\boldsymbol{\varepsilon}_c \end{Bmatrix}$$

The condensed variables $\boldsymbol{\varepsilon}_c$ must be evaluated such that $\boldsymbol{\sigma}_c = \mathbf{0}$, therefore their values must be determined iteratively.

Let us define the following indices:

- i indicates the global step;
- l indicates the global iterations required for every step i;
- k indicates the material iterations required for every iteration l.

No other iterations are required as only non-iterative elements and sections are presented in this work.

- **Iterative condensation** · At the material level iteration $k+1$, the corrective update of $\boldsymbol{\varepsilon}_c$ is computed as

$$\Delta\boldsymbol{\varepsilon}_c^{k+1} = -\left(\mathbf{C}_{t,cc}^{i}\right)^{-1}\boldsymbol{\sigma}_c^{k+1}, \qquad \boldsymbol{\varepsilon}_c^{k+1} = \boldsymbol{\varepsilon}_c^{i} + \Delta\boldsymbol{\varepsilon}_c^{k+1}$$

  The procedure continues until the residual $\|\boldsymbol{\sigma}_c^{k+1}\|$ falls below a prescribed tolerance. The condensed tangent stiffness is then given by

$$\mathbf{k}_m = \mathbf{C}_{t,mm} - \mathbf{C}_{t,mc}\,\mathbf{C}_{t,cc}^{-1}\,\mathbf{C}_{t,cm}$$

- **Non-iterative condensation** · At the global level iteration $l+1$, the material response from the previous element iteration is considered linear, avoiding the inner Newton-Raphson loop at the material level. In this case, the condensed strains are updated as

$$\Delta\boldsymbol{\varepsilon}_c^{l+1} = -\mathbf{C}_{t,cm}^{l}\left(\mathbf{C}_{t,mm}^{l}\right)^{-1}\Delta\boldsymbol{\varepsilon}_m^{l+1}, \qquad \boldsymbol{\varepsilon}_c^{l+1} = \boldsymbol{\varepsilon}_c^{l} + \Delta\boldsymbol{\varepsilon}_c^{l+1}$$

  The condensed stresses and tangent operator follow as

$$\boldsymbol{\sigma}_m^{l+1} = \boldsymbol{\sigma}_m^{l} + \mathbf{k}_m^{l}\,\Delta\boldsymbol{\varepsilon}_m^{l+1}, \qquad \mathbf{k}_m^{l+1} = \mathbf{C}_{t,mm}^{l} - \mathbf{C}_{t,mc}^{l}\left(\mathbf{C}_{t,cc}^{l}\right)^{-1}\mathbf{C}_{t,cm}^{l}$$

This algorithm provides the link between the fiber-level constitutive behavior and the cross-section response, ensuring consistency in the nonlinear beam formulation while retaining the efficiency of the fiber discretization approach.

The procedure is synthetically reported in Figure 4.26.

4.6.2 Material response

Different material models are considered in this work, as introduced in Chapter 3. Since the numerical procedures adopted to evaluate the response of each material are already well established and do not introduce novel contributions, they are not reported here in detail; the reader is referred to the specific works for a comprehensive description.

Nevertheless, some aspects relevant to the present formulation deserve emphasis:

- each fiber requires the complete stress vector $\boldsymbol{\sigma}_m$ corresponding to a given strain state $\boldsymbol{\varepsilon}_m$; however, this evaluation is only meaningful for fibers belonging to the cementitious matrix, where experimental evidence highlights the role of shear stresses. Accordingly, a

3D constitutive law is adopted for concrete-like materials;

- longitudinal fibers, such as prestressing tendons and reinforcing bars, are modeled through one-dimensional constitutive laws. These fibers, especially when associated with bond-slip mechanisms, do not contribute to shear unless explicitly prescribed. In the formulation, this is enforced by setting $s_y = s_z = 0$ in the compatibility operators $\mathbf{a}_s$;
- the bond-slip response is evaluated as illustrated in the algorithm of Figure 4.25, by employing generic 1D constitutive relations where the axial stress–strain law $\hat{\sigma}(\varepsilon)$ is replaced by a bond law $\hat{\tau}(u_b)$ relating shear stress to slip;
- the history variables depend on the specific constitutive law (e.g. plastic strains and so on) and they are saved only if global convergence is achieved.

Material state determination

	Iterative	Non iterative	*Description*
m_1	$\Delta\boldsymbol{\varepsilon}_c = -\mathbf{C}_{t,cc}^{-1}\boldsymbol{\sigma}_c$	$\Delta\boldsymbol{\varepsilon}_c = -\mathbf{C}_{t,cm}\left(\mathbf{C}_{t,mm}\right)^{-1}\boldsymbol{\varepsilon}_m$	Compute condensed strains increment
m_2	$\boldsymbol{\varepsilon}_c = \boldsymbol{\varepsilon}_c + \Delta\boldsymbol{\varepsilon}_c$		Update total condensed strains
m_3	$\begin{Bmatrix}\boldsymbol{\varepsilon}_m \\ \boldsymbol{\varepsilon}_c\end{Bmatrix} = \boldsymbol{\varepsilon} \quad \rightarrow \quad \widehat{\boldsymbol{\sigma}} = \begin{Bmatrix}\boldsymbol{\sigma}_m \\ \boldsymbol{\sigma}_c\end{Bmatrix}, \hat{\mathbf{C}}_t = \begin{bmatrix}\mathbf{C}_{t,mm} & \mathbf{C}_{t,mc} \\ \mathbf{C}_{t,cm} & \mathbf{C}_{t,cc}\end{bmatrix}$		Assemble total strains and apply the 3D constitutive law to return the stress and the tangent stiffness
m_4	Repeat until $\lvert\boldsymbol{\sigma}_c\rvert < tol$ or $l > l_{max}$		
m_5	$\mathbf{k}_m = \mathbf{C}_{t,mm} - \mathbf{C}_{t,mc}\left(\mathbf{C}_{t,cc}\right)^{-1}\mathbf{C}_{t,cm}$		Condense tangent stiffness

Figure 4.26. Material state determination algorithm

Chapter 5

Numerical applications

This chapter presents numerical applications designed to validate the formulations introduced in Sections 2.2–2.4, together with the corresponding element state determination strategies of Section 4.4, by assessing their performance in representing structural problems. The studies are organized in three blocks, following the structure of Chapter 2.

First, classical Euler-Bernoulli and Timoshenko beam formulations are benchmarked to expose lack of objectivity under softening, including pathological localization, mesh sensitivity, and the limited effectiveness of fracture-energy regularization when used alone. This initial block sets the reference problems and the metrics used across the chapter.

Second, the bond-slip beam formulations are extended to prestressed members, covering externally and internally prestressed configurations, time staging, bond that vary along the member and in time to represent different interfaces and materials, Timoshenko kinematics and coupled damage-plasticity. This block focuses on validations against experiments to demonstrate the extension to prestressing, building on the relevant literature discussed in Chapter 2 [50, 52, 53].

Third, the enhanced elements are tested with sectional warping displacements combined with bond-slip. In these applications, the beneficial effects of considering bond-slip and warping together on beam elements are highlighted, as the bond law produces physically consistent crack formation and spacing, while the warping field restores the objectivity deficiencies that remain when fracture-energy regularization is used alone. The resulting kinematics regularizes the global response under severe tensile softening at cracking stages.

The objectives of this chapter are threefold: validation of the proposed formulations at the element, section, and global levels, assessment of accuracy and robustness with respect to mesh and regularization choices, solution reliability in terms of convergence and path following. A specific distinction is made between localization and regularization in compression, which has been extensively studied in the literature, and localization at first cracking in tension, which represents the novel focus of this work.

All enhanced models used in Sections 5.2 and 5.3 are implemented in a general-purpose finite element solver developed in MATLAB. The applications in Section 5.1 that use standard fiber elements are reproduced in OPENSEES for reference and cross-checking. The nonlinear solution employs Newton-Raphson schemes with displacement or load control and an arc-length option

where needed. Because wall-clock times depend on hardware and discretization, only indicative remarks are provided; for the meshes reported, runs complete within minutes, and the discussion focuses on accuracy and objectivity rather than efficiency.

The narrative follows this order:

1. Section 5.1 establishes the reference problems and quantifies mesh dependence in classical settings, clarifying the limitations of fracture-energy regularization in tension when used alone or not used at all;

2. Section 5.2 presents prestressed members with bond-slip, including time-staged analyses and spatial/stage bond variability, and compares predictions with experimental evidence;

3. Section 5.3 demonstrates that coupling bond-slip with sectional warping degrees of freedom restores the numerical objectivity for both local and global responses, improving the consistency of the results as the mesh gets finer.

For each application, geometry and boundary conditions, section discretization and integration rules, warping layout when present, constitutive parameters for steel, concrete, bond, and prestress are reported together with mesh and refinement checks used to verify convergence and objectivity. Input files and plotting scripts are organized to allow straightforward reruns in MATLAB for the enhanced models and in OPENSEES for the classical references.

5.1 Numerical objectivity issues of classical beam elements

Despite numerous advancements, classical beam models still face challenges in accurately representing critical phenomena such as bond–slip interaction and cracking [89, 17]. This chapter examines these limitations by discussing numerical issues in standard finite element formulations, with particular emphasis on bond–slip effects.

DB models are widely used for their simplicity and ease of implementation, but under severe nonlinearities the assumed kinematics becomes inadequate. This leads to inaccurate solutions unless fine meshes are employed, and may cause numerical instabilities or convergence problems under large deformations or complex loading conditions [54]. FB models, in contrast, can capture nonlinear behavior and complex loading scenarios with a single element per structural member, making them highly effective in nonlinear analyses [37, 10, 5].

Both DB and FB models are commonly coupled with fiber sections to represent the axial force–moment–curvature (PMM) interaction. The choice of constitutive models is therefore crucial. However, when softening is involved, strain localization makes results strongly mesh-dependent. Regularization strategies, such as local and nonlocal strategies, are required to restore objectivity and ensure mesh-independent predictions [73, 5, 90, 72].

Further developments have addressed the limitations of classical kinematic assumptions. The hypothesis that plane sections remain plane is effective for slender beams but fails in several applications: thin-walled members may undergo warping deformations [92], deep beams experience shear lag, and curved or dynamically loaded beams exhibit complex non-planar modes [123, 124].

The interaction between concrete and reinforcement, particularly bond–slip behavior, is another

critical aspect often oversimplified by assuming perfect bond. This leads to inaccurate predictions of stiffness, strength, and crack development [94]. Bond–slip can be introduced explicitly, by modeling relative displacements with springs or interface elements, or implicitly, by enriching the element formulation with modified constitutive laws, additional degrees of freedom, or enhanced interpolations [47, 49, 52, 27, 94].

Recent studies [94] have shown that both explicit and implicit strategies are effective in capturing reinforcement–concrete interaction, significantly improving the predictive capability of beam finite element models in scenarios where bond–slip plays a dominant role.

Even though regularization techniques mitigate localization problems, they do not fully resolve objectivity issues, as highlighted in this section. The enhanced beam formulations developed in this work not only extend the modeling capabilities of RC structures affected by cracking, bond–slip, and warping, but also improve the accuracy and objectivity of conventional approaches, while at the same time revealing their intrinsic limitations in structural analysis.

5.1.1 Numerical outcomes of beam elements with perfect-bond and bond-slip

This section is structured to address the numerical challenges in beam finite element formulations with a focus on bond-slip effects, presenting practical test cases. It explores bending tests on plain concrete and RC beams with perfect-bond and bond-slip models, examining how these models perform under different conditions and highlighting where mesh-dependency issues occur.

Only flexural failure is considered in the analyses as it helps emphasize objectivity issues. Therefore, two models are considered in this section:

1. Perfect bond fiber-section models
2. Explicit bond-slip models

The explicit bond-slip models are based on the following assumptions:

- steel rebars are modeled using truss elements;
- rigid links and unidirectional springs are used to model the bond-slip behavior between the concrete fiber section and the steel rebars;
- uniaxial constitutive laws describe both the concrete fibers and the steel trusses response. Finally, a bond-slip relationship is assigned to the unidirectional springs that represents the bond interface.

In the former, the steel rebars are discretized as fibers fully bonded to the concrete fibers. In the latter, the steel rebars are modeled explicitly as truss elements connected to the beam element through nonlinear nodal springs that allow relative displacements and then a bond-slip relationship. Figs. 5.1 and 5.2 show the numerical setups that introduce bond-slip between beam and truss elements.
The simulations are run in OpenSees [39] and STKO [125] is used to process the results.

Three different constitutive laws are introduced for concrete, steel and bond-slip interface, respectively.

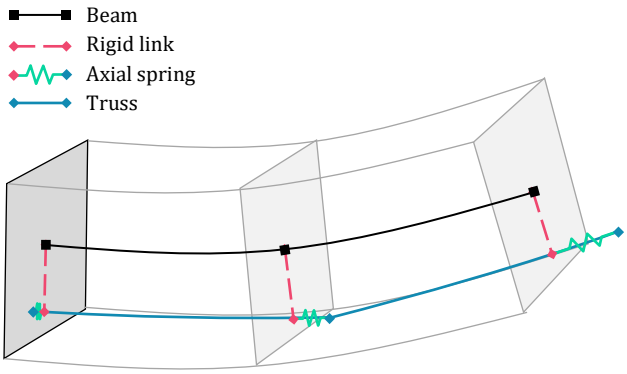

Figure 5.1. Explicit configuration of beam-with-bond model.

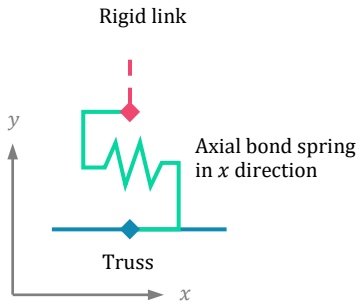

Figure 5.2. Axial spring configuration in the local initial undeformed configuration.

The concrete model is available in OpenSees and is based on the damage-plastic constitutive law proposed in [9]. It has a Bezier interpolation scheme for the damage evolution and a plasticity algorithm, and uses a parameter ranging from 0 to 1 which controls the yielding region, where 0 corresponds to a Drucker-Prager criterion [74] and 1 corresponds to a modified criterion presented in [100]. Another parameter ranging from 0 to 1 controls damage using different interpolation points in tension and compression to allow for a non-symmetric response. The 1D unconfined version is used here. An example of the cyclic behavior is shown in Fig. 5.3.

The steel model is based on Menegotto and Pinto [3] as of Section 3.4.1, while the bond-slip interface model is by Lowes et al [126] as of Section 3.4.3.

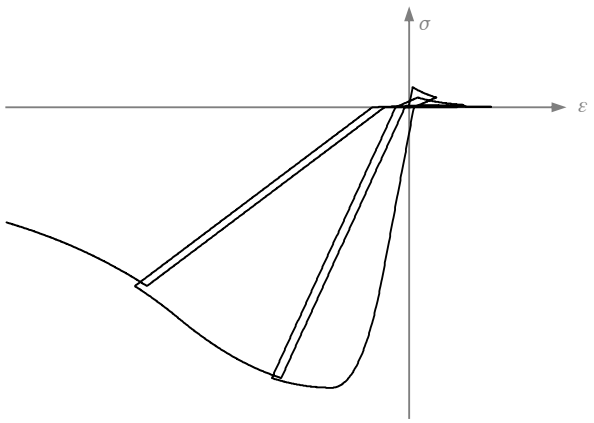

Figure 5.3. Concrete constitutive model available in OpenSees [9].

This chapter investigates the performance of fracture energy-based regularization methods, as these are widely adopted due to their straightforward implementation, in attempting to obtain objective results in presence of strain-softening behavior, as in case of reinforced concrete elements, according to Section 4.3.2.
In this case, the post-peak softening response is controlled by two different fracture energy parameters, labeled as G_t and G_c for tension and compression, respectively. A characteristic length, l_{ch}, is introduced, evaluated as the ratio of the length of the damaging zone, and the mesh integration length [90].

Numerical tests on the simple beam schematically shown in Fig. 5.4 and labeled beam J4 in [127] are carried out. Geometric and mechanical data are reported in Table 5.1. For symmetry, only half of the beam is represented and the left end with restrained rotation is the beam midspan.

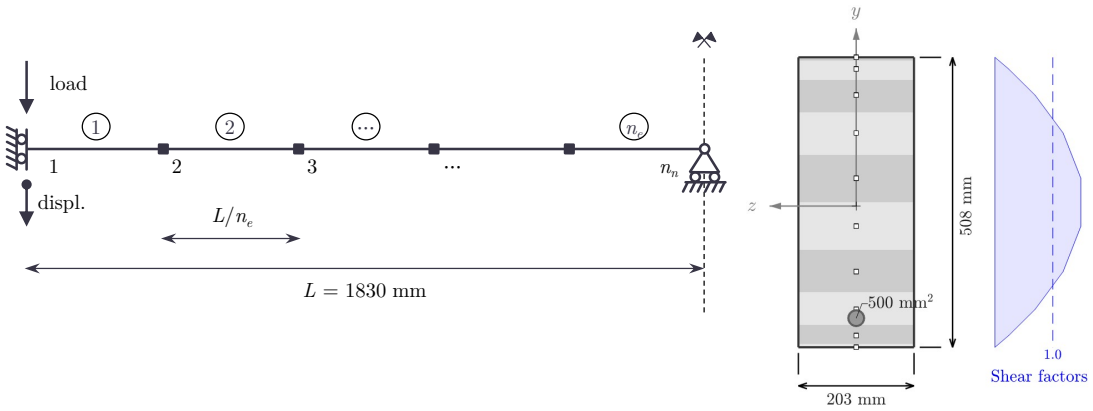

Figure 5.4. Static configuration and numerical discretization of beam J4.

Concrete		Steel	
$E_c\ [MPa]$	26200	$E_s\ [MPa]$	203395
$f_t\ [MPa]$	2.4	$\sigma_y\ [MPa]$	309.65
$f_c\ [MPa]$	33.24	b	0.01
$G_t\ [N/mm]$	0.0875	$A_s\ [mm^2]$	$100 \div 1000$

Table 5.1. Geometric and mechanical parameters of beam J4.

5.1.2 Bending test on plain concrete beam

First, a fiber-section beam model is used to study the numerical response of the unreinforced beam. The beam is discretized using an increasing number of FEs ranging from 10 to 320. In the first test, curvature and axial strain always localize in the first element to the left of midspan, as it is the only one experiencing cracking. In Fig. 5.5, on the left, the global response is shown for DB and FB elements. A Gauss-Lobatto integration scheme, involving two quadrature points, is used here for both approaches, requiring the FB elements to be regularized considering half mesh length i.e., by using a double fracture energy amount. A similar behavior can here be observed for both approaches, and it is clear that the peak point, that corresponds to the crack formation, keeps moving until eventually, in the limit case labeled as "infty" in Fig. 5.5(a), concrete does not crack at all and responds as a ductile material. In Fig. 5.5(b) the fiber tensile response shows the effect of the fracture energy regularization.

Fig. 5.6 shows the first section top (compression-left) and bottom (tension-right) fibers' strain

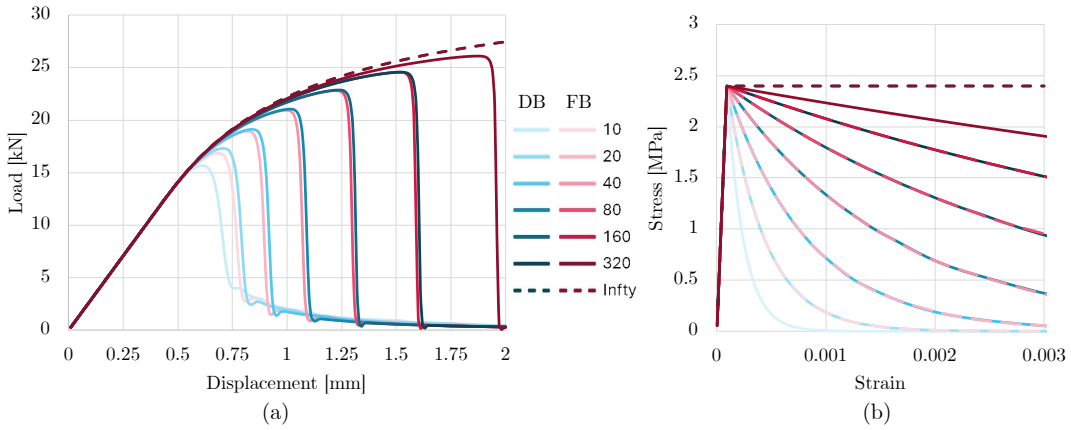

Figure 5.5. (a) global response for DB and FB approaches and (b) lower fiber tensile stress vs strain, both for a progressively increasing number of FEs.

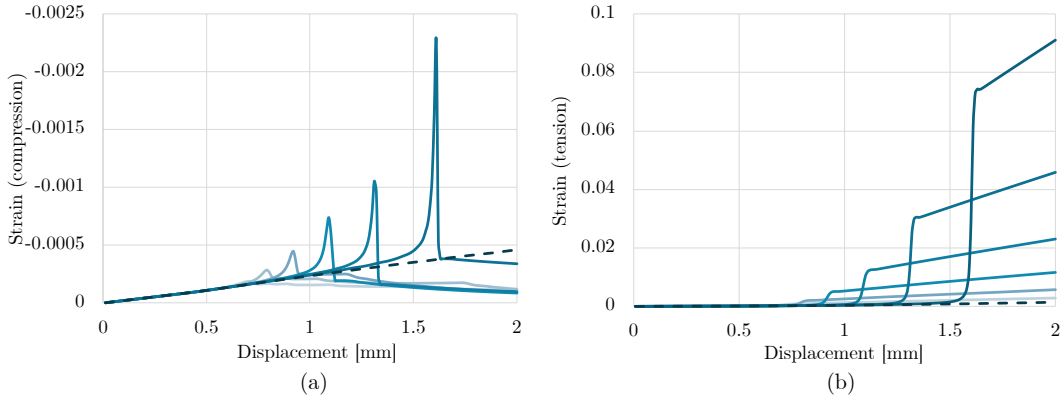

Figure 5.6. (a) compressed top fiber strain over global displacement for the DB case; (b) tensile bottom fiber strain over global displacement for the DB case.

evolution as the midspan displacement increases. The concrete compression softening branch is never engaged here as concrete cracking leads to sudden element failure and the descending response in compression in Fig. 5.6 represents stress unloading. Peaks correspond to cracking stages. The two figures clearly show that the fracture energy regularization performs poorly: the post-cracking softening curve is indeed regularized but the overall response is still largely subject to numerical dependencies. Convergence can be achieved when an infinite amount of fracture energy is considered, but this represents a non-realistic case.

5.1.3 Bending tests on reinforced concrete beam with perfect-bond and with bond-slip

This section details the impact of the interaction between concrete and steel under the assumptions of perfect bond and bond-slip. It is organized as follows:

- response of fiber section with perfect-bond beam element;
- response of concrete fiber section beam element plus rebars with bond-slip with different reinforcement ratios and with different bond conditions (perfect-bond and low-bond);
- effect of the mesh refinements with variable reinforcement ratio;

- effect of bond on explicit models;
- non-regularized case for explicit models.

In this section, only results on DB elements are shown since similar outcomes are also expected for FB elements, as shown in Section 5.1.2 where a plain concrete section is tested. The response of a classical fiber beam with perfect bond is studied first. A specimen with very little reinforcement ratio ρ is analyzed ($\rho = A_s/A_c = 0.1\%$, where A_s is the steel area and A_c is the concrete section gross area). The mesh is progressively refined, and the response is studied with and without regularization. The aim is to highlight the softening branch after first cracking and display the different behaviors. Fig. 5.7(a) clearly highlights the effects of the tension fracture energy regularization: the softening branches show similar trends but start at different peak stages. This is clearly shown by the steel response, which yields at different stages for each mesh. Without regularization (Fig. 5.7(b)), both peaks and softening trends are completely different, as for non-regularized cases, a pathological mesh dependency is expected.

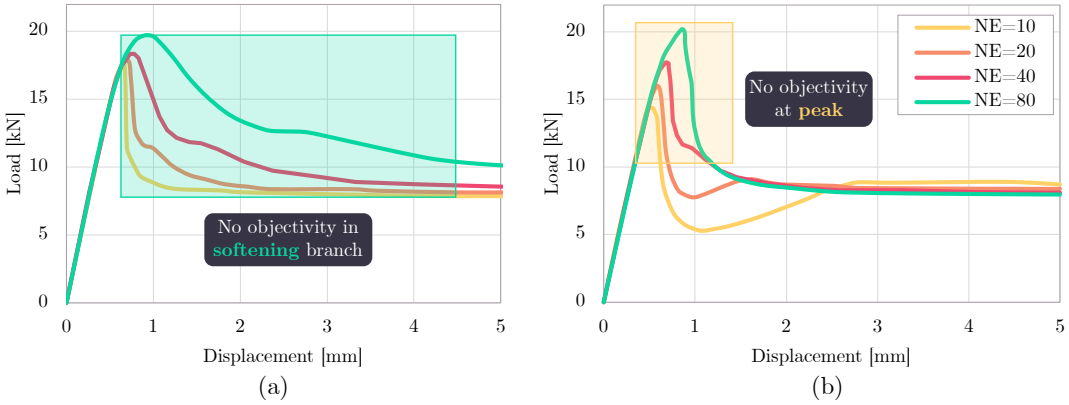

Figure 5.7. Global responses considering a low amount of steel, equal to $\rho = 0.1\%$, for (a) non-regularized FE model and (b) fracture energy regularized FE model.

The effect of bond is investigated in Fig. 5.8 for a medium amount of reinforcement $\rho = 0.5\%$. The mesh is discretized with 10 regularized FEs. When the bond is relatively poor, the overall contribution of steel is low and only one crack is formed. When the maximum bond stress is $\max(\tau) > 1$ MPa, more cracks are formed along the beam at an increasing density as the bond intensity improves.

Three different steel reinforcement ratios are used in Fig. 5.9, $\rho = 0.1\%$, $\rho = 0.5\%$ and $\rho = 1.0\%$. Both perfect-bond and low-bond cases are represented employing explicit modeling: in both cases only one crack at the midspan forms, and the response is overestimated with respect to the experimental case.

By assuming a realistic bond-slip law, as in this case where $\max(\tau) = 2$ MPa, results are non-objective as the mesh changes. Fig. 5.10 shows that, for three reinforcement ratios and for numbers of FEs from 10 to 1280, the global response does not regularize and convergence is not achieved at the cracking stage.

Fig. 5.11 shows the evolution of the steel strain for all the considered cases. Although it eventually converges in the hardening stage for highly refined meshes, the yielding strain is

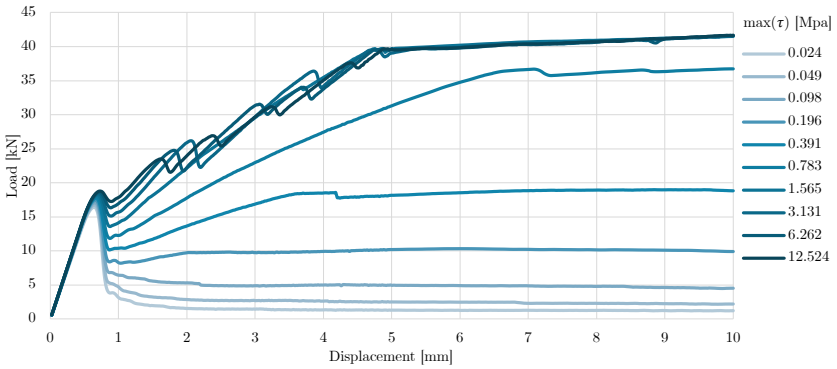

Figure 5.8. Global response with $\rho = 0.5\%$ with variable bond strength $\max(\tau)$ using 10 elements for every case.

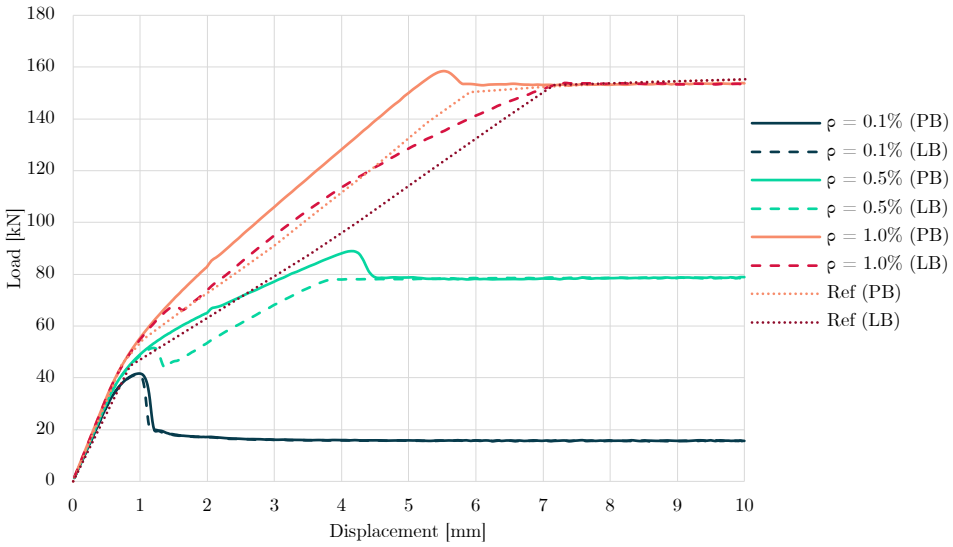

Figure 5.9. Global response with variable amount of reinforcement ratio ρ using 40 elements to discretize the beam. Experimental comparisons (ref) are reported for perfect- (PB) and low-bond (LB) as a comparison.

different for every case.

Fig. 5.12 shows the displacement at which the second crack forms (left) and the distance between the first two cracks. The left diagram shows no sign of convergence, and no cracks are observed, in a concentrated sense, for more than 80 FEs. The right diagram shows that a general correspondence between analytic and numerical results is achieved at 40-80 elements, but there is no overall objectivity. Fig. 5.13 shows how the steel reinforcement responds in various cases: while the post-yielding steel strain eventually stabilizes for a high number of FEs, the yielding strain occurs at different midspan displacements, which might still differ from the infinite fracture energy limit case. Curvatures and fiber stress for the first three meshes are reported in Fig. 5.14. Curvature peaks indicate that a crack has opened in that region. Fig. 5.14(a,b,c) correspond to a lower reinforcement ratio, therefore a lower interaction area and poor bond, while Fig. 5.14(d,e,f) correspond to a higher reinforcement ratio.

In addition, tests without regularization were intentionally carried out for the $\rho = 0.5\%$ case. As shown in Fig. 5.15, the resulting curves are quite regular. This regularity arises because, even

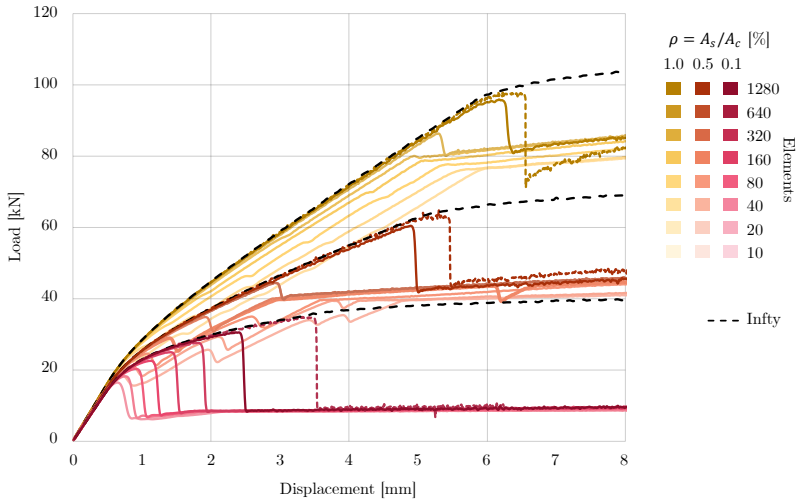

Figure 5.10. Global response with increasing number of FEs to discretize the beam. Experimental comparisons (ref) are reported for perfect- (PB) and low-bond (LB) as a comparison.

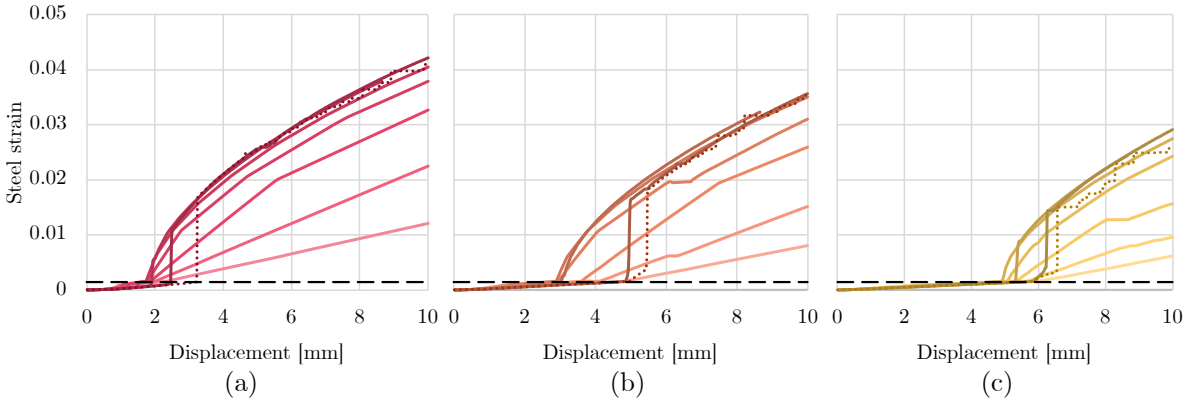

Figure 5.11. Steel strain vs displacement for all the meshes and $\rho = 0.1 - 0.5 - 1.0\%$ from left to right. The black dashed line represents the steel yielding strain threshold.

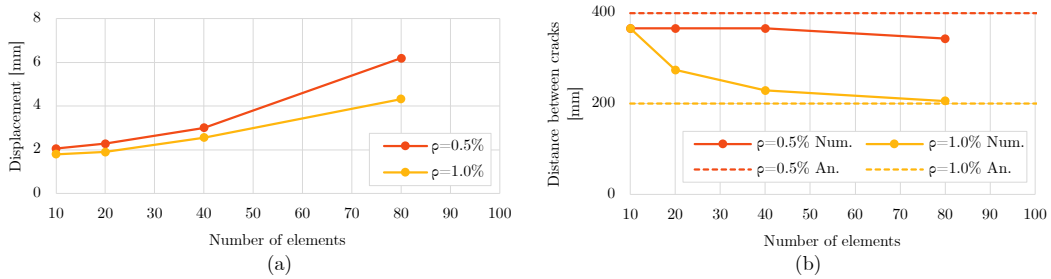

Figure 5.12. Steel behavior for different reinforcement ratios: (left) steel strain in midspan section at specified displacements and (right) midspan displacement at steel yielding.

with the initial mesh, the softening behavior is very stiff due to the low tensile fracture energy of concrete. Consequently, there are minimal changes observed as the mesh refines. When examining the curvature distributions, which indicate the cracks' locations, similar patterns emerge across all meshes. This similarity is especially apparent in the finer meshes. However, an unrealistic issue arises: the curvature tends to spread across adjacent elements. This spread suggests that

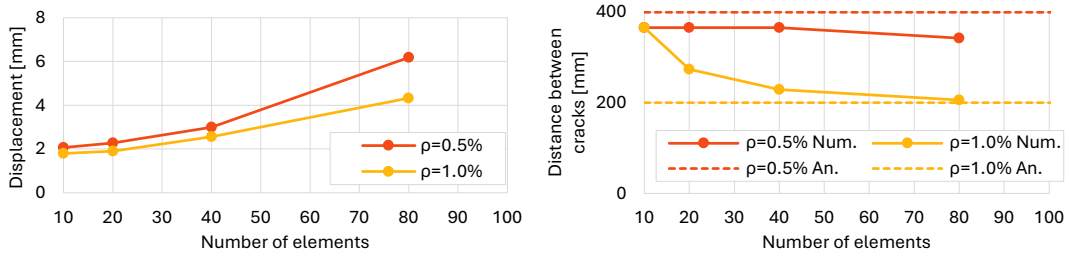

Figure 5.13. Evolution of cracking for different meshes: (left) midspan displacement corresponding to second crack opening and (right) distance between the first and the second crack.

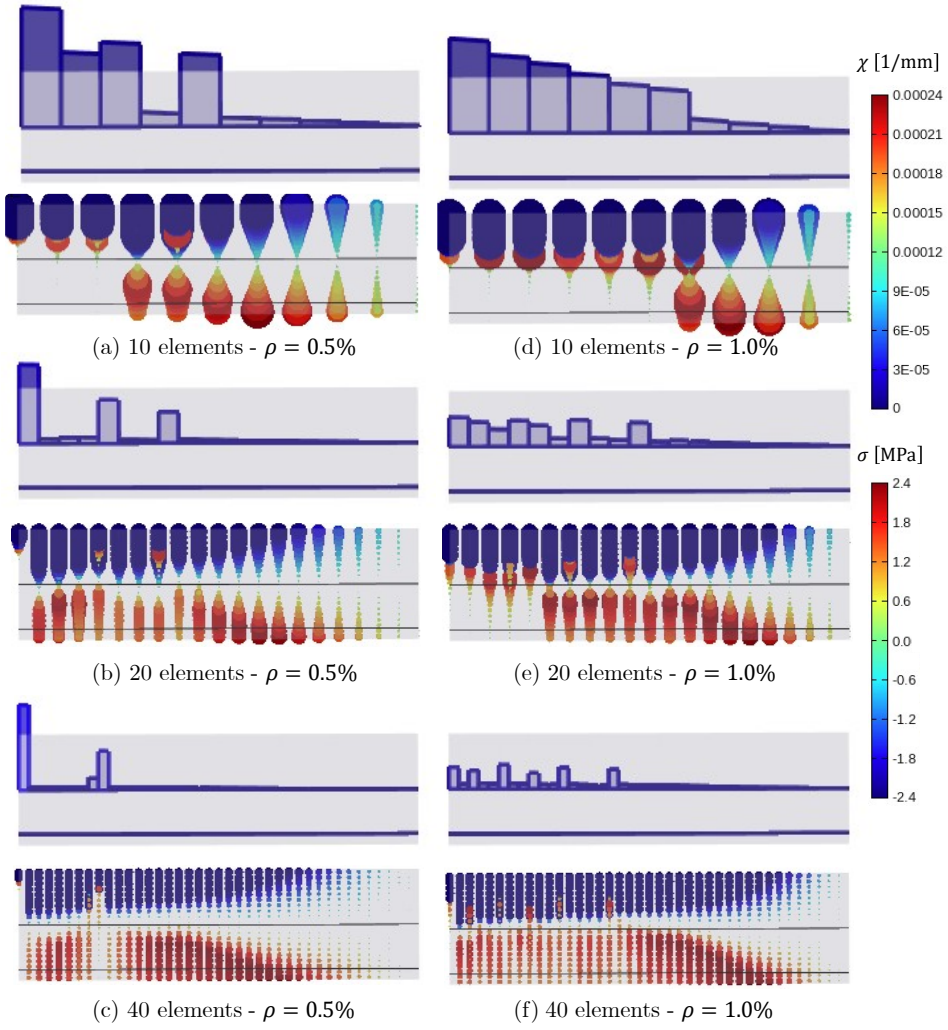

Figure 5.14. Curvature (top) and fiber stress (bottom) distributions for three meshes and two reinforcement ratios in the pre-yielding stage.

cracks are diffused, which is not representative of the mechanical behavior of concrete. Thus, this model also fails to accurately capture the expected localized cracking.

It is shown that that traditional perfect-bond assumptions can lead to significant inaccuracies, especially in scenarios involving complex loading and crack propagation.
Bond-slip models better describe the interactions between concrete and steel reinforcement, although, even using the fracture energy regularization, fail to correctly address mesh dependency

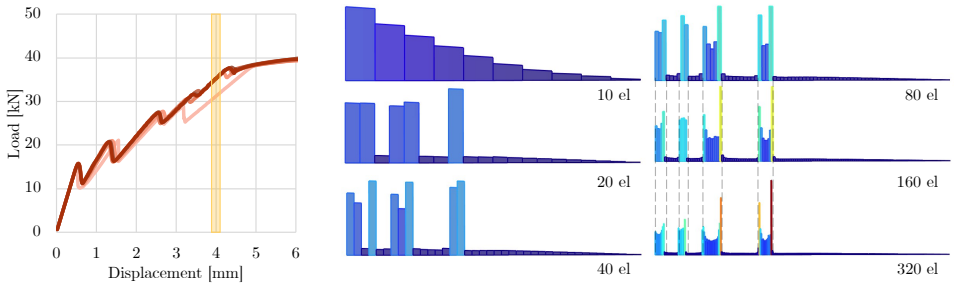

Figure 5.15. Global structural response for the model without regularization for $\rho = 0.5\%$ (left) and curvatures (right) for different meshes.

and realistically capture localized damage.

5.2 Numerical applications of beam elements with bond-slip

Three case studies are presented to showcase the proposed element characteristics and performance, the first is the analysis of several post-tensioned concrete girders with different bond conditions applied [128], the second is the analysis of CFRP-strengthened concrete beams with time-dependent losses [129], and the third is a study on shear behavior of prestressed I-beams without stirrups [130].

5.2.1 Benchmark and convergence studies

In this section, a simple numerical case study is presented to verify the element behavior under linear conditions and to illustrate the impact of varying the number of interpolation points on the solution. The configuration consists of a cantilever beam with a single reinforcement bar, as shown in Figure 5.16. The section is square, and two limit cases are examined for the bond condition between the reinforcement and the concrete: a perfect bond scenario and a no-bond scenario.

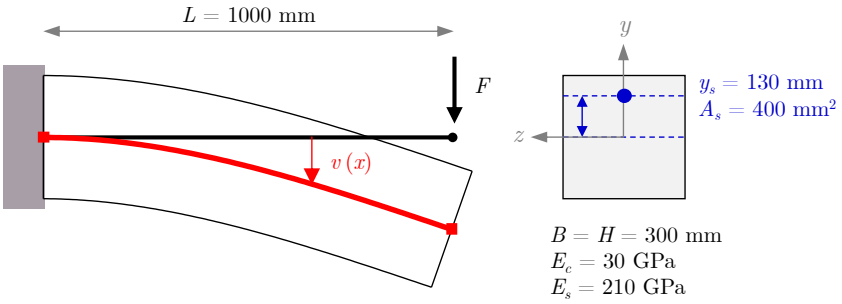

Figure 5.16. Numerical configuration where only one rebar element is considered, mechanical properties and section geometry.

In the perfect bond case, the reinforcement rotates together with the concrete section at the end and behaves as if it were rigidly connected (Figure 5.17, left). Conversely, in the no-bond case, the reinforcement and the concrete act like two parallel beams that are not bonded together (Figure 5.17, right).

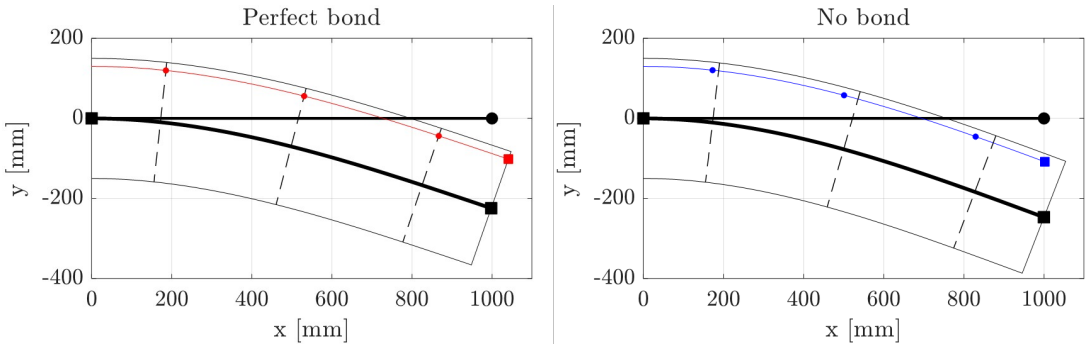

Figure 5.17. Deformed configurations in two limit cases of bond between the rebar and concrete: perfect bond (left) and no bond (right).

The local responses of the fiber section and of the bond section are reported in Figure 5.18 as the number of bond-slip interpolation points m_b is varied. Increasing m_b from two to four

makes the fiber-section response converge toward the analytical solution, while with fewer points the approximation is less accurate. For the bond-slip strain ε_b, since it is directly interpolated from the number of bond-slip interpolation points, the trend is captured well even with a small number of points, being essentially a linear function.

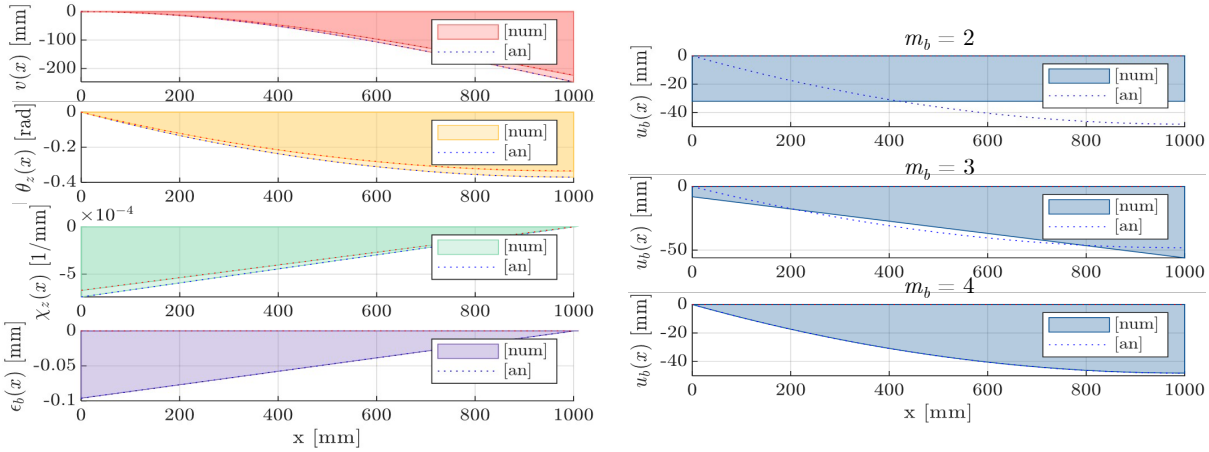

Figure 5.18. Generalized strain values along the element with perfect-bond (red) and no-bond (blue) of the fiber section (left) and the bond sections varying the number of bond-slip interpolation points m_b (right).

Finally, Figure 5.19 reports a sweep of the bond rigidity, ranging from very low ($\sim 10^{-2}$) to very high values ($\sim 10^{3}$). The vertical displacement at the free end $v(x = L)$ and the bond-slip evaluated as a section displacement $u_b(x = L)$ and as a nodal value u_{bj} are shown. As the number of interpolation points m_b increases, the sectional and nodal values of bond-slip converge, confirming the improved consistency of the discretization.

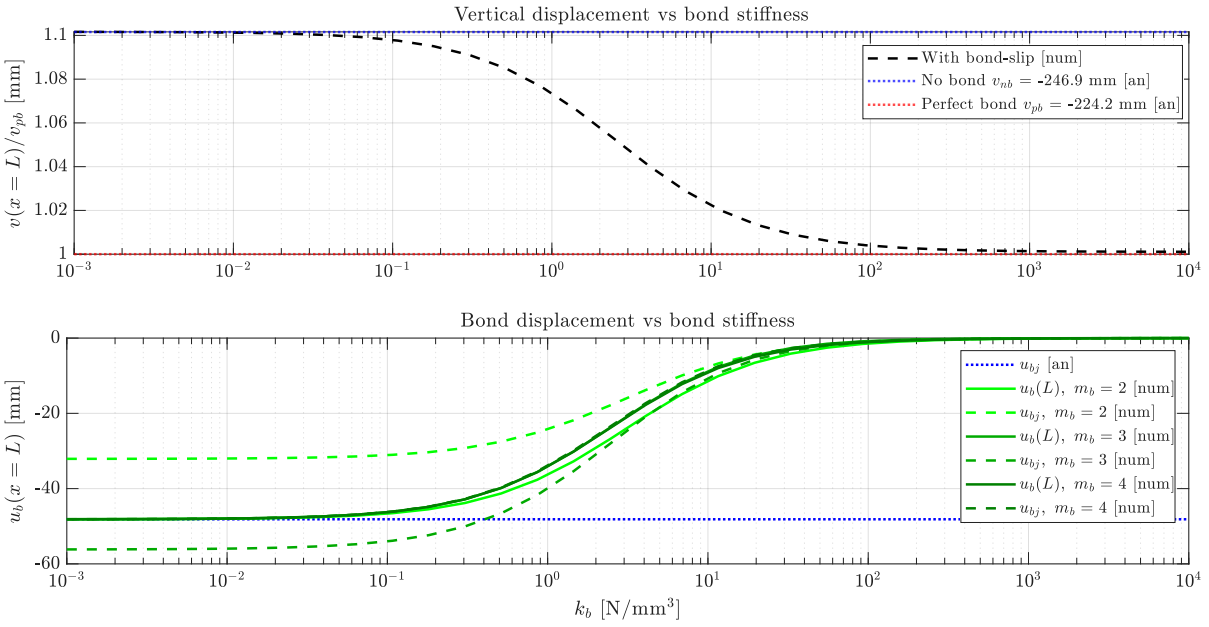

Figure 5.19. Vertical end displacement $v(x = L)$ (top) and bond-slip as a section displacement $u_b(x = L)$ and as a nodal value u_{bj} using different numbers of bond-slip interpolation points m_b (bottom).

These numerical benchmarks demonstrate how the element behaves under linear conditions and how the choice of interpolation points influences the accuracy and consistency of the results.

5.2.2 Post-Tensioned Concrete Girders

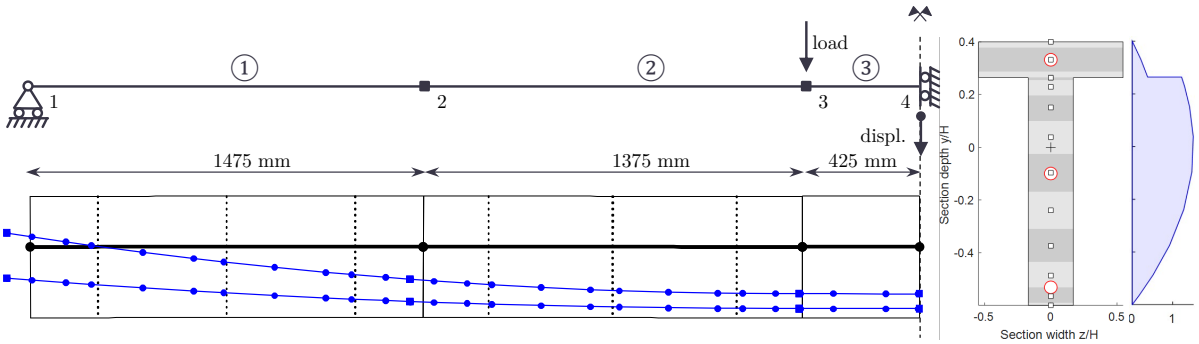

Figure 5.20. Numerical model of beams T1 and T2 after prestressing has been applied.

The first case study relies on the results of the study by Losanno et al. [128] that provides a detailed benchmark for assessing the nonlinear flexural response of post-tensioned concrete bridge girders and serves as a reference for validating the numerical model. The campaign includes six 1:5 scale specimens: among them, T1 is fully bonded and T2 is fully unbonded. These specimens are representative of typical Italian prestressed concrete (PC) bridge girders and were designed to evaluate the combined influence of grouting conditions and prestressing levels on the beams' flexural behavior. Each specimen is 6600 mm long, 440 mm deep and has a 150 mm flange width. All the tests were conducted under a four-point bending setup. The corresponding numerical model is illustrated in Figure 5.20. Given the beam symmetry with respect to the mid-section, only one half of the beam is modeled.

Only three elements are used to model the beam. The number of Gauss points for the fiber and bond sections is selected to ensure the minimum integration order. The section is discretized with 10 layers since this is a uniaxial case. The resulting model has very low computational demand.

Elastic and plastic parameters						
E [MPa]	ν	H_k [MPa]	H_i [MPa]	σ_t [MPa]	σ_c [MPa]	
37	0.2	21000	300	20	60	
Damage parameters						
Y_{t0}	a_t	b_t	Y_{c0}	a_c	b_c	β
$6{\cdot}10^{-5}$	1	$1{\cdot}10^{-4}$	$4{\cdot}10^{-4}$	1	$2{\cdot}10^{-3}$	1

Table 5.2. Material parameters for the damage-plastic concrete model used in Figure 3.3

The prestressing system consists of two unbonded monostrands with a parabolic profile, with maximum eccentricity at midspan. The prestressing steel has modulus of elasticity $E = 195{,}000$ MPa, yield strength $f_y = 1670$ MPa, and ultimate strength $f_u = 1969$ MPa. The mild reinforcement has $E = 203{,}400$ MPa and $f_y = 450$ MPa. Ducts were constructed to provide fully bonded, partially bonded, or unbonded conditions. The constitutive model parameters for the concrete are reported in Table 5.2. The resulting uniaxial cyclic behavior is shown in Figure 5.21. The specimens were tested numerically under monotonic displacement-controlled loading until failure, consistent with the experimental tests. However, in the unbonded case, the tests were stopped at a midspan deflection of 140 mm due to the actuators reaching their stroke limit.

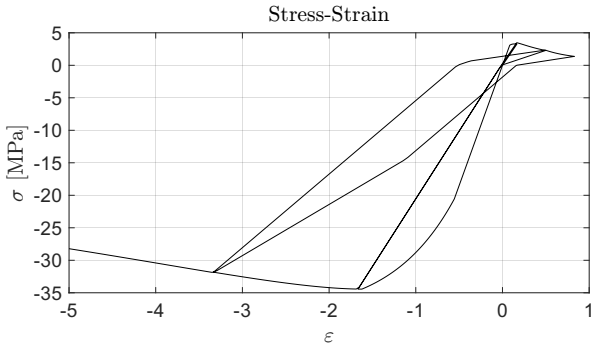

Figure 5.21. Concrete constitutive law.

The results highlight the pivotal role of grouting in influencing the bond-slip interaction and the ultimate load capacity of the girders. The specimens with fully bonded tendons demonstrated superior strength, whereas the unbonded tendons led to a significant reduction in flexural performance.

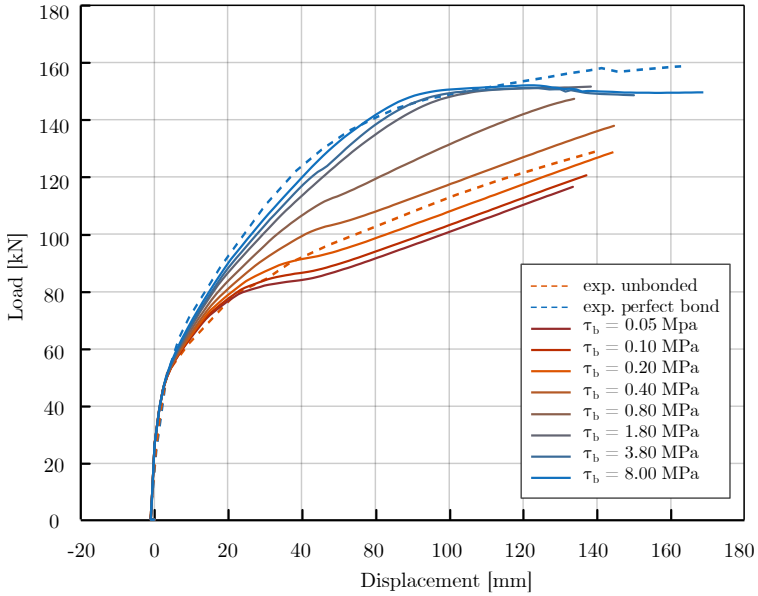

Figure 5.22. Global pushover numerical and experimental comparison of T1 (perfect bond) and T2 (unbonded) specimens along with an intermediate case, used to show the influence of bond.

Figure 5.22 reports the comparison between experimental and numerical pushover responses. The labels "B" and "U" refer to bonded and unbonded configurations, while "HP" indicates high prestressing, as defined in [128]. The same input parameters were used across all numerical cases. Only the bond-slip law was modified. Specifically, a peak bond strength of $\tau_b = 8$ MPa is the best fit for T1 (bonded), while $\tau_b = 0.2$ MPa is the best fit for T2 (unbonded), as some bond is still realistically expected in the unbonded specimen.

Figure 5.23 shows the local bond–slip response at the section level. The quadrature point experiencing the maximum slip is not fixed, since the activation of nonlinear bond behavior depends on the instantaneous force distribution along the tendon. In other words, the location where bond failure initiates cannot be predicted, as it results from the interplay of axial and bending forces in the element.

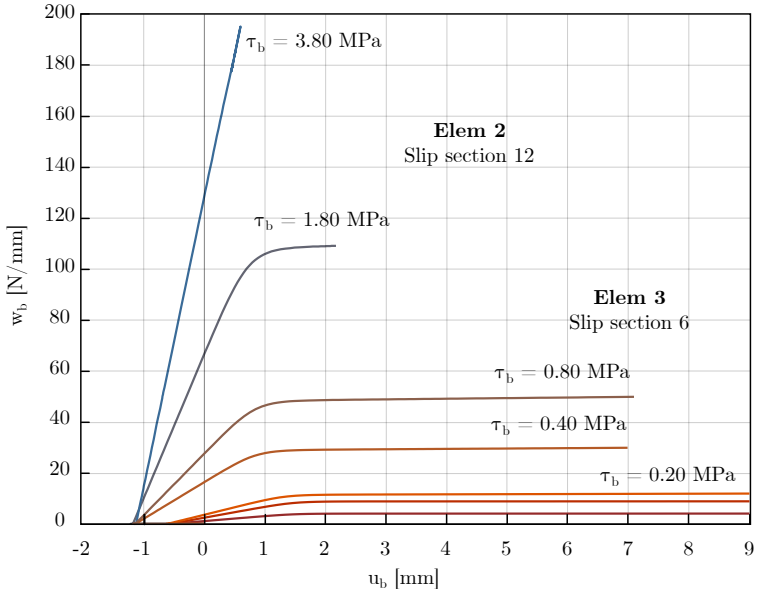

Figure 5.23. Bond-slip local results for all bonding conditions in the quadrature points where the highest slip displacements localize: element 3 - section 6 up to $\tau_b = 0.80$ MPa, element 2 - section 12 for the rest.

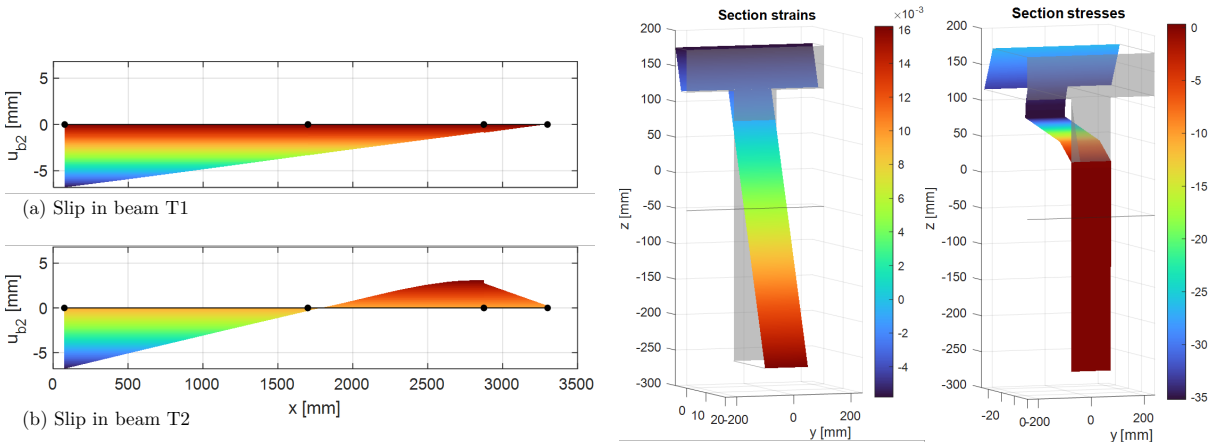

(a) **(b)**

Figure 5.24. (a) Slip displacement in the unbonded beam with $\tau_b = 0.2$ MPa. The blue, orange and green profiles correspond to prestressing, cracking and final stages, respectively in Figure 5.22; (b) T1 beam midspan concrete response at collapse [MPa].

In the numerical results of Figure 5.22, beam T2 ($\tau_b = 0.2$ MPa) undergoes immediate decompression and cracking as load increases. The intermediate bond case experiences debonding and cracking at a later stage, while beam T1 ($\tau_b = 8.0$ MPa) shows a progressive cracking evolution with no debonding prior to failure. In all configurations, collapse is governed by concrete crushing in the top compression zone at midspan.

Figure 5.24a reports the slip displacement distribution along the tendons. For T1, following the initial prestressing, the bond-slip remains negligible and does not evolve during loading. Conversely, in T2, slip displacements increase progressively throughout the test. Figure 5.24b shows the stress distribution in the fiber section at midspan of beam T1 at failure, where concrete softening in the compression fibers is clearly observed.

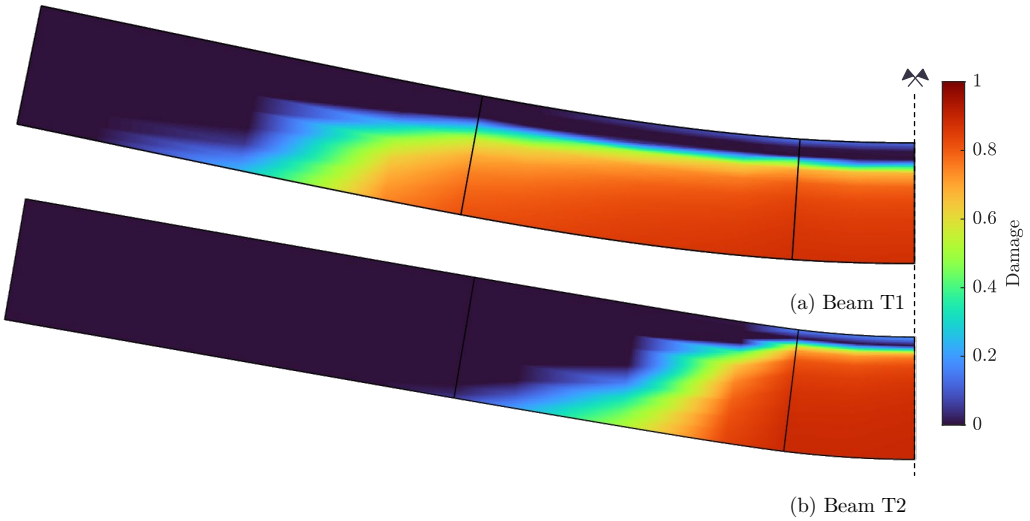

Figure 5.25. Damage distributions of beams T1 and T2.

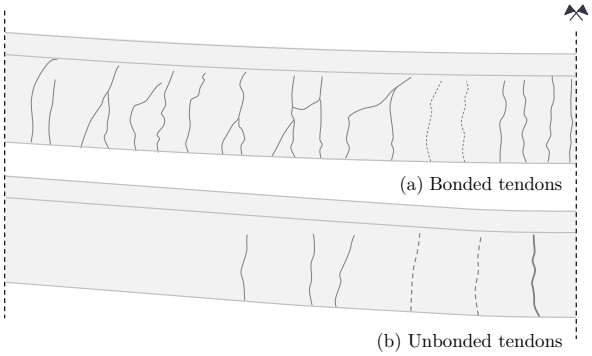

Figure 5.26. Cracks distribution in the beams tested experimentally.

The damage patterns at an imposed displacement of 40 mm at node 3 are shown in Figure 5.25 (displacements are magnified 10 times for visualization). Beam T1 exhibits a deeper neutral axis and more distributed damage, while T2 displays localized damage near the loading points. This behavior is attributed to the bond-slip interaction in the bonded tendon, which facilitates a more uniform stress transfer along the beam. This finding is corroborated by the experimental crack patterns in Figure 5.26, where larger and more concentrated cracks are observed in the unbonded case. Although explicit crack widths are not computed in the continuum damage model, the damage and tensile strain fields are consistent with the experimental cracking behavior.

One final remark concerns the mesh requirements: very few elements are sufficient for convergence, provided that a sufficient number of quadrature points is used to ensure proper numerical integration. In this case, varying either the number of elements or the quadrature points only marginally affects the solution.

5.2.3 CFRP-Strengthened Concrete Beams with Time-Dependent Losses

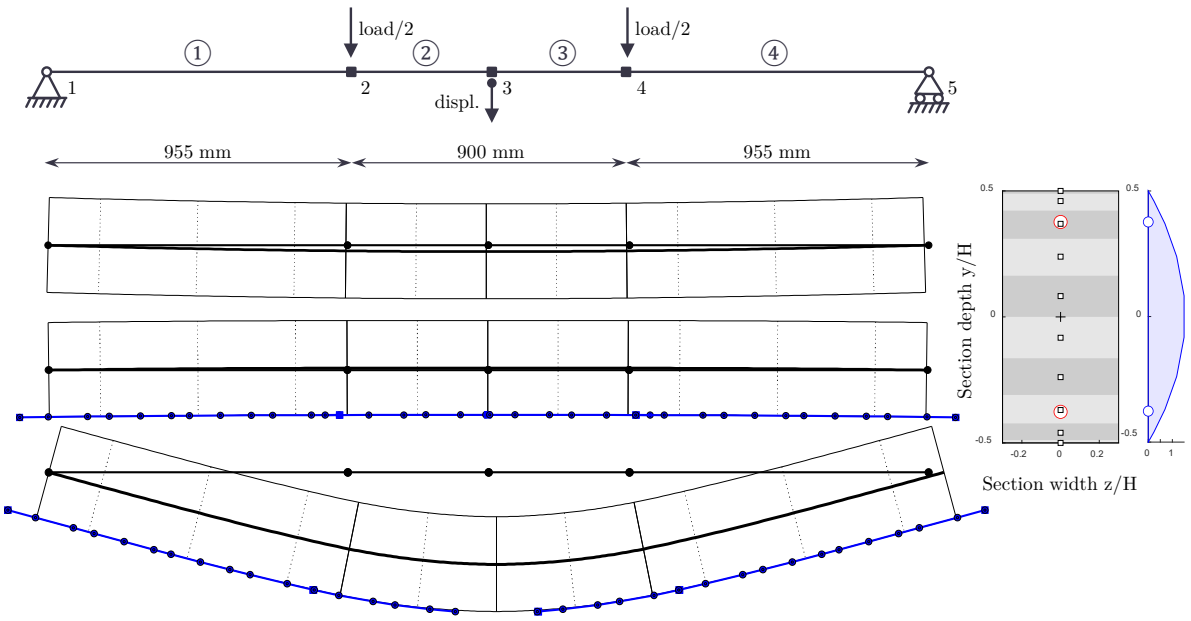

Figure 5.27. Numerical model and loading scheme. Top: the beam at day 174 prior to strengthening, after time-dependent effects; middle: configuration immediately after CFRP installation and prestressing; bottom: collapse state at day 181.

This numerical study investigates reinforced concrete beams strengthened with externally bonded, prestressed CFRP laminates. The analyses include specimens BS-0, BS-20, and BS-48-identical in geometry but differing in the level of prestress-and specimen CB-2, an unstrengthened control beam, all based on the experimental campaign by Slaitas et al. [129]. Time-dependent phenomena are considered, including concrete shrinkage, creep, and prestress losses due to CFRP relaxation. These effects are modeled following the same framework proposed in [72]. The strain in the CFRP fiber is expressed as:

$$\varepsilon_{\text{fiber}}(t) = \varepsilon_0 - \varepsilon_d(t) \tag{5.1}$$

where ε_0 is the initial prestress strain, and $\varepsilon_d(t)$ represents the time-dependent reduction, including shrinkage, creep, and relaxation. The total delayed strain is given by:

$$\varepsilon_d(t) = \varepsilon_{cs}(t) + \varepsilon_{cc}(t) \tag{5.2}$$

The shrinkage strain $\varepsilon_{cs}(t)$ evolves as a function of time, while creep strain $\varepsilon_{cc}(t)$ is stress-dependent and modeled via the compliance function $J(t,\tau)$:

$$\varepsilon_{cc}(t) = J(t,t_0)\sigma_c(t_0) + \int_{t_0}^{t} J(t,\tau)\frac{\partial \sigma_c(\tau)}{\partial \tau}\, d\tau \tag{5.3}$$

For numerical implementation, the following incremental formulation is adopted:

$$\varepsilon_{cc}^{n+1} = \varepsilon_{cc}^{n} + \Delta J(t^{n+1},t^0)\sigma_{c0} + \sum_{k=1}^{n} \Delta J(t^{n+1},t^k)\Delta\sigma_c^k \tag{5.4}$$

Relaxation losses in the CFRP laminate are approximated by:

$$\varepsilon_{d,p}(t) = J(t, t_0)\sigma_p(t_0) \tag{5.5}$$

assuming a constant initial prestress and time-dependent modulus decay.

Elastic and plastic parameters						
E [GPa]	ν	H_k [MPa]	H_i [MPa]	σ_t [MPa]	σ_c [MPa]	
35.4	0.2	21000	300	12	25	
Damage parameters						
Y_{t0}	a_t	b_t	Y_{c0}	a_c	b_c	β
$1{\cdot}10^{-7}$	0.99	$1{\cdot}10^{-4}$	$8{\cdot}10^{-4}$	1	$3{\cdot}10^{-3}$	1

Table 5.3. Material parameters for the damage-plastic concrete model used in the simulations.

The beam geometry and loading setup are illustrated in Figure 5.27. The CFRP laminate is characterized by a tensile strength of 2627 MPa and an elastic modulus of 170 GPa. To capture its brittle behavior, a Menegotto and Pinto constitutive law (Figure 3.9) is used. A partial bond is introduced to simulate the epoxy layer between the CFRP and the concrete substrate. The reinforcing steel is modeled using the Menegotto–Pinto constitutive law, with parameters calibrated from [129]. The concrete behavior follows the damage-plastic formulation with material parameters provided in Table 5.3.

To simulate realistic long-term behavior, a three-stage loading sequence was implemented:

1. *Pre-strengthening (Day 0 to 174):* The beam undergoes creep and shrinkage under self-weight. No external CFRP reinforcement is applied.

2. *Post-strengthening (Day 174 to 181):* CFRP laminates are prestressed and bonded. Additional creep and shrinkage evolve, and CFRP relaxation starts.

3. *Testing (Day 181):* The beam is loaded monotonically to failure, with accumulated time-dependent effects considered.

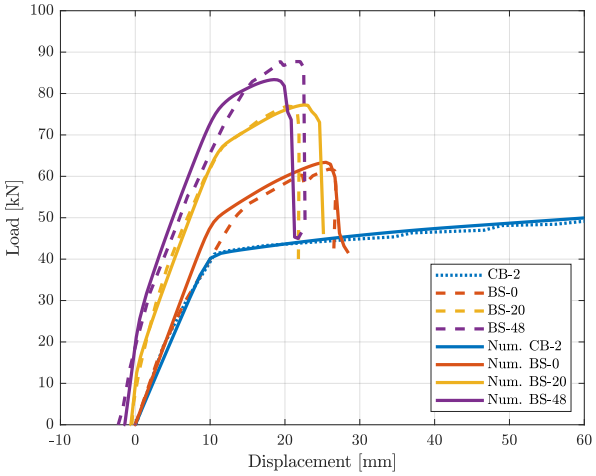

Figure 5.28. Comparison between experimental and numerical pushover curves for BS-0, BS-20, and BS-48 specimens.

The simulation results show that the control beam CB-2 fails due to concrete crushing in the

top compression zone. In contrast, the CFRP-strengthened beams-BS-0, BS-20, and BS-48-all fail by rupture of the CFRP laminate. Despite the different prestressing levels, the governing mechanism in the strengthened beams is consistent: the CFRP reaches its ultimate tensile strain ε_{fu} and fails in a brittle manner, while the concrete remains uncrushed at the point of rupture. As a result, after CFRP failure, all beams retain a residual load-carrying capacity close to that of CB-2, corresponding to the internal action of concrete and steel alone, although no convergency is achieved after the sharp drop due to a high nonlinearity. These results highlight the brittle nature of the CFRP rupture and the importance of post-peak ductility considerations.

Figure 5.28 illustrates good agreement between numerical and experimental load-displacement curves. The model correctly captures the increased strength and stiffness due to prestressing, and the sharp drop associated with CFRP rupture. Rupture correctly occurs earlier as prestress increases.

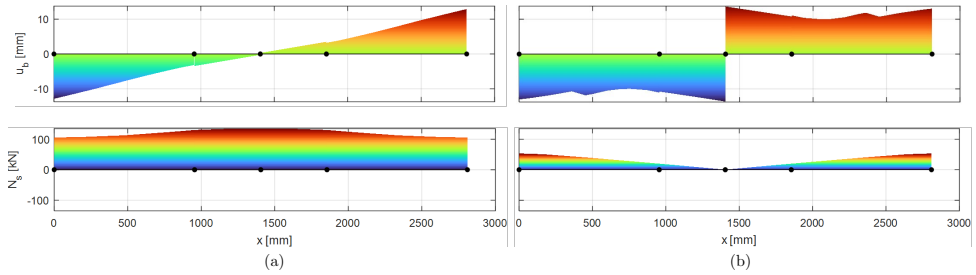

Figure 5.29. Slip and axial force in the CFRP laminate for beam BS-20.

The structural response is highly sensitive to the bond properties and, more specifically, to the concrete tensile strength, which strongly influences the initial stiffness. In the experimental curves, the BS-20 and BS-48 specimens exhibit different initial stiffness, despite having similar prestressing levels, an inconsistency likely due to the variation in the effective tensile concrete strength between specimens. For this reason, since the prestressing noticeably induces cracking in the concrete in the experimental campaign, the tensile strength is realistically averaged to 0.5 MPa in the numerical model to ensure consistent initial stiffness across the prestressed cases. This assumption could be refined to better match the experimental data if more detailed material information were available. Nevertheless, it is worth noting that the model captures the complex structural behavior while maintaining a low computational cost.

The bond-slip and axial force distributions in the CFRP laminate for specimen BS-20 are presented in Figure 5.29. At peak load, bond-slip is highest near midspan, where the moment demand is maximum. Upon failure, a clear drop in axial force confirms laminate rupture. The discontinuity in bond-slip reveals the creation of a physical gap, consistent with the detachment of the CFRP from the concrete substrate.

5.2.4 Shear behavior of prestressed I-beams without stirrups

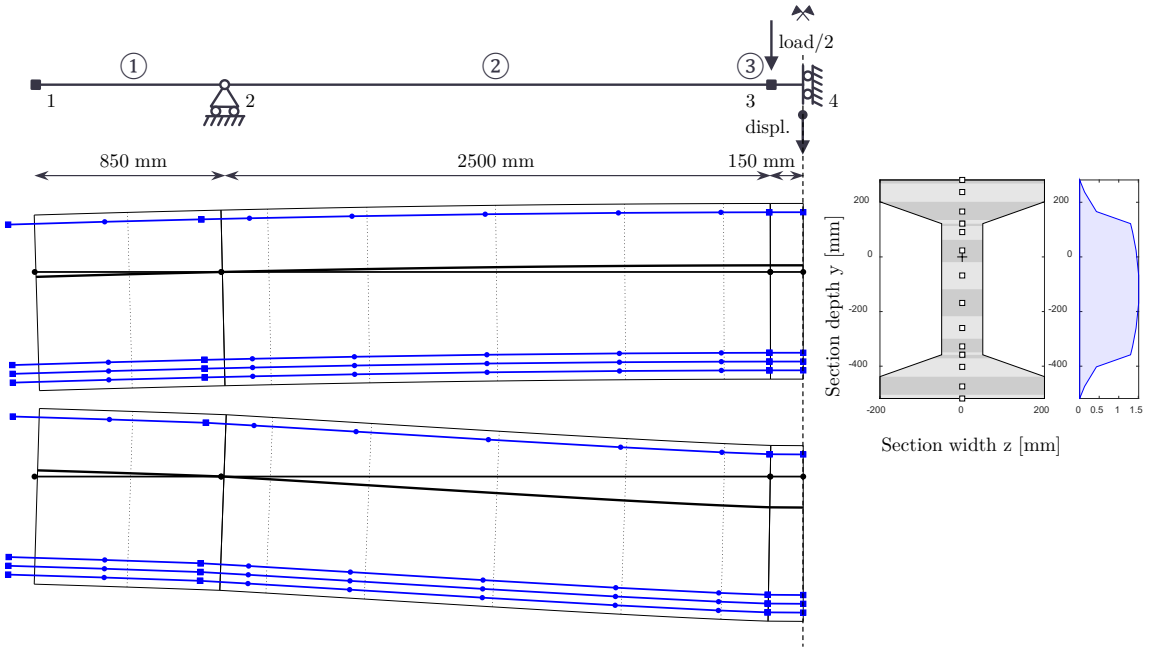

Figure 5.30. Numerical model and loading scheme. Top: configuration after prestressing; bottom: shear collapse state.

The experimental program by Ruiz *et al.* [130] provides an ideal benchmark for validating the proposed mixed bond–slip beam element under pure-shear dominated failure. Eight full-scale High Performance Fibre-Reinforced Concrete (HPFRC) I-girders were cast and tested over a $L_{\text{span}} = 5.30$ m four-point set-up, producing a constant-moment region of only 300 mm. Shear failure was therefore triggered in the web, far from the loading points and without any transverse reinforcement. The eight beams are grouped as follows:

- *BR-B0-1, BR-B0-2*: reference beams – no prestress;
- *BR-B10*: low prestress, target concrete compression $\sigma_{cp} = 10.7$ MPa;
- *BR-B13-1 to BR-B13-5*: high prestress, $\sigma_{cp} = 13.7$ MPa, five nominally identical specimens tested at different ages (59–517 days).

Beam BR-B13-5 is not analyzed as it is an outlier, and its response cannot be captured by the present numerical model in absence of further information. A concise summary of geometry, material strengths, prestress level and test age is reproduced in Table 5.4.

The 3D plastic-damage material is tuned as shown in Table 5.5, an example of the axial constitutive law is shown in Figure 5.31.

Only the shear-critical half-span is model as symmetry is enforced at mid-span. A three-element mesh is sufficient to capture every specimen's response. The central element, labeled ② in Figure 5.30, has nine quadrature points both for the fiber section and the bond interface to correctly display the strain variation, although fewer points are required for mesh convergency.

All beams share the same material parameter set, except three coefficients:

Table 5.4. Key properties of the Ruiz et al. HPFRC beams.

Beam	Age [d]	$f_{c,\mathrm{cyl}}$ [MPa]	σ_{cp} [MPa]
BR-B0-1	179	130	0
BR-B0-2	517	138	0
BR-B10	301	125	10.7
BR-B13-1	59	118	13.7
BR-B13-2	133	125	13.7
BR-B13-3	239	125	13.5
BR-B13-4	279	118	13.6

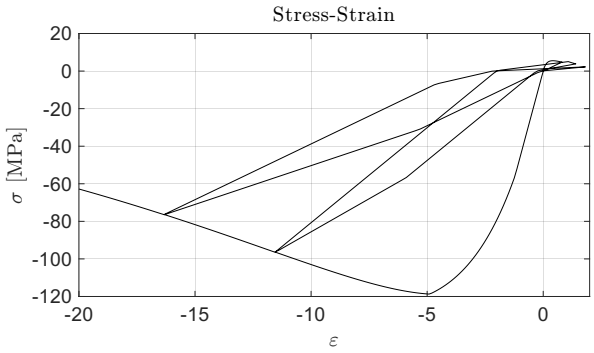

Figure 5.31. Concrete constitutive law used for specimen BR-B13-1.

Elastic and plastic parameters					
E [GPa]	ν	H_k [MPa]	H_i [MPa]	σ_t [MPa]	σ_c [MPa]
46	0.20	30000	300	90	225
Damage parameters					
Y_{t0}	a_t	b_t	Y_{c0}	a_c	b_c	β
$1\cdot10^{-5}$	0.95	b_t	Y_{c0}	0.85	$6.7\cdot10^{-3}$	1

Table 5.5. Material parameters for the damage-plastic concrete model used in the Ruiz simulations. Parameters $b_t = 2.17 \div 3.40 \cdot 10^{-3}$ and $Y_{c0} = 0.87 \div 1.42 \cdot 10^{-3}$ are tuned per specimen.

- compressive strength f_c (118–138 MPa) modified acting on paremeter Y_{c0};
- tensile strength f_t (3.45–4.62 MPa) modified acting on paremeter b_t;
- age-dependent creep factor ϕ, applied via $E_c^{\mathrm{eff}} = 46\,\mathrm{GPa}/(1+\phi)$ where ϕ here is computed according to the fib Model Code [131].

Prestressing is introduced by pulling the tendons by $18 \div 24$ mm in the initial stage, as this induces an average axial stress on the concrete fibers which agrees with the experimental measurements reported in Table 5.4. After the prestressing stage, grouting is applied and a good bond condition is considered. The peak bond shear stress is 8 MPa which is considered a reasonable value [131], while the bond interface is different for every specimen, according to Figure 6 of Ruiz et al. [130]. In this case, an average value is considered for every bond quadrature point.

Figure 5.32 compares the numerical and experimental shear-displacements envelopes for the full test series. Some things are to be noted:

- all the numerical models show critical shear damage across the central element, both in the

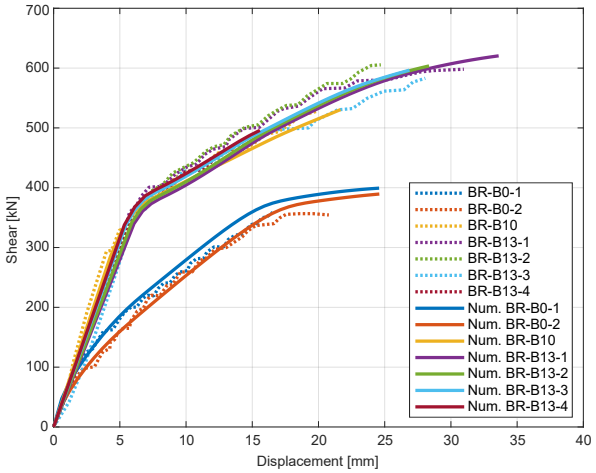

Figure 5.32. Numerical vs. experimental pushover curves.

simply reinforced cases and the prestressed cases;

- two visible slope changes are visible in the diagrams. The first corresponds to the decompression zone and the beginning of shear cracking, while the second one, which reaches the summit almost asymptotically, is when most fibers are cracked.

There is additional capacity after the peak as the beam can still exhibit some residual flexural resistance, however most fibers' response is zero as these are almost completely damaged, causing the analysis to break sometimes after a sudden drop, which makes the model capable of realistically modeling a shear brittle failure.

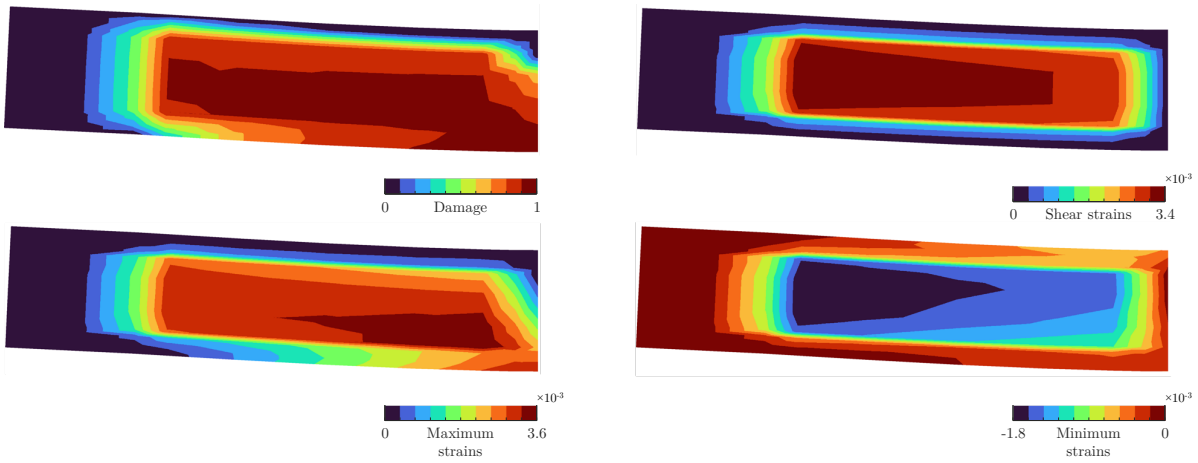

Figure 5.33. Damage and strains for reinforced specimen BR-B0-1 at displacement $v = 11$ mm.

Figures 5.33 and 5.34 show the damage distribution, the shear strains, and the principal strains for the reinforced and the prestressed specimens. It can be noted that most damage is in the web and is because of shear, while some flexural damage can also be observed in the bottom at the midspan. This agrees with experimental findings. Again, by looking at the principal strains, it can be noted that most strains arise from the shear action as these are almost identical to the shear strain distribution. Since this is a beam continuum damage model, it is not possible to have the correct shear distribution, nor to visualize the crack pattern with such coarse mesh [91], also because the shear stress is constant throughout the central element, which doesn't allow

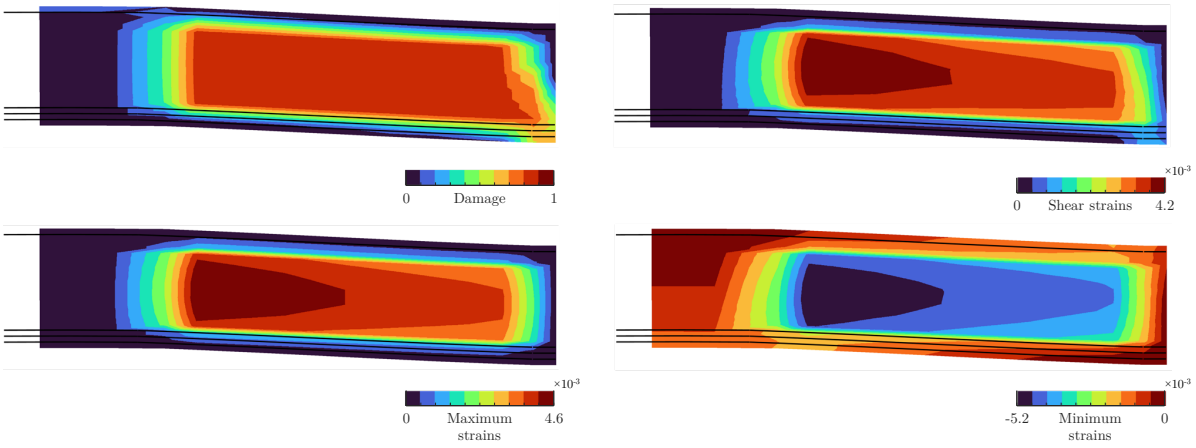

Figure 5.34. Damage and strains for prestressed specimen BR-B13-1 at displacement $v = 11$ mm.

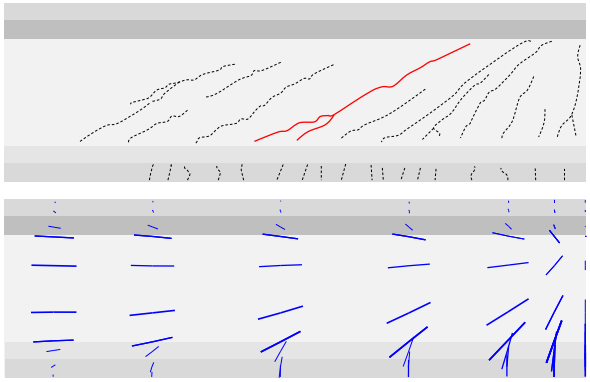

Figure 5.35. Experimental cracks (top) vs numerical crack planes, orthogonal to principal directions, (bottom) for specimen BR-B13-1.

for a complex strain distribution, according to the force-based formulation.

Finally, Figure 5.35 compares the numerical cracking planes, simply plotted as lines orthogonal to the principal directions in the fibers, with the physical cracks observed during the experiments. Even though shear is constant throughout the element, it is still allowing for a quite accurate visualization. The cracking planes can finely predict the cracking slopes and, with a reasonable approximation, their position, showing where shear and flexural actions are acting together.

5.3 Numerical applications of beam elements with warping and bond-slip

The numerical assessment of Section 5.1.1 demonstrated that, even with local regularization techniques, classical DB models exhibit significant numerical issues when analyzing RC beam elements. The numerical analyses presented next aim to show how the observed objectivity issues can be restored, and how the realism of crack modeling can be improved by introducing warping in the section kinematics.

Research has sought to enhance DB models to better capture RC behavior. Bond-slip modeling, which incorporates the relative displacement between concrete and steel reinforcement, has shown to be promising in improving crack representation. In [91], explicit bond-slip models that introduce nonlinear springs at the interface are proposed, while implicit formulations embed bond-slip behavior directly into the element's kinematics. Integrating bond-slip effects and warping deformation modes significantly enhances DB model performance by localizing cracks within single elements rather than spreading them unrealistically across the mesh [94].
Bond-slip has shown to be mainly responsible for controlling flexural cracks' width and density, in particular high bond stiffness interfaces lead to more dense but smaller cracks, while low bond stiffness interfaces lead to to more fewer but larger cracks, as shown in Figure 5.8 where changing only the maximum shear stress is enough to highlight this effect across the numerical tests. This numerical evidence is aligned with experimental findings, as shown in Figure 5.26 for example.

Adding warping, i.e. out-of-plane deformation of the beam cross-sections, the section kinematics is another relevant enhancement. Traditional plane section assumptions can fail in reproducing realistic cracking scenarios, where warping becomes significant. By incorporating warping into the section kinematics, enhanced DB models can represent realistic crack-induced deformations more accurately [94].
Compared to bond-slip, warping is a physical effect that does not require parameter tuning. In D-BW and M-BW elements, the only choices concern the number of interpolation points and section functions' number which, according to Section 4.1.1, determines the minimum number of quadrature points-and the accuracy of the warping interpolation over the sections, i.e., how many section DOFs are allocated for warping.
Warping is responsible for the correct strain localization over the element and allows to solve the deformation spreading to adjacent elements when a crack is formed, as shown in Figure 5.15 and Sio et al [94]. Overall, it also improves the fracture energy regularization effect. Numerical evidences supporting this statement are presented in this section.

The analyses focus on a simply supported RC beam subjected to a midspan concentrated load, with material properties and geometrical dimensions matching those of [127] and also reported in Section 5.1. In this case though, to reduce the number of possible outcomes, only the case of steel rebars $\rho = A_s/A_c = 1\%$ is used as in Sio et al [94] and the experimental outcomes of Burns et al [127]. Simulations were carried out using different meshes to highlight the enhanced numerical objectivity and the more accurate representation of crack behavior.

5.3.1 Objective Numerical Results obtained with D-BW elements

In these tests, all bond-slip and warping displacements are fixed at midspan to respect symmetry conditions.
The results show the performance of the models, highlighting:

- non-objective crack patterns and global response curves in classical beam elements;
- objective, localized crack representation and global response curves in enhanced beam elements with bond-slip and warping.

When a classical DB beam model is used, non-objective results are obtained, as detailed in Section 5.1, when the number of elements (NE) is progressively increased. In that case, not only the crack pattern and the local results show mesh dependency, but also non-objective global response curves are obtained. The load and displacement values are the nodal quantities at midspan. However, when the enhanced DB element with warping and bond-slip is used, both the global and the local strain and crack results improve, as shown in Fig. 5.36, where crack formations can be identified by tiny negative load drops. Even though a relatively fine mesh is used, good results are obtained in this case even with coarser meshes, and the cracks' locations and distribution prediction is in line with the experimental and the analytical outcomes [127]. Specifically, basing off simplified analytical formulae and with the current mechanical and geometrical properties, flexural cracks at a distance of around 400 mm are expected.

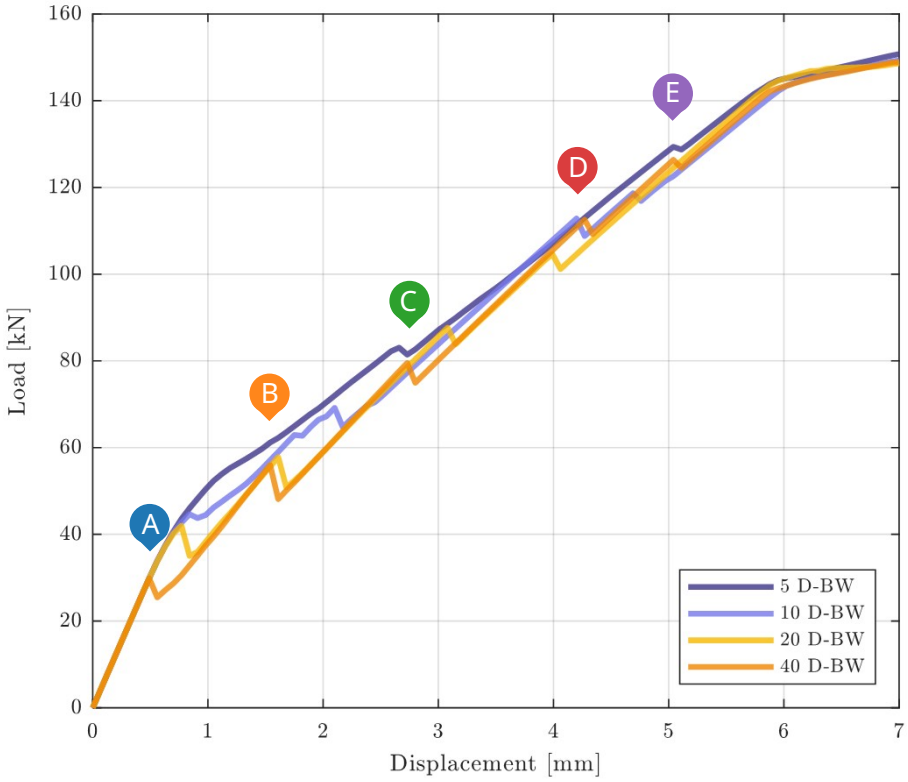

Figure 5.36. Structural responses for different discretization refinements for the D-BW elements. Letters A to E refer to the steps selected to display local results in the finest mesh case (NE = 40).

By looking at the local results instead, for example the steel fiber strain, the results converge when the number of elements is increased. Fig. 5.37 shows that where classical beam elements failed to capture the correct reinforcement steel strain, and therefore stress, the enhanced beam elements show improved results both with coarser and finer meshes. Practically identical results are obtained before yielding occurs, while more sparse results were obtained for classical beam elements, and yielding is always obtained at 6 mm, which is in line with the experimental observations.

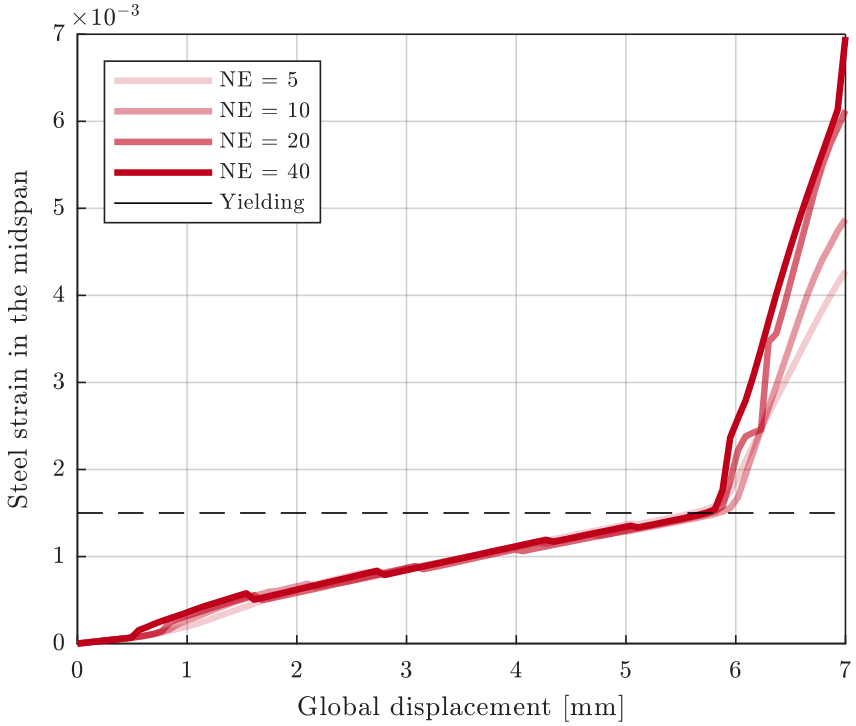

Figure 5.37. Evolution of the strain of the steel fiber with bond-slip over global displacements for different NE.

The slip displacement distributions in Fig. 5.38 show that cracks occur at the expected locations, where the slip displacement drops. The curvature concentrations also indicate where the cracks have formed: even though they are different, as expected as the curvature tends to infinite in the discontinuity, the localization occurs in the same locations although with a reduced error compared to classical elements.

By looking at the bond-slip distributions of Figure 5.39 at specific global steps, those labeled as A, B, C, D and E in Figure 5.36, the cracks' formation order can be determined for the highest mesh density (NE = 40). Specifically, as expected the first crack forms at midspan at $x = 0$ mm. Then, the following cracks form at $x \simeq 400$ mm, then at $x \simeq 800$ mm, and then the fourth or fifth crack may appear in different locations, due to small numerical discrepancies but overall converging as the NE increases. Force concentrations are also observed where a crack is formed, growing over time as curvature rises.

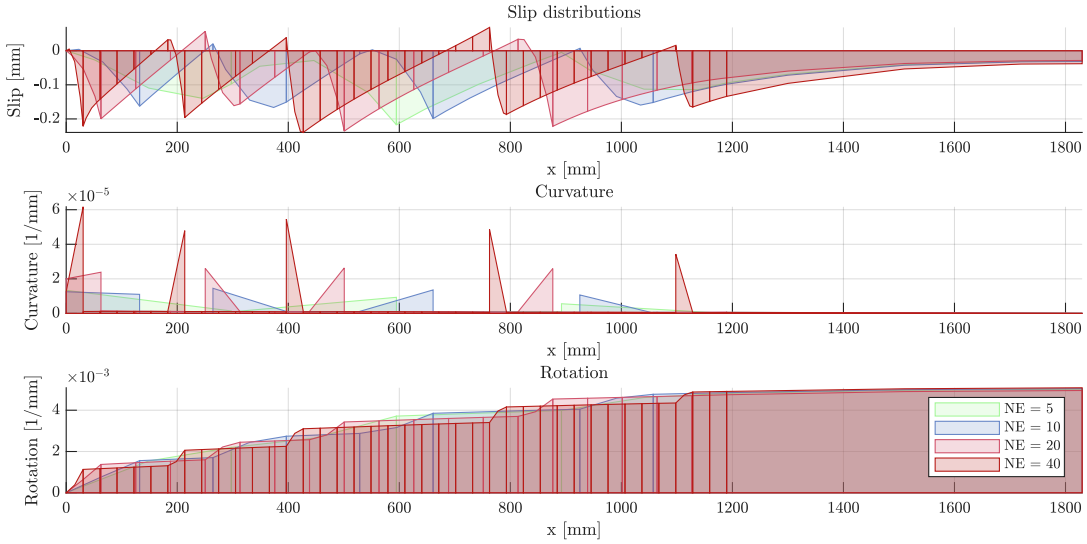

Figure 5.38. Bond-slip displacements, curvature and rotation over the element length for the four meshes.

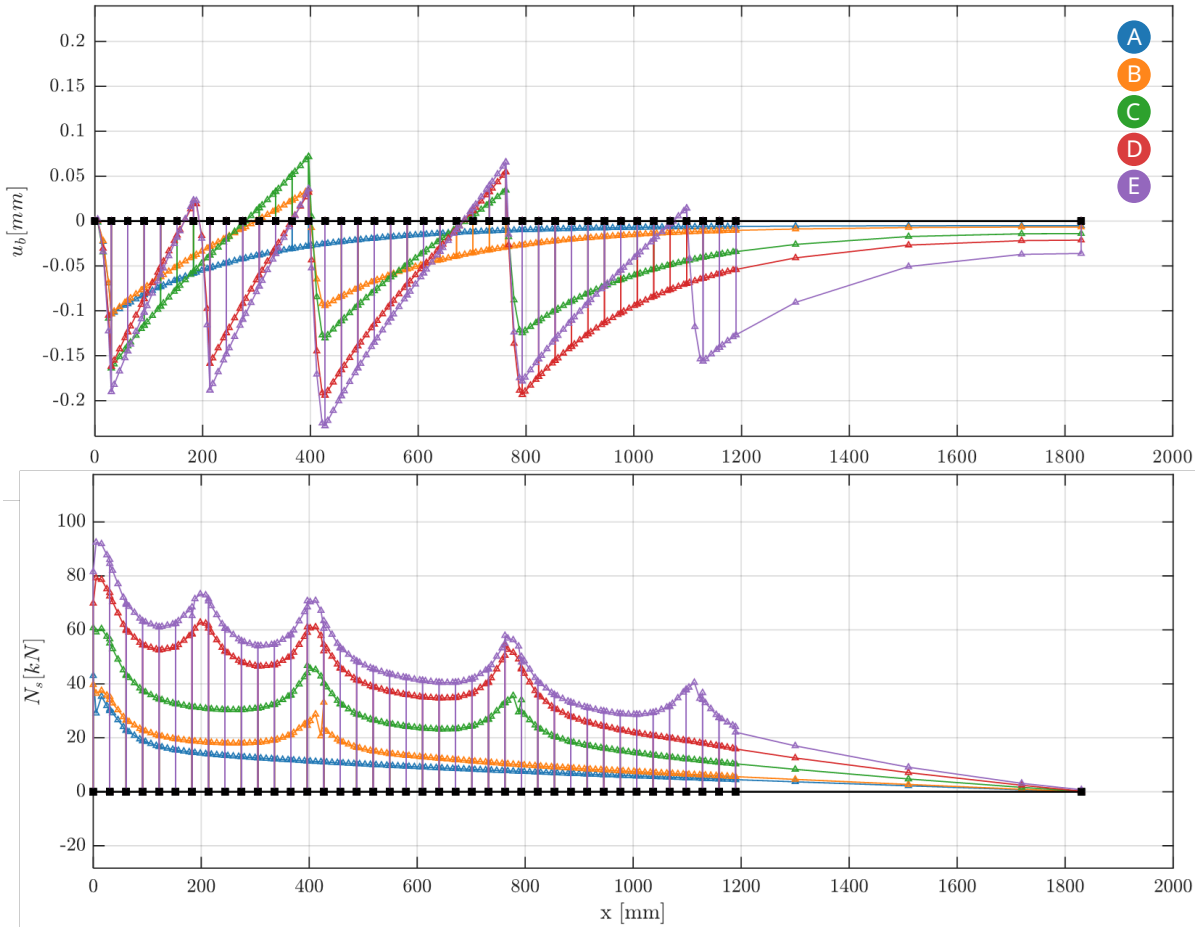

Figure 5.39. Bond-slip displacements $u_b(x)$ and steel fiber's axial force $N_b(x)$ over the element at five special steps reported in Figure 5.36.

It is worth looking at the curvature distributions at steps A to E of Figure 5.40. The midspan curvature does not grow at the left end, as a result of the slip displacement being constrained for symmetry. The warping displacements show a trend that is similar to the bond-slip displacement distributions.

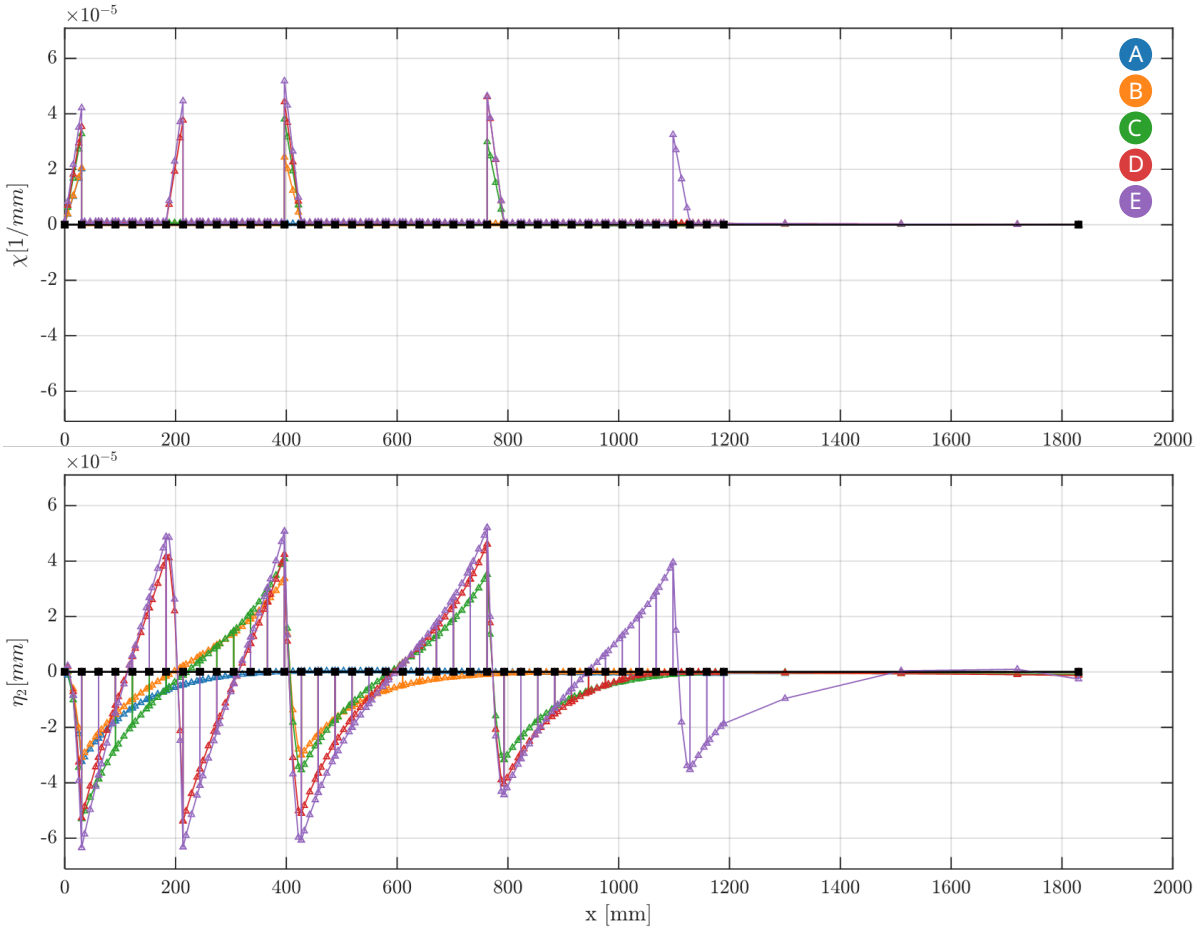

Figure 5.40. Curvature $\chi_z(x)$ and warping field $\eta_2(x)$ (cubic section shape) over the element at five special steps reported in Figure 5.36.

5.3.2 Objective Numerical Results obtained with M-BW elements

The same tests are now performed using M-BW elements leading to similar conclusions.
As expected from mixed elements, where exact equilibrium is imposed for the section's axial force and moments and the other forces are interpolated, more severe tensile softening occurs even though the fracture energy regularization is correctly applied. This leads to slightly earlier cracks formation but is generally comparable to the previous D-BW and experimental results, as shown in Figure 5.41.
Once again, steps A to E are identified to show when and where cracks are located.

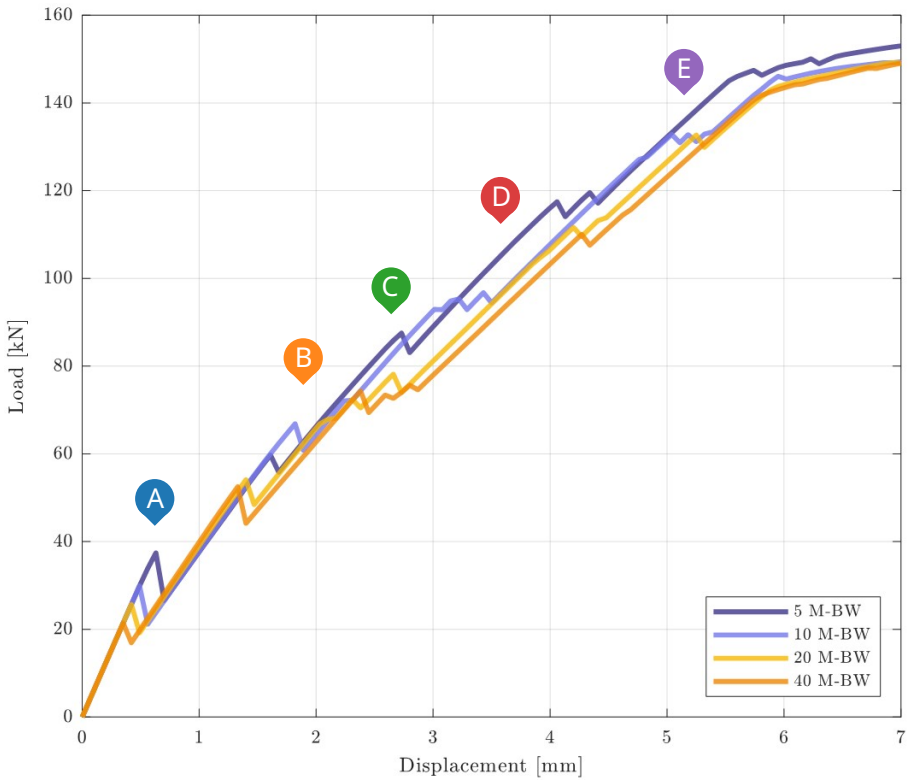

Figure 5.41. Structural responses at different discretization refinements for the D-BW elements. Letters A to E refer to special steps chosen to display local results in the finest mesh case (40 D-BW elements).

Figure 5.42 again shows the steel fiber strain for the four meshes and again, convergence is achieved even on a sensitive local result. In this case it is shown that mixed approaches do not always lead to good evaluations at the fiber level with coarse meshes, but convergence is shown to be faster.

Figure 5.43 shows the same results as before, using M-BW elements instead. The curvature is localizing in the quadrature points instead of the element end's points, as expected.

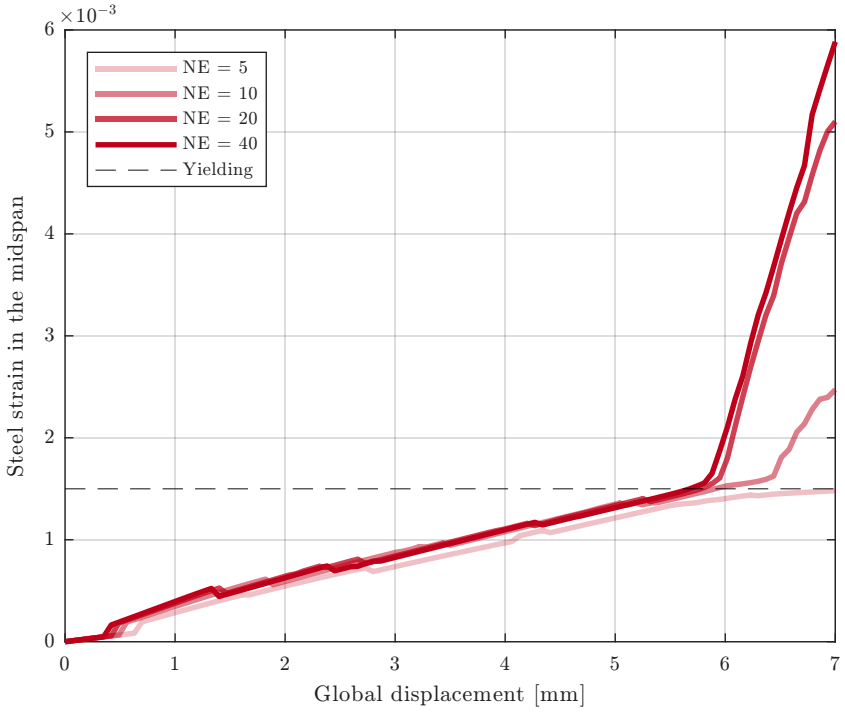

Figure 5.42. Evolution of the strain of the steel fiber with bond-slip over global displacements.

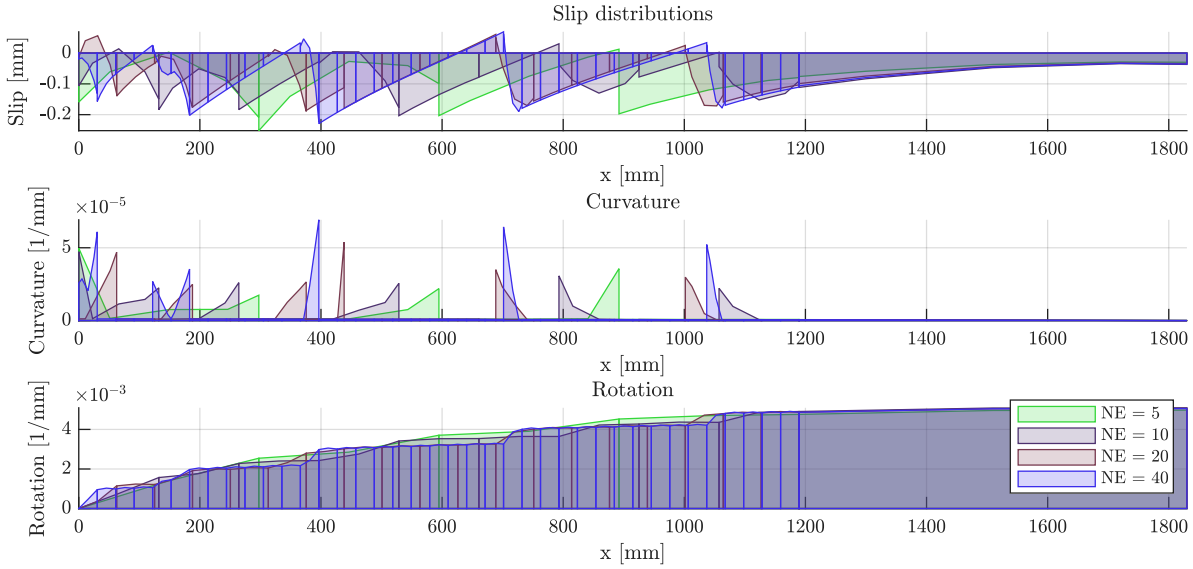

Figure 5.43. Bond-slip displacements, curvature and rotation over the element length for the four meshes.

For the highest number of elements (NE = 40) five cracks form in almost the same locations of the D-BW elements, as shown in Figure 5.44.

Results similar to those of Figure 5.45 are obtained for the curvature and the warping displacement distributions over the beam lengths.

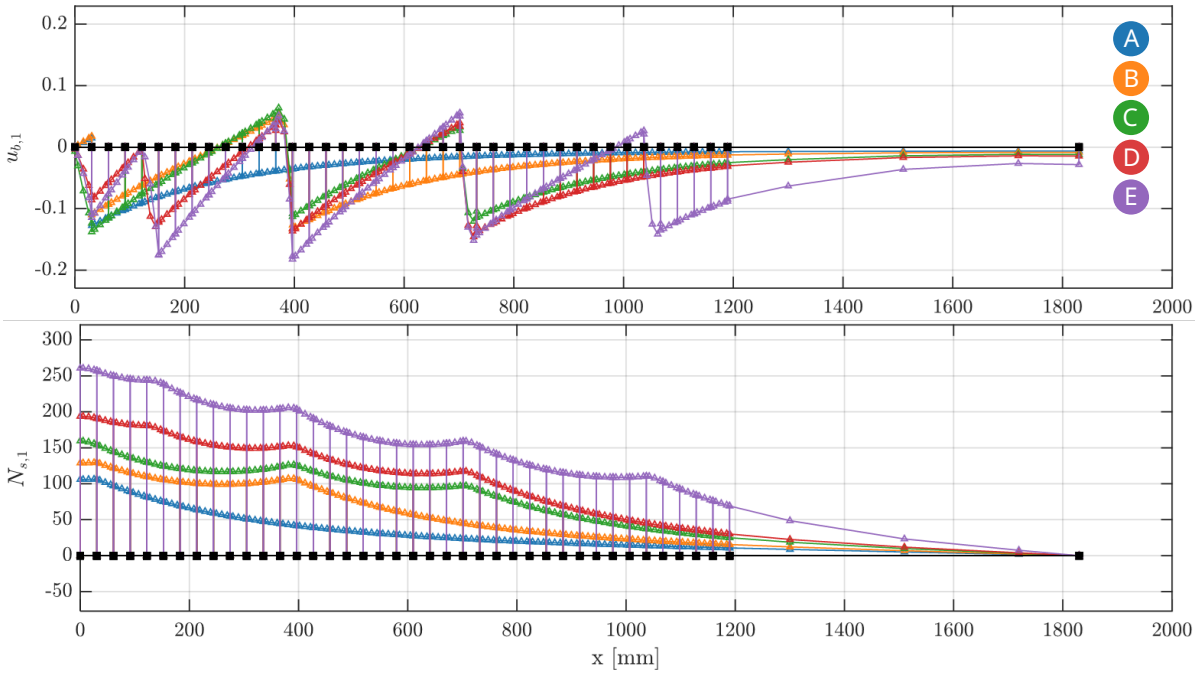

Figure 5.44. Bond-slip displacements $u_b(x)$ and steel fiber's axial force $N_s(x)$ over the beam at the five steps reported in Figure 5.41 (NE = 40).

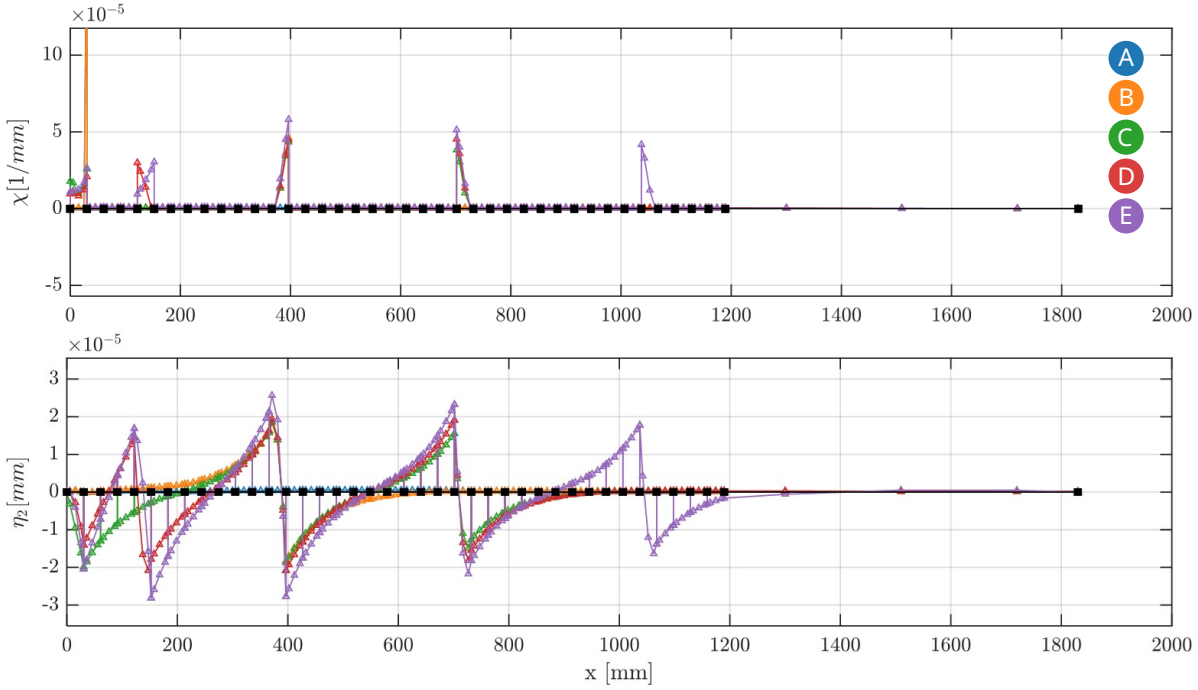

Figure 5.45. Curvature $\chi_z(x)$ and warping field $\eta_2(x)$ (cubic section shape) over the elements at five special steps reported in Figure 5.41 (NE = 40).

In the following figures, the axial strain $\varepsilon_x(x, y, z)$, the axial stress $\sigma_x(x, y, z)$ and the warping displacements $u_w(x, y, z)$ are shown.
Figure 5.46 shows the strain and stress distributions for the finest mesh (NE = 40) of the D-BW element. By looking at the positive strain and stress accumulations, the flexural cracks are easily identified. It is also worth observing how the stress in the concrete is distributed in Figure 5.46b. The highest compression stress is achieved in the top fibers at the cracks' locations, whereas zero tension is shown at the bottom fibers. Gradually, some concrete tension builds up elsewhere meaning damage is mostly concentrated in the cracks, although this is a continuum model, allowing for a very accurate and realistic representation of strain localization.

Figure 5.47 shows the strains and stresses for several M-BW element meshes. As the mesh density increases, more accurate, objective and converging results are obtained.

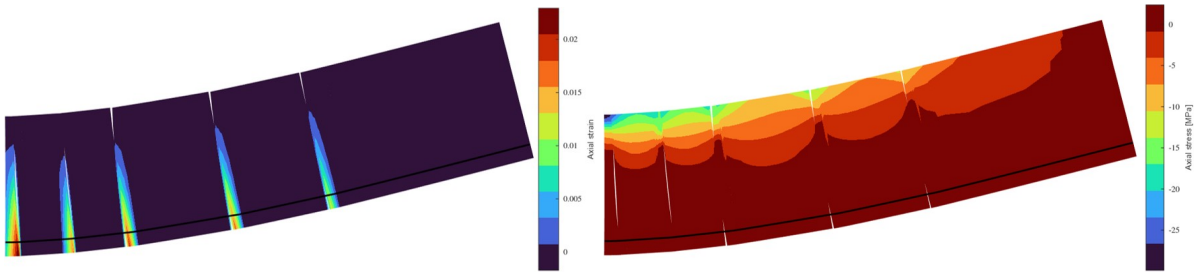

(a) **(b)**

Figure 5.46. Material point values using 40 D-BW elements: (a) axial strain $\varepsilon_x(x, y, z)$ and (b) axial stress $\sigma_x(x, y, z)$.

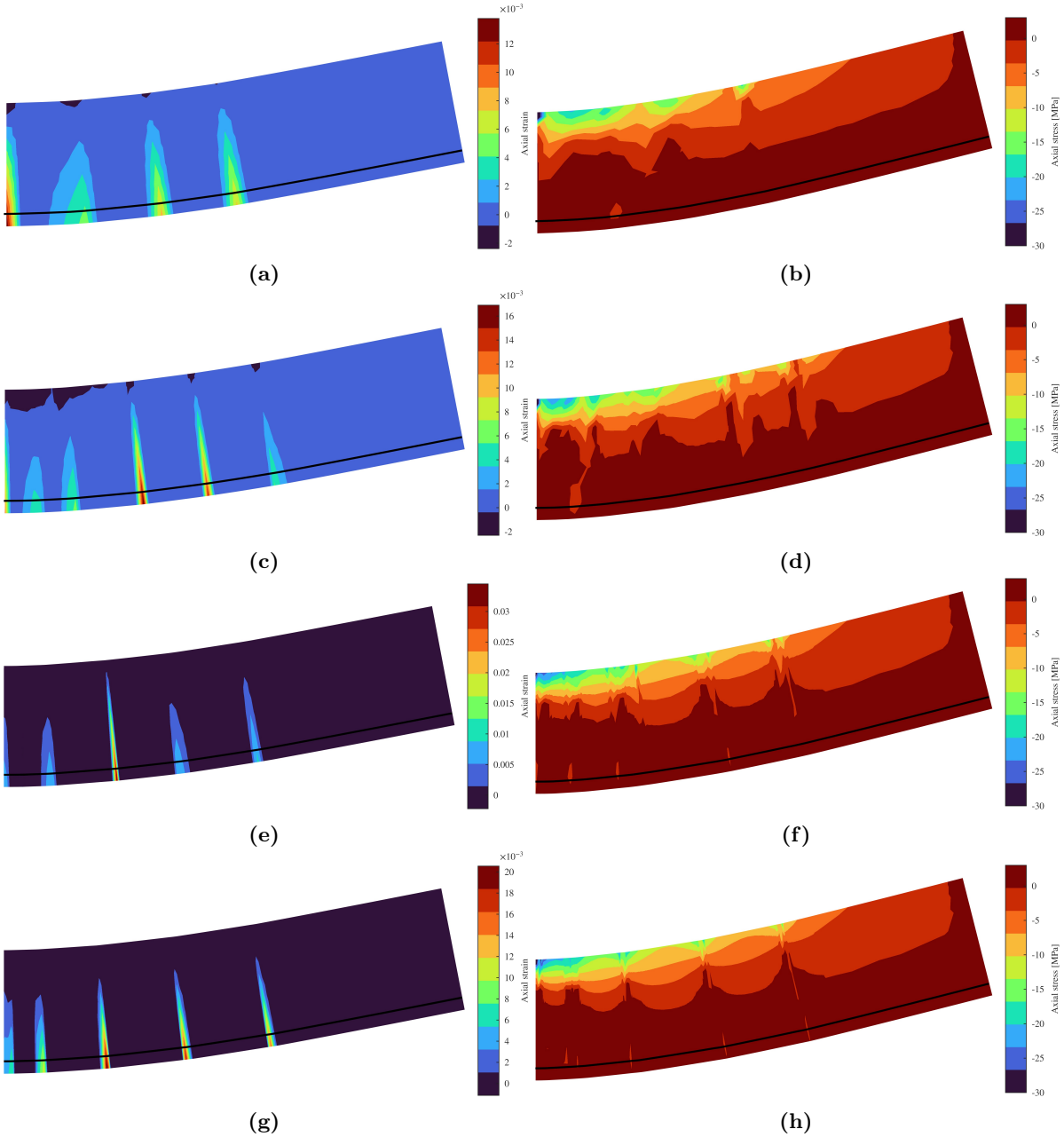

Figure 5.47. M-BW elements material point values: (a) axial strain $\varepsilon_x(x, y, z)$ (NE = 5), (b) axial stress $\sigma_x(x, y, z)$ (NE = 5), (c) axial strain $\varepsilon_x(x, y, z)$ (NE = 10), (d) axial stress $\sigma_x(x, y, z)$ (NE = 10), (e) axial strain $\varepsilon_x(x, y, z)$ (NE = 20), (f) axial stress $\sigma_x(x, y, z)$ (NE = 20), (g) axial strain $\varepsilon_x(x, y, z)$ (NE = 40), (h) axial stress $\sigma_x(x, y, z)$ (NE = 40).

Finally, the warping displacements are shown in Figure 5.48 for different M-BW element meshes. In this case, even though their distribution is not straightforward, it is interesting to note how they are distributed across the sections and the elements.

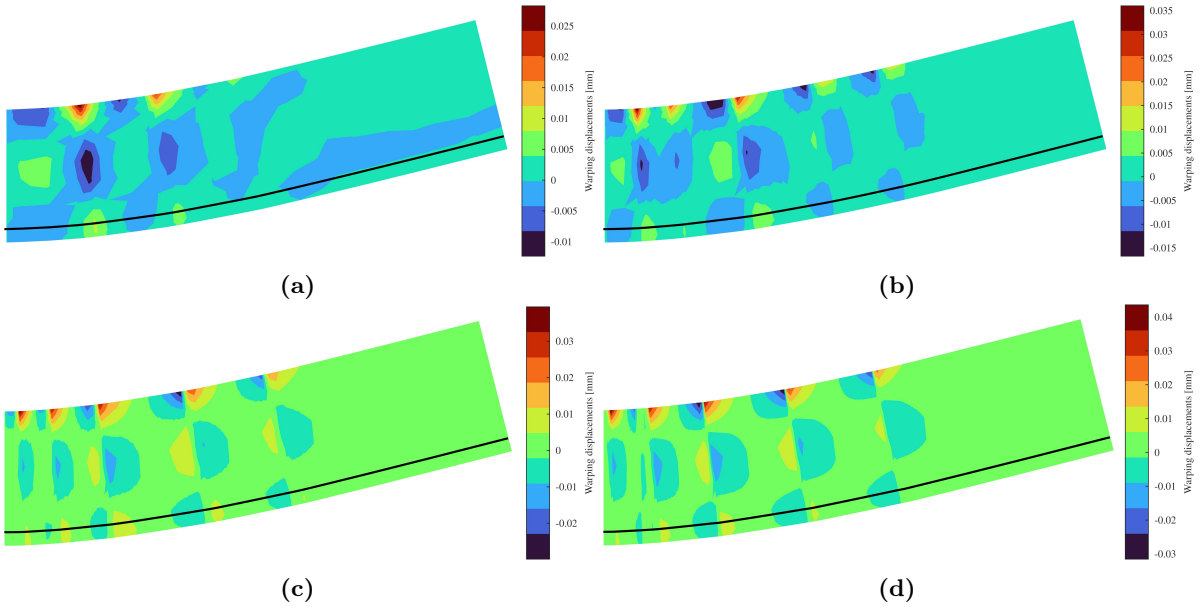

Figure 5.48. M-BW elements warping displacements $u_w(x, y, z)$ at material points: (a) NE = 5, (b) NE = 10, (c) NE = 20, (d) NE = 40.

This study demonstrates the potential of enhanced displacement-based and mixed beam elements incorporating bond-slip and warping effects to address numerical objectivity issues at cracking in RC beam analysis. Three main advantages are shown when using enhanced elements:

- Mesh independency: simulations using classical beam elements show significant mesh dependency, where cracks unrealistically spread across elements with increased mesh density. In contrast, the inclusion of bond-slip localizes the cracks within single elements
- Impact of warping: introducing warping notably improves the section kinematics, allowing the model to capture realistic deformation patterns. Simulations demonstrate convergence and accurate crack localization when warping is included.
- Comparative analysis: results comparing classical and enhanced beam elements underline the advancements. The classical model exhibits non-objective behavior, while the enhanced beam shows convergence and reduced strain localization.

Chapter 6

Summary and conclusions

New beam finite element models are proposed for the analysis of reinforced concrete, composite, and prestressed concrete structures. The goal is to integrate and disseminate advanced, implementation-ready models into modern analysis codes, improving predictive fidelity for complex structural responses while maintaining computational speed and robustness, with reduced convergence issues.

This final chapter is structured into three sections. The first one summarizes the contents of the thesis, the second one highlights the novelties, findings, and conclusions, and the third one explores potential improvements and points to directions for future developments.

6.1 Summary

Starting from well-established beam models [10, 23, 5] and building on more recent proposals for elements with enhanced kinematics, such as bond-slip [50] and warping [61, 94], the main objective of this work is to extend these formulations to the analysis of RC, prestressed, and composite frames, while improving their numerical robustness and reliability.
This is achieved at different levels:

1. Classical formulations are revisited first, including displacement-based, force-based, and mixed beam elements formulated on a consistent Timoshenko-type kinematics. It is shown that, under small-strain assumptions, the mixed and the force-based approaches are mathematically equivalent, thus providing a unified framework for classical beam models.

2. A new bond-slip formulation is developed, extending the force-based procedure to account for reinforcement-concrete interaction and prestressing effects. Also in this case, the mixed approach leads to the same formulation of the force-based element when only the force fields are interpolated. The introduction of the bond-slip degrees of freedom allows prestressing to be modeled directly at the element level, enabling the definition of construction stages and the inclusion of time-dependent phenomena such as creep and shrinkage in a consistent manner.

3. Warping is incorporated at the section level by interpolating the additional displacement field with shape functions constructed through a Gram-Schmidt orthogonalization. This approach requires only a limited number of degrees of freedom to represent the warping

modes, thus significantly reducing the size of the section operators with respect to alternative formulations [7, 61] and, in turn, the overall computational cost of the elements. Among the different formulations, the fully mixed warping and bond-slip element (force-based interpolations for the internal forces and bond, displacement interpolations for the section warping) constitutes a new contribution to the literature.

4. A wide set of constitutive models for materials and sections is implemented, including classical plasticity laws, a three-dimensional damage/plastic-damage model, and several one-dimensional cyclic laws for steel reinforcement, prestressing tendons, concrete bond-slip and other materials. Within this framework, a consistent tangent matrix for the 3D damage/plasticity model is derived, providing a novel contribution integrated into the global solution scheme.

5. Computational developments are carried out to support the proposed formulations and ensure their efficient implementation. The discussion begins with the choice of shape functions, which are selected to ensure the numerical consistency and improve the robustness of the element response. Particular attention is paid to prestressed members, for which specific rotation matrices are introduced to describe curved tendons within the fiber sections. Since the adopted constitutive models inherently exhibit softening, local regularization techniques are required to mitigate mesh sensitivity. Although such approaches facilitate implementation, with respect to nonlocal rules, they only partially remove objectivity issues, thus motivating the need for the enriched formulations with warping. Building on these foundations, the complete set of nonlinear state-determination algorithms is derived at the element, section, and material levels, together with their consistent linearizations, providing the basis for the global Newton-Raphson solution scheme.

6. Applications are presented with three main focuses: the illustration of objectivity problems in both displacement-based, force-based and mixed elements, and their resolution through the proposed regularization techniques and enriched models; the analysis of prestressed members with staged operations and improved tendon interpolation; and the demonstration that bond-slip and warping enrichments enable objective crack localization within single elements and enhance the predictive capacity of beam models. The correlation studies cover mesh- and integration-objectivity benchmarks, cantilever and beam tests under different bond assumptions, torsion- and warping-dominated members, and prestressed beams with draped tendons and staged transfer, each case isolating a specific modeling feature and assessing its effect on both global response and local fields.

6.2 Conclusions

The following conclusions can be drawn from this work:

1. An enhanced force-based fiber beam element for perfectly bonded prestressed concrete members is developed. The formulation, based on three-dimensional Timoshenko kinematics, incorporates nonlinear constitutive laws for both steel and concrete, allows the direct inclusion of tendon profiles through a rotation matrix, and applies prestressing by means of equivalent initial strains. The model proves accurate and efficient with a limited number of integration points and fibers, and is suitable for both static and time-dependent analyses of bridges and prestressed structures in general. Thanks to its block-wise organization, the formulation can be naturally extended to different materials and cross-section types.

2. The capabilities of force-based beam models are extended to include bond-slip mechanisms, evolving bond conditions, and staged time-dependent effects. A consistent integration of bond-slip at the fiber level is proposed, enabling the simulation of arbitrary tendon layouts, construction stages, and aging phenomena. The formulation incorporates curved tendons, history-dependent bond-slip laws, and time-stepping algorithms that account for creep, shrinkage, and prestress relaxation, thus providing a general framework applicable to pre- and post-tensioned members.

3. Enhanced beam elements incorporating both bond-slip and warping are formulated, including a fully mixed warping and bond-slip element that represents a new contribution to the literature. Warping is implemented through special section shape functions, reducing the number of additional degrees of freedom and lowering computational cost. These enrichments improve section kinematics and provide objective crack localization, overcoming the spurious mesh dependency typical of classical displacement- and force-based models.

4. The numerical applications carried out demonstrate that the proposed models are computationally efficient, accurate, and stable under nonlinear static and time-dependent conditions. Enhanced formulations restore objectivity in the presence of softening, provide realistic crack patterns, and extend the range of applicability of beam finite elements to complex RC, prestressed, and composite structures. Comparative analyses against experimental data and benchmark studies confirm the predictive capabilities of the models.

6.3 Recommendations on future developments

Several additional developments can be envisaged to extend the study presented in this thesis. A first and immediate perspective concerns further applications of the proposed models. While the focus is mainly on the shear effects, it would be of interest to investigate torsional responses and to apply the formulations to more complex bridge sections, assessing their accuracy with respect to refined numerical models.

Another line of development involves the material constitutive law. The current 3D damage-plasticity model can be extended to better reproduce tri-axial compressive stress states and simulate confinement effects, which are of major relevance in RC structures. This could be achieved relatively easily by modifying the condensed tri-axial state and imposing non-zero transverse stresses, rather than the null values presently adopted. A more advanced extension would allow confinement to improve the shear response as well, explicitly incorporating the role of transverse reinforcement such as stirrups.

A further enhancement concerns the adoption of a geometrically nonlinear framework, for instance through a corotational formulation, whose application in FE layered frameworks would be particularly straightforward. This would be particularly beneficial when analyzing dense meshes or crack propagation problems, and would extend the applicability of the elements to structures undergoing severe torsional or shear deformations, as well as to the buckling and post-buckling response of thin-walled frames.

Finally, another promising direction is the extension of the models to dynamic analyses. Given that plasticity and damage cyclic laws are already implemented, the formulations are readily adaptable to cyclic simulations, thus opening the way to nonlinear seismic assessments and to the study of hysteretic dissipation in RC and prestressed concrete members.

Notation

The notation adopted in the following formulations is grouped according to its level: *local*, *basic*, *section*, *material*, plus the additional fields for *bond-slip* and *prestressing*.

Local level

$\mathbf{u}_l$	local displacement vector (12 components)
$\mathbf{u}_{li} = \{u_i, v_i, w_i\}^T$	translational displacements at node i
$\boldsymbol{\vartheta}_{li} = \{\vartheta_{xi}, \vartheta_{yi}, \vartheta_{zi}\}^T$	rotational displacements at node i
$\mathbf{u}_{lj}, \boldsymbol{\vartheta}_{lj}$	analogous translational and rotational DOFs at node j
$\mathbf{p}_l$	local nodal force vector (12 components)
$\mathbf{p}_{li} = \{p_{xi}, p_{yi}, p_{zi}\}^T$	nodal forces at node i
$\mathbf{m}_{li} = \{m_{xi}, m_{yi}, m_{zi}\}^T$	nodal moments at node i
$\mathbf{p}_{lj}, \mathbf{m}_{lj}$	analogous nodal forces and moments at node j
$\mathbf{a}_l$	transformation operator (global $\rightarrow$ local DOFs)
$\mathbf{k}_l$	element stiffness matrix in local coordinates
$\mathbf{p}_l^{ext}, \mathbf{p}_l^{int}$	external and internal local force vectors
$\mathbf{N}_l(x)$	local shape function matrix (interpolating $\mathbf{u}_l$)
$\mathbf{B}_l(x)$	strain–displacement operator in local coordinates
$\mathbf{w}_q(x)$	distributed load vector along the element axis
$\tilde{\mathbf{u}}_l = \{\mathbf{u}_l^T\ \mathbf{u}_{bl}^T\ \mathbf{u}_{wl}^T\}^T$	enriched local displacement vector (bond-slip, warping)
$\tilde{\mathbf{p}}_l = \{\mathbf{p}_l^T\ \mathbf{p}_{bl}^T\ \mathbf{p}_{wl}^T\}^T$	enriched local force vector (bond-slip, warping)
$\mathbf{u}_{bl,i}, \mathbf{u}_{bl,j}$	nodal bond-slip displacements at nodes i and j
$\mathbf{p}_{bl,i}, \mathbf{p}_{bl,j}$	nodal bond-slip forces at nodes i and j
$\mathbf{u}_{wl}$	nodal warping displacements (DOFs of section warping)
$\mathbf{p}_{wl}$	nodal warping generalized forces
$\tilde{\mathbf{p}}_{lp}$	equivalent local force vector (zeros in bond-slip/warping DOFs)
$\tilde{\mathbf{p}}_{l0}$	additional local force vector (initial strains/load equivalence)
$\tilde{\mathbf{p}}_l^{int}$	internal enriched local force vector ($\tilde{\mathbf{a}}_g^T \tilde{\mathbf{q}}$)
$\tilde{\mathbf{a}}_g$	compatibility matrix eliminating rigid-body modes (enriched local system)
$\mathbf{a}_{bg}$	compatibility sub-matrix for bond-slip DOFs (from integration by parts)

Basic level

$\mathbf{v}$	basic displacement vector (6 components)
$\mathbf{q}$	basic force vector (6 components)
$\mathbf{a}_b$	kinematic transformation matrix (local $\rightarrow$ basic DOFs)
$\mathbf{k}$	element tangent stiffness matrix in basic system
$\mathbf{f} = \mathbf{k}^{-1}$	basic flexibility matrix
$\mathbf{b}(x)$	equilibrium matrix (relating section forces to $\mathbf{q}$)
$\mathbf{b}_q(x)$	operator relating distributed loads to section forces
$\mathbf{N}_b(x)$	basic shape function matrix
$\mathbf{B}_b(x)$	strain–displacement operator in basic system
$\tilde{\mathbf{v}} = \{\mathbf{v}^T\ \mathbf{v}_b^T\ \mathbf{v}_w^T\}^T$	enriched basic displacement vector (bond-slip, warping)
$\tilde{\mathbf{q}} = \{\mathbf{q}^T\ \mathbf{q}_b^T\ \mathbf{q}_w^T\}^T$	enriched basic force vector (bond-slip, warping)
$\mathbf{v}_b$	bond-slip displacement vector at interpolation points (size $m_f n_f$)
$\mathbf{q}_b$	bond-slip force vector at interpolation points (size $m_f n_f$)
$\mathbf{v}_w$	warping displacement vector at interpolation points (size $m_w n_w$)
$\mathbf{q}_w$	warping generalized force vector at interpolation points (size $m_w n_w$)
$\tilde{\mathbf{k}}$	enriched element stiffness matrix in basic system
$\tilde{\mathbf{q}}_0$	enriched equivalent basic force vector (initial strains and loads)
$\tilde{\mathbf{f}}$	enriched element flexibility matrix
m_f, n_f	interpolation points per slipping fiber; number of slipping fibers
m_w, n_w	interpolation points per warping DOF; number of warping DOFs
$\tilde{\mathbf{a}}_b$	compatibility matrix in enriched basic formulation

Section level

Timoshenko (rigid section)

$\mathbf{u}_s(x)$	generalized section displacement vector
$\mathbf{e}(x)$	generalized section deformation vector
$\mathbf{s}(x)$	generalized section force vector
$\mathbf{D}_s(x)$	operator mapping displacements $\rightarrow$ section strains
$\mathbf{D}_s^*(x)$	operator enforcing sectional equilibrium
$\mathbf{a}_s(y,z)$	compatibility operator mapping section to fibers
$\mathbf{k}_s(x)$	section tangent stiffness, $\int_A \mathbf{a}_s^T \mathbf{k}_m \mathbf{a}_s \, dA$
$\mathbf{f}_s(x) = \mathbf{k}_s^{-1}(x)$	section flexibility matrix
$\hat{\mathbf{s}}(x)$	constitutive section response
$A,\ I_y,\ I_z,\ J,\ A_y^*, A_z^*$	geometric parameters and shear correction factors

Section loads

$\mathbf{p}(x)$	distributed section load vector
$\mathbf{s}_p(x)$	section forces due to distributed loads

Bond-slip specific

$\mathbf{u}_b(x)$	section bond-slip displacement vector (n_f components)
$\mathbf{e}_b(x) = \dfrac{\partial \mathbf{u}_b}{\partial x}$	bond-slip "strain" along the axis
$\mathbf{s}_b(x)$	axial forces in fibers with bond-slip
$\mathbf{p}_b(x)$	bond forces per unit length, $\int_{l_b} \boldsymbol{\tau}_b \, dl$
$k_{sb}(x)$	section bond stiffness, $\int_{l_b} k_b \, dl$
$\hat{\mathbf{p}}_b(x)$	constitutive response of bond interface (section level)
$\mathbf{b}_b(x),\ \mathbf{b}_{b,x}(x)$	interpolation/equilibrium matrices for $\mathbf{s}_b$ and its derivative
$\boldsymbol{\delta}_b$	selector (row) for slipping fibers

Warping specific

$\boldsymbol{\eta}(x)$	section warping DOFs (n_w components)
$\boldsymbol{\eta}_x(x) = \dfrac{\partial \boldsymbol{\eta}}{\partial x}$	derivatives of warping DOFs
$\mathbf{M}_\eta(y,z)$	warping shape function matrix over the section
$\mathbf{M}_{\eta,y}(y,z),\ \mathbf{M}_{\eta,z}(y,z)$	derivatives of $\mathbf{M}_\eta$ wrt y and z
$\mathbf{B}_w(x),\ \mathbf{B}_{w,x}(x)$	interpolation matrices for $\boldsymbol{\eta},\ \boldsymbol{\eta}_x$
$\mathbf{s}_w(x)$	generalized section forces conjugate to warping DOFs

Bond-slip and warping enriched section

$\tilde{\mathbf{e}}(x) = \{\mathbf{e}, \mathbf{e}_b, \mathbf{e}_w\}$	enriched section strain vector
$\tilde{\mathbf{s}}(x) = \{\mathbf{s}, \mathbf{s}_b, \mathbf{s}_w\}$	enriched section stress/force vector
$\tilde{\mathbf{a}}_s(y, z)$	enriched section operator including slip and warping
$\tilde{\mathbf{k}}_s(x)$	enriched section tangent stiffness matrix
$\tilde{\mathbf{f}}_s(x) = \tilde{\mathbf{k}}_s^{-1}(x)$	enriched section flexibility matrix
$\hat{\mathbf{s}}_w(x)$	constitutive response of warping components

Partitioned operators (mixed formulation)

$\mathbf{k}_{ss}(x), \mathbf{k}_{sw}(x)$	partitioned section stiffness blocks
$\mathbf{k}_{ws}(x), \mathbf{k}_{ww}(x)$	
$\mathbf{b}_s(x) =$	extended equilibrium matrix for s-fields
$\text{diag}(\mathbf{b}(x), \mathbf{b}_b(x))$	
$\mathbf{k}_w(x)$	reduced section stiffness for warping fields
$\mathbf{b}_{sw}(x), \mathbf{b}_{ws}(x)$	mixed coupling operators between s- and w-fields

Material level

$\boldsymbol{\varepsilon}_m(x, y, z)$	material strain vector at a fiber
$\boldsymbol{\sigma}_m(x, y, z)$	material stress vector at a fiber
$\hat{\boldsymbol{\sigma}}_m(x, y, z)$	constitutive material stresses (from constitutive law)
$\mathbf{k}_m(x, y, z)$	material tangent stiffness matrix at a fiber (condensed)
$\mathbf{C}_{t,mm}, \mathbf{C}_{t,mc}$	3D tangent sub-matrices (for condensation)
$\mathbf{C}_{t,cm}, \mathbf{C}_{t,cc}$	3D tangent sub-matrices (for condensation)

Prestressing

$\mathbf{P}_f$	tendon nodal coordinates input matrix
$\varepsilon_{0,p}$	imposed axial strain in the tendon axis (initial prestress)
$\mathbf{t}_f(x)$	tendon tangent vector along the element axis
$\mathbf{R}(x)$	tendon rotation matrix (Rodrigues)
$\bar{\boldsymbol{\beta}}(x)$	unnormalized rotation axis vector
$\boldsymbol{\beta}(x)$	normalized rotation axis vector
$\widehat{\boldsymbol{\beta}}(x)$	skew-symmetric matrix of $\boldsymbol{\beta}$
$\boldsymbol{\beta}(x) \otimes \boldsymbol{\beta}(x)$	dyadic product of $\boldsymbol{\beta}$

Bibliography

[1] V. S. Gopalaratnam and Surendra P. Shah. Softening Response of Plain Concrete in Direct Tension. *Journal Proceedings*, 82(3):310–323, 5 1985.

[2] I. Demir Karsan and James O. Jirsa. Behavior of Concrete Under Compressive Loadings. *Journal of the Structural Division*, 95(12):2543–2564, 12 1969.

[3] Marco Menegotto and Paolo Emilio Pinto. Method of analysis for cyclically loaded RC plane frames including changes in geometry and non-elastic behavior of elements under combined normal force and bending. In *Proc. of IABSE Symposium on Resistance and Ultimate Deformability of Structures Acted on by Well Defined Repeated Loads*, 1973.

[4] Laura N. Lowes and Arash Altoontash. Modeling Reinforced-Concrete Beam-Column Joints Subjected to Cyclic Loading. *Journal of Structural Engineering*, 129(12):1686–1697, 12 2003.

[5] Daniela Addessi and Vincenzo Ciampi. A regularized force-based beam element with a damage–plastic section constitutive law. *International Journal for Numerical Methods in Engineering*, 70(5):610–629, 2007.

[6] M. H. Scott and O. M. Hamutçuoğlu. Numerically consistent regularization of force-based frame elements. *International Journal for Numerical Methods in Engineering*, 76(10):1612–1631, 12 2008.

[7] Paolo Di Re, Daniela Addessi, and Filip C Filippou. Mixed 3D Beam Element with Damage Plasticity for the Analysis of RC Members under Warping Torsion. *Journal of Structural Engineering*, 144(6):1–13, 2018.

[8] Mohd Hisham Mohd Yassin. *Nonlinear Analysis of Prestressed Concrete Structures under Monotonic and Cycling Loads*. PhD thesis, University of California, 1994.

[9] Massimo Petracca, Luca Pelà, Riccardo Rossi, Stefano Zaghi, Guido Camata, and Enrico Spacone. Micro-scale continuous and discrete numerical models for nonlinear analysis of masonry shear walls. *Construction and Building Materials*, 149:296–314, 9 2017.

[10] Enrico Spacone, Filip C Filippou, and Fabio Taucer. Fibre beam-column model for non-linear analysis of R/C frames: Part I. Formulation. *Earthquake Engineering & Structural Dynamics*, 25(7):711–725, 7 1996.

[11] Marco Petrangeli, Paolo Emilio Pinto, and Vincenzo Ciampi. Fiber Element for Cyclic Bending and Shear of RC Structures. I: Theory. *Journal of Engineering Mechanics*,

125(9):994–1001, 9 1999.

[12] Enrico Spacone. *Flexibility-based finite element models for the nonlinear static and dynamic analysis of concrete frame structures.* University of California, Berkeley, 1994.

[13] Enrico Spacone, Vincenzo Ciampi, and Filip C. Filippou. Mixed formulation of nonlinear beam finite element. *Computers & Structures*, 58(1):71–83, 1 1996.

[14] Daniela Addessi, Sonia Marfia, and Elio Sacco. A plastic nonlocal damage model. *Computer Methods in Applied Mechanics and Engineering*, 191(13-14):1291–1310, 1 2002.

[15] Giorgio Monti and Enrico Spacone. Reinforced Concrete Fiber Beam Element with Bond-Slip. *Journal of Structural Engineering*, 126(6):654–661, 6 2000.

[16] J Coleman and Enrico Spacone. Localization issues in force-based frame elements. *Journal of Structural Engineering*, 127(11):1257–1265, 2001.

[17] R H J Peerlings, M G D Geers, R De Borst, and WAM1032 Brekelmans. A critical comparison of nonlocal and gradient-enhanced softening continua. *International Journal of solids and Structures*, 38(44-45):7723–7746, 2001.

[18] M. J. Turner, R. W. Clough, H. C. Martin, and L. J. Topp. Stiffness and Deflection Analysis of Complex Structures. *Journal of the Aeronautical Sciences*, 23(9):805–823, 9 1956.

[19] R. Clough. The Finite Element Method in Plane Stress Analysis. In *Proc. ASCE Conf. on Electronic Computation*, 1960.

[20] K J Bathe. *Finite Element Procedures.* Prentice Hall, 1996.

[21] M A Crisfield. *Non-linear Finite Element Analysis of Solids and Structures.* Wiley, 1986.

[22] Stephen P. Timoshenko and Paul Ehrenfest. On the correction for shear of the differential equation for transverse vibrations of prismatic bars. *The London, Edinburgh, and Dublin Philosophical Magazine and Journal of Science*, 41(245):744–746, 5 1921.

[23] R. L. Taylor, F. C. Filippou, A. Saritas, and F. Auricchio. A mixed finite element method for beam and frame problems. *Computational Mechanics*, 31(1-2):192–203, 5 2003.

[24] K. D. Hjelmstad and E. Taciroglu. Mixed methods and flexibility approaches for nonlinear frame analysis. *Journal of Constructional Steel Research*, 58(5-8), 2002.

[25] Ansgar Neuenhofer and Filip C. Filippou. Evaluation of Nonlinear Frame Finite-Element Models. *Journal of Structural Engineering*, 123(7):958–966, 7 1997.

[26] Ashraf Ayoub and Filip C Filippou. Mixed Formulation of Bond-Slip Problems under Cyclic Loads. *Journal of Structural Engineering*, 125(6):661–671, 1999.

[27] Suchart Limkatanyu and Enrico Spacone. Reinforced Concrete Frame Element with Bond Interfaces. I: Displacement-Based, Force-Based, and Mixed Formulations. *Journal of Structural Engineering*, 128(3):346–355, 3 2002.

[28] Enrico Spacone and Suchart Limkatanyu. Responses of reinforced concrete members including bond-slip effects. *ACI Structural Journal*, 97(6), 2000.

[29] M. Reza Salari, Enrico Spacone, P. Benson Shing, and Dan M. Frangopol. Nonlinear Analysis of Composite Beams with Deformable Shear Connectors. *Journal of Structural Engineering*, 124(10):1148–1158, 10 1998.

[30] Remo Magalhaes De Souza. *Force-based Finite Element for Large Displacement Inelastic Analysis of Frames*. PhD thesis, University of California, Berkeley, Berkeley, CA, USA, 2000.

[31] J P Almeida, S Das, and R Pinho. Adaptive force-based frame element for regularized softening response. *Computers & Structures*, 102-103:1–13, 2012.

[32] M. Reza Salari and Enrico Spacone. Analysis of Steel-Concrete Composite Frames with Bond-Slip. *Journal of Structural Engineering*, 127(11):1243–1250, 11 2001.

[33] Michael H Scott and Gregory L Fenves. Plastic Hinge Integration Methods for Force-Based Beam & Column Elements. *Journal of Structural Engineering*, 132(2):244–252, 2006.

[34] Graham H. Powell and Paul Fu-Song Chen. 3D Beam-Column Element with Generalized Plastic Hinges. *Journal of Engineering Mechanics*, 112(7):627–641, 7 1986.

[35] V Ciampi and L Carlesimo. A Nonlinear Beam Element for Seismic Analysis of Structures. In *Proceedings of the 8th European Conference on Earthquake Engineering*, page 6.3/73–6.3/80, Lisbon, Portugal, 1986. Laboratório Nacional de Engenharia Civil.

[36] CA Zeris. *Three-dimensional nonlinear response of reinforced concrete buildings*. PhD thesis, University of California, Berkeley, 1986.

[37] Christos A. Zeris and Stephen A. Mahin. Analysis of Reinforced Concrete Beam-Columns under Uniaxial Excitation. *Journal of Structural Engineering*, 114(4):804–820, 4 1988.

[38] F Taucer, E Spacone, and FC Filippou. A fiber beam-column element for seismic response analysis of reinforced concrete structures. Technical report, Earthquake Engineering Research Center, College of Engineering, University of California, Berkeley, 12 1991.

[39] F McKenna, G L Fenves, and M H Scott. Open System for Earthquake Engineering Simulation, 2000.

[40] Robert L Taylor. FEAP-A finite element analysis program, 2014.

[41] M Petrangeli. *Modelli numerici per Strutture monodimensionali in cemento armato*. PhD thesis, University of Rome "La Sapienza", Rome, Italy, 1996.

[42] G. Meschke, R. Lackner, and H. A. Mang. An anisotropic elastoplastic-damage model for plain concrete. *International Journal for Numerical Methods in Engineering*, 42(4):703–727, 6 1998.

[43] K Washizu. On the variational principles of elasticity and plasticity. Technical report, Massachusetts Inst Of Tech Cambridge Aeroelastic And Structures Research Lab, 1955.

[44] M Petrangeli and V Ciampi. Equilibrium based iterative solutions for the non-linear beam problem. *International Journal for Numerical Methods in Engineering*, 40(3):423–437, 2 1997.

[45] Suchart Limkatanyu and Enrico Spacone. Effects of reinforcement slippage on the non-linear response under cyclic loadings of RC frame structures. *Earthquake Engineering and Structural Dynamics*, 32(15):2407–2424, 12 2003.

[46] Filip C. Filippou. A Simple Model for Reinforcing Bar Anchorages Under Cyclic Excitations. *Journal of Structural Engineering*, 112(7):1639–1659, 7 1986.

[47] Ashraf Ayoub and Filip C. Filippou. Mixed Formulation of Nonlinear Steel-Concrete Composite Beam Element. *Journal of Structural Engineering*, 126(3):371–381, 3 2000.

[48] Ashraf Ayoub. Nonlinear Analysis of Reinforced Concrete Beam-Columns with Bond-Slip. *Journal of Engineering Mechanics*, 132(11):1177–1186, 2006.

[49] Ashraf Ayoub and F C Filippou. Finite-Element Model for Pretensioned Prestressed Concrete Girders. *Journal of Structural Engineering*, 136(4):401–409, 5 2010.

[50] Chin-Long Lee. *Hu-Washizu three-dimensional frame formulations including bond-slip and singular section response*. PhD thesis, University of California, Berkeley, 2008.

[51] Chin-Long Lee and Filip C. Filippou. Frame elements with mixed formulation for singular section response. *International Journal for Numerical Methods in Engineering*, 78(11):1320–1344, 2009.

[52] Chin-Long Lee and Filip C Filippou. Frame Element with Mixed Formulations for Composite and RC Members with Bond Slip. I: Theory and Fixed-End Rotation. *Journal of Structural Engineering*, 141(11):4015039, 2015.

[53] Chin-Long Lee and Filip C Filippou. Frame Element with Mixed Formulations for Composite and RC Members with Bond Slip. II: Correlation Studies. *Journal of Structural Engineering*, 141(11):4015040, 2015.

[54] Erik Åldstedt and Pål G Bergan. Nonlinear Time-Dependent Concrete-Frame Analysis. *Journal of the Structural Division*, 104(7):1077–1092, 1978.

[55] Afsin Saritas. *Mixed formulation frame element for shear critical steel and reinforced concrete members*. PhD thesis, University of Berkeley, California, 2006.

[56] Veronique Le Corvec. Nonlinear 3d frame element with multi-axial coupling under consideration of local effects, 2012.

[57] Mohammed Khalil Ferradi, Xavier Cespedes, and Mathieu Arquier. A higher order beam finite element with warping eigenmodes. *Engineering Structures*, 46:748–762, 1 2013.

[58] Mohammed Khalil Ferradi and Xavier Cespedes. A new beam element with transversal and warping eigenmodes. *Computers & Structures*, 131:12–33, 1 2014.

[59] R. F. Vieira, F. B.E. Virtuoso, and E. B.R. Pereira. A higher order thin-walled beam

model including warping and shear modes. *International Journal of Mechanical Sciences*, 66:67–82, 1 2013.

[60] R. F. Vieira, F. B.E. Virtuoso, and E. B.R. Pereira. A higher order beam model for thin-walled structures with in-plane rigid cross-sections. *Engineering Structures*, 84:1–18, 2 2015.

[61] Daniela Addessi, Paolo Di Re, and Gabriele Cimarello. Enriched beam finite element models with torsion and shear warping for the analysis of thin-walled structures. *Thin-Walled Structures*, 159:107259, 2 2021.

[62] Paolo Di Re and Daniela Addessi. Computational Enhancement of a Mixed 3D Beam Finite Element with Warping and Damage. *Journal of Applied and Computational Mechanics*, 8(1):260–281, 1 2022.

[63] Bijan O Aalami. Load Balancing: A Comprehensive Solution to Post-Tensioning. *ACI Structural Journal*, 87(6), 1 1990.

[64] André Picard, Bruno Massicotte, and Josée Bastien. Relative Efficiency of External Prestressing. *Journal of Structural Engineering*, 121(12):1832–1841, 1995.

[65] N A Vu, A Castel, and R François. Response of post-tensioned concrete beams with unbonded tendons including serviceability and ultimate state. *Engineering Structures*, 32(2):556–569, 2010.

[66] Kang Su Kim and Deuck Hang Lee. Nonlinear analysis method for continuous post-tensioned concrete members with unbonded tendons. *Engineering Structures*, 40:487–500, 2012.

[67] Leandro S Moreira, João Batista M Sousa, and Evandro Parente. Nonlinear finite element simulation of unbonded prestressed concrete beams. *Engineering Structures*, 170:167–177, 4 2018.

[68] De Cheng Feng, Gang Wu, and Chao-Lie Ning. A regularized force-based Timoshenko fiber element including flexure-shear interaction for cyclic analysis of RC structures. *International Journal of Mechanical Sciences*, 160:59–74, 2019.

[69] De Cheng Feng and Xiaodan Ren. Implicit gradient-enhanced force-based Timoshenko fiber element formulation for reinforced concrete structures. *International Journal for Numerical Methods in Engineering*, 122(2):325–347, 2021.

[70] De Cheng Feng, Xin Chen, Frank McKenna, and Ertugrul Taciroglu. Consistent Nonlocal Integral and Gradient Formulations for Force-Based Timoshenko Elements with Material and Geometric Nonlinearities. *Journal of Structural Engineering*, 149(4):4023018, 2023.

[71] Heather Anne Doty. *A Module for Finite Element Analysis of Prestressed Concrete Bridges.* PhD thesis, Department of Civil, Environmental and Architectural Engineering, University of Colorado, Boulder, USA, 2001.

[72] Luca Parente, Daniela Addessi, and Enrico Spacone. A fiber beam element based on plastic and damage models for prestressed concrete structures. *Engineering Structures*, 292:116501,

10 2023.

[73] D Addessi and V Ciampi. A beam finite element based on damage mechanics for dynamical structural analysis, 2002.

[74] D C Drucker and W Prager. Soil mechanics and plastic analysis or limit design. *Quarterly of Applied Mathematics*, 10(2):157–165, 1952.

[75] J C Simo and J W Ju. Strain- and stress-based continuum damage models—I. Formulation. *International Journal of Solids and Structures*, 23(7):821–840, 1987.

[76] R. I. Gilbert. Shrinkage, Cracking and Deflection-the Serviceability of Concrete Structures. *Electronic Journal of Structural Engineering*, 1(1):15–37, 1 2001.

[77] Tiejiong Lou, Sergio M.R. Lopes, and Adelino V. Lopes. Nonlinear and time-dependent analysis of continuous unbonded prestressed concrete beams. *Computers & Structures*, 119:166–176, 4 2013.

[78] Tiejiong Lou, Sergio M R Lopes, and Adelino V Lopes. A finite element model to simulate long-term behavior of prestressed concrete girders. *Finite Elements in Analysis and Design*, 81:48–56, 8 2014.

[79] Andrea Dall'Asta and Alessandro Zona. Non-linear analysis of composite beams by a displacement approach. *Computers and Structures*, 80(27-30):2217–2228, 11 2002.

[80] Andrea Dall'Asta and Alessandro Zona. Finite Element Model for Externally Prestressed Composite Beams with Deformable Connection. *Journal of Structural Engineering*, 131(5):706–714, 5 2005.

[81] Alessandro Zona, Laura Ragni, and Andrea Dall'Asta. Finite element formulation for geometric and material nonlinear analysis of beams prestressed with external slipping tendons. *Finite Elements in Analysis and Design*, 44(15):910–919, 11 2008.

[82] João Batista M. Sousa, Claudio E.M. Oliveira, and Amilton R. da Silva. Displacement-based nonlinear finite element analysis of composite beam-columns with partial interaction. *Journal of Constructional Steel Research*, 66(6):772–779, 6 2010.

[83] João Batista M. Sousa, Evandro Parente, Esio M.F. Lima, and Michelle V.X. Oliveira. Beam-tendon finite elements for post-tensioned steel-concrete composite beams with partial interaction. *Journal of Constructional Steel Research*, 159:147–160, 8 2019.

[84] Ayman El-Zohairy, Hani Salim, Hesham Shaaban, Suzan Mustafa, and Ashraf El-Shihy. Finite-Element Modeling of Externally Posttensioned Composite Beams. *Journal of Bridge Engineering*, 20(12), 12 2015.

[85] Ayman El-Zohairy, Hani Salim, Hesham Shaaban, Suzan Mustafa, and Ashraf El-Shihy. Finite element analysis and parametric study of continuous steel–concrete composite beams stiffened with post-tensioned tendons. *Advances in Structural Engineering*, 21(6):933–945, 4 2018.

[86] Tiejiong Lou, Sergio M.R. Lopes, and Adelino V. Lopes. Numerical modeling of externally

prestressed steel-concrete composite beams. *Journal of Constructional Steel Research*, 121:229–236, 6 2016.

[87] R. Emre Erkmen and Mario M. Attard. Displacement-based finite element formulations for material-nonlinear analysis of composite beams and treatment of locking behaviour. *Finite Elements in Analysis and Design*, 47(12):1293–1305, 12 2011.

[88] Gianluca Ranzi, Andrea Dall'Asta, Laura Ragni, and Alessandro Zona. A geometric nonlinear model for composite beams with partial interaction. *Engineering Structures*, 32(5):1384–1396, 5 2010.

[89] René De Borst. Some recent developments in computational modelling of concrete fracture. *International Journal of Fracture*, 86(1-2):5–36, 1997.

[90] Massimo Petracca, Luca Pelà, Riccardo Rossi, Sergio Oller, Guido Camata, and Enrico Spacone. Regularization of first order computational homogenization for multiscale analysis of masonry structures. *Computational Mechanics*, 57(2):257–276, 2 2016.

[91] L. Parente, D. Addessi, B.A. Izzuddin, and E. Spacone. Objectivity and Consistency of the Cracking Response of RC Beams with Conventional Models. *Proceedings of the Fifteenth International Conference on Computational Structures Technology*, 9:1–16, 8 2024.

[92] Paolo Di Re. *3D beam-column finite elements under tri-axial stess-strain states: non-uniform shear stress distribution and warping*. PhD thesis, University of Rome, Sapienza, Rome, 2 2017.

[93] Cristina Gatta, Daniela Addessi, and Fabrizio Vestroni. Static and dynamic nonlinear response of masonry walls. *International Journal of Solids and Structures*, 155:291–303, 2018.

[94] João Sio, Huma Khalid, and Bassam A. Izzuddin. Objective modelling of reinforced concrete planar frame sub-systems under extreme loading. *Structures*, 60:105863, 2 2024.

[95] Graham H. Powell. Theory of Nonlinear Elastic Structures. *Journal of the Structural Division*, 95(12):2687–2702, 12 1969.

[96] R. W. Clough, K. L. Benuska, and E. L. Wilson. Inelastic earthquake response of tall buildings. In *Third World Conference on Earthquake Engineering*, Wellington, New Zealand, 1965.

[97] Melbourne F. Giberson. Two Nonlinear Beams With Definitions of Ductility. *Journal of the Structural Division*, 95(2):137–157, 2 1969.

[98] Marco Menegotto and Paolo E. Pinto. Slender RC Compressed Members in Biaxial Bending. *Journal of the Structural Division*, 103(3):587–605, 3 1977.

[99] Zdenek P. Bazant. Instability, ductility, and size effect in strain-softening concrete. *ASCE J Eng Mech Div*, 102(2):331–344, 4 1976.

[100] J Lubliner, J Oliver, S Oller, and E Oñate. A plastic-damage model for concrete. *International Journal of Solids and Structures*, 25(3):299–326, 1989.

[101] H B Kupfer, H K Hilsdorf, and H Rusch. Behavior of Concrete Under Biaxial Stresses. *ACI Journal Proceedings*, 66(8):656–666, 1969.

[102] A A Griffith. The phenomena of rupture and flow in solids. *Philosophical Transactions of the Royal Society of London. Series A, Containing Papers of a Mathematical or Physical Character*, 221(582-593):163–198, 1 1921.

[103] A. Hillerborg, M. Modéer, and P.-E. Petersson. Analysis of crack formation and crack growth in concrete by means of fracture mechanics and finite elements. *Cement and Concrete Research*, 6(6):773–781, 11 1976.

[104] T Belytschko, J Fish, and B E Engelmann. A finite element with embedded localization zones. *Computer Methods in Applied Mechanics and Engineering*, 70(1):59–89, 1988.

[105] Eduardo N. Dvorkin, Alberto M. Cuitiño, and Gustavo Gioia. Finite elements with displacement interpolated embedded localization lines insensitive to mesh size and distortions. *International Journal for Numerical Methods in Engineering*, 30(3):541–564, 8 1990.

[106] F J Vecchio and M P Collins. Response of reinforced concrete to in-plane shear and normal stresses. Technical Report 82, Department of Civil Engineering, University of Toronto, 1982.

[107] Zdeněk P. Bažant and Pietro G. Gambarova. Crack Shear in Concrete: Crack Band Microplane Model. *Journal of Structural Engineering*, 110(9):2015–2035, 9 1984.

[108] Jacky Mazars. A description of micro- and macroscale damage of concrete structures. *Engineering Fracture Mechanics*, 25(5-6):729–737, 1 1986.

[109] J. Mazars and G. Pijaudier-Cabot. Continuum Damage Theory—Application to Concrete. *Journal of Engineering Mechanics*, 115(2):345–365, 2 1989.

[110] Jean Lemaitre. Coupled elasto-plasticity and damage constitutive equations. *Computer Methods in Applied Mechanics and Engineering*, 51(1-3):31–49, 9 1985.

[111] J Lee and G L Fenves. Plastic-damage model for cyclic loading of concrete structures. *Journal of Engineering Mechanics*, 124(8):892–900, 1998.

[112] W F Chen and A F Saleeb. *Constitutive Equations for Engineering Materials*. Elsevier, 1994.

[113] J Lemaitre and J L Chaboche. *Mechanics of Solid Materials*. Cambridge University Press, 1994.

[114] J C Simo and T J R Hughes. *Computational Inelasticity*, volume 7 of *Interdisciplinary Applied Mathematics*. Springer-Verlag, New York, 1998.

[115] R de Borst, M A Crisfield, J J C Remmers, and C V Verhoosel. *Nonlinear Finite Element Analysis of Solids and Structures*. Wiley, 2012.

[116] Chin-Long Lee and Filip C. Filippou. Efficient Beam-Column Element with Variable Inelastic End Zones. *Journal of Structural Engineering*, 135(11), 2009.

[117] Filip C. Filippou, Egor P. Popov, and Vitelmo V. Bertero. *Effects of bond deterioration on hysteretic behavior of reinforced concrete joints.* Earthquake Engineering Research Center, University of California ;, Berkeley, Calif. :, 1983.

[118] Paolo Di Re and Daniel Macabeo Benaim Sanchez. Finite difference technique for the evaluation of the transverse displacements in force-based beam finite elements. *Computer Methods in Applied Mechanics and Engineering*, 428:117067, 8 2024.

[119] Carl R. J. De Boor. A Practical Guide to Splines. *Mathematics of Computation*, 34(149):325, 1 1980.

[120] R. W. Brockett. Robotic manipulators and the product of exponentials formula. *Lecture Notes in Control and Information Sciences*, pages 120–129, 1984.

[121] De Cheng Feng, Xiaodan Ren, and Jie Li. Implicit Gradient Delocalization Method for Force-Based Frame Element. *Journal of Structural Engineering*, 142(2):4015122, 2016.

[122] J. Oliver. A consistent characteristic length for smeared cracking models. *International Journal for Numerical Methods in Engineering*, 28(2):461–474, 2 1989.

[123] John M Hedgepeth. *Stress concentrations in filamentary structures.* National Aeronautics and Space Administration, 1961.

[124] Paolo Di Re, Daniela Addessi, and Elio Sacco. A multiscale force-based curved beam element for masonry arches. *Computers & Structures*, 208:17–31, 10 2018.

[125] M Petracca, F Candeloro, and G Camata. Scientific Toolkit for Opensees, 2017.

[126] Laura N Lowes, Nilanjan Mitra, and Arash Altoontash. A beam-column joint model for simulating the earthquake response of reinforced concrete frames. Technical report, Pacific Earthquake Engineering Research Center, University of California, Berkeley, 8 2003.

[127] Ned Hamilton Burns. *Load-Deformation Characteristics of Beam-Column Connections of Reinforced Concrete.* PhD thesis, University of Illinois at Urbana-Champaign, 1962.

[128] Daniele Losanno, Simone Galano, Fulvio Parisi, Maria Rosaria Pecce, and Edoardo Cosenza. Experimental Investigation on Nonlinear Flexural Behavior of Post-Tensioned Concrete Bridge Girders with Different Grouting Conditions and Prestress Levels. *Journal of Bridge Engineering*, 29(3):4023121, 2024.

[129] Justas Slaitas and Juozas Valivonis. Concrete cracking and deflection analysis of RC beams strengthened with prestressed FRP reinforcements under external load action. *Composite Structures*, 255:113036, 1 2021.

[130] Rafael Ruiz, Miguel Fernández Ruiz, Leonardo Todisco, and Hugo Corres. Shear resistance of prestressed HPFRC beams without stirrups: A mechanical analysis of shear-transfer actions based on detailed experimental measurements. *Engineering Structures*, 306:117711, 5 2024.

[131] Luc Taerwe, Stijn Matthys, and others. *fib Model Code for Concrete Structures.* Ernst & Sohn, Wiley, 2013.